Femtosecond-laser Irradiation as a Platform for Tailoring the Optoelectronic Properties of Silicon

by
Matthew John Smith

B.S. Materials Science and Engineering
Johns Hopkins University, 2007

SUBMITTED TO THE DEPARTMENT OF
MATERIALS SCIENCE AND ENGINEERING IN
PARTIAL FULFILLMENT OF THE REQUIREMENTS FOR THE DEGREE OF

DOCTOR OF PHILOSOPHY IN MATERIALS SCIENCE AND ENGINEERING
AT THE
MASSACHUSETTS INSTITUTE OF TECHNOLOGY

June 2012

Signature of Author: _____
Department of Materials Science and Engineering
May 24, 2012

Certified by: _____
Silvija Gradečak
Thomas Lord Assistant Professor in Materials Science and Engineering
Thesis Supervisor

Accepted by: _____
Gerbrand Ceder
R. P. Simmons Professor of Materials Science and Engineering
Chair, Departmental Committee on Graduate Students

Femtosecond-laser Irradiation as a Platform for Tailoring the Optoelectronic Properties of Silicon

by
Matthew John Smith

Submitted to the Department of Materials Science and Engineering
on May 24, 2012 in Partial Fulfillment of the
Requirements for the Degree of Doctor of Philosophy in
Materials Science and Engineering

Abstract

Silicon is the most abundant semiconductor on earth and benefits from decades of technological development driven by the integrated circuit industry. Furthermore, silicon allows for facile n-type and p-type doping, has a naturally passivating surface oxide, and long minority carrier lifetimes. The major drawback of silicon is that it has an indirect band gap at 1.1 eV. It is therefore a poor light absorber and is naturally transparent to light in the infrared. Femtosecond (fs) laser irradiation offers multiple unique approaches to improving the optoelectronic properties of silicon, enabling both thin-film silicon photovoltaics and silicon-based IR photodetectors. In this thesis I study the structure-property-processing relationships related to the fs-laser irradiation of silicon in the context of both *surface texturing* and *optical hyperdoping*.

Fs-laser surface texturing enables the use of thinner silicon wafers through efficient light trapping at the surface, but laser induced damage can degrade the performance of optoelectronic devices. The first part of this thesis investigates the relevant mechanisms of plastic deformation during surface texturing with fs-laser irradiation. Through a combination of Raman spectroscopy and TEM, I show that pressure-induced silicon polymorphs (amorphous silicon, Si-XII, Si-III) form beneath the surface during fs-laser irradiation. Combining characterization of the surface morphology using scanning electron microscopy, Raman investigations of the formation of Si-XII and Si-III, and TEM investigations of the spatial distribution of the amorphous silicon, we report that pressure-induced phase transformations are closely coupled to micron-scale surface texturing.

Next, I identify the pressure generation mechanisms responsible for the pressure-induced phase transformations through a systematic investigation into the relationship between irradiation conditions and silicon polymorphs formation. Beginning with the observation that rastering the Gaussian laser beam drastically increases the amount of Si-XII formed, I use Raman spectroscopy to investigate silicon polymorph formation and residual lattice strains following irradiation at constant fluence and irradiation under modulated fluence. A strong increase in Si-XII formation is reported in laser spots that received a combination of high-fluence and low-fluence irradiation, as is generated by rastering the Gaussian laser beam across the surface. TEM investigations confirm that low-fluence irradiation increases the melt depth and that the spatial distribution of silicon polymorphs is correlated with melting and resolidification on roughened

surfaces. Based on these investigations, it is concluded that resolidification-induced stresses are responsible for the observed pressure-induced plastic deformation.

Optical hyperdoping, the subject of the second half of this thesis, refers to the use of pulsed laser irradiation to drive supersaturated concentrations of dopants into a semiconductor. Fs-laser hyperdoping of silicon with chalcogens has been shown to extend the responsivity of silicon photodiodes into the near-infrared and increase absorption in the visible and infrared. First, hyperdoping from a thin-film dopant precursor is investigated through the comparative structural (SEM and TEM), electronic (p-n diode formation), and optical (UV-VIS-NIR spectrophotometry) characterization of silicon irradiated with fs-laser pulses following the deposition of a selenium thin film on the surface, silicon irradiated in the presence of a gaseous dopant precursor, and silicon irradiated without dopant present. The use of a thin-film dopant precursor is found to have significant consequences on the resulting microstructure and dopant distribution compared to fs-laser doping from a gaseous precursor; producing large, discontinuous volumes of polycrystalline hyperdoped material. The observed microstructure and dopant distribution can account for the increased sub-band gap absorptance and poor diode rectification exhibited by thin-film hyperdoped surfaces. Next, advanced structural investigations into the selenium distribution with annealing show significant selenium segregation and precipitation. With this information, previous investigations into the optical deactivation of selenium with annealing are revisited and shown to be consistent with a kinetic model for optical deactivation by precipitation.

To improve the dopant distribution achieved by thin-film fs-laser doping, the dopant incorporation process is elucidated by monitoring the surface structure (SEM) and dopant distribution (TEM) with variedMJS laser fluence and number of laser pulses. From very early stages of irradiation, the crystallization of hyperdoped material is found to be closely coupled to the surface structuring process, likely due to the effects that surface roughness has on local energy deposition and heat dissipation. The large, polycrystalline peaks are shown to form through a novel regime of crystallization-driven growth, which transitions into ablation-dominated surface structuring after many laser pulses. Finally, the suppression of localized recrystallization is achieved by irradiation with many pulses (100) at very low fluences (1.2-1.4 kJ/m^2), resulting in a thin, continuous layer of hyperdoped material.

The investigations presented in this thesis present progress towards controllable and optimized implementation of fs-laser irradiation as a platform for improving the optoelectronic properties of silicon through both surface texturing and optical hyperdoping.

Thesis Supervisor: Silvija Gradečak
Title: Thomas Lord Assistant Professor of Materials Science and Engineering

Acknowledgments

I will remember my time at MIT for the incredible community of talented, ambitious, and inspiring people that I have been fortunate enough to meet over the last five years, both in and out of lab. This thesis would have not been possible without the tangible and intangible contributions of my thesis committee, collaborators, friends, and family, all to whom I am indebted.

First and foremost, I would like to thank my advisor Silvija Gradečak for the countless hours she has spent mentoring me. Silvija's critical scientific thinking, willingness to tackle difficult problems, and emphasis on effective communication have defined for me what it means to be a scientist. I would also like to thank the members of my thesis committee: Prof. Tonio Buonassisi, who has provided extensive guidance and insight over the course of my thesis; Prof. Gene Fitzgerald, whose breadth of knowledge continually pushed me to broaden my own perspective; and Prof. Jeff Grossman, who I've had the great pleasure of TA-ing for and who bravely accepted the baton from Gene in the final stages of my thesis.

This thesis is the result of a fruitful and fun collaboration between a handful of different research groups, and because of this I have had the opportunity to develop strong working relationships and friendships with a number of collaborators. I must begin by acknowledging the many tangible contributions that several graduate students in Eric Mazur's Group at Harvard made to the work presented in this thesis. Dr. Mark Winkler prepared the original selenium-hyperdoped samples and performed the electrical and optical characterization in Chapter 6. Meng-Ju (Renee) Sher prepared the samples investigated in Chapters 4, 5, and 6 and did the profilometry experiments in Chapter 7. Yu-ting Lin also helped with sample preparation and was a great asset in getting me started on Raman spectroscopy. Ben Franta prepared the samples presented in chapter 7. In addition to their experimental contributions, Mark, Renee, Yu-ting, and Ben were an indispensable source of feedback, support, and encouragement for which I am extremely grateful. The electron tomography presented in Chapter 6 was done by Georg Haberfehlner (CEA-LETI), who is a talented microscopist and made an exceptional host during my visit to Grenoble, France. I also benefitted greatly from valuable scientific discussions and moral support from Dr. Bonna Newman, Dr. Christie Simmons, Joe Sullivan, Prof. Mike Aziz, Dr. Dan Recht, Dr. Jacob Krich, Dr. Elif Ertekin, Dr. Filippo Fabbri, and Dr. Giancarlo Salviati.

In 2007, I was the 4th person to join the Gradečak group and I owe special thanks to the more senior graduate students who took me under their respective wings. Dr. Mike Tambe provided hours of patient instruction and the entire group is indebted to his efforts developing the research group infrastructure. Dr. Sung-Keun Lim provided a wealth of knowledge about TEM and was always willing to help me after I completely botched the alignment of the 2010F. Dr. Megan Brewster taught me the ropes of graduate school, gave me chocolate whenever I needed it (usually after messing up TEM alignment), and continues to serve as a mentor and role model. The facility managers around CMSE have also provided invaluable mentorship, thank you Yong Zhang, Shiahn Chen, Patrick Boisvert, Tim McClure, Libby Shaw, and Scott Speakman. I would also like to acknowledge the peers that I had the opportunity to mentor as a graduate student, and

who ended up teaching me much more than I taught them: Arthur Reading, currently a Ph.D. student at UCSB whose senior thesis got me involved in this project, Sandra Abago, an inspiring young scientist and artisan sample polisher, and Scott Hubeny, whose sincere enthusiasm in for teaching and science will inspire the next generation of materials scientists.

My officemates here in 13-5130 have served as a consistent resource for inspiration, scientific feedback, and distractions as needed. By sitting in close proximity for days, months, and years (in a room with poor temperature control) I have sintered lasting friendships with Smooth Zach Ruff, the Nanotube King Chun-Hao Tseng, Eric Beardly Jones, and Paul Wreckmaster. Brahul Malik spent enough time in 13-5130 to be an honorary office member, and we were happy to have him.

In the past 5 years the Gradečak group has grown by over 300%, and through our regular group meetings this growing army of thoughtful scientists provided critical feedback that influenced this work, especially with regards to microscopy and effective communication. In addition to those previously mentioned, thank you Sam Crawford, Jordan Chesin, Xiang Zhou, Sema Ermez, Jayce Cheng, John Hanson, Dr. Sehoon Chang, Dr. Kamal Baloch, Dr. Mingsheng Wang, and Dr. Shenqiang Wang.

I only made it across the tightrope walk of graduate school because of the infallible safety net that I had in my friends and family. I would like to thank my family for years of unwavering encouragement and support, despite that I had to frantically work on my MRS poster everything Thanksgiving and could never afford to buy them nice things. Thank you Dad, Mom, Barbara, Bill, Becky, Lauren, Ali, Sean, Connor, and Max! My best friends from high school and college have played the important role of keeping me grounded while here at MIT, thank you Kevin, Ian, Casey, Hal, Shivank, Josh, Naveen, Marco, Steve, Nate, Mike, Gabe, and Danny. Finally, I have been incredibly fortunate in the quality of friends that I have made here at MIT. It began with my classmates in the Fall of 2007, who have since become some of my best friends. Thank you Alex Scott, Joan Mao, Michiel Vanhoutte, Noémie Chocat, Dave Bradwell, Kevin Huang, Sal Barriga, Rob Mitchell, Agustin Mohedas and others. Every year we met more incredible people entering the department and invited them onto our mailing list for organizing social events. This group of continually expanding friends, fondly referred to as awesom-o, has become an irreplaceable outlet in my life. I am afraid to try and name everyone for fear of forgetting someone; you all know who you are, and thank you for being so awesome. I owe a special thank you to Lexi for her support over these past few stressful months. I would also like to acknowledge Sarah Wood and Shannon Yee for showing me just what is possible with a heaping dose of optimism and enthusiasm (and an incredible amount of talent). Finally, this wouldn't be complete without a special shout-out to my housemates of 4 years: Sal Barriga, Brian Beliveau, and Tom Fellows. It has been a magical run in the palace and I couldn't have asked for it any better.

Last but certainly not least, I acknowledge the Chesonis Family Foundation and the NSF ERC – QESST (*EEC-1041895*) for the generous financial support that made this thesis possible.

Table of Contents

Chapter 1 Introduction 19

1.1 Silicon and Optoelectronic Applications 19

1.2 Surface texturing 22

1.3 Optical Hyperdoping 24

1.4 Outline of Thesis 27

Chapter 2 Fs-laser irradiation of Silicon: A Primer 29

2.1 Laser-material interactions following a single fs-laser pulse 29

2.1.1 Absorption 30

2.1.2 Melting and Resolidification 31

2.1.3 Surface temperatures, ablation, and thermoelastic pressure generation 33

2.1.4 Ionic plasma formation and recoil shock waves 35

2.2 Laser-material interactions over many pulses 36

2.2.1 Incubation effect 37

2.2.2 Surface texturing 38

2.2.3 Resolidification-induced stresses 40

2.3 Summary 41

Chapter 3 Experimental Methods 43

3.1 Femtosecond-laser irradiation 43

3.1.1 Femtosecond laser beam and rastering 43

3.1.2 Dopant introduction during fs-laser irradiation 45

3.2 Optical characterization of fs-laser irradiation silicon 46

3.2.1 UV-VIS-NIR Spectrophotometry 46

3.2.2 Raman Spectroscopy 46

3.3 Electron Microscopy 49

3.3.1 Introduction to electron microscopy 49

3.3.2 Scanning electron microscopy 50

3.3.3 Transmission electron microscopy 50

Chapter 4 Pressure-induced transformations Pt. 1: Hyperdoping, Spatial distribution & Stability 57

4.1 Introduction 57

4.2 Experimental 60

4.3 Results 61

4.3.1 Silicon Polymorphs and Doping 61
4.3.2 Spatial Distribution of Silicon Polymorphs 63
4.3.3 Silicon polymorph formation and evolution over many laser pulses 65
4.3.4 Thermal Stability of Silicon Polymorphs 68
4.4 Discussion 70
4.4.1 Pressure-induced Phase Transformations 70
4.4.2 Polymorph spatial distribution and evolution with shot number: a surface-morphology driven effect 71
4.4.3 Polymorph relaxation and optical deactivation 72
4.5 Conclusions 73
Chapter 5 Pressure-induced transformations Pt. 2: Identifying pressure-generation mechanisms driving plastic deformation 75
5.1 Introduction 75
5.2 Experimental 76
5.3 Results 77
5.3.1 Rastering vs. stationary laser spots 77
5.3.2 Fluence dependence of Si-XII/III nucleation 83
5.3.3 Effect of fluence modulation 87
5.3.4 Microstructure of Rastered vs. Fluence-modulated Surfaces 91
5.4 Discussion 94
5.4.1 Resolidification-induced stresses and the nucleation of Si-XII 95
5.4.2 Effects of local heating on plastic deformation mechanisms 97
5.4.3 Low-fluence laser annealing: Si-III formation and surface relaxation 97
5.4.4 Si-XII suppression at high fluences 98
5.5 Conclusions 99
Chapter 6 Thin-film Fs-laser Doping pt. 1: Bulk properties, Dopant Distribution & Deactivation 101
6.1 Introduction 101
6.2 Bulk properties and microstructure 108
6.2.1 Introduction 108
6.2.2 Experimental 108
6.2.3 Results and Discussion 109
6.2.4 Conclusions 114
6.3 Optical Deactivation of Selenium Dopant 115
6.3.1 Introduction 115

6.3.2 Experimental 115
6.3.3 Results and Discussion 116
6.3.4 Conclusions 126
6.4 Conclusions 127
Chapter 7 Thin-film Fs-laser Hyperdoping pt. 2: Dopant incorporation mechanisms 129
7.1 Introduction 129
7.2 Effect of thin film on surface texturing and dopant incorporation 134
7.2.1 Introduction 134
7.2.2 Experimental 134
7.2.3 Results and Discussion 135
7.2.4 Conclusions 147
7.3 Optimizing parameter space for thin-film laser doping 149
7.3.1 Introduction 149
7.3.2 Experimental 149
7.3.3 Results and Discussion 149
7.3.4 Conclusions 157
7.4 Summary and Conclusions 157
Chapter 8 Conclusions 161
8.1 Summary of the thesis 161
8.2 Suggested future work 164
8.2.1 Pulsed-laser surface texturing and laser-induced damage 164
8.2.2 Thin-film fs-laser doping 165
Bibliography 169

List of Figures

Figure 1.1. Band diagram of silicon showing the lowest energy indirect (1.1 eV, green) and direct (3.43, red) band gaps, figure adapted from Tull [5]. 20

Figure 1.2. Linear absorption coefficient (α_L) and absorption depth ($1/\alpha_L$) plotted versus wavelength. The wavelengths corresponding to the indirect and direct transitions are indicated. The spectral distribution of terrestrial solar irradiance, which extends beyond 1400 nm, is included in the background. The silicon optical properties are from [8] and solar irradiance spectra is the standard ASTM Global Tilt Terrestrial Reference Spectra for Photovoltaic Performance Evaluation [9]. 21

Figure 1.3. Illustration of the optical path of light incident on microstructured silicon surfaces, determined for λ = 600 nm and assuming an unaffected index of refraction of silicon (n_{Si} = 4 at 600 nm). (a) Silicon textured by etching a (100) surface with NaOH, revealing (111) planes which form an internal angle of 70.5°. (b) Silicon textured by fs-laser irradiation in SF_6 gas under conditions which produced an internal angle of 42°. The size and internal angle of the laser-structured surfaces can be tuned by changing the irradiation conditions. Figure adapted from [23]. 22

Figure 1.4. Temperature-dependent solubility of sulfur (red), selenium (blue) and tellurium (green) in silicon, compared with concentrations achieved by fs-laser hyperdoping which is a factor of 10,000 times higher. When doped to such high concentrations with chalcogens, silicon exhibits broad sub-band gap absorption (inset). Solubility data is from [33-35] and absorptance data is from [5]. 25

Figure 1.5. Schematic of the band structure of an intermediate band semiconductor. The presence of an intermediate band enables 2 low energy electronic transitions (E_1, E_2) that are otherwise unavailable. Theoretical operation of an impurity band semiconductor has an increased short-circuit current without compromising the open circuit voltage, because two photons with energy E_{photon}, such that $E_{1,2} < E_{photon} < E_g$, can excite an electron into the conduction band..... 26

Figure 2.1. Timescales of processes in laser-excited solids. Each bar represents an approximate range of characteristic times over which the processes take place. Adapted from [45]..... 29

Figure 2.2. (a) Surface temperature of silicon irradiated in ultra-high vacuum (τ = 100 fs, λ = 620 nm) determined by flight-mass spectroscopy. Figure from [54]. 34

Figure 2.3 Accumulation curve plotting the threshold fluence of laser-induced damage of silicon, Fmod, versus number of laser pulses, N, with (τ = 130 fs, λ = 800 nm) in air. The solid line presents a least square fit where ξ = 0.84. Figure from [58]. 37

Figure 2.4. SEM images of a silicon surface (τ = 100 fs, λ = 800 nm, 8 kJ/m^2, 1 kHz, in SF_6 ambient) after (a) 1, (b) 10, (c) 20, and (d) 50 laser pulses. Images taken at 45° tilt. Figure adapted from [79]. 38

Figure 2.5. SEM (45°) of silicon surface showing conical spike formation (a) after 1000 pulses at 8.4 kJ/m^2 (τ = 80 fs, λ = 800 nm) and (b) after 3000 pulses at 35 kJ/m^2 (τ = 32 fs, λ = 308 nm). The insets show the relative height of the laser spot with respect to the surface. Irradiation conditions determine whether spikes grow upwards or form solely through material removal. Figure adapted from [90]..... 40

Figure 2.6. (a) Geometry of the model of a trench with a resolidified surface layer (dark grey). (b) Finite element model of trench after solidified layer with a negative thermal expansion coefficient is cooled

from 1300 K to 300 K, illustrating spatial distribution of both tensile and compressive stresses. Figure adopted from [94]. 41

Figure 3.1. Schematic of femtosecond-laser irradiation set-up used in this thesis. From [50]. 44

Figure 3.2. (a) Schematic of the Gaussian laser spot and the relative step sizes used to prepare a the 88 shots/area sample studied in this section. Inset is the full-width-have-max of the laser spot. The laser beam is polarized in the x-direction. The grey ring at the base of the Gaussian peak is to guide the eye. (b) The fluences of the fs-laser pulses received by a single point on the surface as the laser spot is rastered in the x-direction (line scan, blue) and rastered over a 2-D area (blue and red). 45

Figure 3.3. Femtosecond laser doping can be accomplished by fs-laser irradiation (a) in the presence of a gaseous dopant precursor or (b) depositing a thin film of dopant onto the surface prior to irradiation. 46

Figure 3.4. Schematic of the variety of signals generated during the interaction of a high-KV electron beam with a sample. Adapted from reference [99]. 49

Figure 3.5. (a) Diagram of conventional TEM mode or parallel-beam mode in the TEM. (b) Example lens diagram of convergent-beam/probe mode in the TEM. The exact approach to creating a probe varies from microscope to microscope. Adapted from [99]. 52

Figure 3.6. Schematic illustrating the range of detectors that can be used in scanning TEM mode: The bright-field (BF) detector collects transmitted and slightly off-axis electrons. The dark-field (DF) detector and high-angle annular dark field (HAADF) detector collect electrons scattered at wider angles. The large the collection angle the more sensitive the image is to atomic weight and less sensitive to diffraction contrast. Figure adapted from [99]. 53

Figure 3.7. Illustration of interactions between incident electrons and core electrons that are used for chemical characterization in a TEM via energy dispersive x-ray spectroscopy (EDX) and electron energy loss spectroscopy (EELS). 55

Figure 4.1. The irreversible reaction pathways that silicon undergoes during pressure loading and unloading at moderate temperatures. The formation of Si-XII, Si-III, and a-Si are very sensitive on the rate of pressure unloading, the temperature, and the phase of the surrounding silicon matrix. 59

Figure 4.2. (a) SEM micrographs showing the surface morphology of fs-laser irradiated Si. The laser scan direction and polarization was in the horizontal direction. (b) Stokes Raman spectra of SF_6:Si, Se:Si, and N_2:Si, offset to show individual spectra. The rescaled inset highlights the Raman modes corresponding to a-Si, Si-III, and Si-XII. The color designation is the same in both plots. (c) The position of the Si-XII and Si-III modes and their relative intensities, plotted with standard deviation. Dashed lines indicate the positions of the Si-XII (350 cm^{-1}) and Si-III (432 cm^{-1}) Raman modes reported in nanoindentation studies [96]. 62

Figure 4.3. Cross-sectional BF-TEM images of N_2:Si (a) and SF_6:Si (b). SAD patterns from the regions highlighted by the dashed circles (inset) correspond to the Si-I [101] zone axis. White arrows indicate contrast in the core of the peaks arising from areas of transformed material (20-200 nm in diameter), shown to be a-Si. BF-TEM (c) of an isolated region of a-Si from the core of an SF_6:Si spike. Numbered spots 1 and 2 correspond to c-Si and a-Si points probed using CBED (d) and EELS (e). BF-TEM (f) of region in (b) that shows nanocrystals (black arrows) inside the a-Si. 64

Figure 4.4. (a) BF-TEM image of Se:Si peak, showing a polycrystalline region and small volumes of a-Si (white arrows). (b) SAD pattern from region corresponding to dashed circle in (a). Spots corresponding to Si-III [101] zone axis can be identified within the Si-I polycrystalline pattern (grey rings), and lower order spots are identified by red circles. 65

Figure 4.5. (a) SEM micrographs of the Se:Si surface morphology with an increasing number of laser shots/area. The laser scan direction and polarization was in the horizontal direction. (b) Stokes Raman spectra of Se:Si irradiated with an increasing number of laser pulses, offset to show the individual spectra. The inset is rescaled to highlight the Raman modes corresponding to a-Si, Si-III, and Si-XII. The color designation is the same in both plots. (c) Bar graphs showing the position of the Si-XII and Si-III modes and their relative intensities after 25, 42, and 88 laser pulses, plotted with standard deviation. 66

Figure 4.6. Cross-sectional BF-TEM images of the surface after irradiation with (a) 10 shots/area and (b) 25 shots per area. After 10 shots/area there is an amorphous layer (white arrow) that formed through melting and resolidification on the surface. After 25 shots/area, pockets of amorphous material form beneath the melt depth (black arrow), confirming the onset of pressure-induced phase transformations. . 67

Figure 4.7. (a) Absorptance spectra of Se:Si after a 30 min anneal at the indicated temperatures. Included for reference are spectra from a not annealed (NA) sample, the absorptance spectra of a sample irradiated in N_2 without a dopant present and a silicon wafer. (b) Stokes Raman spectra of the same samples (250 – 500 cm^{-1}). Spectra are offset to highlight the a-Si, Si-III, and Si-XII peaks and their evolution with annealing. (c) Bar graphs showing the position of the Si-XII and Si-III modes and their relative intensities with annealing, plotted with standard deviation. 69

Figure 5.1 (a) The average intensity and standard error of the Si-III (blue) and Si-XII (red) Raman peaks from 20 spectra collected from surface that received 88 shots/area with a 4 kJ/m^2 Gaussian laser spot; surface morphology shown in inset and representative Raman spectrum shown in (b), with peak intensities provided. 78

Figure 5.2. (a) The average intensity and standard error of the Si-III (blue) and Si-XII (red) Raman peaks measured across a 1-D line scan that received 11 shots/area at peak fluence of 4 kJ/m^2. Data represents average of 5 Raman line scans perpendicular to the direction of laser motion (white dashed line, left inset). The right inset shows the surface morphology in the center of the spot following irradiation, and a representative Raman spectrum from the center of the laser-affected stripe is shown in (b). (c) The average intensity and standard error of the Si-III (blue) and Si-XII (red) Raman peaks measured across a spot that received 88 pulses from a stationary Gaussian laser beam at peak fluence of 4 kJ/m^2. Data represents line scans across 5 different laser spots in the direction perpendicular to laser polarization (white dashed line, left inset). The surface morphology from the center of the peak is shown in the right inset. (d) A representative Raman spectrum from the outer rim of the stationary laser spot, which shows barely detectable amounts of Si-XII. 79

Figure 5.3. (a) The average position of the Si-I LO/TO peak in the rastered surface, across the fs-laser line scan, and mapped across the stationary laser spot, shown with standard error and indicated in the legend. The reference position of this peak is 520 cm^{-1} (dashed grey line). The Raman maps across the fs-laser line scan and the stationary spot don't extend sufficiently beyond the laser irradiated region to show the completely relaxed silicon peak position, but reference spectra were used to calibrate all Raman signals. (b) The average peak position of the Si-XII peak for all three samples plotted with standard error. Only peaks with intensities above the noise (1500) are used to determine average position. 81

Figure 5.4. SEM images of (a) laser spots following 88 pulses at the fluence indicated (2.0 – 3.6 kJ/m^2) and (b) the surface morphology in the center of each laser spot. (c) Graphical representation of the irradiation conditions used, presented in a Fluence-Shot number plot for comparison with Figure 3.2(b). For each irradiation condition, Raman line scans were taken across 5 distinct laser spots perpendicular to the direction of laser polarization (vertically). The average peak intensities and standard error is plotted for Si-XII (d) and Si-III (e). The Si-III peak intensities are below the noise limit (~1500) for all samples. Increases in the Si-III signal up to ~1000 a.u. are artifacts due to amorphous silicon around the edge of the spot. 82

Figure 5.5. SEM images of laser spots irradiated with 88 fs-laser pulses with a peak fluence of (a) 4.0 kJ/m^2 and (b) 3.2 kJ/m^2. Raman spectra were collected across the area of each laser spot and the intensity of the Si-XII peak is plotted for the (c) 4.0 kJ/m^2 and (d) 3.2 kJ/m^2 spots. Dashed lines indicate approximate fluence thresholds for the activation and suppression of Si-XII formation. 84

Figure 5.6. (a) The average position of the Si-I LO/TO peak, extracted from the same Raman spectra used to generate Figure 5.3(d,e), with standard error included. The reference position of this peak is 520 cm^{-1} (dashed grey line). (b) The average peak position of the Si-XII peak (plotted with standard error) shows no strong trends with fluence. Only peaks with intensities above the noise (1500 a.u.) are used to determine average position. 85

Figure 5.7. (a) SEM images of laser spots following irradiation under the conditions reported in Table 5.1. (b) SEM images showing the surface morphology in the center of each laser spot. (c) Representation of the irradiation conditions used presented in a fluence-shot number plot for comparison with Fig. 4.3.1(b). To monitor the spatial distribution of the crystalline polymorphs, 3 Raman line scans were taken across each laser spot perpendicular to the direction of laser polarization (vertically) and the average peak intensities and standard error of Si-XII is plotted in (d) and Si-III is plotted in (e). The standard error is negligibly small because the line scans reflect averaging 3 line scans across the same spot, whereas previous line scans were averaged across multiple distinct laser spots. 89

Figure 5.8. (a) The average position of the Si-I LO/TO peak, extracted from the same Raman spectra used to generate Fig. 4.3.5. (d,e), plotted with standard error. The reference position of this peak is 520 cm^{-1} (dashed grey line). (b) The average peak position of the Si-XII peak plotted with standard error for FM5, compared with the Si-XII peak position for the stationary 4.0 kJ/m^2 laser spot and the areal raster. Only peaks with intensities above the noise (1500 a.u.) are used to determine average position..... 90

Figure 5.9. Cross-sectional BF-TEM showing the microstructure of the (a) FM4 and (b) FM5 laser spots. Black arrow in (b) indicates crystallization on the surface. These samples were prepared using FIB and have a protective layer of Pt deposited on the surface. (c) BF-TEM of the 88 shot/area rastered surface, showing distribution of amorphous silicon pockets (white arrows) with respect to surface morphology. This sample was prepared by polishing and is covered in electron-transparent glue. (d) Higher-magnification image of bump indicated in (a) (dashed line), which contains stacking faults and dislocations near the surface (black arrows) and amorphous pockets in the core of the peak (white arrow). (e,f) BF-TEM and DDF-TEM of region indicated in (b), respectively. BF-TEM shows considerable strain contrast within the surface peak and the DDF-TEM image highlights nanocrystals that have formed below the melt depth..... 92

Figure 6.1. Comparison of Si(100) surfaces irradiated with 500 pulses at a peak fluence of 10 kJ/m^2 in the presence of (a) SF_6 and (b) vacuum viewed at an angle of 45° from the surface normal. The laser spot size was 200 μm. Figure from [134]. 102

Figure 6.2. (a) Near-unity sub-band gap absorptance exhibited by silicon irradiated in the presence of sulfur containing gases with a fs-laser beam irradiated with a peak fluence of 10 kJ/m^2 and 600 shots/area, compared to unirradiated crystalline silicon. Adapted from [136]. (b) Wavelength dependence of the optical absorptance of silicon irradiated in the presence of non-sulfur-containing gasses, irradiated with a peak fluence of 11 kJ/m^2 with varied translational speeds. Adapted from [28, 50]. Data in both (a) and (b) have been recalibrated by M.-J. Sher to account for errors in originally published data. 102

Figure 6.3. (a) Cross-sectional TEM images of a silicon surface irradiated with a peak laser fluence of 8 kJ/m^2, 500 shots/area, in 500 mTorr SF_6. *Upper right:* High-magnification view of the disordered region at the tip of the spike, indicated on main image with dashed square. *Lower right:* Selected area electron diffraction pattern obtained from the disordered region showing polycrystalline nature. Figure adapted from [29]. (b) Responsivity of a photodiode textured with fs-laser irradiation in the presence of SF_6 gas, under various low bias conditions, compared to a commercial silicon p-i-n diode. *Inset:* Device geometry showing both front and back gold electrodes deposited onto irradiated silicon wafer. Figure adapted from [32, 50]. 103

Figure 6.4. Scanning electron microscope images of silicon surfaces irradiated with a rastered beam with a peak fluence of 10 kJ/m^2 such that each point received ~1400 shots/area, using (a) sulfur powder, (b) selenium powder, (c) tellurium powder, (d) sulfur hexafluoride gas as a dopant precursor. In each image the surface is at the 45 angle. Figure from [12]. (d) Absorptance of each of the powder-doped samples imaged in (a-c) before and after a 30 minute anneal at 502°C (775 K). Figure adapted from [12], and absorptance data has been recalibrated by M.-J. Sher to account for errors in originally published data. 104

Figure 6.5. Results of kinetic investigation by Tull et al. [122] (a) Average absorptance from 1250 to 2500 nm for sulfur-doped (circles), selenium-doped (squares), tellurium-doped (triangles) silicon and samples irradiated in N_2 (diamonds) after various thermal anneals at T ≤702°C. The larger marker indicates the longer anneal (from smallest to largest: 10 min, 30 min, 100 min, 6 h, 24 h). (b) Normalized absorptance spectra for sulfur-doped (circles), selenim-doped (squares) and tellurium doped (triangles) silicon after various thermal anneals versus diffusion length of the respective dopant. The average infrared absorptance from (a) has been re-normalized, so that the maximum is the pre-annealed value and the minimum is the infrared absorptance of the unirradiated silicon wafer. Note also the artifacts in this data discussed on pg. 107. 106

Figure 6.6. (a) Normalized and offset X-ray absorption spectra of highly Se-doped samples annealed at various temperatures. (b) IR absorption versus the component of state A determined by principle component analysis. The inset table gives the fraction of state A and state B after each of the investigated anneals. Figures from [138]. 107

Figure 6.7. (a) Absorptance spectra of all samples studied in section 6.2. (b) Current density vs. bias curves of Se:Si-1 and SF_6:Si-1 at room temperature. 110

Figure 6.8. (a-d) SEM micrographs showing surface morphology of fs-laser irradiated Si. The laser scan direction and polarization was in the horizontal direction. (e) RMS of the surface height. Error bars reflect

standard deviation for five independent measurements. (f) Height profiles of representative surfaces and the relative thickness of the 75 nm Se film (dashed). 111

Figure 6.9. Cross-sectional BF-TEM images taken along the Si [011] zone axis with corresponding selected area diffraction patterns (insets). Black arrows indicate selenium-free valleys in (c), and identify the sulfur-rich surface layer in (b,d)..... 112

Figure 6.10. (a) DF-STEM image of Se:Si-2, dashed boxes highlight the regions shown in (b) and (c). (b) Selenium EDX line scan across the doped-undoped interface. (c) DF-STEM image showing the location of Se K_α EDX point spectra shown in (d). 113

Figure 6.11. (a) Absorptance of Se-hyperdoped silicon without any post-treatment annealing (green), after a 30 min anneal at 575°C (blue) and after a 30 min anneal at 950°C (red), with the absorptance of untreated silicon wafer for reference (black). (b) Normalized and averaged sub-band gap absorptance of samples presented in (a) plotted versus diffusion length, overlaid onto the data collected for sulfur (circle), selenium (square) and tellurium (triangle) hyperdoped silicon in the previous kinetic study of deactivation by Tull et al. [122] Note that the overlay is only a qualitative comparison due to the artifacts present in Tull's data. The new data does not contain artifacts from imperfect reflection in the integrating sphere and, relatedly, the optical decay doesn't plateau at 0.3. 117

Figure 6.12. (a) Z-contrast image of a peak on the non-annealed surface of selenium-hyperdoped silicon. Brighter contrast within the peak is due to increased concentrations of selenium. (b) Bright-field STEM image of the interface between the polycrystalline hyperdoped region and the undoped silicon substrate, from region indicated in (a). (c) BF-STEM image of a grain boundary within the polycrystalline region. (d) Z-contrast image of the interface in (b), showing diffuse contrast due to increased selenium concentrations, with some segregation already visible. (e) Z-contrast image of the grain boundary in (c), showing no visible signs of segregation. The darks spot visible in the Z-contrast image are voids..... 117

Figure 6.13. (a) Z-contrast image of a peak on the surface of selenium-hyperdoped silicon that was annealed for 30 minutes at 575°C. (b) Bright-field STEM image of the interface between the polycrystalline hyperdoped region from region indicated in (a), showing both a void and a grain boundary. (c) Z-contrast image of the interface in (b), showing evidence of selenium segregation to the boundaries of the void and the grain boundary..... 118

Figure 6.14. (a) Z-contrast image of a peak on the surface of selenium-hyperdoped silicon that was annealed for 30 minutes at 950°C. The base of the peak contains precipitates of selenium-rich material and segregation to grain boundaries in the body of the peak is also visible. (b) Bright-field STEM image of a faceted Se-rich precipitate, from region indicated in (a). (c) BF-STEM image of a grain boundary within the polycrystalline region. Region indicated in (a) is a best estimate of the AOI imaged. (d) Z-contrast image of the precipitate in (b), confirming that it is selenium rich. Lighter contrast visible in (c) and (d) is ion beam damage due to sample preparation. (e) Z-contrast image showing selenium segregation to grain boundary in (c). 119

Figure 6.15. HAADF-STEM Tomography reconstruction of selenium-hyperdoped silicon extracted from the center of the polycrystalline peaks, showing selenium distribution (a) before annealing (b) after a 30 minute anneal at 575°C, and (c) after a 30 minute anneal at 950°C. 120

Figure 6.16. The normalized absorptance of (a) selenium- and (b) sulfur-hyperdoped silicon after annealing over a range of temperatures (302°C – 702°C, originally reported as 575 – 975 K) and times

(10 m – 24 h) plotted versus $t^{-1/3}$. For clarity, the anneal series relevant to this study of diffusion-controlled coarsening are colored. Linear fits are shown for regions that satisfy the Lifshitz-Wagner theory. The data presented here was collected and published by Tull et al. [122]. 123

Figure 7.1. (a) Cross-sectional TEM of a n-Si(111) wafer ion implanted with sulfur to a dose of 1×10^{16} ions/cm^2 and irradiated with a single 18 kJ/m^2 fluence laser pulse from an $XeCl^+$ excimer laser pulse (λ = 308 nm, τ_p = 50 ns). (b) Lattice resolved TEM image of the same sample showing crystallinity. Figure from [159]. (c) Sub-band gap absorptance spectra of sulfur-hyperdoped Si(111) prepared the same way but with a peak fluence of 14 kJ/m^2. Annealing data is for sequential 30 minute anneals at each temperature, conducted on the same sample. Figure from [11]. 131

Figure 7.2. (a) Schematic showing relative size of laser-structured surface and profilometer stylus with 5 μm radius of curvature. (b) Example profilometry line scan across a stationary laser spot irradiated with 30 pulses. The average height in the center 30 μm (shaded) is measured with respect to the height of the unirradiated silicon wafer and used to quantify trends in the height of the surface (ΔH) with shot number. 135

Figure 7.3. (a) SEM images of the evolving surface morphology taken at a 45° angle. The numbers in the upper left indicate the number of stationary laser shots. (b) Average height of the features with respect to the native silicon substrate (ΔH), measured using a profilometer line scan across the entire laser spot. . 136

Figure 7.4. (a) Bright-field TEM image of silicon surface after a single laser pulse, including a selenium droplet on the surface. (b) High-magnification TEM of the modified silicon surface, from the region indicated in (a). 137

Figure 7.5. BF-TEM micrograph of the roughened surface following 5 fs-laser pulses at 4 kJ/m^2. Platinum (Pt*) and carbon (C*) layers were deposited during FIB sample preparation. 139

Figure 7.6. BF-TEM images of representative crystallized regions following 5 laser pulses at 4 kJ/m^2. The selenium composition (at. %) was determined using EDX (red spots). 140

Figure 7.7. Binary phase diagram of selenium-silicon [146]. 142

Figure 7.8. BF-TEM images of polycrystalline peaks on the surface 10 pulses (a,b) and 20 pulses (c) at 4 kJ/m^2. EDX point scans in (a) and (c) show the selenium composition in different regions of the surface. Inset in (c) is an EDX map of the selenium signal at the base of the peak (red dashed box). 144

Figure 7.9. Schematic of the microstructure of the 20-shot peak shown in Fig. 6.7(c). The columnar grain structure at the base of the peaks is indicative of solid phase epitaxy. The darker blue color for polycrystalline silicon indicates regions in which there was too much contrast to easily resolve the grain structure. The formation of pressure-induced amorphous silicon is discussed in Chapters 4 and 5. 145

Figure 7.10. BF-TEM of the surface structure following 50 pulses at a fluence of 4 kJ/m^2. White circles highlight the columnar grain structure that is evidence of continued crystallization-driven growth during fs-laser irradiation. 147

Figure 7.11. SEM images of the evolving surface morphology as a function of fs-laser pulse number (1-100) and laser fluence (0.7 – 4 kJ/m^2). 150

Figure 7.12. (a) SEM image of laser spot after 10 pulses at a peak fluence of 4 kJ/m^2. The white box indicates the low-fluence region investigated, shown in (b). (c) Cross-sectional BF-TEM image of a

region irradiated with ~1.66 kJ/m^2 fluence. EDX line scans show oxygen and selenium distribution, and point scans quantify the amount of selenium present. (d) BF-TEM image of a region irradiated with ~1.27 kJ/m^2 fluence with EDX line scans and point scans quantifying the amount of selenium present. (e) High-magnification image of the region presented in (d). 152

Figure 7.13. (a) SEM image of laser spot after 100 pulses at a peak fluence of 4 kJ/m^2. The low-fluence region investigated is shown in (b). 154

Figure 7.14. (a) Cross-sectional BF-TEM of surface irradiated with 100 pulses at a fluence of roughly 1.45 kJ/m^2 reveals polycrystalline spikes. EDX line scan shows selenium is concentrated at the base of the spike. (b) BF-TEM image of surface irradiated with 100 pulses at 1.4 kJ/m^2 shows LIPPS have a continuous crystalline surface layer with a discontinuous distribution of a-Si on the surface. EDX point scans indicate selenium composition in surface layer of around 1%. For clarity, the crystalline substrate (c-Si), hyperdoped silicon (hd-Si), amorphous silicon (a-Si), and protective coatings (C, Pt) are indicated. Similar features are visible after irradiation at 1.30 kJ/m^2 (c) and 1.25 kJ/m^2 (d). 154

Figure 7.15. Thickness of the hyperdoped surface layer plotted as a function of fluence show slight trend of increasing surface layer thickness with increasing fluence. The thickness measurements were made across the entire 100-pulse TEM sample (Figure 7.14) and then binned into 4 groups. 155

List of Tables

Table 1.1. Texturing methods and the resulting minimum reflection (R%) for mono-crystalline (c-Si) and multi-crystalline (mc-Si) wafers. Table adopted from [15] and [24]. 24

Table 2.1. Experimental fluence thresholds for the onset of melting, adopted from [47]. 32

Table 5.1. Irradiation conditions used to prepare the series of fluence modulated samples investigated. Each sample began with 5 pulses of 4 kJ/m^2, and then received irradiation in the order it is listed down to the row of the sample name, as illustrated in Figure 5.7(c). 87

Table 6.1. Notation and corresponding doping parameters for samples used in section 6.2. 109

Chapter 1 Introduction

1.1 Silicon and Optoelectronic Applications

Silicon is the most abundant semiconductor in the world, as it composes 28% of the earth's lithosphere by mass [1]. It is also the most well-understood semiconductor due to several prolific decades of technological development driven by the integrated circuit industry. In addition, silicon has many outstanding material properties that make it well-suited for electronic device fabrication, such as high carrier mobilities, long minority carrier lifetimes, a naturally passivating surface oxide, and facile n-type and p-type doping [2]. Due to these advantages, silicon is remains the foundation of the integrated circuits industry and crystalline silicon currently has an 85% market share in the photovoltaics industry [3].

When engineering optoelectronic devices, such as photodetectors, photovoltaics, or light-emitting diodes, silicon has a major disadvantage arising from its indirect band gap (1.1 eV) [4], illustrated in Figure 1.1. Excitation of an electron across the *band gap* of silicon, which is the minimum amount of energy required to excite the electron from the valence to the conduction band, requires a change in the electron momentum. The electron must gain or lose momentum through interactions with a phonon during the absorption process. The introduction of a third-particle into the interaction (the phonon) makes such indirect transitions much less probable than direct transitions. In a direct transition no phonon interactions are necessary and the transition is therefore much more probable; the direct band gap of silicon is significantly higher in energy (3.43 eV).

The practical consequence of the indirect band gap is that silicon is inherently poor at absorbing light. The linear absorption of light in a semiconductor can be expressed using the Beer-Lambert law:

$$I = I_0 e^{-\alpha(\lambda)t} \tag{1.1}$$

Here $\alpha(\lambda)$ is the wavelength-dependent absorption coefficient, t is the distance travelled into the material, and I_0 is the intensity of incident light. The absorption coefficient, $\alpha(\lambda)$, and the corresponding absorption depth, $1/\alpha(\lambda)$, are shown in Figure 1.2. In silicon the absorption depth above the indirect band gap is on the order of 10^{-4} – 10^{-3} m (100 μm – 1 mm). This is in contrast to above the direct band gap transition where the absorption depths are on the order of microns

or less, typical for direct-gap semiconductors. At energies below the indirect band gap of silicon (1.1 eV, corresponding to wavelengths longer than 1100 nm) the absorption coefficient drops off dramatically and silicon becomes effectively transparent.

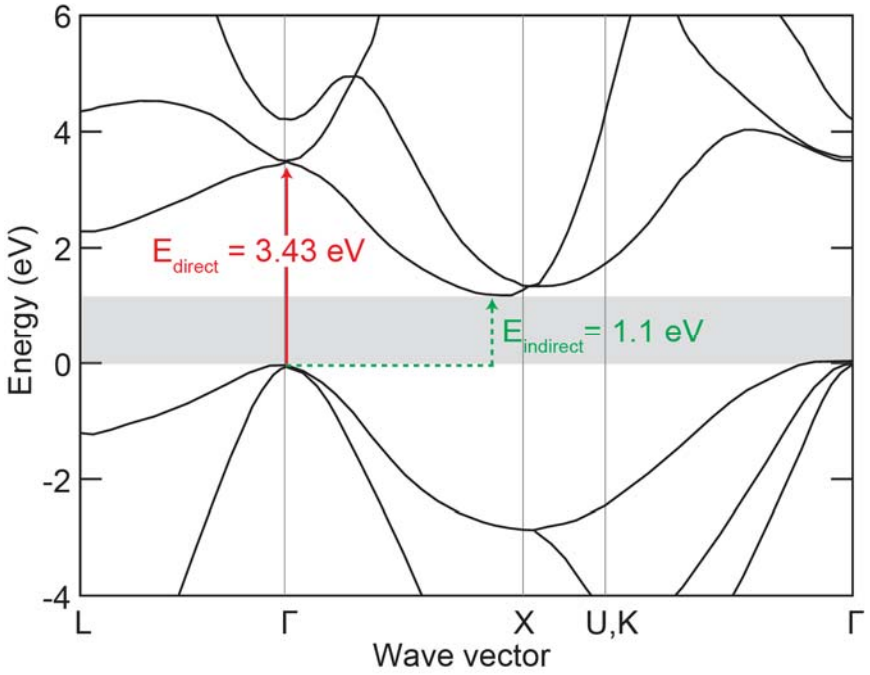

Figure 1.1. Band diagram of silicon showing the lowest energy indirect (1.1 eV, green) and direct (3.43, red) band gaps, figure adapted from Tull [5].

The optical limitations resulting from the indirect band gap of silicon are two-fold: First, a significant amount of material is required to absorb light between 1.1 eV and 3.43 eV. Comparing the band structure of silicon with the distribution of solar irradiance, included in the background of Figure 1.2, shows that silicon's behavior in the visible range of the electromagnetic spectrum will be dominated by the indirect transition. Due to its poor absorption, industrial crystalline silicon wafers used today in photovoltaics are typically 180 μm thick [2] and account for 40% of the total module cost [6]. In contrast, photovoltaics made from direct band-gap semiconductors are only microns thick [7]. Increasing the ability of silicon to absorb light in this regime would reduce the necessary wafer thickness, resulting in less material usage and a reduction in the overall cost of electricity generation by silicon-based photovoltaics.

The second limitation of silicon in optoelectronic devices is that it is transparent to light with energies below the indirect band gap of 1.1 eV. As such, silicon photodetectors cannot detect into the infrared. With respect to photovoltaic applications, silicon is transparent to 24% of

the energy delivered by the sun. Improving the optoelectronic behavior of silicon in the infrared could enable silicon-based infrared photodetectors and increase the efficiency of silicon-based photovoltaics.

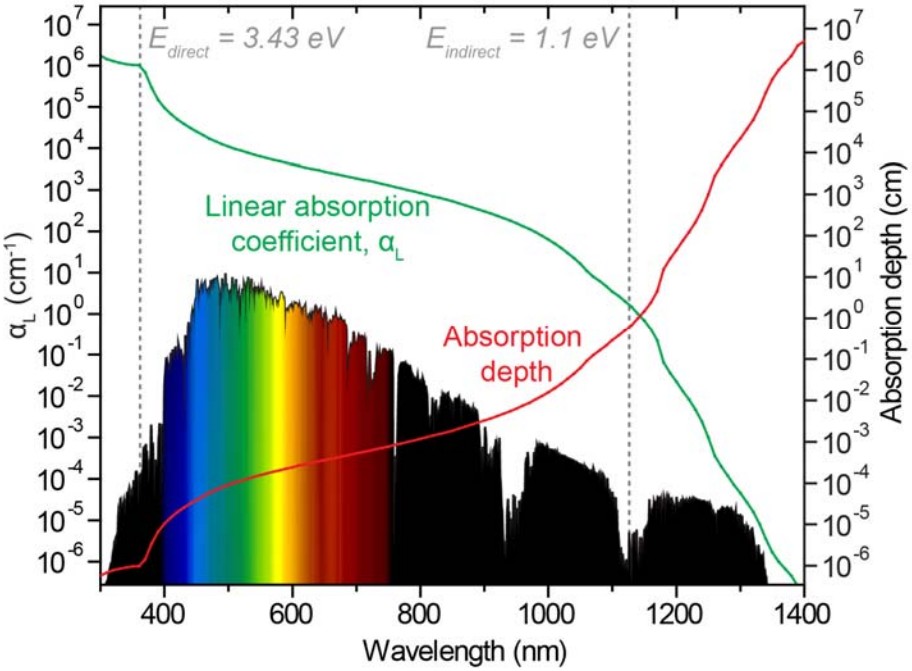

Figure 1.2. Linear absorption coefficient (α_L) and absorption depth ($1/\alpha_L$) plotted versus wavelength. The wavelengths corresponding to the indirect and direct transitions are indicated. The spectral distribution of terrestrial solar irradiance, which extends beyond 1400 nm, is included in the background. The silicon optical properties are from [8] and solar irradiance spectra is the standard ASTM Global Tilt Terrestrial Reference Spectra for Photovoltaic Performance Evaluation [9].

In this thesis we investigate the use of femtosecond-laser irradiation to improve the ability of silicon to interact with light across the visible and infrared regions of the electromagnetic spectrum. *Fs-laser surface texturing* decreases the reflectivity and increase the optical path length of light at the surface [10], resulting in improved absorption of radiation with energies above the band gap of silicon. *Fs-laser hyperdoping* can modify the band structure of silicon by driving high concentrations of deep-level impurities into the semiconductor, increasing the absorption coefficient across the visible and into the infrared [11, 12]. In the following we review surface texturing and hyperdoping, their demonstrated ability to improve the behavior of silicon-based optoelectronics, and how the investigations in this thesis address critical barriers behind the development of fs-laser irradiation as a platform for improving silicon-based optoelectronic devices.

1.2 Surface texturing

Texturing a silicon wafer can cause light to reflect multiple times on the surface, increasing the optical path length and decreasing the reflectivity (Figure 1.3) [10]. Such approaches to light trapping at the surface have produced significant gains in solar cell performance [13] and allows for the use of thinner silicon wafers [14]. The high index of refraction of silicon, n, makes silicon well suited for surface texturing; the optical path length can be increased by a factor of $4n^2$ by micron-scale surface texturing, meaning that the path length in silicon can be increased by a factor of ~50 [14].

In commercial silicon solar cells, light trapping is traditionally accomplished using a combination of wet etching and the deposition of an anti-reflection coating. The reflectance of untreated silicon is around 34% in the visible. Anisotropic chemical etching using alkaline solutions and isotropic chemical etching using an acidic mixture can reduce the reflectivity to 10-15%, but suffer from lack of size control, poor reproducibility, and, in the case of the anisotropic etch, can only be applied to (100) surfaces [15]. Additional approaches to surface texturing have also been proposed, including reactive ion etching [16], mechanical texturing [17], nanoporous surfaces [18, 19], and wet etchings [20-22].

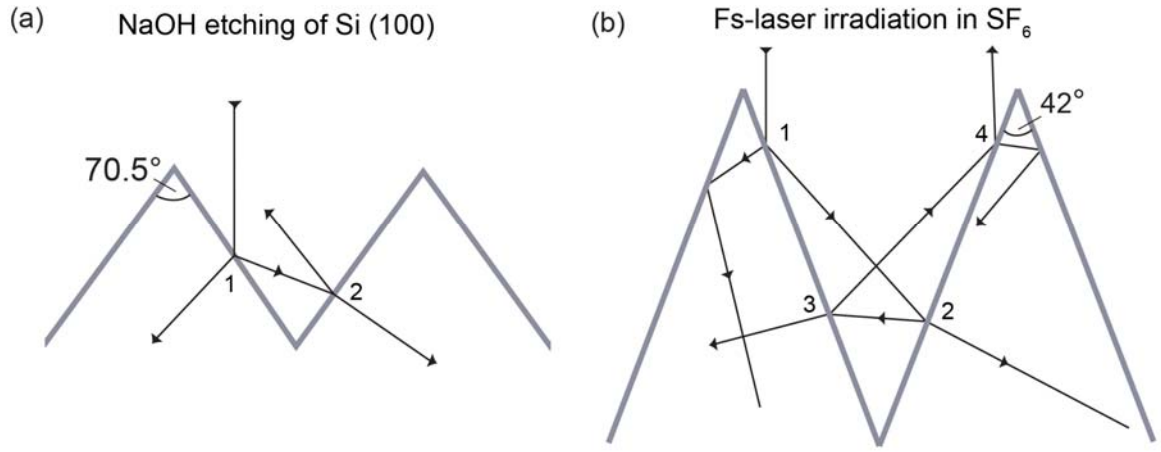

Figure 1.3. Illustration of the optical path of light incident on microstructured silicon surfaces, determined for $\lambda = 600$ nm and assuming an unaffected index of refraction of silicon ($n_{Si} = 4$ at 600 nm). (a) Silicon textured by etching a (100) surface with NaOH, revealing (111) planes which form an internal angle of 70.5°. (b) Silicon textured by fs-laser irradiation in SF_6 gas under conditions which produced an internal angle of 42°. The size and internal angle of the laser-structured surfaces can be tuned by changing the irradiation conditions. Figure adapted from [23].

Fs-laser irradiation has many benefits as a surface-texturing platform. The ablation processes that drive surface texturing are relatively isotropic, enabling uniform texturing on multi-crystalline silicon solar cells [15,24, 25]. The periodicity and dimensions of the surface texturing can be controlled through careful selection of the irradiation parameters (e.g. pulse wavelength, duration, fluence, pulse number, ambient gas) and the resulting texture is highly reproducible [10]. The laser process is dry (as opposed to wet chemical etches), can be incorporated inline, and uses less material than wet chemical etches [25]. Finally, the micron-scale surface texturing achieved through pulsed laser irradiation is extremely effective at reducing reflectivity from the UV to IR [15].

Simulations of the effect of laser-induced surface structuring illustrate the efficacy of periodic micron-scale surface texturing for decreasing the reflectivity and increasing the optical path length (Figure 1.3) [10]. The optical path calculations assume 600 nm light incident on silicon, with an index of refraction (n) of 4. The surface created by chemical etching (Figure 1.3(a)) has a texture determined by the orientation of the (111) planes in silicon and thus has a fixed internal angle of 70.5°. This geometry results in two reflections at the surface, compared to the fs-laser structured surface (Figure 1.3(b)) which has 4 reflections at the surface. The surface in Figure 1.3(b) was irradiated in SF_6 to produce an internal angle of 42°, though the exact geometry of the surface textured using fs-laser irradiation is tunable by changing the irradiation conditions and ambient gas. Pulsed-laser irradiation can reduce the reflectivity to less than few percent independent of the angle of incidence [15]. The remarkable ability to reduce reflectivity with fs-laser surface texturing is contextualized in Table 1.1, which shows reported reflectivities achieved through different surface-texturing methods.

The ability to improve solar cell performance using pulsed-laser surface texturing has been demonstrated both in labs and commercially. Nayak et al. used fs-laser texturing in combination with a chemical etchant to achieve a 14.2% conversion efficiency [15]. Torres et al. demonstrated a 57% increase in the photocurrent using fs-laser irradiation of silicon in vacuum [24]. SiOnyx has commercialized a platform for pulsed-laser texturing that yields a 0.3% increase in absolute efficiency and tighter process binning, while also proving the scalability of laser-based surface treatments for photovoltaics [25].

Technique	Applicable to	Substrate used	R(%) in visible	Reference
Mechanical grooving	c-Si & mc-Si	mc-Si	>15	[17]
Isotropic acidic texturing	mc-Si	mc-Si	15	[20]
Isotropic acidic texturing	mc-Si	mc-Si	10-12	[26]
NaOH + IPA	c-Si	c-Si	10	[22]
Na_2CO_3	c-Si	c-Si	10	[21]
Ag nanoparticle	c-Si & mc-Si	c-Si	<5	[19]
Au nanoparticle	c-Si & mc-Si	c-Si	<2	[18]
RIE	c-Si & mc-Si	mc-Si	<2	[16]
Ns-laser texture (N_2 ambient)	c-Si & mc-Si	c-Si	<5	[27]
Fs-laser texture (vacuum)	c-Si & mc-Si	c-Si & mc-Si	3%	[24]
Fs-laser texture (SF_6 ambient)	c-Si & mc-Si	c-Si	<3	[28]
Fs-laser texture (SF_6 ambient)	c-Si & mc-Si	c-Si	<3	[15]

Table 1.1. Texturing methods and the resulting minimum reflection (R%) for mono-crystalline (c-Si) and multi-crystalline (mc-Si) wafers. Table adopted from [15] and [24].

One major potential drawback of using fs-laser surface texturing in optoelectronic applications is the laser-induced damage that can occur beneath the surface, such as defects, stacking faults, and phase transformations. For example, Nayak et al. used fs-laser surface texturing to fabricate a cell with 14.2% efficiency compared to 14% efficiency of an untextured reference sample. In the same study, however, industry-standard wet chemical etching resulted in an efficiency of 16.4% despite the less optimal surface geometry. The fs-laser textured sample had a higher short-circuit current, indicative of efficient light trapping but a higher recombination current attributed to laser-induced defects. Minimizing defect formation during fs-laser surface texturing is critical for the design of high-efficiency photovoltaics and the optimization of fs-laser hyperdoping, and is the subject of Chapter 4 and Chapter 5 of this thesis.

1.3 Optical Hyperdoping

Optical hyperdoping is the use of pulsed laser irradiation to dope semiconductors to beyond-solubility-limit concentrations (Figure 1.4). Doping of semiconductors is traditionally done with shallow impurities with the intent of modifying the electronic properties of the semiconductor. It is also possible, however, to significantly modify the optical properties of a semiconductor by doping to very high concentrations with deep-level impurities. Hyperdoping silicon with chalcogens (sulfur, selenium, and tellurium) to concentrations on the order of 0.1-1% results in a drastic increase in both the visible and infrared absorptance [29, 30], illustrated in the inset of Figure 1.4. A combination of computational and experimental investigations has shown that the broad sub-band gap absorptance in selenium-hyperdoped silicon arises from the

merging of the defect band and the conduction band, and the magnitude of the resulting absorption coefficient is similar to that of a direct band gap semiconductor [31]. Such changes in band structure drastically reduce the amount of silicon required to absorb electromagnetic radiation across the spectrum. In addition, fs-laser hyperdoping of silicon with sulfur has been used to fabricate an IR photodetector with responsivities out to 0.8 eV [32], proving the concept that fs-laser hyperdoping can be used to realize silicon-based IR-photodetectors.

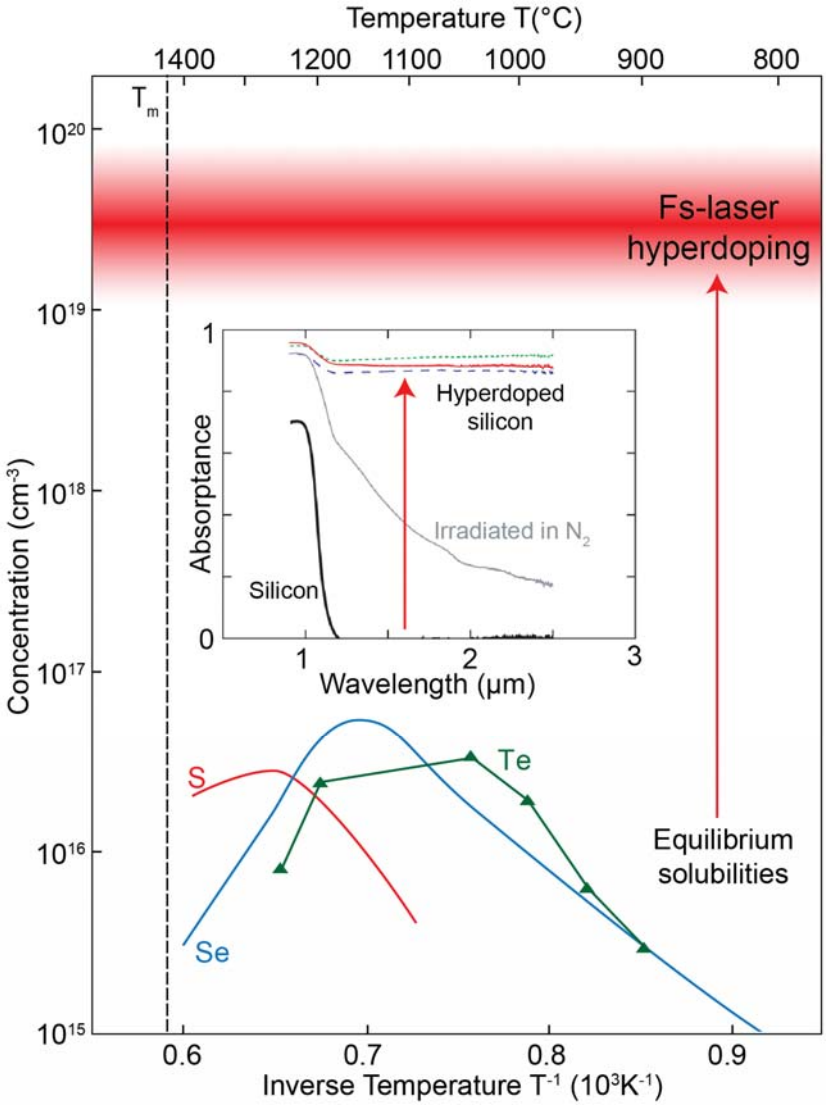

Figure 1.4. Temperature-dependent solubility limits of sulfur (red), selenium (blue) and tellurium (green) in silicon, compared to the concentrations achieved by fs-laser hyperdoping which is a factor of 10,000 times higher. When doped to such high concentrations with chalcogens, silicon exhibits broad sub-band gap absorption (inset). Solubility data is from [33-35] and absorptance data is from [5].

Doping semiconductors with supersaturated concentrations of deep-level impurities is also a potential route to synthesizing an intermediate band semiconductor, a high-efficiency photovoltaic concept through which single-junction solar cells have theoretical efficiency limits greater than 50% [36], exceeding the Shockley and Queisser limit [37]. In an intermediate band semiconductor the high concentrations of dopants lead to the formation of an impurity band inside the band gap [38-40]. Such intermediate band materials allow the up-conversion of 2 infrared photons into one high energy electron, while also absorbing high energy photons via excitation across the band gap (Figure 1.5). There have been several proof-of-concept demonstrations of intermediate band solar cells [41-43], though there are still outstanding questions on the ability to achieve reasonable minority carrier lifetimes in an impurity band material [44].

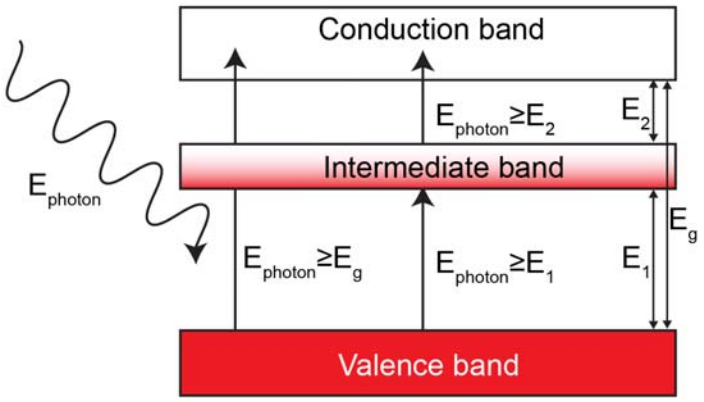

Figure 1.5. Schematic of the band structure of an intermediate band semiconductor. The presence of an intermediate band enables 2 low energy electronic transitions (E_1, E_2) that are otherwise unavailable. Theoretically, an impurity band semiconductor can have an increased short-circuit current without compromising the open circuit voltage, because two photons with energy E_{photon}, such that $E_{1,2} < E_{photon} < E_g$, can excite an electron into the conduction band.

Designing optoelectronic materials using optical hyperdoping, whether for IR-photodetectors or impurity band photovoltaics, requires careful consideration of the distribution of impurity states in the band gap. Different impurities occupy unique energy states within the band gap, and the extent to which the band structure of silicon can be modified using fs-laser hyperdoping therefore is limited by the elements available for doping. In Chapter 6 and Chapter 7 we investigate the effect of the dopant precursor on fs-laser doping in order to broaden the hyperdoping process to a wider range of materials systems.

1.4 Outline of Thesis

The central theme of this thesis is understanding the relationship between fs-laser irradiation conditions and the resulting structure and properties in order to enable the improvement of silicon-based optoelectronic devices through both surface texturing and optical hyperdoping.

Chapter 2 is a review of the laser-material interactions that occur during the fs-laser irradiation of silicon. It begins with a summary of the energy absorption and dissipation processes following a single fs-laser pulse and then reviews the more complicated phenomena relevant to repeated fs-laser irradiation.

Chapter 3 is a collection of the experimental methods used in this thesis, with an emphasis on the fundamental details necessary to accurately interpret the results presented in this work. It begins by introducing the fs-laser irradiation set-up and the details of rastering the laser beam across the surface. Next, the optical characterization methods used in this thesis, UV-VIS-NIR spectrophotometry and Raman spectroscopy, are reviewed. Finally, the electron microscopy-oriented techniques used to study surface morphology, microstructure, and dopant distribution are discussed.

The investigations presented in this thesis fall into two major categories: First, we investigate the pressure-induced phase transformations in silicon during fs-laser irradiation (Chapters 4 and 5). Chapter 4 begins with a review of the current understanding of pressure-induced phase transformations in silicon. Then, we investigate the relationship between the pressure-induced formation of silicon polymorphs and optical hyperdoping, surface morphology, and post-treatment annealing. Scanning electron microscopy (SEM), Raman spectroscopy, and transmission electron microscopy (TEM) are used to identify a strong relationship between pressure-induced phase transformations and the surface texturing process.

In Chapter 5 we study the pressure generation mechanisms that are causing the observed phase transformations in silicon through a systematic investigation of the relationship between irradiation conditions and silicon polymorph formation. In addition, the sensitivity of silicon polymorph formation to the surrounding environment provides insights into the conditions at the surface during fs-laser surface texturing.

In the second half of this thesis (Chapters 6 and 7) we elucidate the effects of a selenium thin-film dopant precursor on the fs-laser doping process. Chapter 6 begins with a review of fs-

laser doping and highlights the open questions relevant to this work. Then, we investigate the effect of the selenium thin film precursor on the resulting optical and electronic properties. The observed trends are explained through characterization of the microstructure and dopant distribution using SEM and TEM. This chapter concludes with an investigation into the behavior of selenium with annealing and provides insights into the relevant optical deactivation mechanisms in chalcogen-hyperdoped silicon.

Chapter 7 begins with a review of pulsed laser doping as a general platform, in order to highlight the unique attributes of thin-film fs-laser doping. Following this, we use SEM and TEM across a range of irradiation conditions to understand the dopant incorporation process. By understanding the relationship between dopant incorporation, localized recrystallization, and surface texturing, we are able to improve the distribution of hyperdoped material produced during thin-film fs-laser doping.

Chapter 8 summarizes the conclusions of this thesis and highlights the most exciting areas of future work arising from the conclusions of our investigations.

Chapter 2 Fs-laser irradiation of Silicon: A Primer

Femtosecond laser irradiation has found applications in a range of industries due to the unique laser-material interactions associated with sub-picosecond pulse lengths. In this thesis, we focus on femtosecond-laser irradiation as a unique platform for surface structuring and hyperdoping of silicon for optoelectronic applications. This chapter reviews the complex series of events that occur following a single fs-laser pulse and discusses the additional mechanisms that become relevant over many fs-laser pulses, with an emphasis on the laser-material interactions relevant to pressure-induced phase transformations in silicon (Chapter 4 and Chapter 5) and thin-film femtosecond-laser hyperdoping (Chapter 6 and Chapter 7).

2.1 Laser-material interactions following a single fs-laser pulse

A semiconductor irradiated with a fs-laser pulse undergoes a relatively long series of reactions compared to the duration of the pulse, the specifics of which depend strongly on the irradiation conditions (Figure 2.1). In this section we review the laser-material interactions during irradiation with a single fs-laser pulse, beginning with non-linear absorption at the surface and the critical role it plays the subsequent laser-material interactions. We focus on the laser-material interactions most relevant to conditions used in this investigation: the irradiation of silicon with a Ti:Sapphire laser with a wavelength of 800 nm and a pulse duration of 80 femtoseconds.

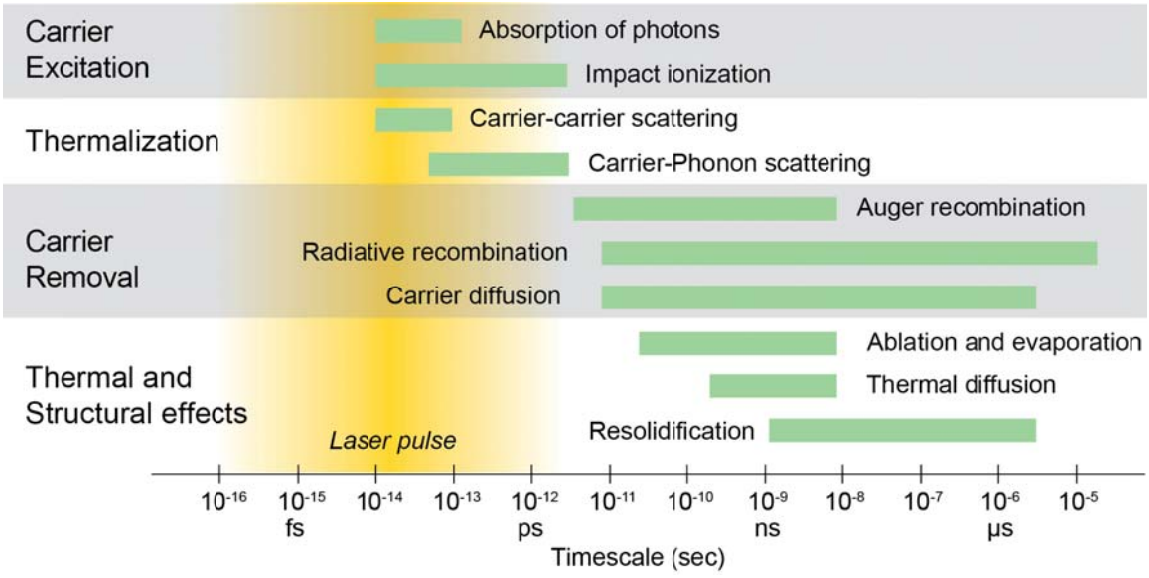

Figure 2.1. Timescales of processes in laser-excited solids. Each bar represents an approximate range of characteristic times over which the processes take place. Adapted from [45].

2.1.1 Absorption

Atoms in solids vibrate with a frequency on the order of picoseconds, much slower than the femtosecond-scale laser pulse duration. As a result, the energy in the fs-laser beam is absorbed first by valence electrons in the semiconductor, creating a dense electron-hole plasma which then interacts with the remainder of the laser pulse. This generation of carriers by photoexcitation increases the absorption coefficient significantly, a side effect of which is that the energy thresholds for fs-laser material processing are much smaller than that of nanosecond laser pulses [46].

The non-linear light absorption depth of fs-laser irradiation in silicon can be approximated by including the absorption coefficients for both one and two-photon absorption [47-49]. Following the analysis presented by Korfiatis et al., an effective absorption coefficient which takes into account one-photon absorption (α_L) and two-photon absorption (β) can be defined as:

$$\alpha_{eff} = \alpha_L + \beta I \tag{2-1}$$

The light intensity (I) is related to the incident laser fluence (F) by taking into account the pulse length τ_p (sec) and the reflectivity, R:

$$F = \frac{I\tau_P}{1-R} \tag{2-2}$$

This expression can be used to define the light absorption depth, δ, in terms of the incidence fluence:

$$\delta = \frac{1}{\alpha_{eff}} = \frac{\tau_p}{\alpha_L\tau_p + \beta F(1-R)} \tag{2-3}$$

For silicon at a wavelength of 800 nm, the linear absorption coefficient, α_L, is 850 cm^{-1} [8], the two-photon absorption coefficient, β, can be estimated to be 9 cm/GW, and the reflectivity, R, at 800 nm is 0.34. Therefore for a pulse duration of 80 fs the effective light absorption depth is 327 nm, two orders of magnitude shorter than what is predicted by considering only linear absorption ($1/\alpha_L$ = 11 μm).

The nonlinear absorption at the surface decreases the interaction depth and therefore increases the energy density at the surface. To illustrate the extreme conditions created at the surface, we estimate the energy density [5] and electric field [50] induced by femtosecond laser irradiation under conditions similar to those used in this thesis. The Ti:Sapphire laser pulses used

in this investigation are focused to a spot ~300 μm in diameter, with an energy of 8 mJ deposited over 80 fs. These conditions result in a peak energy density on the order of 4.0 kJ/m^2 and a peak intensity of 5×10^{13} W/m^2! The average irradiance on the surface (or Poynting vector), $\langle S \rangle$, is related to the electric field, E, by Maxwell's equations:

$$\langle S \rangle = \frac{1}{2} c \epsilon_0 E^2 \tag{2-4}$$

Using these values to calculate the peak electric field gives a value of 3×10^{10} V/m, an order of magnitude higher than the binding fields of an electron to an atom, which are on the order of 10^9 V/m [51].

Immediately following the laser pulse, a hot electron gas (several 1000 K) is formed inside a room temperature lattice [51]. This extremely non-equilibrium environment leads to a series of non-equilibrium and equilibrium processes, and the exact pathway depends strongly on the local energy density [52]. In the context of a single laser pulse, these extreme conditions induced by fs-laser irradiation lead to unique melting and ablation mechanisms and, over many laser pulses, unique surface texturing processes.

2.1.2 Melting and Resolidification

Following absorption of the fs-laser pulse by the valence electrons in the semiconductor, melting can occur through both *thermal* and *non-thermal* pathways. Thermal melting occurs when the excited valence electrons transfer their energy to the lattice through electron-phonon collisions and the atoms gain enough kinetic energy to overcome the binding potential of the stable crystalline structure, which occurs over the relatively long time of several picoseconds [49]. Melting is exclusively thermal during irradiation with laser pulses longer than a few picoseconds [47].

Non-thermal melting is an alternative pathway to losing the crystalline order of the solid, and occurs if the laser pulse is sufficient to excite 10-15% of the valence electrons from bonding states [45]. Following sufficient electronic excitation, the binding potential initially present in the crystalline lattice is instantaneously transformed into a repulsive potential. The atoms are capable of changing coordination and gaining kinetic energy in a time scale on the order of a single vibrational period, achieving structural disorder over ~300 fs (0.3 ps) [48, 49]. This ultra-fast melting occurs on a time scale faster than the electrons are capable of transferring their energy into the lattice, hence *non-thermal* melting occurs before the lattice heats up.

Thermal melting can occur at fluences lower than are necessary for non-thermal melting [48]. The reported melting threshold in literature, defined as the minimum laser fluence at which melting is first observed, therefore is understood to refer to the onset of thermal melting. Melting thresholds are very sensitive to irradiation conditions such as laser wavelength and pulse duration, and thus a range of melting thresholds have been reported. Table 2.1 illustrates the range of experimentally reported fs-laser fluence thresholds for the onset of melting in silicon. The variation in reported melting thresholds is partly related to the effect of wavelength on optical absorption depth (as expressed in equation (2-3), above), but some uncertainty in laser fluence will also contribute to this variation. In the context of this work, we will refer to 2 kJ/m^2 as the melting threshold but acknowledge that this is an approximation.

Fluence, F (kJ/m^2)	Pulse duration, τ_p (fs)	Wavelength, λ (nm)	Reference
1.7	100	625	[53]
1.5	100	620	[54]
1.5	130	620	[55]
1.2	90	620	[56]
1.5	130	790	[57]
2.6	130	800	[58]
2.7	130	800	[59]
≤2.9	150	780	[60]

Table 2.1. Experimental fluence thresholds for the onset of melting, adopted from [47].

The non-thermal melting threshold can be approximated as ~1.5 times the thermal melting threshold [47-49]. Given that the reported thermal melting thresholds vary from 1.5 kJ/m^2 – 2.7 kJ/m^2 under conditions similar to ours, we might therefore expect the onset of nonthermal melting to occur between 2.25 – 4 kJ/m^2. The non-thermal melting threshold for the irradiation of silicon with 800 nm radiation and a 83 fs laser pulse, conditions almost identical to ours, has been experimentally observed to be 4 kJ/m^2 [61].

At irradiation above the nonthermal melting threshold both nonthermal and thermal processes can contribute to the overall melt depth [62]. Nonthermal melting creates a superheated liquid layer on the surface, which can heat surrounding material above the melting temperature as heat diffuses outwards. If the fluence is below the melting threshold then

annealing occurs as the hot carriers relax over several picoseconds by electron-electron and electron-phonon scattering, transferring the energy to the lattice via delayed Auger heating [63].

Molten silicon on the surface cools quickly through thermal conduction due to the drastic temperature difference between the room-temperature substrate and the absorbing layer on the surface. The molten layer resolidifies on the order of nanoseconds after irradiation [64, 65], but the nature of the resolidification process depends on kinetic limitations imposed by the resolidification velocity. There is an upper limit on the speed at which epitaxial growth of silicon can occur, and if the resolidification front is moving faster than 15 m/s [66] then epitaxial growth is inhibited and the resolidified layer will be amorphous. The speed of the resolidification front is related to the magnitude of the thermal gradient generated in the molten silicon. The shallow absorbing depths arising due to nonlinear effects create steeper thermal gradients and therefore, during fs-laser irradiation of silicon, the formation of amorphous silicon is often favored. It has also been reported, however, that fs-laser irradiation of silicon at fluences above 5.8 kJ/m^2 can lead to recrystallization due to excess energy from the laser heating the silicon substrate and reducing the thermal gradient at the surface [59].

2.1.3 Surface temperatures, ablation, and thermoelastic pressure generation

The observation of thermal melting implies that the surface temperature exceeds the melting temperature of silicon (1414°C) during fs-laser irradiation above the melting threshold. Much greater temperatures can be achieved at the surface, however, and rapid superheating can lead to additional structural changes through ablation and thermoelastic pressure generation. The flux of silicon atoms from the surface depends exponentially on the surface temperature and can be used to understand the fluence dependence of the surface temperature [54]. The results from time of flight experiments are shown in Figure 2.2 for λ = 620 nm and τ = 100 fs. The surface temperature increases monotonically with increasing fluence up to the ablation threshold, and there is no significant discontinuity in the surface temperature between thermal and nonthermal melting regimes [54].

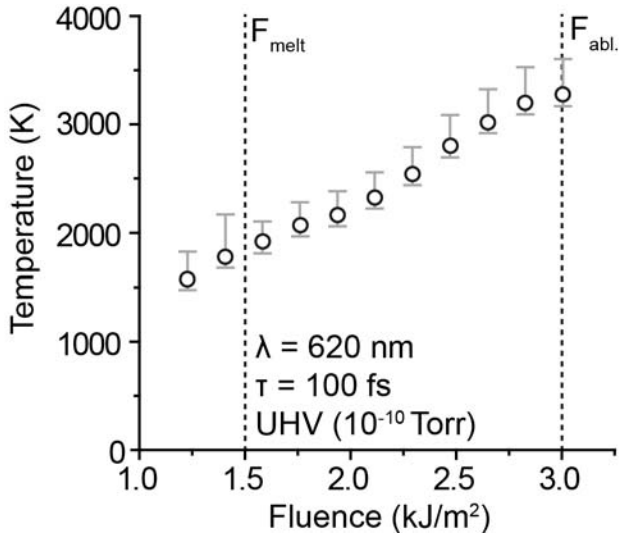

Figure 2.2. (a) Surface temperature of silicon irradiated in ultra-high vacuum (τ = 100 fs, λ = 620 nm) determined by flight-mass spectroscopy. Figure from [54].

Heating of the substrate during fs-laser irradiation occurs so quickly that the material is effectively heated under constant volume, and the compression is released through both ablation at the surface and pressure waves within the substrate. This *thermoelastic* pressure build up can be relieved in several ways: spallation, phase explosion, fragmentation, and ionic plasma formation. Here, we summarize the processes occuring as a consequence of thermoelastic pressure generation based on the experimental and theoretical work presented by Perez et al. [52]

- Spallation is the fracture of a solid due to thermoelastically generated tensile stresses, discussed below.
- Phase explosion occurs if the superheated liquid homogeneously nucleates the gas phase at sufficiently high rates. Such explosive boiling leads to substantial material ejection [54, 58]. Phase explosion is the most common cause of ablation in the femtosecond regime, and most reported ablation thresholds refer to the onset of phase explosion. Similar to the thermal melting thresholds discussed above, reported ablation thresholds vary due to their dependence on irradiation conditions but are generally reported to be around 3-4 kJ/m^2 for fs-laser irradiation of silicon [54, 58]. Ablation is an important mechanism behind surface texturing over many laser pulses, as will be discussed in section 2.2.
- Fragmentation is the decomposition of silicon into ejected clusters, observed in systems under large strain rates. Photo-mechanical fragmentation occurs as a result of the

conversion of stress induced by thermoelastic pressure build-up into strain during subsequent expansion.

- Ionic plasma generation occurs at even higher fluences (>10 kJ/m^2) and is discussed in the following section.

The dominant process depends on the local energy density, which varies across the absorption depth and thus these proccesses can occur simultaneously at the surface.

The relaxation of the thermoelastic compression releases two pressure waves within the material: one travelling towards the surface and one towards the bulk. Under sufficiently low fluences, the pressure wave travelling towards the surface will be reflected elastically and becomes tensile. Low-fluence thermoelastic pressure generation thus has a compressive maximum followed by a broader tensile component. At sufficiently high fluences the surface is unable to elastically reflect the pressure wave due to thermal softening (the decrease in tensile strength observed with increasing temperature). The pressure wave at the surface dissipates energy through the formation of defects, and the pressure wave propagating into the substrate is only compressive.

In terms of magnitudes, the relaxation of thermoelastic pressure build-up can result in pressures in the range of GPa [67]. As the thermoelastic pressure build-up is driven by the amount of heating that occurs within the absorption volume, the magnitude of the thermoelastically-generated pressure wave increases linearly with fluence [68]. Molecular-dynamics modeling of thermoelastic pressure generation estimates the profile of the compressive pressure wave to rise and fall on the scale of picoseconds [52, 69]. Thermoelastic pressure generation is not directly related to ablation and therefore is still relevant at fluences below the ablation threshold. It can lead to substantial plastic deformation and defect formation, which reflects both the magnitude of pressure generation and also the reduced yield strength of materials with increasing temperature [70, 71].

2.1.4 Ionic plasma formation and recoil shock waves

At high enough energies the surface layer of the target is completely atomized and expands at very high speeds, resulting in the ejection of an ionic plasma [52]. The plasma formation threshold is roughly 5 times the ablation threshold [54], and laser-induced shock wave studies often use fluences in the 1000's of kJ/m^2. In silicon, the plasma formation threshold is

around 10 kJ/m^2 for 800 nm wavelength irradiation and varies slightly as a function of wavelength due to the changing absorption depth influencing the local energy density [54, 72].

The expansion of the ionic plasma drives a recoil shock wave into the substrate [73]. The resulting shock wave catches up to and overtakes the thermal wave and then travels further into the substrate than the thermal wave [74]. Fs-laser irradiation with fluences from 110-330 kJ/m^2 in aluminum have been shown to generate shock waves with magnitudes of 95-255 GPa [69]. Laser-driven shock waves in silicon following fs-laser irradiation at fluence of 3,900 kJ/m^2 achieved pressures of 10's of GPa [75]. Interestingly, the intensity of the laser-induced shock wave can be increased an order of magnitude by covering the material with a transparent glass plate during fs-laser irradiation, restricting plasma expansion [76].

The pressure profile of a recoil shock wave generated during plasma formation rises over picoseconds and decays over 10's of picoseconds [69, 77, 78]. As the shock wave travels ahead of and beyond the extent of the thermal wave, the material experiences local temperature increases due to the shock compression and is then rapidly cooled during expansion. This environment makes fs-laser induced shock waves particularly suitable for quenching high-pressure phases [73, 75, 76]. For example, it has been shown that the irradiation of silicon with a single 2,400 kJ/m^2 fs-laser pulse is able to quench several high-pressure phases of silicon: β-Sn (Si-II, 10-13 GPa), Imma (13-16 Gpa), and simple hexagonal (16+ Gpa) [75]. This is in contrast to the pressure-induced transformations to a-Si, Si-XII, and Si-III discussed in Chapter 4 and Chapter 5.

2.2 Laser-material interactions over many pulses

Irradiation with a single pulse triggers a complex series of events depending on the irradiation conditions. In many applications of fs-laser irradiation, including surface texturing and fs-laser optical hyperdoping, tens to hundreds of laser pulses are often used [15, 79]. Repeated fs-laser irradiation complicates the scenario further, as the permanent modifications from the previous pulse (e.g. phase transformations, plastic deformation, surface texturing) influence the laser-material interactions of the subsequent laser pulse [58, 79, 80]. The work presented in this thesis is primarily focused on laser-material interactions over many laser pulses and we draw on these phenomena heavily to contextualize our results.

2.2.1 Incubation effect

Over many laser pulses the fluence thresholds for laser-material interactions gradually decrease [81]. This incubation effect is observed in both metals and semiconductors, and is attributed to an accumulation of energy into plastic stress-strain of the material [58, 81]. It has been shown empirically that the log of the product of the laser modification threshold after N-pulses and the incident pulse number, $Log(\phi_{th}(N) \times N)$, is linear with the log of the pulse number, $Log(N)$ [58, 80, 81]. From this observation the equation can be derived:

$$\phi_{th}(N) = \phi_{th}(1) \cdot N^{\xi-1} \tag{2-4}$$

Where the slope, ξ, is the material-dependent incubation parameter; the farther it deviates below 1 the stronger the incubation effects. The incubation parameter can be determined for a given material by irradiating the sample with a stationary fs-laser spot with a Gaussian intensity profile [58, 80]. With an increasing number of laser pulses the ablated region in the laser spot will grow due to the onset of ablation at lower fluences over multiple pulse numbers. Knowledge of the laser profile enables the conversion of the change in diameter to a decrease in fluence thresholds, and a linear fit to the resulting accumulation curve yields the incubation parameter, ξ. An example *accumulation curve* extracted for fs-laser irradiated silicon (λ=800 nm, τ = 130 fs) is shown in Figure 2.3 [58], yielding an incubation parameter of 0.84 for silicon under these irradiation conditions. Irradiation under slightly different conditions (λ = 775 nm, τ = 150 fs) yielded an incubation parameter for silicon of 0.7 [80], suggesting that the incubation parameter is sensitive to irradiation conditions.

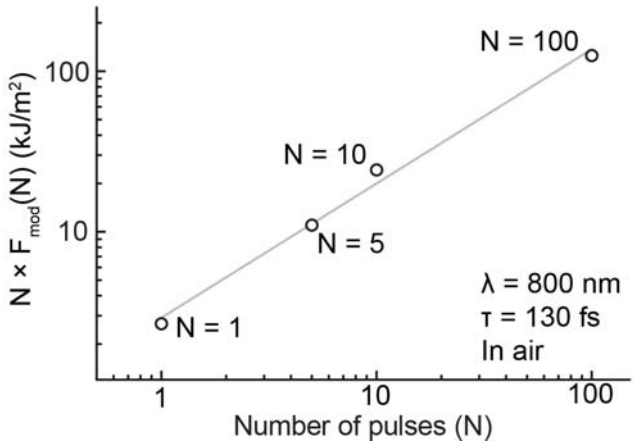

Figure 2.3 Accumulation curve plotting the threshold fluence of laser-induced damage of silicon, Fmod, versus number of laser pulses, N, with (τ = 130 fs, λ = 800 nm) in air. The solid line presents a least square fit where ξ = 0.84. Figure from [58].

2.2.2 Surface texturing

The pulsed laser irradiation of a surface with many laser pulses of sufficient fluence will produce surface texturing, which has been demonstrated across a wide range of materials and pulse durations. The surface texturing of silicon using pulsed laser irradiation is of particular interest for light trapping, and has received a considerable amount of attention [15, 24, 25]. In this section we will review how surface texturing arises through repeated melting and ablation and influenced local rates of energy deposition.

It is a general phenomenon that pulsed laser irradiation initially produces ripples on the surface, called Laser Induced Periodic Surface Structures (LIPSS) [82], though the exact mechanisms of their formation depend on the material and the irradiation conditions [83]. In most cases, the orientation of the "ripples" is perpendicular to the electric-field vector and their lateral period is slightly smaller than the wavelength of the laser. Such surface structures are referred to as low spatial frequency LIPSS (LSFL) and their formation is understood to arise from interference effects between the latter-half of the incident pulse and incident light scattered off defects at the surface [84]. LSFL, shown in Figure 2.4(b), are visible in silicon after 2 pulses with a 8 kJ/m^2 Ti:sapphire laser (λ = 800 nm, τ = 100 fs) in the presence of SF_6. Though the formation of LSFL has been observed across a range of pulse durations (nanoseconds-femtoseconds), irradiation with fs-laser pulses can have unique effects on ripple formation. High spatial frequency LIPSS (HSFL) are observed only under specific conditions during fs-laser irradiation and have ripples with periods 1/3-1/10 times the wavelength of the incident laser light [83, 85-87]. HSFL have been of great interest recently because their formation cannot be explained by the interference model and their formation mechanism is still a topic of debate.

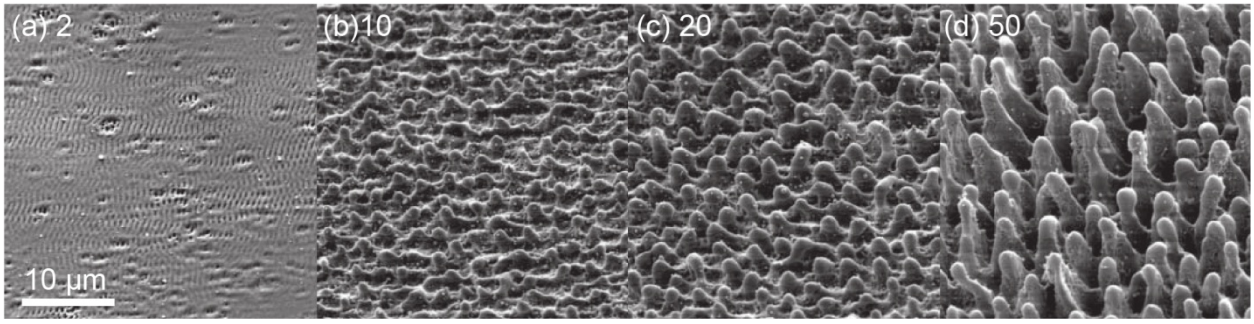

Figure 2.4. SEM images of a silicon surface (τ = 100 fs, λ = 800 nm, 8 kJ/m^2, 1 kHz, in SF_6 ambient) after (a) 1, (b) 10, (c) 20, and (d) 50 laser pulses. Images taken at 45° tilt. Figure adapted from [79].

With continued laser irradiation, the ripple structures evolve into beads on the surface, which in turn become micron-scale spikes (Figure 2.4(b-d)). Figure 2.5(a) illustrates peak formation occurring through material removal during fs-laser irradiation in SF_6. As the initial laser-induced periodic ripple structures grow into larger structures, light is preferentially reflected from the sides of the inclined surfaces and is focused into the valleys between spikes. This increases the local laser fluence in the valley, which in turn increases the rate of ablation. The preferential ablation of material from the valleys creates the appearance that the surface spikes are growing with increasing shot number (Figure 2.4), though Figure 2.5(a) shows clearly that material is being removed. Through this combination of processes, relatively low-fluence fs-laser irradiation can achieve high ablation rates in localized areas on the surface. Due to these self-focusing effects it has been suggested that irradiation of a textured surface with fluences around the ablation threshold of silicon (3 kJ/m^2) can result in ionic plasma formation, even though the threshold for ionic plasma formation is 10 kJ/m^2 [5]. The background gas also plays a large role in the surface texturing process [28], though the general mechanisms are believed to be similar to fs-laser irradiation in SF_6.

Similar to LIPSS, micron-scale spikes are a general phenomenon that occur across a range of materials and pulse durations, though the mechanisms of peak formation and growth are strongly dependent on the irradiation conditions. An example of the effect of irradiation conditions on surface peak generation is illustrated by comparing Figure 2.5(a) to Figure 2.5(b). Figure 2.5(b) shows the surface morphology after irradiation with 3,000 pulses from an XeCl laser (λ = 308 nm, τ = 32 ns) at a peak fluence of 35 kJ/m^2 in the presence of SF_6. The inset indicates clearly that surface texturing occurs through a combination of material removal and peak growth *upwards*. It is proposed that peak growth occurs through material incorporation from the intense flux of Si-rich vapor produced by ablation into the molten surface of the spikes. [88]. The spikes formed using nanosecond laser irradiation are single crystalline [89], suggesting epitaxial incorporation through the melt.

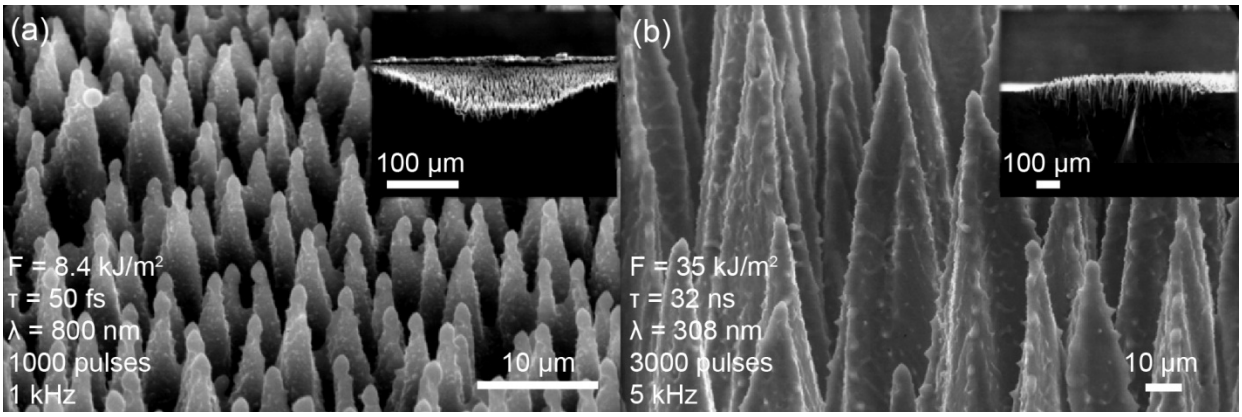

Figure 2.5. SEM (45°) of silicon surface showing conical spike formation (a) after 1000 pulses at 8.4 kJ/m^2 (τ = 80 fs, λ = 800 nm) and (b) after 3000 pulses at 35 kJ/m^2 (τ = 32 fs, λ = 308 nm). The insets show the relative height of the laser spot with respect to the surface. Irradiation conditions determine whether spikes grow upwards or form solely through material removal. Figure adapted from [90].

2.2.3 Resolidification-induced stresses

Laser-induced melting and resolidification is a well-documented source of residual stresses in semiconductors [91], which are strongly affected by the presence of surface texturing. In the context of resolidification-induced stresses, silicon is unique because molten silicon has a higher density (2.55 g/cm^3) than amorphous silicon (2.29 g/cm^3) [92] and crystalline silicon (2.33 g/cm^3) [4]. The resolidification of amorphous silicon from liquid silicon during pulsed laser irradiation results in a ~11% increase and the solidification of polycrystalline produces a 9% increase in volume.

The density changes that occur during resolidification would be accommodated by volume expansion if completely uninhibited. On a roughened surface, however, the surface curvature combined with volumetric expansions creates frustration and this can generate substantial stress in the underlying substrate. The resolidification of molten silicon on a roughened surface during laser irradiation has been shown to generate residual stresses in silicon in the GPa range [70, 93]. The melt-front velocity threshold for the formation of amorphous silicon during resolidification is 15 m/sec [66], which means that the upper bound for resolidification of a 100 nm amorphous layer is ~7 ns. This is significantly slower than the picosecond pressure cycles generated by thermoelastic stresses and recoil pressures from ionic plasma formation. The residual stresses in the substrate indicate, however, that there is

incomplete relaxation and implies that the frustrated relaxation process likely occurs on an even slower timescale.

The solidification of molten silicon on the surface can induce both compressive and tensile stresses in the surface layer [91], which depends largely on the surface morphology. We can gain insights into the relationship between surface morphology and induced stresses by referring to Borowiec et al.'s finite element modeling of residual surface stresses in a 1-D trench due to the cooling of a surface layer with a negative thermal expansion coefficient (Figure 2.6) [94]. At the bottom of the trench there is a tensile stress resulting from the desire of the surface layer to expand laterally. Conversely, this volume expansion induces compressive stresses on the sides of the trench. Although this is not the same morphology as studied in this thesis, we can use this model to draw important insights into the spatial stress distribution during surface texturing (section 5.4.1).

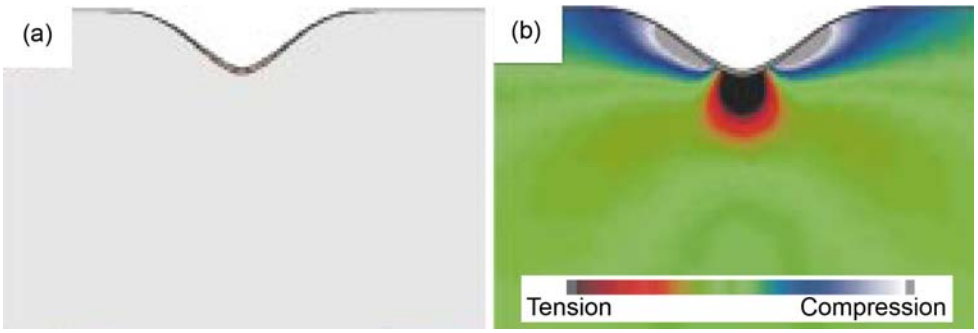

Figure 2.6. (a) Geometry of the model of a trench with a resolidified surface layer (dark grey). (b) Finite element model of trench after solidified layer with a negative thermal expansion coefficient is cooled from 1300 K to 300 K, illustrating spatial distribution of both tensile and compressive stresses. Figure adopted from [94].

2.3 Summary

Femtosecond laser irradiation induces a complex chain of events that are strongly dependent on the irradiation conditions, material properties, and history of prior irradiation. In this section we reviewed the broad scope of laser-material interactions that can occur during the fs-laser irradiation of silicon, with an emphasis on the unique attributes of irradiation on the femtosecond time scale and the mechanisms that are relevant to our investigations of pressure induced phase transformations and thin-film femtosecond laser doping.

Energy deposition during fs-laser irradiation of silicon occurs through the excitation of valence electrons, generating a hot electron-hole plasma in the presence of a cold atomic lattice. This highly non-equilibrium scenario can result in ultra-fast non-thermal melting if >10-15% of the valence electrons are excited out of their bonding state, and can also result in thermal melting over the next several picoseconds as the energy is transferred to the lattice through electron-phonon scattering. The fluence threshold for thermal melting under irradiation conditions used in this study is around 2 kJ/m^2. Sufficient heating will lead to ablation through the homogeneous and explosive nucleation of a gas phase within the molten layer. The ablation threshold of silicon under irradiation conditions used in this study is between 3-4 kJ/m^2. The rapid increase in temperature under constant volume generates large thermoelastic stresses in the superheated surface layer, which can be partially relieved through ablation but will also produce picosecond-scale pressure waves in the material. Femtosecond laser irradiation of silicon at fluences above 10 kJ/m^2 will cause explosive ejection of atoms from the surface. The ejection of an ionic plume is coupled with a strong recoil pressure wave which, similar to thermoelastic pressure waves, has a period on the order of picoseconds.

The processes occurring at the surface become more complicated when we consider the effects of repetitive laser irradiation. Incubation effects will lead to a gradual decrease in the modification thresholds of silicon, and surface texturing will lead to an increase in the local fluence at the surface through self-focusing effects. Surface texturing will also enhance the pressure generated by resolidification of the molten surface layer, and lead to strong residual stresses present within the material.

The background provided in this section begins to illustrate the complexity involved with using fs-laser irradiation as an engineering tool. This summary, however, has focused on the laser-material interactions following fs-laser irradiation at a single point. Surface texturing and hyperdoping of large areas with fs-laser irradiation requires rastering the Gaussian laser spot over the surface, which adds yet another layer of complexity arising from each point on the surface receiving irradiation with a wide range of fluences. This tertiary layer of complexity is explained further in section 3.1.1 and will be drawn on extensively in Chapter 5.

Chapter 3 Experimental Methods

In this chapter we review the material fabrication and characterization techniques used in this thesis. First, we review the experimental set-up for fs-laser irradiation and then discuss the different dopant introduction methods available. Then, we review the basic operating principles of the optical and electron microscopy-based characterization techniques used in this thesis. In both sections, an emphasis is placed on the details relevant to accurate interpretation of the results presented in the following chapters, and the capabilities and limitations of each technique. For each section, references containing more detailed descriptions of the synthesis and characterization techniques are provided.

3.1 Femtosecond-laser irradiation

3.1.1 Femtosecond laser beam and rastering

In the investigations presented in this thesis, we employ fs-laser pulses from a Ti:sapphire laser (λ = 800 nm, τ = 80 fs). The Ti:sapphire pulse train can be delivered with a frequency that is any integer division of 1000. The laser spot has a Gaussian intensity profile, $I(x,y)$, described by the expression:

$$I(\mathrm{x},\mathrm{y}) = I_0 \mathrm{e}^{-\frac{\mathrm{x}^2}{2\sigma_\mathrm{x}^2} - \frac{\mathrm{y}^2}{2\sigma_\mathrm{y}^2}} \tag{3-1}$$

and therefore will have a full-width-half-max (w) expressed as

$$w_i = 2\sqrt{2 \times \ln(2)} \times \sigma_\mathrm{i} \tag{3-2}$$

where $i = x$ or y. During irradiation the wafer is positioned in the focus of the fs-laser pulse and normal to the direction of irradiation. A CCD camera is used to precisely measure the spatial profile of the laser pulse, which will be important for spatially mapping fluence across the laser spots. The set-up through which the train of laser pulses is directed is shown in Figure 3.1, and described in greater detail in references [5, 50].

Large areas can be treated with fs-laser irradiation by translating the wafer underneath the pulsing laser beam, which is a common technique in both surface texturing and hyperdoping. The irradiation received under rastered conditions is a function of the full-width half-max of the laser spot, w, the translation speed, v, and the frequency, f. The irradiation conditions generated during laser rastering can be condensed into a single term, *shots per area*, which describe the number of laser pulses a single spot receives that are at an intensity equal to or greater than half the peak fluence. Shots per area can be written explicitly as [50]:

$$S/A = \frac{\pi w_x w_y}{\Delta_x \Delta_y} = \frac{f \cdot \pi w_x w_y}{v \Delta_y} \tag{3-3}$$

Where $\Delta_x = v/f$. In the work presented in this thesis the wafer is translated in the x-direction, which is also the direction of E-field polarization vector, across the entire distance being irradiated and then stepped perpendicularly a single increment, Δ_y, before being translated back along the x-axis. Irradiation conditions are chosen such that the number of steps along each axis of the laser spot are equal, or $w_x/\Delta_x = w_y/\Delta_y$.

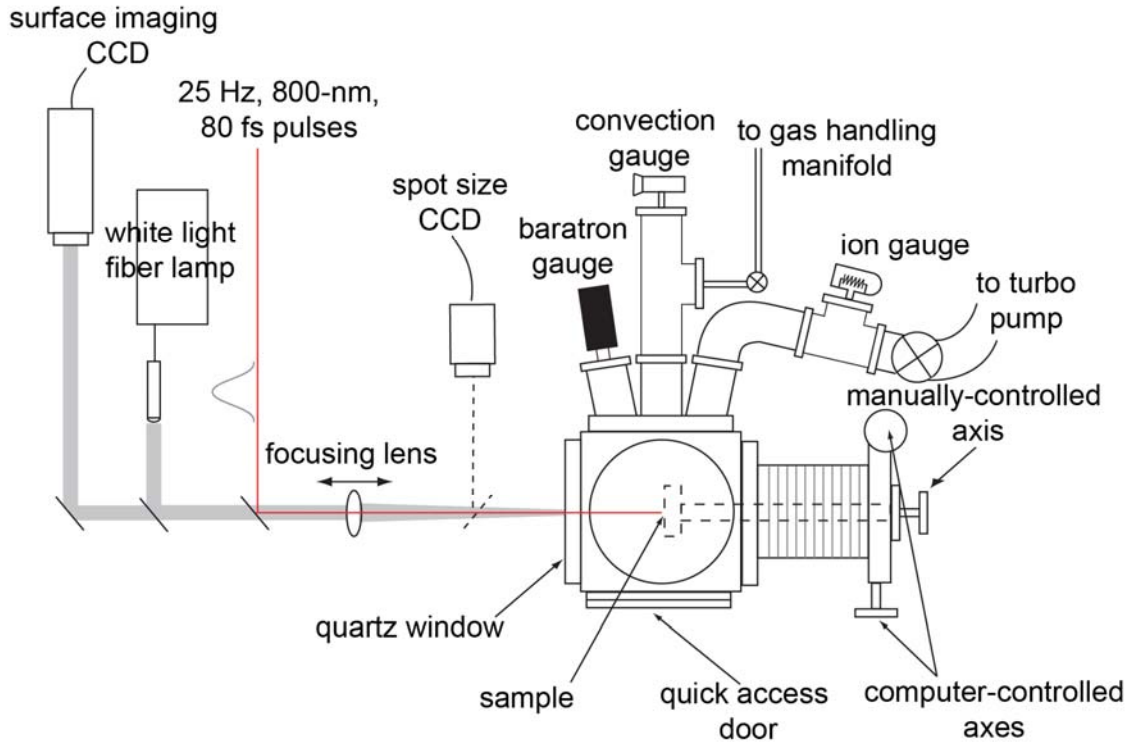

Figure 3.1. Schematic of femtosecond-laser irradiation set-up used in this thesis. From [50].

Reporting laser rastering in shots per area (s/a) has been widely adopted because of its ease of use, but it should be emphasized that this unit does not comprehensively describe the irradiation conditions at the surface during laser rastering. Figure 3.2(a) illustrates the rastering of a 4 kJ/m^2 peak fluence laser beam over the surface under conditions corresponding to 88 shots/area, as these are the most common irradiation conditions used in this thesis. In this example, w_x = 372 um and Δ_x = 50 um, w_y = 471 um and Δ_y = 63 um. The step sizes have been scaled with asymmetries in the beam size such that $w_x/\Delta_x \cong w_y/\Delta_y \cong 7.4$. Figure 3.2(b) illustrates explicitly the fluences received by a single spot on a surface as the laser beam is

rastered across it; the fluences received at the surface vary drastically throughout laser rastering. While there are 88 pulses between 2 - 4 kJ/m^2, a single spot on the surface also receives over 300 pulses between 0.1 - 2 kJ/m^2. The blue segment in Figure 3.2(a) and (b) illustrates the fluence delivered in a 1-D line scan across the surface, which under these conditions results in 11 shots/area.

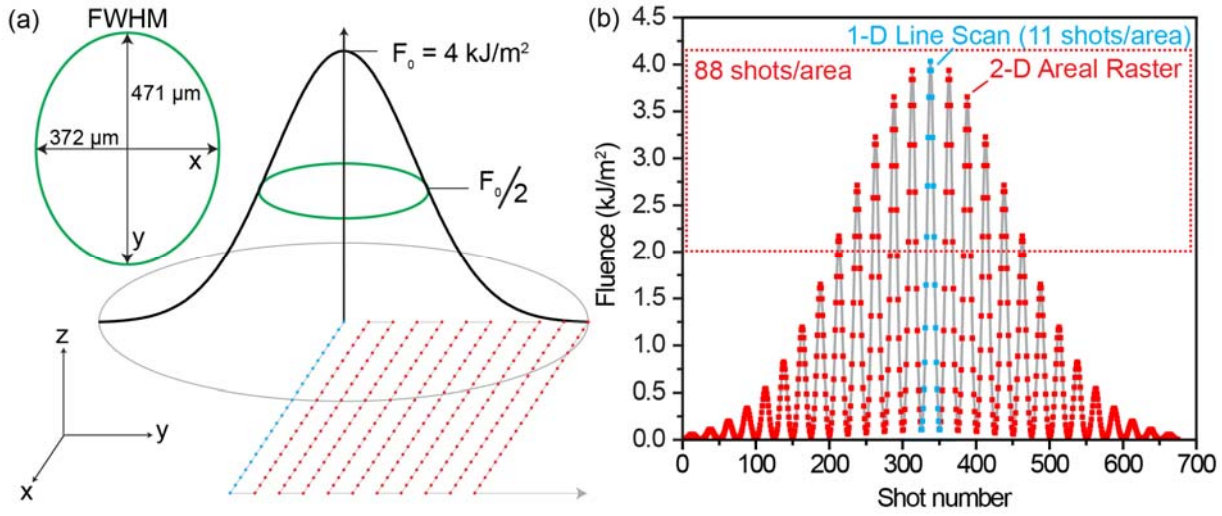

Figure 3.2. (a) Schematic of the Gaussian laser spot and the relative step sizes used to prepare a the 88 shots/area sample studied in this section. Inset is the full-width-have-max of the laser spot. The laser beam is polarized in the x-direction. The grey ring at the base of the Gaussian peak is to guide the eye. (b) The fluences of the fs-laser pulses received by a single point on the surface as the laser spot is rastered in the x-direction (line scan, blue) and rastered over a 2-D area (blue and red).

3.1.2 Dopant introduction during fs-laser irradiation

The ultrafast melting and resolidification that follows fs-laser irradiation can be used to achieve ultra-high concentrations of dopants in the molten material, so long as dopants are present in the surrounding environment during irradiation. There have been two demonstrated approaches to fs-laser doping: Irradiation in the presence of a gaseous dopant precursor (Figure 3.3(a)) or the deposition of a film onto the surface prior to irradiation (Figure 3.3(b)). For a complete history of these techniques see section 6.1.

In this thesis we compare doping from a gaseous dopant precursor, a thin-film dopant precursor, and irradiation without dopants present in order to understand the role that the dopant precursor plays on pressure-induced phase transformations and on the dopant incorporation and surface texturing processes (Chapters 6 and 7). Investigations into thin-film fs-laser doping use a 75 nm thin film of selenium, thermally evaporated onto the silicon, as a dopant precursor. We

immediately load the wafer into the vacuum chamber and evacuate the chamber to pressures $\leq 10^{-5}$ Pa. In the case of thin-film doping or irradiation with no dopant present, the chamber is then back filled with 6.7×10^{4} Pa (500 Torr) of N_2. When doping from a gas phase, the vacuum chamber is filled to the same pressure with SF_6 gas.

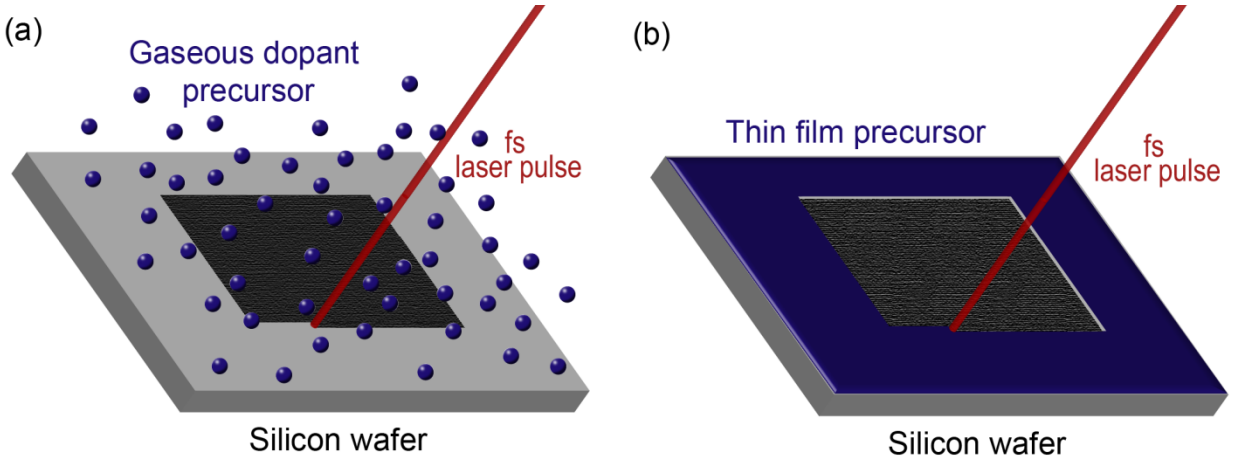

Figure 3.3. Fs-laser doping can be accomplished by fs-laser irradiation (a) in the presence of a gaseous dopant precursor or (b) depositing a thin film of dopant onto the surface prior to irradiation.

3.2 Optical characterization of fs-laser irradiation silicon

3.2.1 UV-VIS-NIR Spectrophotometry

Silicon hyperdoped with chalcogens exhibits a strong increase in sub-band gap absorptance. This phenomena is interesting in its own right and also makes the silicon-chalogen material system a powerful model system for studying hyperdoping because the broad sub-band gap absorptance can be used to estimate the amount of hyperdoping on the surface. The infrared absorptance of samples irradiated with a rastered laser beam is measured with a UV-VIS-NIR spectrophotometer equipped with an integrating sphere. The diffuse and specular reflectance (R) and transmittance (T) were measured for the wavelength range of 0.9 - 2.5 μm, enabling the determination of the absorptance, A ($A = 1 - R - T$).

3.2.2 Raman Spectroscopy

Raman spectroscopy relies on the inelastic scattering of monochromatic light with phonons, resulting in a measurable shift in the energy of the laser light. The phonon can absorb

energy from the photon (Stokes shift) or transfer energy to the photon (Anti-stokes shift), and the resulting shifts in the photon energy provides information about the phonon modes in the system. Crystalline phases with long-term order have discreet phonon modes, and these can be used to identify the crystal structure of the material being probed. For example, diamond cubic silicon has a signature LO/TO mode at 520 cm^{-1} whereas amorphous silicon has a broad hump around 480 cm^{-1} [59].

In this work we use Raman spectroscopy to detect the presence of silicon present in three polymorphic crystal structures: the familiar diamond cubic phase (Si-I), an R8 phase known as Si-XII and a BC8 structure coined Si-III [95]. The formation of these phases is described in detail in section 4.1. Important to the discussion here is that both Si-XII and Si-III are crystalline and have signature phonon modes which can be easily distinguished from the 520 cm^{-1} peak of Si-I in the Raman spectra. In this work, we focus on the most easily distinguishable Raman modes: the Si-XII peak at 350 cm^{-1} and the Si-III peak at 443 cm^{-1}.

The peak intensities, peak positions, and peak widths in Raman spectra can be used to understand a great deal about the material being characterized. To estimate the relative volumes of silicon phases present in the sample, we compare the intensity (integrated area under the peak) of the Si-XII mode at 350 cm^{-1}, the Si-III mode at 443 cm^{-1}, and the Si-I mode at 520 cm^{-1} [96]. Stress in the system will lead to shifts in the energy of the phonon modes, and thus Raman peak positions can also be used to measure residual stresses in the specific crystalline phases being probed. The shifts in the position of the 520 cm^{-1} peak of Si-I are well calibrated. The induced stress in Si-I can be calculated through the following relation [93]:

$$Local\ Stress\ (GPa) = \frac{Local\ peak\ position\ -\ 520\ cm^{-1}}{1.55\ cm^{-1}GPa^{-1}} \qquad (3\text{-}4)$$

The values in the denominator,1.55, is the experimentally determined Raman shift-stress relationship for the Si-LO/TO peak. A reference spectra from the substrate was used to calibrate the Si-I LO/TO peak to 520 cm^{-1}, so shifts seen in all laser-irradiated spectra are due to laser irradiation. The shifts of the Si-XII (350 cm^{-1}) and Si-III (443 cm^{-1}) Raman modes are not as well studied, though changes in wavenumber can be qualitatively translated into residual stresses based on the empirical investigations of Olijnyk and Jephcoat [97].

All Raman spectra presented in this thesis were collected under the following "standard" conditions to minimize instrument-based variations and enable qualitative comparison between samples. We used a Raman spectrometer with a 10 mW 632.8 nm HeNe laser, recorded through a 20x objective (0.4 NA) with a spot size of ~10 μm, and projected onto a CCD using a 1200-g/mm diffraction grating. This set-up has a programmable stage, which we use to spatially map trends in the Raman spectra. The precise position and background-subtracted intensity of the Si-I (520 cm^{-1}), Si-XII (350 cm^{-1}) and Si-III (443 cm^{-1}) peaks were quantified by Renishare WiRE 3.0 software. Additional details on spectra collection are presented in the experimental sections of each chapter.

All of the spectra in this thesis were collected under identical conditions to enable comparison between samples, but it is important to acknowledge the effect of surface roughness on the resulting Raman spectra. As discussed in section 1.2, surface texturing drastically increases light scattering at the surface. Scattering at the surface will influence the overall peak intensity and may also influence the homogeneity of signal generation; certain regions may receive a greater intensity of incident laser light due to the self-focusing effects. In order to reduce the effects of surface morphology, a low NA (0.4) was used with a relatively large spot size (10 μm). The absorption depth at the wavelength of the incident laser (632.8 nm) is larger than the surface features we study in most of this thesis (~ 3 μm), so we still expect the entire volume of the textured-region to be probed under these conditions. Due to the variations in surface roughness, our investigations into peak intensities are limited to qualitative comparison between samples. It is not expected, however, for surface roughness to influence the positions of Raman modes or the relative intensities in reported Si-XII/Si-III ratios. In the analyses in this thesis we investigate trends in both peak position and peak intensity, and will consider effects of surface morphology accordingly.

3.3 Electron Microscopy

3.3.1 Introduction to electron microscopy

There are several powerful advantages to using electron microscopy for structural and chemical characterization. The first is the spatial resolution enabled by using electrons instead of visible light for imaging. The spatial resolution in optical microscopy, δ, is limited by the wavelength of the radiation being used, λ, according to the Rayleigh criterion:

$$\delta = 0.61\lambda/NA \qquad (3\text{-}5)$$

Here *NA* is the numerical aperture [98]. The wavelength of visible light is 100's of nanometers, but the wavelength of an accelerated electron is on the order of picometers, 4-5 orders of magnitude smaller. The resolution achievable by electron microscopy-related techniques is not limited by the wavelength of the electrons, but rather the optics of the system and scattering within the sample.

The second advantage of electron-based characterization is that the interaction between the highly energetic electrons and the sample generates a number of different signals that contains a broad range of information about the sample (Figure 3.4). In the following we will review the specific electron-microscopy based techniques used in this thesis and the fundamental mechanisms of signal generation behind each of them.

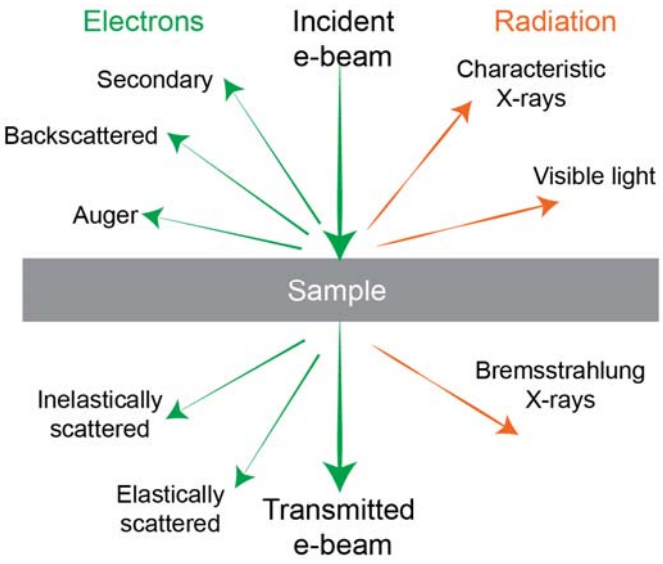

Figure 3.4. Schematic of the variety of signals generated during the interaction of a high-KV electron beam with a sample. Adapted from reference [99].

3.3.2 Scanning electron microscopy

Scanning electron microscopy is a valuable tool for imaging surfaces. Images are formed with a beam of low(er) energy incident electrons (0.5-40 kV), converged to a 1-10 nm probe and scanned over the surface. Secondary and back-scattered electrons provide both morphological and chemical information about the surface of the sample. Throughout this thesis we use scanning electron microscopy with a secondary electron detector to study the surface morphology following fs-laser irradiation. Additional signals contain information about the composition of the surface (energy dispersive x-ray spectroscopy) and local band structure (cathodoluminescence), but electron scattering, x-ray scattering, and carrier drift limit the spatial resolution achieved using these techniques in an SEM. A more thorough discussion of scanning electron microscopy can be found in [100].

3.3.3 Transmission electron microscopy

If the electrons are accelerated to higher voltages (80 – 300 kV) and the sample is sufficiently thin (~100 nm) then a great deal of information can be extracted by passing electrons through the sample, this family of characterization techniques is referred to as transmission electron microscopy (TEM). Critical to TEM characterization is the preparation of samples that are thin enough to be electron transparent. This can be done in a variety of ways depending on facilities available, the material system, and the desired type of characterization. In this thesis we use two techniques for sample preparation: tripod polishing and the focused ion beam (FIB) lift-out technique. Tripod polishing allows for the preparation of either plan-view or cross-sectional samples with relatively large transparent regions. In this thesis we use a South Bay Technologies tripod polisher, diamond polishing films, and a Struers Labopol-4 polishing wheel. Following polishing, final thinning is done using a Gatan PIPPS broad-beam Ar^+ ion mill. The FIB lift-out technique was carried out using a FEI Helios 600 Dual beam FIB. Sample preparation using FIB allows for excellent spatial control and good control over the resulting sample thickness, but typically results in a smaller electron-transparent region than tripod polishing.

TEM is a mature characterization platform and a wide range of techniques to have been developed around it. This introduction will focus on the TEM-based techniques employed in this thesis: Bright-field TEM (BF-TEM), selected area diffraction (SAD), bright-field scanning TEM

(BF-STEM), dark-field scanning TEM (DF-STEM), high-angle annular dark field STEM (HAADF-STEM), convergent beam electron diffraction (CBED), electron energy loss spectroscopy (EELS), and energy dispersive x-ray spectroscopy (EDX). Here we will focus on the fundamentals of each imaging technique to prepare the reader for proper interpretation of the images and spectra presented in this thesis. Williams and Carter [99] offer an excellent comprehensive review of TEM-based characterization in case the reader would like to explore TEM in greater detail.

There are three mechanisms by which contrast is generated in TEM imaging, each a result of unique physical mechanisms: Mass-thickness contrast, diffraction contrast, and phase contrast. Mass-thickness contrast arises from incoherent elastic scattering of electrons, referred to as Rutherford scattering. Rutherford scattering is a strong function of the mass, density, and thickness of the specimen. The scattering angle in Rutherford scattering is a function of the atomic number, *Z*, and thus collecting electrons scattered at wide angles is more sensitive to composition (see Z-contrast imaging, below). Diffraction contrast arises due to scattering at specific angles for which the orientation of the crystalline sample and the incident electron beam satisfy the Bragg diffraction conditions. In the scope of this work, diffraction contrast is particularly useful for resolving grains of different orientation within a polycrystalline sample, as their contrast changes with the orientation of the lattice with respect to the electron beam. Phase contrast arises due to shifts in the phase of the electron beam as it passes through the sample. The interference between the transmitted and scattered beams enables imaging of the lattice of the crystal, referred to as high-resolution TEM (HR-TEM). The characterization techniques in this thesis focus mostly on the use of mass-thickness contrast and diffraction contrast to understand the microstructure and dopant distribution in laser-irradiated silicon.

The TEM techniques used in this thesis can be divided into two categories: Conventional TEM-based techniques (BF-TEM, SAD) in which the electron beam enters the sample as parallel beam of electrons nanometers-microns in spot size (Figure 3.5(a)), or convergent-beam techniques in which the beam is converged to a single point (a probe) that can be a nanometer or smaller (STEM, CBED) (Figure 3.5(b)). In bright-field TEM (BF-TEM), when the parallel electron beam passes through the sample electrons are both scattered inelastically (Rayleigh scattering) and diffracted. The objective aperture allows for the selection of which electrons are used to form the image, and this is magnified by the intermediate and projection lenses.

Therefore the bright-field images in this thesis exhibit strong contributions from diffraction contrast, which is well suited for imaging the grain size distributions in polycrystalline materials.

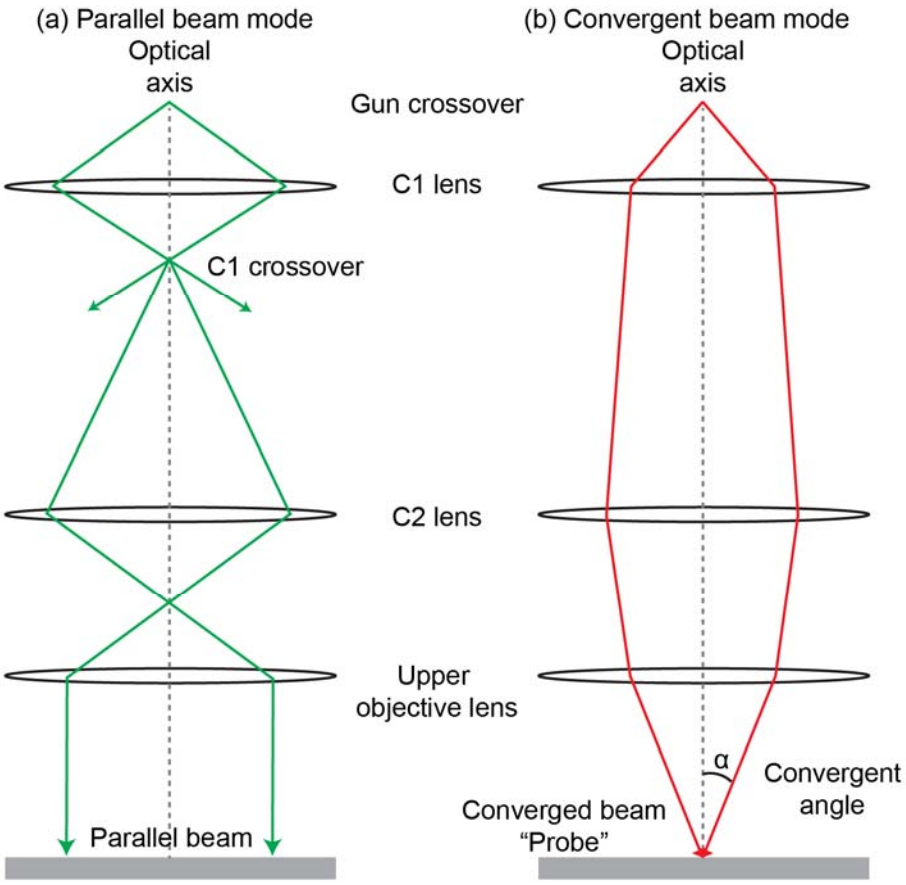

Figure 3.5. (a) Diagram of conventional TEM mode or parallel-beam mode in the TEM. (b) Example lens diagram of convergent-beam/probe mode in the TEM. The exact approach to creating a probe varies from microscope to microscope. Adapted from [99].

A strength of TEM imaging is that both an image and a diffraction pattern can be obtained from the same region. After passing through the sample, the objective lens disperses the emerging electrons such that they create a diffraction pattern in the back focal plane, before recombining to form an image in the image plane. Selected area diffraction (SAD) is the use of the diffraction pattern in the back focal plane to obtain detailed information on the crystal structure of the region selected by the SAD aperture. As the diffraction conditions are sensitive to both the crystal structure and the lattice's relative orientation with respect to the electron

beam, we use this technique to identify crystalline versus polycrystalline regions as well as to identify unique crystal structures that form during fs-laser irradiation.

In scanning TEM (STEM) imaging mode, the electron beam is converged to a probe (Figure 3.5(b)) and scanned over the surface using scan coils. The scan coils simultaneously scan the computer display, thereby forming an image. In STEM mode an electron detector is used to select what electrons are used to create the image, in the same way that an aperture is used in conventional TEM. The differences between BF-STEM, DF-STEM, and HAADF-STEM depend solely on the range of scattering angles that are used to generate the image (Figure 3.6).

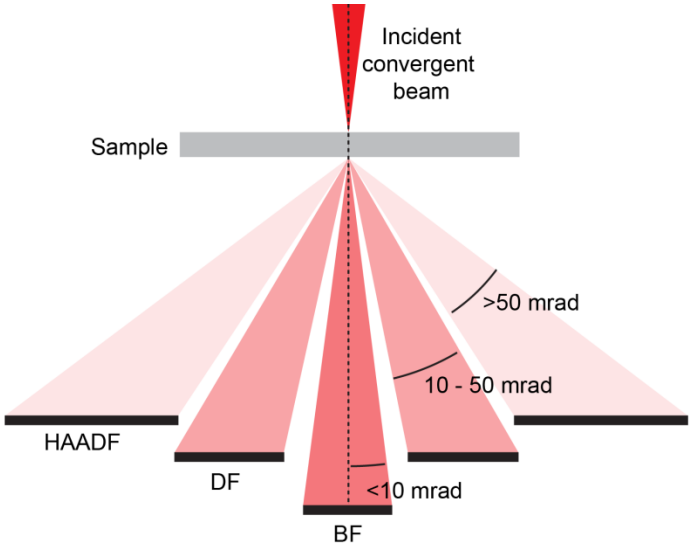

Figure 3.6. Schematic illustrating the range of detectors that can be used in scanning TEM mode: The bright-field (BF) detector collects transmitted and slightly off-axis electrons. The dark-field (DF) detector and high-angle annular dark field (HAADF) detector collect electrons scattered at wider angles. The larger the collection angle the more sensitive the image is to atomic weight and less sensitive to diffraction contrast. Figure adapted from [99].

A bright-field detector uses the transmitted electrons and those scattered to only very small angles ($\leq 0.6°$), which includes both mass-thickness contrast and diffraction contrast. Annular detectors have a hole (*annulus*) in the center to avoid collecting the transmitted beam and electrons scattered to only small angles. The Rayleigh scattering angle is a function of the atomic number, Z, and collecting only electrons scattered to larger angles will result in an image that is more sensitive to atomic number and has less of a contribution due to diffraction contrast. Dark-field STEM, a technique readily available at MIT, increases the amount of chemical contrast in the image but does not completely eliminate diffraction contrast. High-angle annular

DF-STEM relies on collecting only electron with very large scattering angles, thereby creating an image with only chemical contrast. As such, the use of a wide-angle aperture is also referred to as "Z-contrast" imaging. In this thesis we use HAADF-STEM imaging done at both Oak Ridge National Lab and CEA-LETI (Grenoble, France) to study the dopant distribution in hyperdoped silicon.

A convergent beam can also be used to generate diffraction patterns, in a technique called convergent beam electron diffraction (CBED). Compared to SAD, CBED has a higher spatial resolution (limited only by the probe size) and contains more information. CBED patterns can include higher-order Laue zone (HOLZ) lines, which give 3-D crystallographic information about the specimen. The converged beam can be scanned to generate an image (STEM) which then enables precise positioning of the probe, offering great spatial control over where the diffraction pattern is collected from. In this thesis we use CBED in characterizing the crystallinity of features that are only 10's of nanometers large, taking advantage of the higher spatial resolution it affords.

As illustrated in Figure 3.4, much more occurs than just inelastic electron scattering when high energy electrons pass through the sample. Interactions with the core electrons of atoms, in particular, can be used for chemical identification and quantification and, when combined with a converged electron probe, offer high spatial resolution. Interactions between the incident electron beam and core electrons enable chemical identification because the energy levels of core electronic orbitals are strongly affected by the number of protons in the nucleus, and thus act as unique elemental signatures. As shown in Figure 3.7, the processes behind both energy-dispersive x-ray spectroscopy (EDX) and electron energy loss spectroscopy (EELS) begin with a high-energy incident electron ejecting a core electron from its atomic orbital. Some amount of energy is transferred to the ejected electron, E_{trans}, which must be greater than the binding energy of the core electron, $E_{binding}$. An electron from a higher energy orbital will relax to fill the core-hole and emit an x-ray with a characteristic energy. In EDX, an x-ray detector is used to measure the intensity and energy of the emitted x-rays. The composition can be extracted from the relative peak intensities, given that the appropriate scaling factors are taking into account.

In this thesis, EDX is a valuable tool for investigating the distribution of selenium in silicon, though it is not without limitations. One limitation of EDX is the spatial resolution, as both electron scattering and x-ray scattering will generate signals from a volume larger than the

initial electron probe. In addition, EDX is not well suited for the detection of light elements (Li, O, N…) because the x-ray fluorescent yield decreases rapidly with decreasing atomic number. Finally, because the chemical resolution of EDX is on the order of 1% the quantification of EDX spectra presented in this work is still qualitative, capable only of identifying regions that contain selenium concentrations ~3 orders of magnitude above their solubility limit.

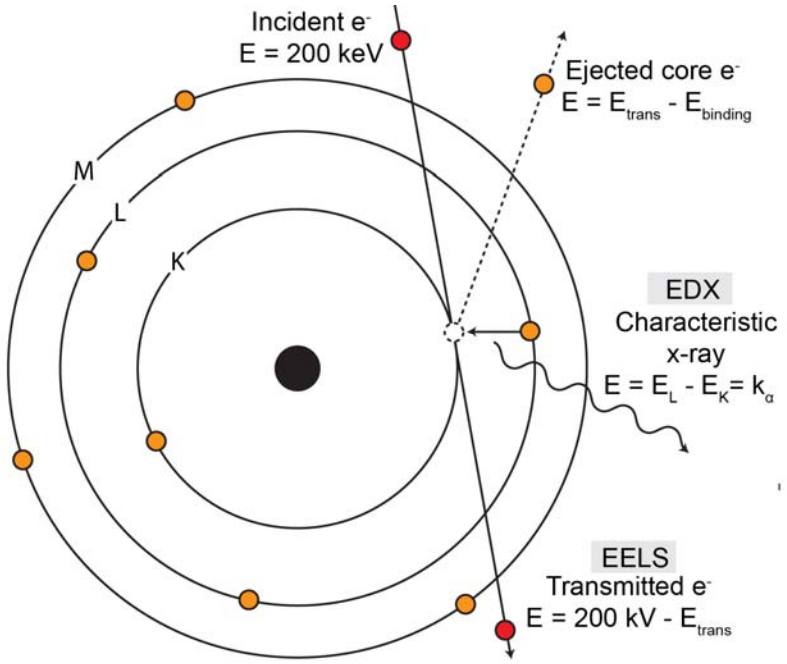

Figure 3.7. Illustration of interactions between incident electrons and core electrons that are used for chemical characterization in a TEM via energy dispersive x-ray spectroscopy (EDX) and electron energy loss spectroscopy (EELS).

EELS is an alternative approach to chemical identification based on monitoring the amount of energy lost by the electrons that travelled through the sample. By passing the transmitted beam through an energy filter, a wide range of inelastic collisions that occurred within the sample can be probed. The same incident electron that ejected the core-electron, leading to x-ray generation in the previous example, loses some amount of energy, E_{trans}. The amount of energy transferred must be greater than or equal to the binding energy, $E_{binding}$, and can be used for chemical identification. The energy-loss spectrum has a series of edges, corresponding to the onset of ionization from different elements and orbitals, which appear at signature binding energies. In this way EELS is similar to EDX except with better spatial

resolution, because there are no secondary scattering effects and EELS has a higher sensitivity to light elements. The higher-energy tail of the core-shell edge in the EELS spectra also contains information about the density of states. In this thesis we use EELS specifically to confirm the presence of amorphous silicon. The sensitivity to light elements makes EELS suitable for confirming the absence of large concentrations of oxygen (ruling out SiO_x) and the fine structure of the silicon $L_{2,3}$-edge is dependent on crystallinity due to the reduction of density of states around the conduction-band minimum in amorphous silicon [101]. For more information on EELS, an excellent review is available in reference [102].

Chapter 4 Pressure-induced transformations Pt. 1: Hyperdoping, Spatial distribution & Stability

Understanding the relationship between surface texturing and pressure-induced phase transformations in silicon is critical for minimizing laser-induced damage during optoelectronic device fabrication. In this chapter we investigate the transformation from diamond cubic Si-I to pressure-induced polymorphic crystal structures (amorphous Si, Si-XII, and Si-III) during femtosecond-laser irradiation using SEM, Raman spectroscopy, and TEM. Amorphous Si, Si-XII, and Si-III are found to form in femtosecond-laser doped silicon regardless of the presence of a gaseous or thin-film dopant precursor. Through studying the spatial distribution and the formation of Si-XII/III with evolving surface morphology, we show that the formation of crystalline polymorphs is closely related to the surface texturing process. Finally, we find that the polymorph phases disappear during annealing more rapidly than the sub-band gap absorptance decreases, enabling us to decouple these two processes through post treatment annealing.

4.1 Introduction

Defect formation in silicon during pulsed laser irradiation can occur through both the imperfect resolidification of molten silicon and pressure-induced plastic deformation. Defects that form during resolidification include excess vacancies and self-interstitials, stacking faults and dislocations, grain boundaries, phase segregation, and, in extreme cases, amorphization. The formation of melting-induced defects and their relation to irradiation parameters is relatively well understood [103, 104]. In addition, they are isolated to the melt depth of the material and therefore can be removed, if desired, by a wet etching step [15].

Much less is understood about pressure-induced plastic deformation during fs-laser surface texturing. For example, amorphous pockets have been observed below the melt depth [105] but their chemical composition and origin remains unexplained. Raman investigations suggest the formation of pressure-induced crystalline phases in silicon following fs-laser irradiation [105, 106] but little is known about their spatial distribution within the material or the mechanisms behind their formation. Finally, there are multiple sources of pressure generation during fs-laser irradiation (Chapter 2) and it is unknown which processes are responsible for plastic deformation during surface texturing.

Pressure-induced plastic deformation in silicon is unique because the preferred mechanism of plastic deformation at moderate temperatures is an irreversible phase transformation [107]. At temperatures lower than 350°C, silicon responds to pressures above 10-

12 GPa by undergoing a series of irreversible phase transformations (Figure 4.1). Because the exact series of pressure-induced phase transformations is sensitive to pressure loading and unloading conditions, studying these transformations provides a novel insight into the conditions at the surface following fs-laser irradiation.

The current understanding of pressure-induced phase transformations in silicon was developed through high-pressure studies using diamond anvil cells [108] and nanoindentation [109]. The relevant processes are illustrated in Figure 4.1. Silicon transforms from its diamond cubic phase (Si-I) to a β-Sn phase (Si-II) at pressures above ~12 GPa and this transformation is irreversible, i.e. Si-II cannot transform back to Si-I during pressure unloading [110, 111]. Upon sufficiently slow pressure release, silicon with R8 structure (Si-XII) nucleates from Si-II and then reversibly transforms to a BC8 structure (Si-III) around 2 GPa [112]. Nanoindentation studies have found that the formation of Si-XII/III from Si-II is nucleation limited; alternatively, there is no activation barrier to the formation of amorphous silicon (a-Si) from Si-II. The nucleation of Si-XII/III can be suppressed by sufficiently fast unloading rates, forcing Si-II to transform completely into a-Si [113]. The formation of crystalline silicon polymorphs is enhanced at slightly increased temperatures [107], but the nucleation of Si-XII is suppressed at temperatures above ~200°C [107]. At temperatures above 350°C there is a rapid decrease in silicon hardness due to the thermal activation of dislocation motion and plastic deformation proceeds, instead, by the formation and motion of dislocations. The pressure-induced silicon polymorphs are metastable: Si-XII, Si-III, and a-Si transform back to polycrystalline Si-I with annealing through intermediate phases. The exact pathway of relaxation depends strongly on the surrounding matrix, residual stresses in the material [114], loading and unloading rates, indenter shape [113], phase of the initial surface (a-Si vs c-Si) [115], and ambient temperature [116]. For example, the Si-II/a-Si interfaces lower the activation barrier for the nucleation of Si-XII [116].

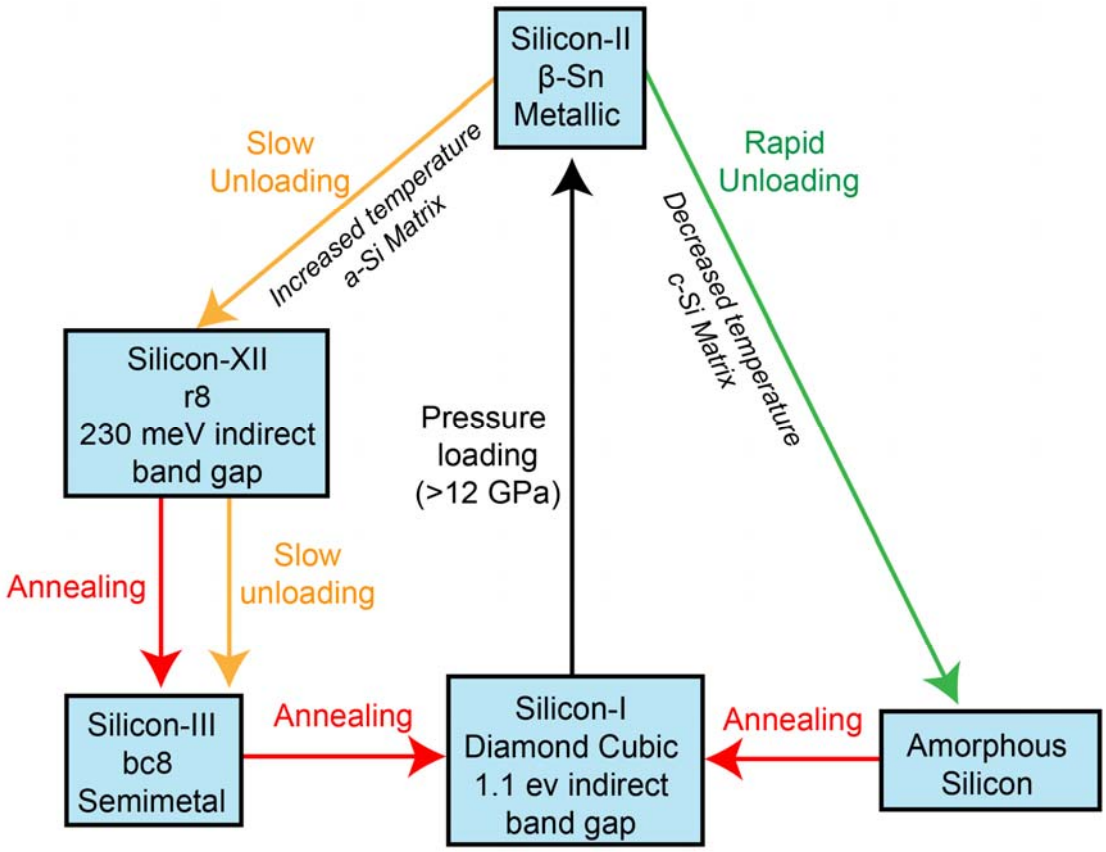

Figure 4.1. The irreversible reaction pathways that silicon undergoes during pressure loading and unloading at moderate temperatures. The formation of Si-XII, Si-III, and a-Si are very sensitive on the rate of pressure unloading, the temperature, and the phase of the surrounding silicon matrix.

Investigations into pressure-induced phases in silicon following fs-laser irradiation have been very limited [105, 106] and there has been no systematic investigation into their formation. Understanding the pressure-induced transformations is critical for the application of fs-laser irradiation to optoelectronic device fabrication because a-Si, Si-III, and Si-XII have different material properties than Si-I and could affect optoelectronic device performance. Si-XII has an indirect band gap of 230 meV [117], Si-III is a p-type semimetal [118], and unpassivated a-Si presents a high density of recombination sites. In addition, due to their sensitivity on pressure loading and unloading conditions, investigating their formation can provide valuable insights into the conditions generated during fs-laser irradiation and the pressure generation mechanisms responsible for plastic deformation. In addition, The silicon polymorphs are stable under ambient conditions but will transform back to Si-I with annealing, and therefore understanding

the annealing conditions necessary to remove the silicon polymorphs following laser irradiation may provide an approach to eliminating them during device fabrication.

In this chapter, we investigate the relationship between high-pressure phase transformations, surface texturing, and optical hyperdoping using fs-laser irradiation rastered over large areas. Using TEM we investigate the spatial distribution of the silicon polymorphs in fs-laser doped silicon and show that the polymorphs form preferentially in the center of the surface spikes. The relationship between phase transformations and surface morphology is studied by monitoring the formation of silicon polymorphs with varied laser-rastering speeds. Finally, we investigate the thermal stability of silicon polymorphs formed during fs-laser irradiation and compare the kinetics of their relaxation with annealing to the evolution of the optical properties of fs-laser doped silicon with annealing.

4.2 Experimental

In this investigation of fs-laser doping over large areas, we compare silicon irradiated in N_2 (N_2:Si), for which we do not expect dopant incorporation or compositional changes during irradiation, to silicon fs-laser doped with S (SF_6:Si) and Se (Se:Si) using a peak fluence of 4 kJ/m^2 and the doping methods described in Chapter 3. Large areas of each sample were prepared by translating the silicon wafer during pulsed-laser irradiation such that, unless otherwise noted, every point on the sample surface received an equivalent of 88 laser pulses. To investigate the relation between silicon polymorphs and irradiation, Se:Si was prepared with a range of rastering speeds, resulting in 10, 25, 42, and 88 laser pulses per area.

Raman spectroscopy was used to detect the presence of high-pressure silicon phases by monitoring the appearance of the most pronounced Si-XII (350 cm^{-1}) and Si-III (432 cm^{-1}) modes. The relative amounts of Si-XII and Si-III are approximated by comparing the area under each peak after background subtraction, referred to as the peak intensity. The residual stress in the polymorphs is probed by monitoring the position of the Si-III (432 cm^{-1}) and Si-XII (350 cm^{-1}) modes. For quantification of the Raman investigations into silicon polymorph formation, spectra were collected from 20 different locations.

The sample morphology was investigated using a FEI Helios 600 scanning electron microscope (SEM) operated at 5 kV accelerating voltage. Cross-sectional transmission electron microscopy (TEM) samples of the rastered surfaces were prepared using a tripod polisher

followed by a brief Ar^+-ion mill at 5 kV. Bright-field (BF) TEM micrographs and selected area diffraction patterns (SAD) were collected with a JEOL 2011 TEM operated at 200 kV. SAD patterns for the crystalline silicon crystal structures were calculated using JEMS software package. Dark-field scanning TEM (DF-STEM), convergent beam electron diffraction (CBED), and electron energy loss spectroscopy (EELS) were carried out on a JEOL 2010F TEM operated at 200 kV, with a Gatan Image Filtering (GIF) system with an energy resolution of 1.2 eV. To remove noise without affecting the overall shape, reported EELS spectra were processed using an 8-point Savitzky-Golay smoothing filter.

To investigate the thermal stability of the silicon polymorphs, samples were annealed in a N_2 atmosphere for 30 minutes over a range of temperatures (325°C, 450°C, 575°C, and 700°C). In a manner similar to previous investigations, Raman spectroscopy was to detect the presence of high-pressure silicon phases by monitoring the decay of the most pronounced Si-XII (350 cm^{-1}) and Si-III (432 cm^{-1}) modes with annealing.

4.3 Results

4.3.1 Silicon Polymorphs and Doping

First, the relationship between silicon polymorph formation and the introduction of dopants during fs-laser irradiation was investigated using Raman spectroscopy; peak positions and relative peak intensities in the Raman spectra were used to understand the extent of the phase transformations and their resulting stress states. All three samples investigated, N_2:Si (reference), SF_6:Si, and Se:Si, develop micron-scale spikes on the surface after 88 fs-laser pulses (Figure 4.2(a)), and exhibit peaks in the Raman spectra indicative of Si-XII (354 cm^{-1}, 395 cm^{-1}), Si-III (387 cm^{-1}, 443 cm^{-1}), and a-Si (broad peaks at 150 cm^{-1}, 300 cm^{-1}, and 470 cm^{-1}) (Figure 4.2(b)) [95]. The intensities of the silicon polymorph Raman modes are at least an order of magnitude lower than the Si-I peak at 520 cm^{-1}, suggesting a relatively small volume of silicon polymorphs are generated compared to the volume of Si-I being probed.

We estimated the residual strain in the high-pressure crystalline polymorphs by measuring the position of the Si-III peak around 443 cm^{-1} and the Si-XII peak around 354 cm^{-1} (these peaks were selected as they are the most clearly pronounced (*continued on page 65)*

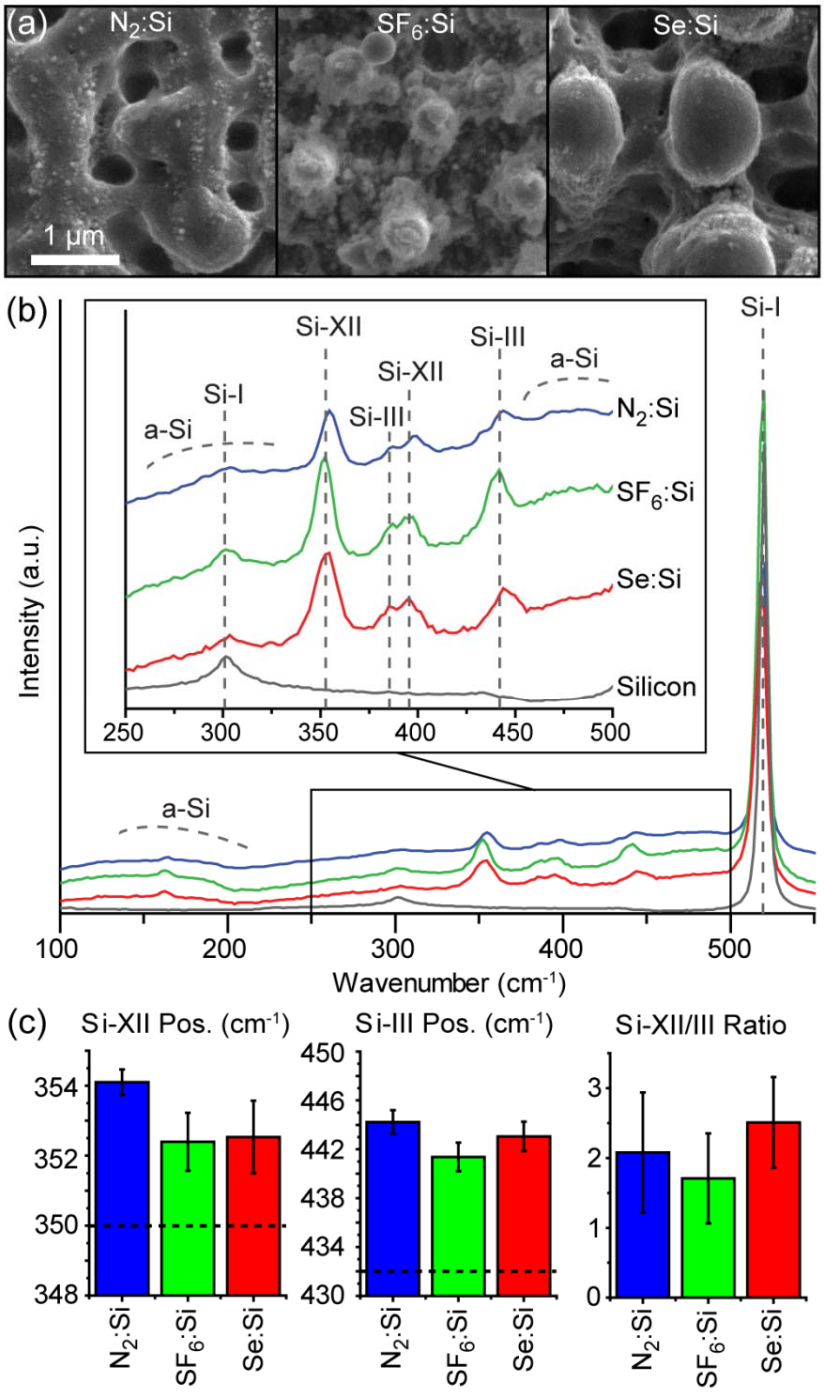

Figure 4.2. (a) SEM micrographs showing the surface morphology of fs-laser irradiated Si. The laser scan direction and polarization was in the horizontal direction. (b) Stokes Raman spectra of SF_6:Si, Se:Si, and N_2:Si, offset to show individual spectra. The rescaled inset highlights the Raman modes corresponding to a-Si, Si-III, and Si-XII. The color designation is the same in both plots. (c) The position of the Si-XII and Si-III modes and their relative intensities, plotted with standard deviation. Dashed lines indicate the positions of the Si-XII (350 cm^{-1}) and Si-III (432 cm^{-1}) Raman modes reported in nanoindentation studies [96].

Raman modes of their respective phases). Though small variations (1-2 cm^{-1}) exist between the 20 spectra recorded at difference positions on each sample, the Si-XII and Si-III peaks are consistently shifted to significantly higher wavenumbers (4-10 cm^{-1}) than values often reported in nanoindentation studies [96], indicating that they exist under compressive stress. The appearance of 2 characteristic peaks for both Si-XII (354 cm^{-1}, 395 cm^{-1}) and Si-III (387 cm^{-1}, 443 cm^{-1}) confirms that these peaks originate from the crystalline polymorphs despite their sizeable shift. Finally, the relative volume ratio of the crystalline phases generated, Si-XII and Si-III, was estimated from the Raman peak intensities at 443 and 354 cm^{-1} (Figure 4.2(c)). N_2:Si, SF_6:Si, and Se:Si have a Si-XII/Si-III ratio around 2, suggesting that the majority of the total crystalline polymorph volume is Si-XII [96].

4.3.2 Spatial Distribution of Silicon Polymorphs

Next, we investigated the spatial distribution of silicon polymorphs using TEM, allowing us to better understand the pressure distribution induced during fs-laser irradiation. The general structure of the N_2:Si and SF_6:Si surface spikes (Figure 4.3 (a) and (b), respectively) is consistent with previous investigations [29]; across the surface a disordered layer forms through melting and resolidification. Irradiation in SF_6 leads to a disordered surface layer with 1% atomic concentrations of sulfur, incorporated from the gas phase. Although SAD patterns show that the spikes are mostly single-crystalline silicon (Figure 4.3(a-b), inset), both samples exhibit strong contrast in the center of the spike.

We identify the contrast as strain contrast in the c-Si matrix surrounding isolated regions of a-Si (20-200 nm). A single region from the center of an SF_6:Si spike is shown in Figure 4.3(c), and CBED patterns (Figure 4.3(d)) confirm that the volume of material is amorphous and the surrounding matrix is crystalline. EELS spectra reveal no chemical difference between the volume of amorphous material and the c-Si matrix. However, the fine structure of the Si-L_{23} edge (99 eV, Figure 4.3(e)) measured in the amorphous region exhibits a shoulder at 102 eV, in contrast to the dip exhibited in the spectra from the c-Si matrix. This fine structure is characteristic of a-Si, resulting from the reduction of density of states around the conduction-band minimum in a-Si [101, 119]. We note that a-Si can form through melting and ultra-fast resolidification following fs-laser irradiation under certain conditions [105, 120], but in our case the a-Si particles are found in regions below the melt depth.

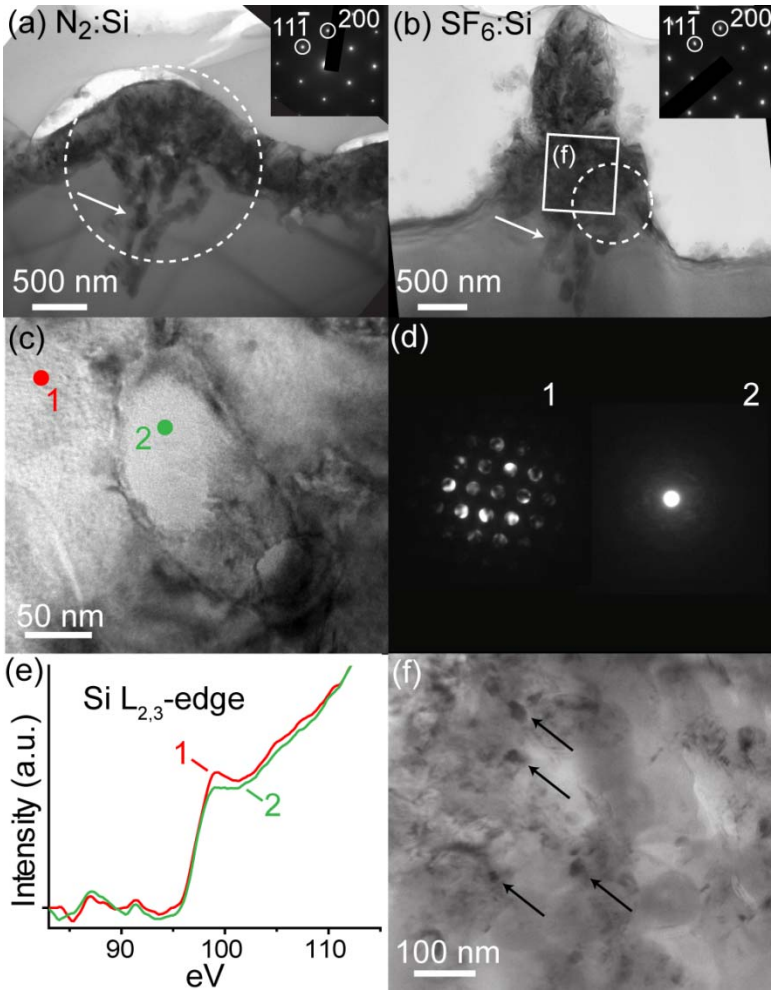

Figure 4.3. Cross-sectional BF-TEM images of N_2:Si (a) and SF_6:Si (b). SAD patterns from the regions highlighted by the dashed circles (inset) correspond to the Si-I [101] zone axis. White arrows indicate contrast in the core of the peaks arising from areas of transformed material (20-200 nm in diameter), shown to be a-Si. BF-TEM (c) of an isolated region of a-Si from the core of an SF_6:Si spike. Numbered spots 1 and 2 correspond to c-Si and a-Si points probed using CBED (d) and EELS (e). BF-TEM (f) of region in (b) that shows nanocrystals (black arrows) inside the a-Si.

Within the a-Si regions we observe nanocrystals 1-10 nm in size (Figure 4.3(f)). The small size of the nanocrystals makes them undetectable by SAD and their structure difficult to confirm, but we might expect Si-XII and Si-III to be present within the a-Si regions because both a-Si and the crystalline polymorphs are products of Si-II. In addition, the formation of a-Si can promote the nucleation of crystalline polymorphs during subsequent laser pulses, as the activation barrier of nucleating Si-XII from Si-II is greatly reduced at a Si-II/a-Si interface [116]. For these reasons, it is possible that the nanocrystals in the a-Si regions are nucleated Si-XII and/or Si-III.

In contrast to the single-crystalline structure of N_2:Si and SF_6:Si surface spikes, the Se:Si spikes are composed of Se-rich polycrystalline silicon (pc-Si) (Figure 4.4(a)). This arises from the use of a thin-film dopant precursor and will be discussed thoroughly in Chapter 6 and Chapter 7. We were not able to identify a-Si in the spike due to the strong diffraction contrast of this polycrystalline region, but a-Si regions can be observed in the single-crystalline base of the spike. In addition, a single crystal of Si-III on the [101] zone axis was identified within the polycrystalline region using SAD (Figure 4.4(b)); this diffraction pattern is most easily identifiable by $(10\bar{1})$ spots corresponding to a spacing of 4.70 Å [121].

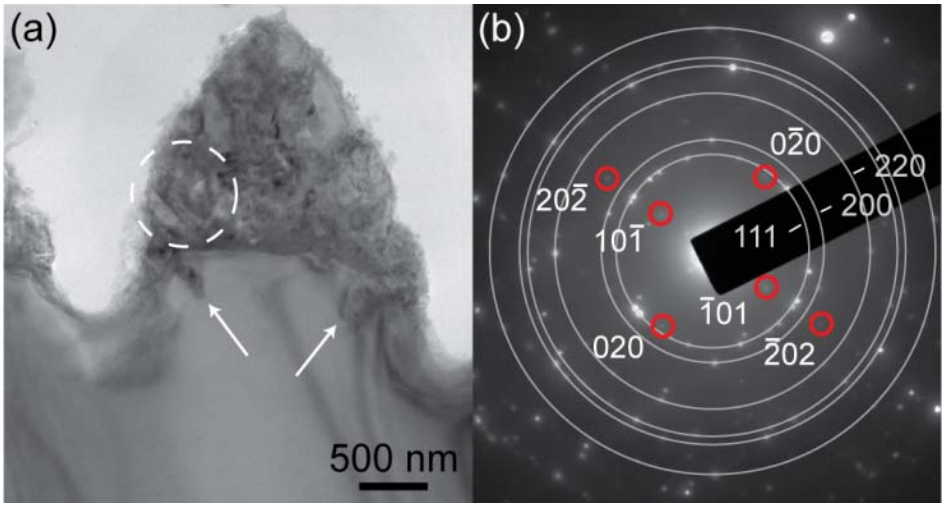

Figure 4.4. (a) BF-TEM image of Se:Si peak, showing a polycrystalline region and small volumes of a-Si (white arrows). (b) SAD pattern from region corresponding to dashed circle in (a). Spots corresponding to Si-III [101] zone axis can be identified within the Si-I polycrystalline pattern (grey rings), and lower order spots are identified by red circles.

4.3.3 Silicon polymorph formation and evolution over many laser pulses

To better understand the high-pressure phase transformations, we monitored the formation of silicon polymorphs in Se:Si with an increasing number of fs-laser pulses by varying the scan rate of the laser across the surface. SEM images of the evolution in surface morphology with an increasing number of laser pulses (Figure 4.5(a)) show the evolution of spikes from ripples over multiple laser pulses. The corresponding Raman spectra (Figure 4.5(b)) reveal that the broad a-Si peak is visible after 10 pulses, though the appearance *(continued on page 69)*

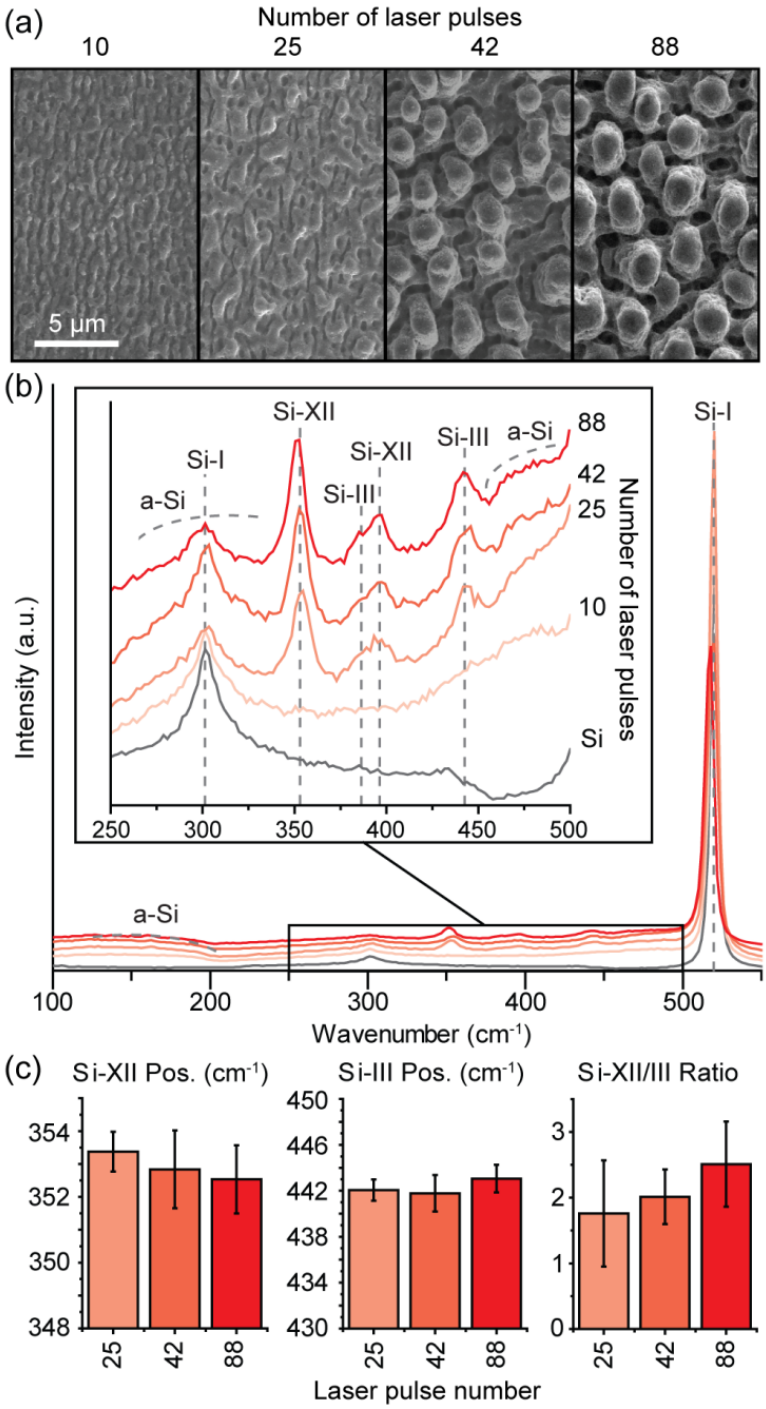

Figure 4.5. (a) SEM micrographs of the Se:Si surface morphology with an increasing number of laser shots/area. The laser scan direction and polarization was in the horizontal direction. (b) Stokes Raman spectra of Se:Si irradiated with an increasing number of laser pulses, offset to show the individual spectra. The inset is rescaled to highlight the Raman modes corresponding to a-Si, Si-III, and Si-XII. The color designation is the same in both plots. (c) Bar graphs showing the position of the Si-XII and Si-III modes and their relative intensities after 25, 42, and 88 laser pulses, plotted with standard deviation.

of amorphous silicon is not necessarily pressure-induced because it can also form on the surface through melting and rapid resolidification. The Si-XII and Si-III Raman modes appear after 25 laser pulses, in parallel with the onset of micron-scale peak formation observed in SEM images. No statistically significant trends in the wavenumber of the Si-XII and Si-III modes with an increasing amount of laser irradiation were observed (Figure 4.5(c)), but the Si-XII/Si-III ratio increases between 25 and 88 laser pulses, indicating that Si-XII is preferentially generated over Si-III in this stage of laser irradiation.

In order to confirm the onset of pressure-induced phase transformations between 10 and 25 shots/area, TEM investigations were used to monitor the formation of sub-surface amorphous silicon (Figure 4.6). After 10 shots/area (Figure 4.6(a)) the amorphous silicon detected in the Raman spectra is observed only on the surface, indicating that it is the result of melting and resolidification. Following 25 shots/area (Figure 4.6(b)), in addition to the melting-induced amorphous layer on the surface, pressure-induced amorphous regions are observed beneath the surface. This observation confirms the onset of pressure-induced phase transformations between 10 and 25 shots/area, which appears related to the surface texturing process.

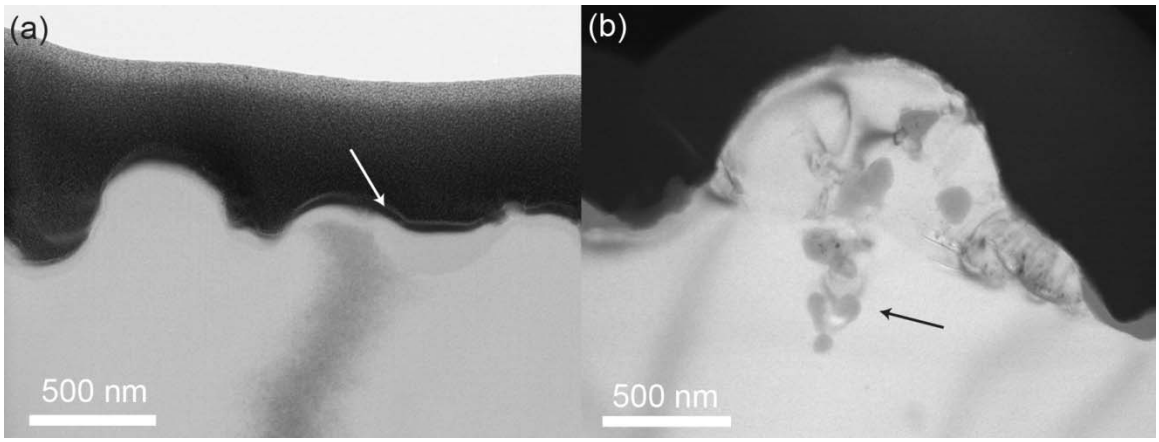

Figure 4.6. Cross-sectional BF-TEM images of the surface after irradiation with (a) 10 shots/area and (b) 25 shots per area. After 10 shots/area there is an amorphous layer (white arrow) that formed through melting and resolidification on the surface. After 25 shots/area, pockets of amorphous material form beneath the melt depth (black arrow), confirming the onset of pressure-induced phase transformations.

4.3.4 Thermal Stability of Silicon Polymorphs

Silicon that is fs-laser doped with chalcogens exhibits strong sub-band gap absorptance that decreases drastically with annealing [122]. Because pressure-induced silicon polymorphs are also metastable and transform back to Si-I with annealing, we compare the relative rates of relaxation of silicon polymorphs and optically active chalcogen species to gain insight into the relative kinetics between these two processes. Selenium fs-laser doped silicon was annealed for 30 minutes in nitrogen at 325°C, 450°C, 575°C, and 700°C, and the average absorptance was measured for each and compared to N_2:Si and untreated Si (Figure 4.7(a)). We observe a characteristic decrease in the sub-band gap absorptance of Se:Si with annealing, from 90% prior to annealing to 44% after the 700°C anneal. The monotonically decreasing absorptance in N_2:Si is due to defect states induced by irradiation [123].

The evolution of the silicon polymorphs with annealing was monitored using Raman spectroscopy (Figure 4.7(b)). The Si-XII and Si-III modes are still visible after annealing at 325°C, but cannot be resolved after the 450°C anneal. The 325°C anneal did not significantly change the position of the Si-XII mode or the Si-XII/Si-III intensity ratio, as expected from previous work [115]. The Si-III mode, however, is shifted to lower wavenumbers (Figure 4.7(c)), which suggests a relaxation of the initial compressive stress with annealing. Finally, the broad a-Si peak at 470 cm^{-1} is still visible after the 575°C anneal, but disappears after the 700°C anneal.

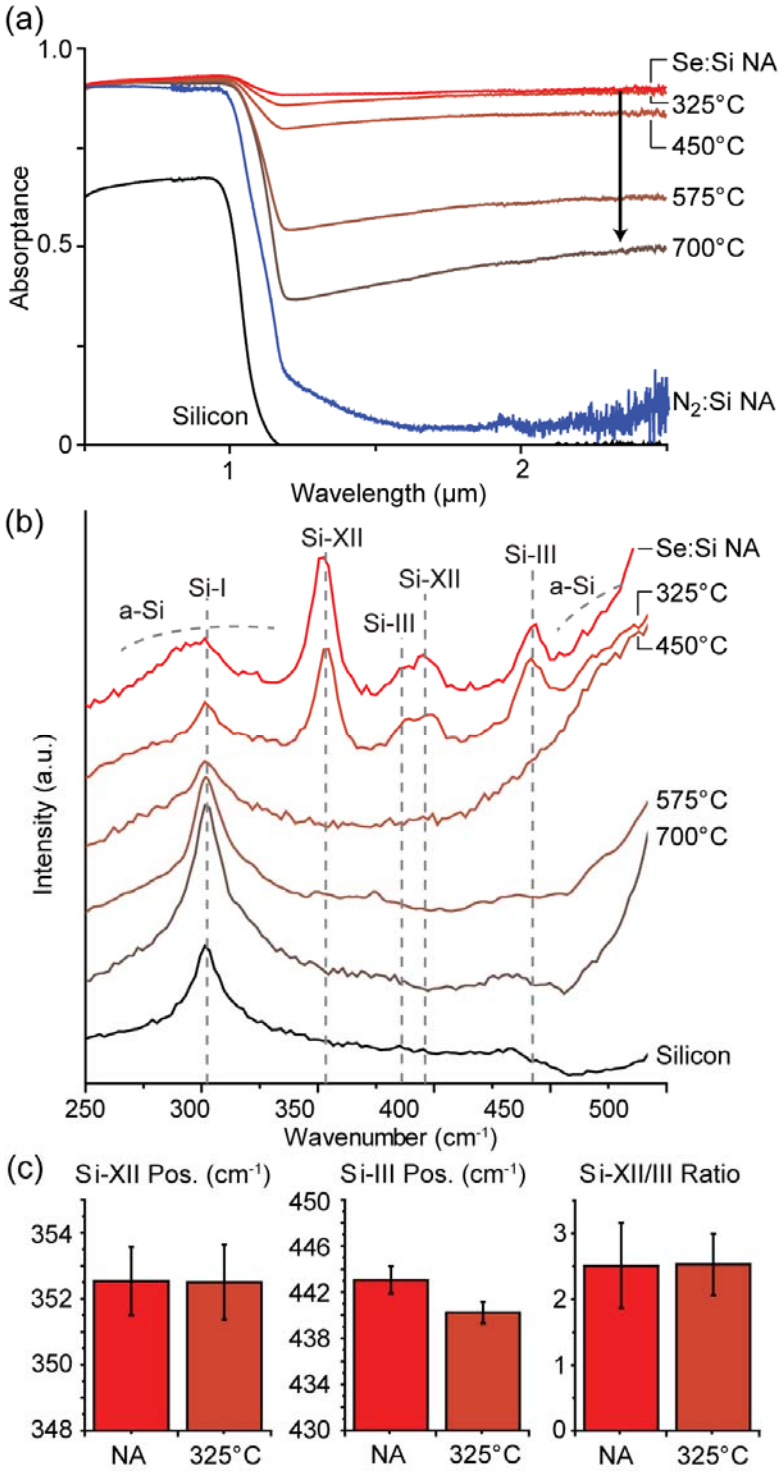

Figure 4.7. (a) Absorptance spectra of Se:Si after a 30 min anneal at the indicated temperatures. Included for reference are spectra from a not annealed (NA) sample, the absorptance spectra of a sample irradiated in N_2 without a dopant present and a silicon wafer. (b) Stokes Raman spectra of the same samples (250 – 500 cm^{-1}). Spectra are offset to highlight the a-Si, Si-III, and Si-XII peaks and their evolution with annealing. (c) Bar graphs showing the position of the Si-XII and Si-III modes and their relative intensities with annealing, plotted with standard deviation.

4.4 Discussion

4.4.1 Pressure-induced Phase Transformations

The variation of the Raman spectra (Figure 4.2(b)) of silicon fs-laser doped using different dopant precursors is not statistically significant, suggesting that the formation of silicon polymorphs is not directly coupled to the doping process, dopant type, or precursor phase. The Raman and TEM results reported in this thesis, including the extent of the phase transformations, Raman peak intensities, and peak positions can be largely attributed to the ultra-fast pressure loading and unloading that fs-laser irradiation induces. TEM investigations show that the transformation to a-Si is limited to 20-200 nm particles that form in close proximity to each other and in the center of the surface spikes. This volume reflects the material transformed to Si-II upon pressure loading, as Si-II cannot transform directly back to Si-I upon pressure release. We propose that the transformation to Si-II is kinetically limited by the short time-scale of pressure loading, and that the volume of a-Si reflects the extent of nucleation and growth of Si-II that occurred before pressure release. During nanoindentation investigations, slow, incremental loading conditions result in silicon polymorph formation over the entire volume subject to sufficient pressures for the Si-I →Si-II transformation [124]. In this scenario, the transformation does not suffer from kinetic limitations, and micron-scale volumes of a-Si and Si-XII/III are kinetically allowed to form. In contrast, the small and kinetically-limited volumes of Si-II generated in fs-laser irradiated Si are an important aspect of the phase transformation process, as the total volume of material transformed to Si-II will influence the subsequent phase transformation pathways. For example, the nucleation of Si-XII from Si-II is less probable in small volumes of Si-II due to the reduced number of available nucleation sites [125].

The relative Raman intensities show that only a limited amount of crystalline high-pressure phases form in our samples. Nanocrystals (1-10 nm) that are possibly Si-XII and Si-III were observed in BF-TEM images within the a-Si volumes and 1- 10 nm in size (Figure 4.3(f)). The crystalline polymorph Raman peak shifts, quantified in Figure 4.2(b), can be qualitatively translated into residual stresses based on empirical studies of the Si-XII and Si-III peak positions with pressure; a shift of the Si-XII peak from 350 cm^{-1} to 354 cm^{-1} and of the Si-III Peak from 432 cm^{-1} to 443 cm^{-1} indicates that both crystalline silicon polymorphs exist under several GPa more compressive stress than when generated using nanoindentation [97]. This is surprising because a-Si, Si-XII, and Si-III formed from Si-II under several GP of pressure, and additional

pressure release would be expected to leave them under tensile stress. The observed residual stress can inform the identification of the pressure-generation mechanisms driving phase transformations in silicon (Chapter 5) and could have implications on the stability of the polymorphs (section 4.3.4).

4.4.2 Polymorph spatial distribution and evolution with shot number: a surface-morphology driven effect

The BF-TEM investigations reveal that high-pressure silicon phases form preferably in the core of the spikes, suggesting that the pressure-induced phase transformations are related to the evolution of the surface morphology over multiple laser pulses. Transformed regions of material have been observed previously in the cores of peaks formed by fs-laser irradiation of silicon [29, 126], but neither their composition nor their mechanism of formation was identified. In addition, we see that the initial laser pulses do not generate sufficient pressures at this fluence (4 kJ/m^2) to drive phase transformation (Figure 4.5(b), Figure 4.6), but identical laser pulses during later-stage irradiation do. The spatial distribution and delayed formation of pressure-induced amorphous silicon thus suggest that the surface texturing process is closely related to the formation of pressure-induced phase transformations. As discussed in Chapter 2, the evolving surface morphology has a strong effect on the local fluence, influencing the local rates of melting and ablation even at low fluences, and resulting in a complex range of processes occurring at the surface. The presence of silicon polymorphs in the core of the spikes (Figure 4.3(a,b)) and the absence of plastic deformation in regions between the peaks show that the peak centers achieve pressures higher than is experienced in the valleys. The resulting plastic deformation occurs in the body of the peaks which could contribute to an increased leakage current and is difficult to remove by surface etching.

In addition to the trends observed with respect to surface morphology, it is worth noting that the phase transformations, which occur over many laser pulses, would be influenced by the formation of a-Si regions from Si-II during earlier laser pulses. An existing a-Si matrix greatly reduces the activation barrier to the nucleation of crystalline polymorphs [116] and would therefore favor the formation of crystalline silicon polymorphs during subsequent laser pulses; this would lead to the formation of nanocrystals of silicon polymorphs within the a-Si matrix, as observed in Figure 4.3(f).

4.4.3 *Polymorph relaxation and optical deactivation*

Comparing the Raman spectra of fs-laser doped silicon annealed at various temperatures (Figure 4.7(b)) with the sub-band gap absorptance (Figure 4.7(a)) provides insights into the relationship between the silicon polymorphs and optical properties, and the ability to decouple these through annealing. Undoped N_2:Si has a very similar Raman spectra to Se:Si (Figure 4.2(b)), but does not exhibit strong absorptance into the IR that is characteristic of the doped samples (Figure 4.7(a)). This is conclusive evidence that the formation of metastable polymorphs does not play a dominant role in increasing the IR absorptance. In addition, Se:Si exhibits 82% average IR absorptance after the 450°C anneal, the point at which the high-pressure crystalline phases are undetectable by Raman spectroscopy. After the 700°C anneal, when the a-Si has recrystallized, the average IR absorptance (44%) is still much greater than N_2:Si. Thus, the metastable phases in selenium fs-laser doped silicon can be annealed out while maintaining moderate IR. Such annealing treatments have been used in the past to improve the device performance of fs-laser doped silicon [32] and the reduction of metastable silicon polymorphs during annealing may be an important contributing factor.

Changes in the Raman peak intensities can also provide insight into the transformation pathways through which the metastable polymorphs transform back to Si-I. We observe pronounced Si-XII and Si-III peaks in Figure 4.7(b) after a 30 minute anneal at 325°C. Investigations of the annealing kinetics of nanoindentation-induced high pressure phases found that the Si-XII and Si-III Raman peaks were undetectable after less than 10 minutes of annealing at 300°C [115]. The increased stability of the fs-laser generated silicon polymorphs could due to their formation within the a-Si regions, as suggested from Figure 4.3(f), which has been shown to make Si-XII and S-III more thermally stable [115]. Additionally, the existence of strong residual stresses, as are reported, will affect the kinetics of the transformation back to Si-I. The crystallization of a-Si after annealing at 700°C agrees with previous investigations which show that formation of c-Si from a-Si requires annealing temperatures exceeding 550°C [127].

It has been reported that Si-III transforms back to Si-I through the formation of an intermediate phase having the lonsdaleite (hexagonal diamond) structure, Si-IV, which has a Raman mode at 508 cm^{-1} [118]. We are unable to detect the formation Si-IV with annealing, though its proximity to the Si-I mode will make it difficult/impossible to detected given the relatively small volumes of crystalline polymorphs we are characterizing compared to those

generated during nanoindentation studies. Additional investigations are necessary to elucidate the phase transformation pathway of silicon polymorphs generated by fs-laser irradiation, as well as to understand the microstructural effects of the annealing process.

4.5 Conclusions

This study revealed several interesting insights about the relationship between fs-laser irradiation conditions, surface morphology, and silicon polymorph formation. First, we found that the phase of the dopant precursor does not directly impact the formation of high-pressure phases of silicon. Raman showed that small volumes of Si-XII and Si-III are generated under compressive stress during the rastering of fs-laser pulses across the surface, with more Si-XII generated than Si-III. The limited formation of a-Si, Si-XII and Si-III, and the preference for Si-XII formation over Si-III, can be attributed to the fast pressure cycles that are generated by fs-laser irradiation. Structural investigations showed that the formation of silicon polymorphs over many laser pulses is correlated with the onset of micron-scale surface texturing, and that the amorphous material generated in the core of the peaks is amorphous silicon generated by pressure-induced phase transformations. These results suggest a strong relationship between surface morphology and pressure-induced phase transformations, which is a valuable insight into the mechanisms responsible for silicon polymorph formation. In Chapter 5, we will investigate further the pressure generation mechanism driving the pressure-induced phase transformations through a systematic study of the relationship between silicon polymorph formation, laser irradiation conditions, and microstructure.

By coupling Raman investigations with absorptance measurements and post-irradiation annealing, we showed that the silicon polymorphs can be removed through anneals similar to what is used in optoelectronic device processing and confirm that the silicon polymorphs are not responsible for the large increase in IR-absorptance. The polymorphs are found to be more thermally stable than when generated by nanoindentation, which could be due to the stabilizing effects of the existing stress states of the polymorphs or the formation of crystalline polymorphs in an a-Si matrix. An important next step in this investigation is to understand the effect of annealing-out the silicon polymorphs on the resulting microstructure. The decay in absorptance of selenium-hyperdoped silicon will be investigated in greater detail in Chapter 6.

Chapter 5 Pressure-induced transformations Pt. 2: Identifying pressure-generation mechanisms driving plastic deformation

In the previous chapter, we found that pressure-induced phase transformations are closely related to the surface texturing process. Surface texturing using femtosecond laser irradiation can reduce the reflectivity of the surface to less than 5%, is an isotropic process with respective to crystal orientation, enables control over the resulting periodicity and feature size, and uses little material. However, the laser-induced damage that can occur in parallel with surface texturing results in increased recombination currents. In this chapter, we identify the mechanism responsible for plastic deformation during surface texturing through a systematic investigation of the relationship between irradiation conditions, the formation of silicon polymorphs, and the resulting microstructure. This investigation brings to light the important role of resolidification induced stresses during fs-laser irradiation, the understanding of which is critical for the optimal application of fs-laser irradiation to optoelectronic devices via both surface texturing and optical hyperdoping.

5.1 Introduction

Surface texturing of silicon using fs-laser irradiation is an effective approach to increasing light absorption in silicon solar cells and has many advantages over other approaches (Table 1.1); fs-laser surface texturing is repeatable, uniform, independent of crystal orientation, dry, and uses less material than wet chemical etches [15, 24, 25]. The major drawback of using laser irradiation for surface texturing is laser induced damage, and we showed in Chapter 4 that the formation of pressure-induced silicon polymorphs is strongly coupled with the surface texturing process. Understanding the mechanisms through which surface texturing is related to plastic deformation is therefore critical for minimizing laser-induced damage during optical hyperdoping and fs-laser surface texturing.

There are three mechanisms by which fs-laser irradiation can generate substantial pressures in the substrate [91, 128]: Recoil shock waves arising from explosive ionic plasma formation, thermoelastic pressure generation following constant-volume heating during laser irradiation, and pressures resulting from resolidification-induced frustration (for more information see Chapter 2). The relationship between surface morphology and pressure-induced phase transformations reported in Chapter 4 could feasibly be a consequence of a number of phenomena: Ionic plasma formation in silicon requires fluences of at least 10 kJ/m^2 [54], but self-focusing on a textured surface can result in ionic plasma formation at fluences as low as 3 kJ/m^2 [5]. The magnitude of a thermoelastically-generated pressure wave increases linearly with

fluence [68], and thus the local fluence increases arising from self-focusing on a textured surface would also increase the local thermoelastic pressure generation. Finally, resolidification-induced stresses arise from the frustrated expansion of molten silicon upon resolidification on a textured surface.

To understand the pressure generation mechanisms driving plastic deformation, we can refer to extensive nanoindentation investigations into pressure induced phase transformations in silicon (see section 4.1). The formation of Si-XII and Si-I depends strongly on both the rate of pressure unloading [124] and the surrounding temperature [107]. The formation of Si-XII/III during nanoindention experiments can be suppressed at pressure release rates on the order of microseconds [111], many orders of magnitude slower than most processes affiliated with fs-laser irradiation. The timescale of recoil shock waves and of thermoelastic pressure cycles are on the order of picoseconds, and thus would be expected to inhibit the formation of Si-XII/III [52, 69]. The intensity of recoil shock waves arising from ionic plasma formation decays so rapidly that the pressure waves have been shown capable of quenching Si-II, kinetically inhibiting even the formation of amorphous silicon upon pressure release [75]. The resolidification of molten silicon on a roughened surface during laser irradiation generates *residual* stresses in silicon in the GPa range [70, 93]. Based on the existence of large residual stresses, we can infer that pressure relaxation is frustrated and that the transient pressures may decay sufficiently slow to allow for the nucleation of Si-XII.

In this investigation we methodically investigate the relationship between irradiation conditions, surface morphology, and phase transformations in order to identify the dominant pressure generation mechanisms responsible for plastic deformation during surface texturing. In the context of this investigation, the sensitivity of Si-XII and Si-III formation to the surrounding environment enables a refined understanding of the conditions at the surface during fs-laser irradiation.

5.2 Experimental

Understanding the fundamental laser-material interactions that lead to the nucleation of Si-XII and Si-III requires that the irradiation conditions are carefully controlled. In order to improve our understanding of fs-laser conditions generated at the surface, we compare surfaces textured via laser rastering with laser spots prepared by stationary irradiation. In this

investigation, silicon (100) wafers were irradiated with Ti:sapphire fs-laser pulses (λ = 800 nm, τ = 80 fs, 25 Hz) in 500 Torr N_2 ambient without any dopant present. The additional irradiation conditions (fluence, pulse number, rastering details) are reported below.

Raman spectroscopy is used to detect the presence of high-pressure silicon phases by monitoring the appearance of the most pronounced Si-XII (354 cm^{-1}) and Si-III (432 cm^{-1}) modes. The relative amounts of Si-XII and Si-III are approximated by comparing the area under each peak after background subtraction, referred to as the peak intensity. As resolidification-induced stresses are central to this investigation, we probe the residual stress in the polymorphs and in the silicon lattice by monitoring the position of the Si-I (520 cm^{-1}), Si-III mode (432 cm^{-1}) and Si-XII mode (354 cm^{-1}) (see section 3.2.2). In order to clarify the conditions favoring Si-XII/III formation, the spatial distribution of silicon polymorphs is mapped across stationary laser spots. Raman line scans were collected with a 5 um step size in a direction perpendicular to the direction of laser polarization and laser rastering. Data from the line scans is spatially binned into 50 μm groups in order to clearly illustrate spatial trends across the laser spot, and are plotted with standard error in order to reflect the uncertainty in the measured average.

The surface morphology was imaged using the InLens detector of a Zeiss Field Ultra55 Field Emission SEM (FESEM) operating at 5 kV. Cross-sectional TEM samples were prepared from the center of select laser spots using the lift-out method on a FEI Helios 600 dual-beam focused ion beam (FIB). Bright-field (BF) TEM micrographs and selected area diffraction patterns were collected with a JEOL 2011 TEM operated at 200 kV.

5.3 Results

5.3.1 Rastering vs. stationary laser spots

Rastering the laser beam across the surface complicates significantly the irradiation conditions at the surface (Figure 3.2). A systematic investigation of the relationship between irradiation conditions and pressure-induced phase transformations requires that we use stationary laser shots, so that the exact pulse number and fluence can be controlled. We therefore begin this investigation by understanding the relationship between polymorph formation and laser-beam rastering. Using a Gaussian laser beam with a peak fluence of 4 kJ/m^2, we characterize the pressure-induced phase transformations on 3 distinct surfaces: (1) a surface that received an 88

shot/area raster; (2) on a line formed by translating the stage in a line under the same conditions as used in (1); and (3) a spot that received 88 pulses from a stationary laser beam.

Figure 5.1(a) shows the average intensities of the SI-XII and Si-III modes on a rastered surface that received 88 s/A. Micron-scale surface roughness has developed (Figure 5.1(a) inset) that is characteristic of silicon irradiated with fs-laser irradiation under these conditions. The Si-XII/Si-III ratio across the rastered surface is 2.5 ± 0.5, comparable to the rastered samples investigated in section 4.2. For visual reference, Figure 5.1(b) shows a Raman spectrum from the rastered surface with representative Si-XII and Si-III peak intensities.

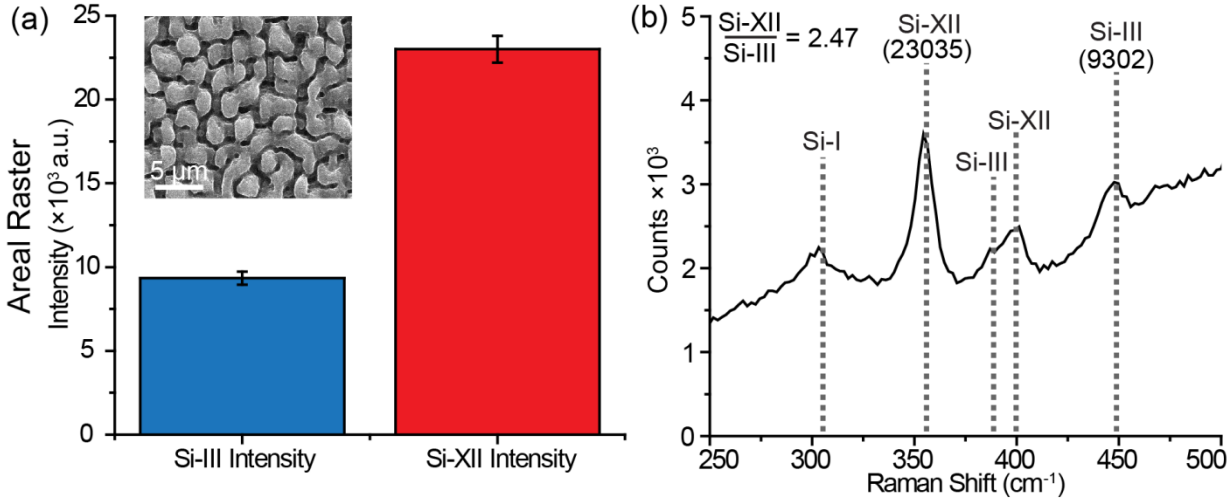

Figure 5.1 (a) The average intensity and standard error of the Si-III (blue) and Si-XII (red) Raman peaks from 20 spectra collected from surface that received 88 shots/area with a 4 kJ/m^2 Gaussian laser spot; surface morphology shown in inset and representative Raman spectrum shown in (b), with peak intensities provided.

To understand the process that leads to silicon polymorph formation, the fs-laser was translated in a straight line under conditions identical to what was used on the rastered surface above (this condition is illustrated by the blue squares in Figure 3.2).

Figure 5.2(a) shows the Si-XII and Si-III peak intensities as a function of distance across the irradiated line. The difference in surface morphology will influence the intensity of the Raman spectra; we might expect rougher surfaces to decrease the peak intensity through increased scattering. However, the peak intensities across the line scan (which is less textured than the rastered surface) is a factor of 4-5 less than what is observed on the rastered surface. The decreased intensity and reduced surface texturing (

Figure 5.2(a)) is likely related to the reduced number of laser pulses received compared to the rastered surface; the center of the line scan *(continued on page 82)*

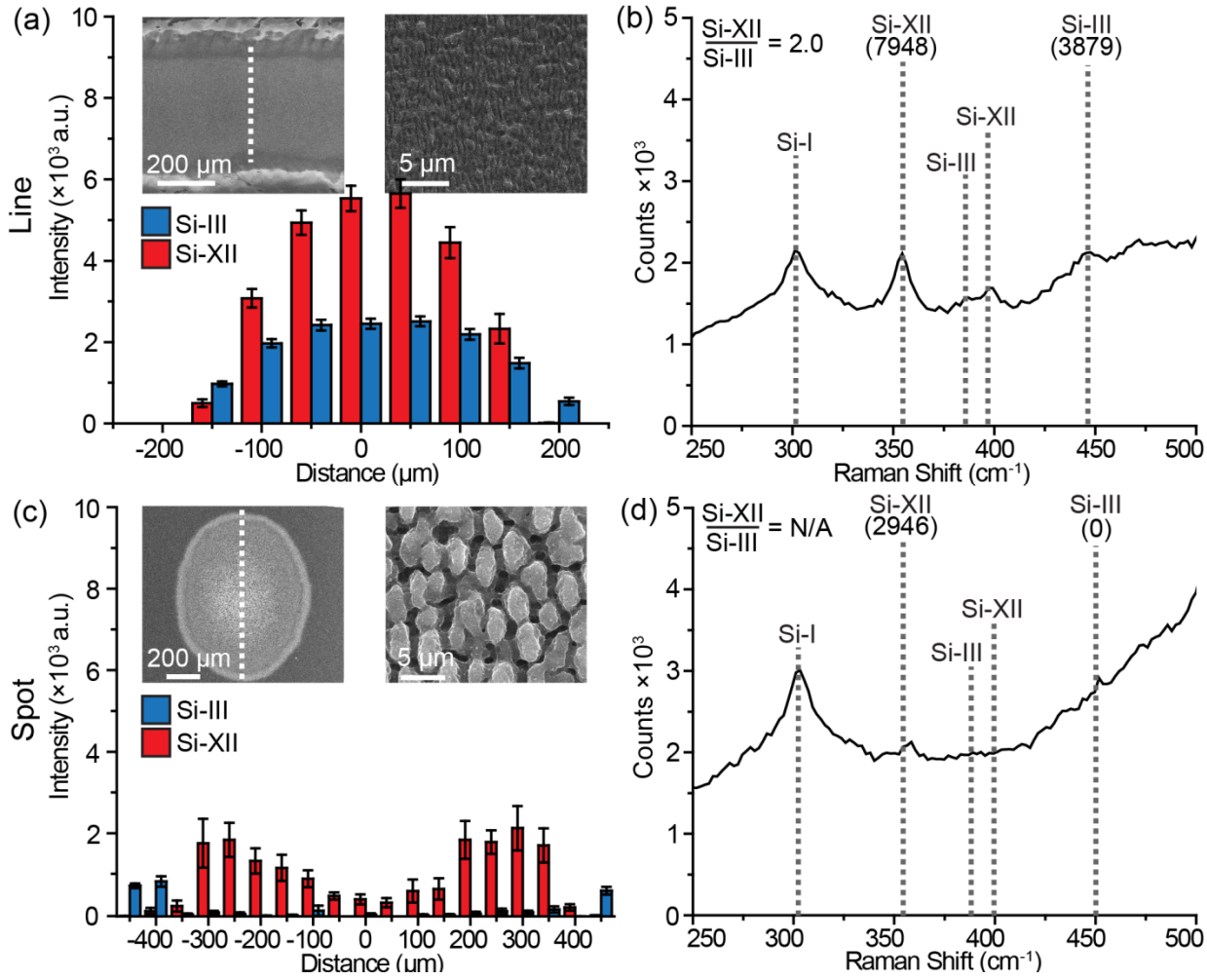

Figure 5.2. (a) The average intensity and standard error of the Si-III (blue) and Si-XII (red) Raman peaks measured across a 1-D line scan that received 11 shots/area at peak fluence of 4 kJ/m^2. Data represents average of 5 Raman line scans perpendicular to the direction of laser motion (white dashed line, left inset). The right inset shows the surface morphology in the center of the spot following irradiation, and a representative Raman spectrum from the center of the laser-affected stripe is shown in (b). (c) The average intensity and standard error of the Si-III (blue) and Si-XII (red) Raman peaks measured across a spot that received 88 pulses from a stationary Gaussian laser beam at peak fluence of 4 kJ/m^2. Data represents line scans across 5 different laser spots in the direction perpendicular to laser polarization (white dashed line, left inset). The surface morphology from the center of the peak is shown in the right inset. (d) A representative Raman spectrum from the outer rim of the stationary laser spot, which shows barely detectable amounts of Si-XII.

received just 11 pulses above 2 kJ/m^2 (compared to the 88 shots above 2 kJ/m^2 received by the rastered surface).

Finally, the crystalline silicon polymorph distribution in a stationary laser spot was investigated.

Figure 5.2(c) shows a map of the Si-XII/III intensities across a laser spot that received 88 pulses at a fluence of 4 kJ/m^2. Compared with the line scan or the rastered surface, this laser spot has received a significantly higher cumulative dosage, which is reflected in the size of the surface peaks in the inset of

Figure 5.2(c) compared with the rastered surface (Figure 5.1(a), inset). The overall intensity of the silicon polymorph modes, however, has decreased dramatically compared to both the line scan and the areal raster. In the peak fitting procedure used, a peak intensity of 1500 or lower is below the noise level; the average values in the center of the peak are well below this limit. Small volumes of Si-XII (peak intensities of ~2000 a.u., compared to >20,000 a.u. in the rastered surface) can be detected 200-300 μm away from the center of the laser beam. This significant difference in intensity could provide insights into the pressure-generation mechanisms. The slight differences in surface morphology will influence the Si-XII peak intensities of the rastered surface and the 4.0 kJ/m^2 stationary spot, but not likely by an order of magnitude. Interestingly, Si-III cannot be detected above the noise limit (1500 a.u.) in the stationary laser spot.

In order to understand the influence that laser motion has on the resulting stress states, the residual stress in both the Si-I matrix and the Si-XII polymorphs is investigated by monitoring their respective mode positions in the Raman spectra (Figure 5.3). The surface irradiated with a stationary laser spot exhibits a shift of the Si-I mode to 0.75 cm^{-1} lower than 520 cm^{-1}, which can be qualitatively interpreted as a residual tensile stress of 0.5 GPa. The rastered surface exhibits less tensile stress than the stationary spot; the Si-I peak is shifted to 519.7 correlating to ~0.2 GPa residual tensile stress. Interestingly, the fs-laser line scan shows the opposite trend and is shifted above 520 cm^{-1} by 0.2 cm^{-1}. This suggests that the surface is under a slight residual compressive stress (~0.1 GPa).

The Si-XII mode is shifted to wave numbers higher than theoretically predicted [129] and observed in nanoindentation studies (350 cm^{-1}) [96] under all irradiation conditions, indicating compressive residual stresses. The relative magnitudes indicate that Si-XII is under more

residual compressive stress in the stationary spot than the rastered surface. Shifts in Si-XII peak positions in this regime are difficult to quantify beyond that the stresses are on the order of several GPa [97], so we base our analysis on the relative shifts as related to laser irradiation conditions.

These investigations show that the amount of crystalline silicon polymorphs and residual stresses generated within the material are strongly influenced by the laser rastering conditions. The relationship between surface morphology and silicon polymorph formation is more complex than initial studies suggested: we detect no Si-XII formation in the center of the 4 kJ/m^2 stationary laser spot, which exhibits micron-scale surface texturing, and detect strong Si-XII formation in the fs-laser line scan, which exhibits much less texturing.

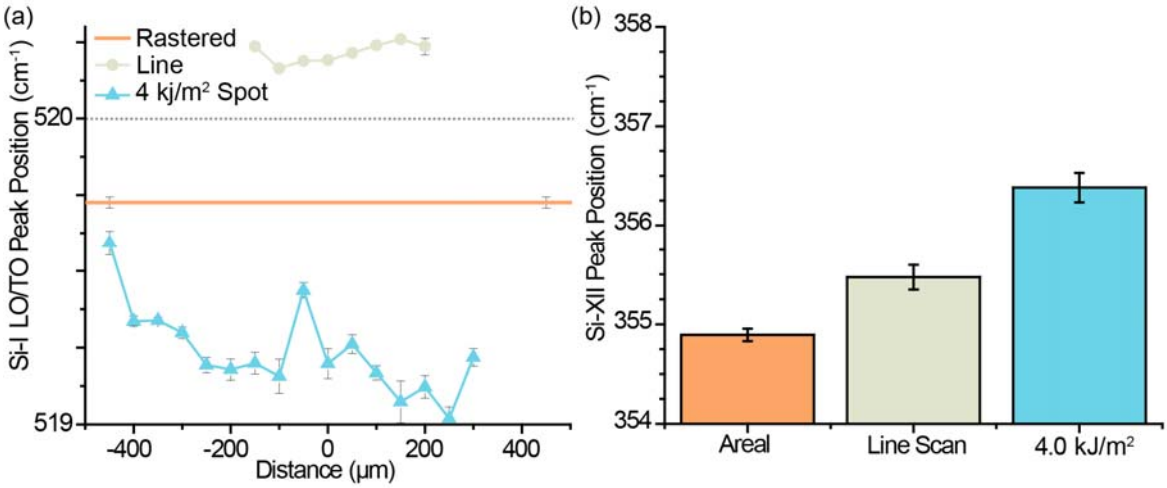

Figure 5.3. (a) The average position of the Si-I LO/TO peak in the rastered surface, across the fs-laser line scan, and mapped across the stationary laser spot, shown with standard error and indicated in the legend. The reference position of this peak is 520 cm^{-1} (dashed grey line). The Raman maps across the fs-laser line scan and the stationary spot don't extend sufficiently beyond the laser irradiated region to show the completely relaxed silicon peak position, but reference spectra were used to calibrate all Raman signals. (b) The average peak position of the Si-XII peak for all three samples plotted with standard error. Only peaks with intensities above the noise (1500) are used to determine average position.

The residual compressive stress detected in the Si-XII polymorphs supports that the crystalline polymorphs are forming due to resolidification-induced stresses. It is generally accepted that the residual stress in the lattice is a product of melting and resolidification on the surface [70, 93], and therefore the formation of crystalline polymorphs under compressive residual stress indicates that polymorph formation and resolidification-induced stresses may be related. The trends in the residual stress detected in the Si-I lattice are more complicated, and

will be elucidated through a combination of Raman and TEM investigations in the following sections.

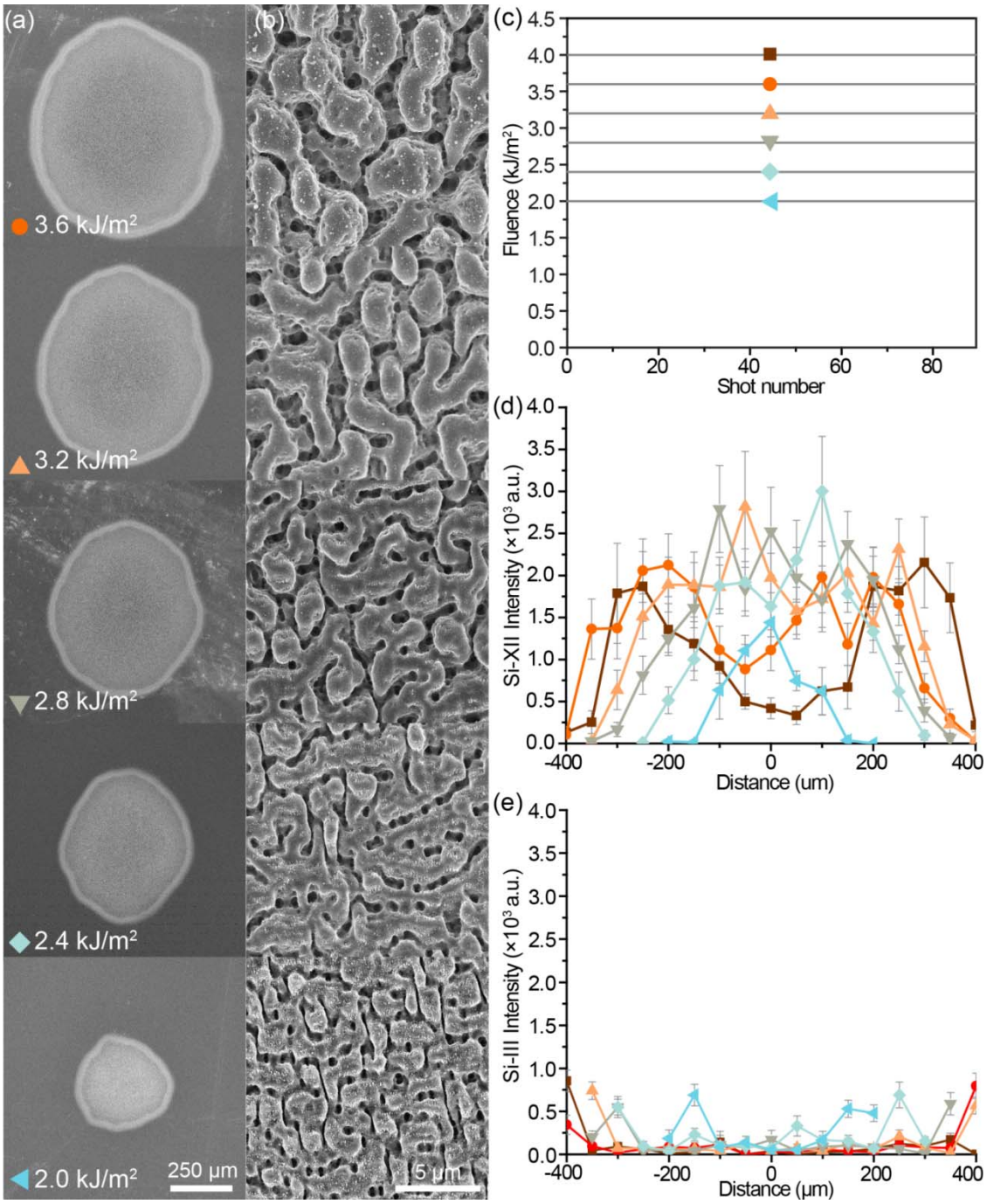

Figure 5.4. SEM images of (a) laser spots following 88 pulses at the fluence indicated (2.0 – 3.6 kJ/m^2) and (b) the surface morphology in the center of each laser spot. (c) Graphical representation of the irradiation conditions used, presented in a Fluence-Shot number plot for comparison with Figure 3.2(b). For each irradiation condition, Raman line scans were taken across 5 distinct laser spots perpendicular to the direction of laser polarization (vertically). The average peak intensities and standard error is plotted for Si-XII (d) and Si-III (e). The Si-III peak

intensities are below the noise limit (~1500) for all samples. Increases in the Si-III signal up to ~1000 a.u. are artifacts due to amorphous silicon around the edge of the spot.

5.3.2 Fluence dependence of Si-XII/III nucleation

Covering a large area with fs-laser irradiation by translating (rastering) the sample under a pulsed laser beam exposes each point on the surface to a wide range of fluences (Figure 3.2). We showed in the previous section that holding the sample stationary produces an order of magnitude less Si-XII than when the laser is rastered with an identical fluence profile, and the Si-XII forms preferentially in a ring 200-300 μm away from the center of the stationary spot. In order to gain insight into the reduced intensity of Si-XII and the spatial distribution, different stationary spots were irradiated with 88 fs-laser pulses of constant fluence, ranging from 4.0 kJ/m^2 to < 2.0 kJ/m^2 (Figure 5.4).

Figure 5.4(a) shows SEM images of the laser spots irradiated with 88 pulses with peak fluences of 3.6, 3.2, 2.8, 2.4, and 2.0 kJ/m^2 respectively. At fluences of 1.6 kJ/m^2 or lower, there was no detectable change in the surface after 88 laser pulses. Although the spot size of the laser is the same for all irradiation conditions, the diameter of the affected region decreases with decreasing peak fluence (Figure 5.4) due to the Guassian decrease in laser fluence dropping below the 88-pulse silicon modification threshold (between 1.6 – 2.0 kJ/m^2) (see section 2.2.1). Figure 5.4(b) shows SEM images of the surface morphology in the center of the laser spot. As the fluence decreases, the micron-scale surface texturing decreases in size, consistent with previous studies [5].

Figure 5.4(c) shows a fluence-pulse number plot illustrating the irradiation conditions that each sample received, and these can be graphically compared with the fluence-pulse number plot in Figure 3.2(b) describing the conditions on the surface during laser rastering. Decreasing the laser fluence from 4 kJ/m^2 to 3.6 kJ/m^2 results in a decreased area in the center of the spot showing suppressed Si-XII formation, and further decreasing the peak fluence to 3.2 kJ/m^2 eliminates the central region of suppressed Si-XII nucleation. The peak intensity of the Si-XII mode, however, remains an order of magnitude less than observed in the rastered surface.

The lack of Si-XII detection in the center of the 4.0 kJ/m^2 and 3.6 kJ/m^2 laser spots suggest that the formation of Si-XII is suppressed at sufficiently high fluences, though we cannot discount the effect of surface morphology on this trend. In the 4.0 kJ/m^2 laser spot, the Si-XII peak intensity map (Figure 5.5(a)) clearly illustrates that the Si-XII signal is suppressed in the

center of the irradiated region, and that the Si-XII signal shows up in regions that received fluences greater than ~3.2 kJ/m^2, forming a ring that extends out to a distance that received roughly 1.6 kJ/m^2. In contrast, the 2D map of the 3.2 kJ/m^2 laser spot (Figure 5.5(b)) confirms that there is no strong Si-XII suppression in the middle of the peak. The region of detectable Si-XII in this case extends out to a fluence of roughly 1.85 kJ/m^2; a threshold similar to what we observed for the 4.0 kJ/m^2 laser spot.

This study revealed a couple of important insights: First, the intensity of the Si-XII peak remains an order of magnitude less than was observed on the rastered surface, regardless of fluence used. Second, the formation of Si-XII appears relatively insensitive to fluence within the range in which they are detectable (1.8 – 3.2 kJ/m^2).

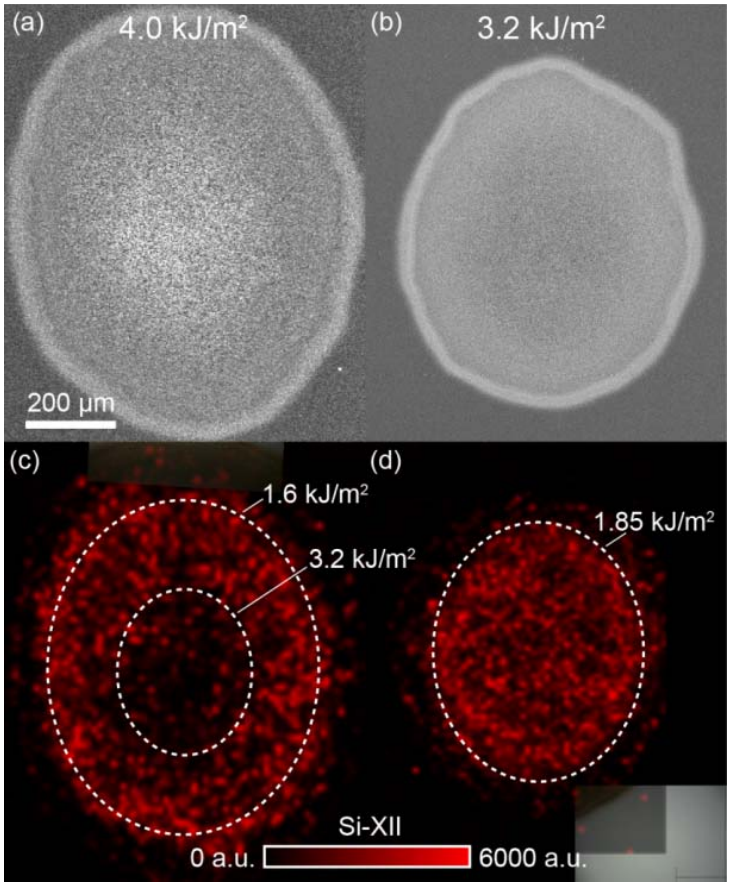

Figure 5.5. SEM images of laser spots irradiated with 88 fs-laser pulses with a peak fluence of (a) 4.0 kJ/m^2 and (b) 3.2 kJ/m^2. Raman spectra were collected across the area of each laser spot and the intensity of the Si-XII peak is plotted for the (c) 4.0 kJ/m^2 and (d) 3.2 kJ/m^2 spots. Dashed lines indicate approximate fluence thresholds for the activation and suppression of Si-XII formation.

To characterize the residual strain in the laser-textured surface, the peak shifts of the Si-I LO/TO Raman mode are plotted in Figure 5.6(a). The centers of the stationary laser spots have comparable Si-I peak shifts, indicating that varying the fluence between 2.0 kJ/m^2 – 4.0 kJ/m^2 does not strongly affect the residual lattice strain. The average position in the center of the stationary laser spots is about 0.75 cm^{-1} lower than the equilibrium condition, corresponding to ~0.5 GPa of residual tensile stress. Unlike the Si-XII mode, the residual stress in the Si-I mode is not reduced in the center of the high fluence peaks (4.0 kJ/m^2, 3.6 kJ/m^2). The position of the Si-XII peak is around 356-357 cm^{-1} for all fluences (Figure 5.6(b)), consistently 1 cm^{-1} higher (under more compressive stress) than observed in the rastered surface.

The relationships observed here between laser fluence and silicon polymorph formation are consistent with resolidification-driven pressure generation. We observe compressive residual strain in the Si-XII polymorphs, which would be expected if resolidification, which is known to cause large residual stresses, was also driving the pressure-induced phase transformations. Before discussing the fluence dependence (or lack thereof), we should note that a rigorous discussion of the effect of laser fluence is difficult because the self-focusing effects of the roughened surface create local regions of increased fluence between the peaks. Therefore, it is possible to qualitatively comment on the effect of fluence but not appropriate to discuss precise thresholds.

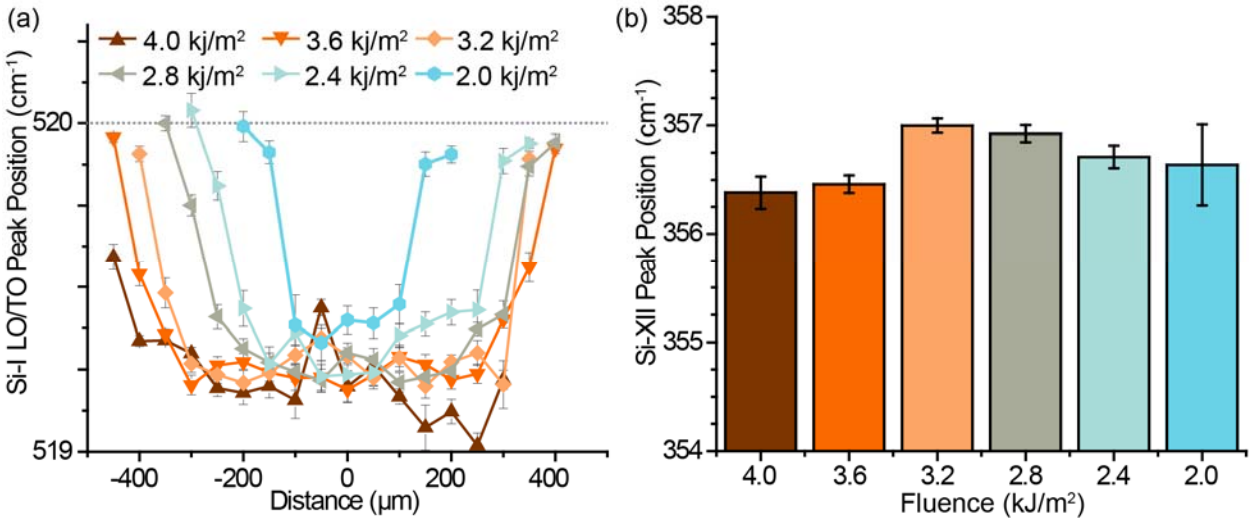

Figure 5.6. (a) The average position of the Si-I LO/TO peak, extracted from the same Raman spectra used to generate Figure 5.3(d,e), with standard error included. The reference position of this peak is 520 cm^{-1} (dashed grey line). (b) The average peak position of the Si-XII peak

(plotted with standard error) shows no strong trends with fluence. Only peaks with intensities above the noise (1500 a.u.) are used to determine average position.

Our investigations have shown that between ~1.8 kJ/m^2 and ~3.2 kJ/m^2 there is *not* strong fluence dependence reflected in the amount of Si-XII generated, the residual compressive strain of the Si-XII, or the residual tensile strain detected in the Si-I lattice. This finding does not align with the trends expected in thermoelastic pressure waves or recoil shock waves; both increase with fluence [52] and this would be expected to produce an increasing volume of silicon polymorphs. One mechanism stands out as a candidate for producing such a trend: melting and resolidification on the surface occurring in parallel with ablation. The surface texturing indicates nontrivial material ablation at fluences greater than 1.8 - 2.0 kJ/m^2. The single-shot ablation threshold is around 3 kJ/m^2, but due to incubation effects (section 2.2.1) there is roughly a factor of 2 decrease in surface modification thresholds after 88 laser pulses. During material ablation some of the deposited energy is dissipated through ablation/evaporation. The remaining energy deposited on the surface leads to melting and resolidification [130], but the amount of amorphous silicon generated during fs-laser irradiation above the ablation threshold is less sensitive to fluence than melting below the ablation threshold [131]. The insensitivity towards fluence of both Si-XII formation and the residual strains when irradiated between 1.8 kJ/m^2 and 3.2 kJ/m^2, therefore, agrees well with what might be expected from stresses induced by resolidification in a regime in which melting following ablation was the predominant event.

Inherent in the previous discussion is that these investigations also identified an upper- and lower-fluence bound the formation of Si-XII. The low-fluence threshold for the formation of Si-XII (~1.8 - 2.0 kJ/m^2) correlates well with observed surface texturing. Varying the peak fluence in 0.4 kJ/m^2 increments showed that silicon modification and Si-XII formation both ceased at 1.6 kJ/m^2. Similarly, in our radial investigation of the fluence dependence (Figure 5.5(c,d)) the Si-XII signal drops off at a distance very close to the limit of observed surface texturing (Figure 5.5(a,b)). Understanding the high-fluence limit is a little more complicated. At fluences above 3.2 kJ/m^2 the formation of Si-XII becomes suppressed, though the residual lattice strain in the substrate is still strongly tensile. In order to understand this behavior we must consider both the temperature dependence of plastic deformation in silicon and the possible effects of surface morphology on Si-XII detection, which will be discussed in section 5.4.4.

Though the fluence investigations yielded several interesting insights, they leave many open questions about the formation of Si-XII and Si-III. Most importantly, across all fluences the concentration of Si-XII in the stationary shots is an order of magnitude lower than what is observed on the rastered surface, and there is no Si-III detected in any of the stationary laser spots. Referring back to Figure 3.2, it is clear that laser rastering results not only in irradiation with different fluences (as replicated here), but irradiation with a range of fluences on the same laser spot. The fluence dependence identified in this section is not sufficient to account for the amount of Si-XII and Si-III that forms during laser rastering, and we explore the effects of fluence modulation in the following section.

5.3.3 Effect of fluence modulation

Investigations into the relationship between laser irradiation conditions and pressure-induced plastic deformation, namely the formation of Si-XII, have shown that the act of rastering the laser beam across the surface drastically enhances the formation of crystalline silicon polymorphs compared to stationary-beam irradiation with constant fluence, regardless of the fluence used. The rastering of a Gaussian fs-laser beam (Figure 3.2(b)) delivers a range of fluences onto the same area, where our investigations into the irradiation under constant fluence did not capture this effect (Figure 5.4(c)). In this section we investigate the effect of fluence modulation on the formation of Si-XII and Si-III by preparing stationary spots that received a combination of the fluences used in section 5.3.2, mimicking the irradiation dose received during laser rastering.

Fluence (kJ/m^2)	Pulse Number	Sample
4	5	FM1
3.6	8	FM2
3.2	12	FM3
2.8	12	FM4
2.4	20	
2	12	
1.6	20	FM5

Table 5.1. Irradiation conditions used to prepare the series of fluence modulated samples investigated. Each sample began with 5 pulses of 4 kJ/m^2, and then received irradiation in the order it is listed down to the row of the sample name, as illustrated in Figure 5.7(c).

Table 5.1 gives the irradiation conditions of the 5 laser spots investigated. Sample FM5 has received the full range of fluences in proportions that imitate the total dosage received by a single point on a rastered surface, thought it does not capture the oscillations in fluence. Samples FM1 – FM4 received only a portion of the fluence series, allowing us to understand the effect of each stage of irradiation on the formation of crystalline silicon polymorphs. Figure 5.7(c) illustrates these irradiation conditions on a fluence-pulse number plot, to allow visual comparison of the irradiation conditions with those of rastering (Figure 3.2).

Figure 5.7(a) shows SEM images of the evolving spot size with each stage of additional irradiation and Figure 5.7(b) shows the evolution of the surface morphology in the center of the laser spot. There is no noticeable difference in surface morphology between FM4 and FM5, indicating that the 1.6 - 2.4 kJ/m^2 dosages do not play a large role in surface structuring. The surface morphology of both FM4 and FM5 is very similar to the surface morphology of the rastered surface (Figure 5.7(a)), confirming that surface texturing is driven by high-fluence irradiation (2.8 – 4 kJ/m^2).

Figure 5.7(d) and (e) show Raman maps across each laser spot of the Si-XII and Si-III peak intensities, respectively. There is no detectable Si-XII signal in FM1, FM2, or FM3, which correspond to the first 25 laser pulses and cover the fluence range from 4.0 – 3.2 kJ/m^2. Irradiation with 12 subsequent pulses at 2.8 kJ/m^2 (FM4) causes an increase of the Si-XII signal to just above the noise limit (~1500 a.u.). Similar to the constant fluence studies, there is no Si-III signal detected in FM1 - FM4 (Figure 5.7(e)).

In the final stage of low-fluence irradiation (FM5), after 20 pulses at 2.4 kJ/m^2, 12 at 2 kJ/m^2, and 20 at 1.6 kJ/m^2, we observe an increase in the intensity of the Si-XII and Si-III signals to levels 4-times higher than achieved by irradiation with any fixed fluence (discussed in section 5.3.2). Although the fluence profile on a rastered surface (Figure 3.2(b)) is much more complicated than the fluence-modulated simulation (Figure 5.7(c)), our crude approximation demonstrates the capability of fluence modulation during laser rastering to drive the nucleation of Si-XII. The decrease of the Si-XII intensity in the center of FM5 is reminiscent of what was observed following constant fluence irradiation with 4.0 kJ/m^2, though the reason behind its appearance is unclear. The Si-III signal grows to barely above the noise levels only after the low-fluence irradiation, which is the first time in a stationary spot (FM5) we observe a detectable

Si-III (Figure 5.7(e)). FM5 exhibits a Si-XII/III ratio of 4.5±2.1, higher than observed on the rastered surface, indicating a stronger preference for Si-XII formation (discussed in 5.4.3).

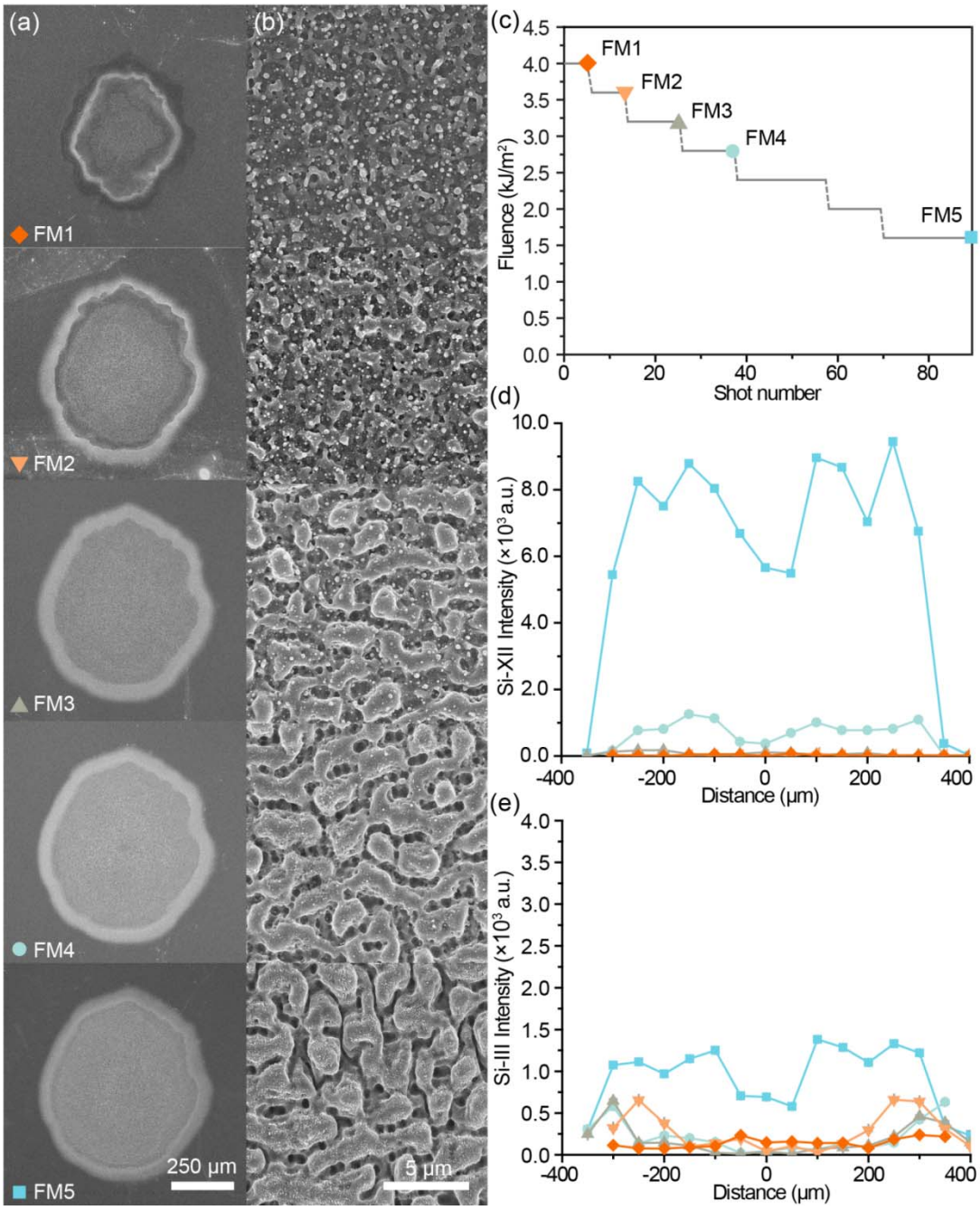

Figure 5.7. (a) SEM images of laser spots following irradiation under the conditions reported in Table 5.1. (b) SEM images showing the surface morphology in the center of each laser spot. (c) Representation of the irradiation conditions used presented in a fluence-shot number plot for comparison with Fig. 4.3.1(b). To monitor the spatial distribution of the crystalline polymorphs, 3 Raman line scans were taken across each laser spot perpendicular to the direction of laser polarization (vertically) and the average peak intensities and standard error of Si-XII is plotted in (d) and Si-III is plotted in (e). The standard error is negligibly small because the line scans reflect

averaging 3 line scans across the same spot, whereas previous line scans were averaged across multiple distinct laser spots.

Next, the effect of fluence modulation on residual strain is investigated by characterizing shifts in the Si-XII and Si-I Raman modes (Figure 5.8). Although FM4 and FM5 do not show drastic differences in surface morphology (Figure 5.7(a)), the low fluence irradiation drives a large increase in Si-XII formation. This trend is mirrored in the tensile stress experienced in the silicon lattice; FM5 exhibits a significantly larger peak shift than FM4 (Figure 5.8(a)). The largest shift of the Si-I mode in FM5 is ~0.9 cm^{-1}, corresponding to 0.58 GPa of residual tensile stress. The Si-XII mode of FM5 is shifted to 357.8 cm^{-1}, again noticeably higher than was observed in the stationary 4.0 kJ/m^2 spot or the rastered surface (Figure 5.8(b)), indicating that the crystalline polymorphs are under considerable compressive stress.

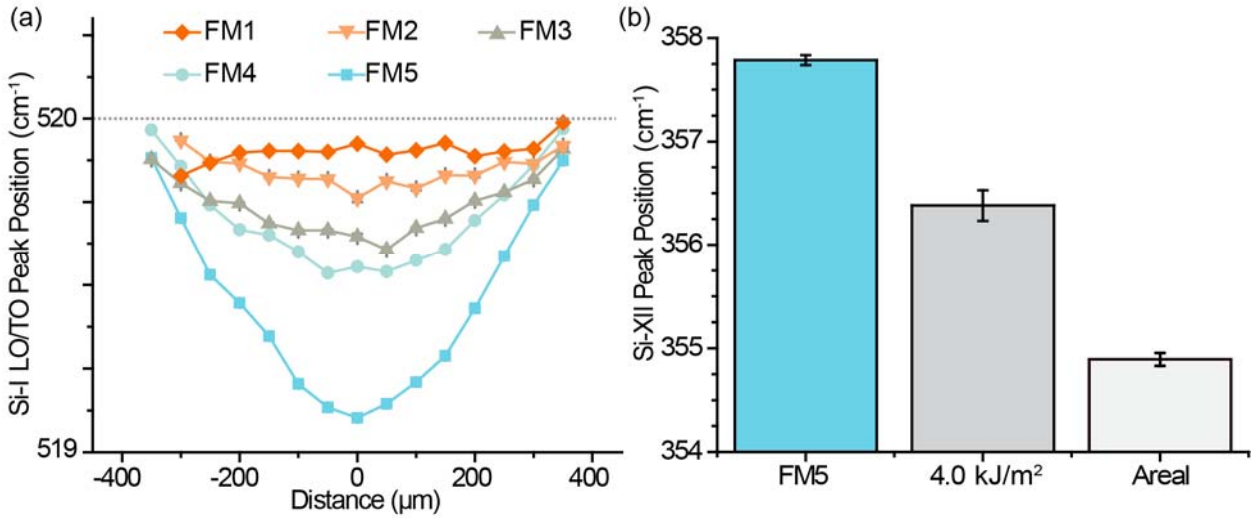

Figure 5.8. (a) The average position of the Si-I LO/TO peak, extracted from the same Raman spectra used to generate Fig. 4.3.5. (d,e), plotted with standard error. The reference position of this peak is 520 cm^{-1} (dashed grey line). (b) The average peak position of the Si-XII peak plotted with standard error for FM5, compared with the Si-XII peak position for the stationary 4.0 kJ/m^2 laser spot and the areal raster. Only peaks with intensities above the noise (1500 a.u.) are used to determine average position.

From the drastic effects following the irradiation of a textured surface (FM4) with a series of low-fluence laser pulses (FM5) it can be concluded that fluence modulation is responsible for the strong silicon polymorph generation on a rastered surface. We observe a strong increase in the Si-XII signal, a factor of 4 higher than any constant-fluence stationary spot, as well as the appearance of Si-III, in FM5. The important role of low-fluence irradiation supports the hypothesis that the formation of Si-XII is driven by melting and resolidification-

induced stresses, as sufficiently low fluences favor melting over ablation. The difference in Si-XII and Si-III peak intensities between FM5 (Figure 5.7) and the rastered surface (Figure 5.1(a)) can be attributed to the quantity of low fluence irradiation received. The 88 shots/area rastered surface contains almost 3 times more Si-XII than FM5. FM5 was irradiated with 20 pulses at 1.6 kJ/m^2 and 12 at 2.0 kJ/m^2, whereas the rastered surface received ~124 pulses between 1-2 kJ/m^2. The difference in the amount of low-fluence irradiation can also explain the trends in residual lattice strain and the Si-XII/III ratio. These effects will be discussed in section 5.4.3.

This investigation into the effects of fluence modulation on Si-XII formation illustrates the significance of low-fluence irradiation of textured surfaces on polymorph formation, supporting the hypothesis that silicon polymorph formation is driven by resolidification-induced stresses. Our Raman investigations are capable of detecting Si-XII and Si-III and measuring lattice strain, but do not provide detailed information on the relationship between fluence modulation, resolidification induced stresses, and the resulting microstructure. In order to further elucidate the effects of fluence modulation on plastic deformation, we use TEM to understand the microstructural differences between FM4, FM5, and the 88 s/A areal raster.

5.3.4 Microstructure of Rastered vs. Fluence-modulated Surfaces

The Raman-based investigations in sections 5.3.2 and 5.3.3 support our hypothesis that resolidification-induced stresses drive polymorph formation during fs-laser surface texturing, but cannot speak to the role of resolidification-induced stresses on other forms of plastic deformation (e.g. pressure-induced a-Si, dislocations, staking faults). In this section we use TEM to clarify the effect of low-fluence irradiation on the resulting microstructure and the relationship between resolidification-induced stresses and plastic deformation. We investigate the surface structure of FM4 (Figure 5.9(a)), FM5 (Figure 5.9(b)), and a rastered surface that received 88 shots/area in N_2 (Figure 5.9(c)) using TEM to complement the previous investigations into the relationship between irradiation conditions, melting and resolidification, surface morphology, and plastic deformation. Specifically, TEM allows us to understand the melting and resolidification that occurs at the surface and the spatial distribution of pressure-generated plastic deformation (amorphous silicon, dislocations, and stacking faults).

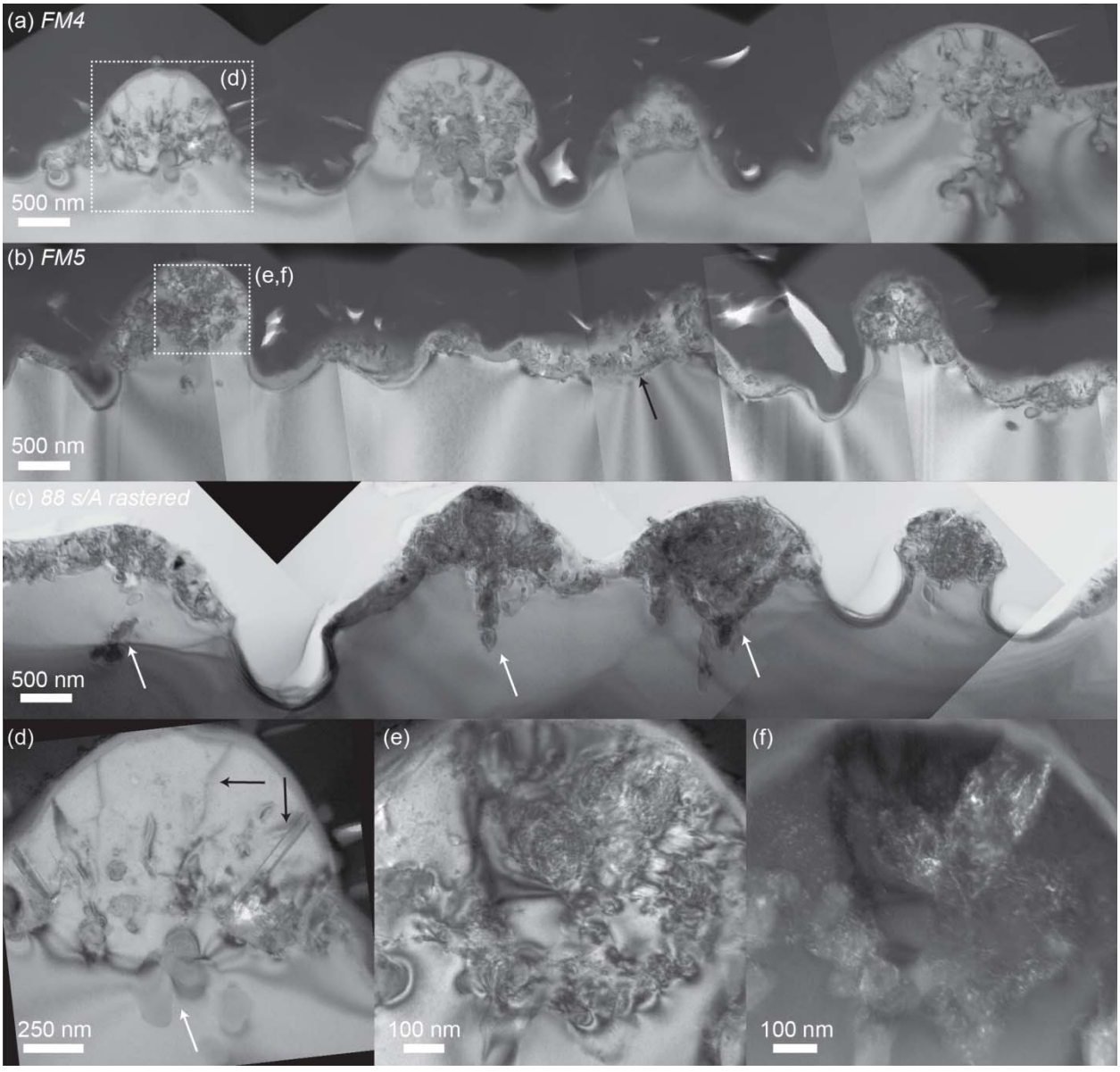

Figure 5.9. Cross-sectional BF-TEM showing the microstructure of the (a) FM4 and (b) FM5 laser spots. Black arrow in (b) indicates crystallization on the surface. These samples were prepared using FIB and have a protective layer of Pt deposited on the surface. (c) BF-TEM of the 88 shot/area rastered surface, showing distribution of amorphous silicon pockets (white arrows) with respect to surface morphology. This sample was prepared by polishing and is covered in electron-transparent glue. (d) Higher-magnification image of bump indicated in (a) (dashed line), which contains stacking faults and dislocations near the surface (black arrows) and amorphous pockets in the core of the peak (white arrow). (e,f) BF-TEM and DDF-TEM of region indicated in (b), respectively. BF-TEM shows considerable strain contrast within the surface peak and the DDF-TEM image highlights nanocrystals that have formed below the melt depth.

Measuring the depth of the resolidified surface layers, which is discernible from the TEM micrographs, provides insights into the extent of melting and resolidification on the surface and its relationship with the amount of low-fluence irradiation delivered. We find that the average thickness of the laser melt depth in FM4 is ~50 ± 20 nm and in FM5 it increases to ~70 ± 30 nm, indicating that the additional irradiation increased the amount of amorphous silicon on the surface. We report only approximate values to reflect the uncertainty in these measurements. The observation that additional low-fluence irradiation increases the extent of resolidification on the surface, which in turn increases the residual lattice strain as well as the concentration of crystalline silicon polymorphs, is further evidence supporting that resolidification-driven stresses drive the formation of crystalline silicon polymorphs.

In contrast to the stationary-spot samples, the rastered sample (Figure 5.9(c)) has a *crystalline* resolidified layer across the surface that is 300 ± 100 nm thick, though the thickness in some regions is difficult to discern due to contrast from pressure-induced a-Si. The only areas without a substantial recrystallized layer are the valleys forming due to increased local rates of ablation (the amorphous layer in the valleys was not included in the thickness measurement). The differences in microstructure between the rastered surface and FM5 can be attributed to the amount of low-fluence irradiation that the rastered surface receives compared to FM5. FM5 was irradiated with 20 pulses at 1.6 kJ/m^2 and 12 at 2.0 kJ/m^2, versus the rastered surface that receives ~124 pulses between 1-2 kJ/m^2. The evidence for resolidification-driven plastic deformation is clear: The increased amount of low-fluence irradiation leads to a deeper cumulative melt depth, which is correlated with a significant increase in the amount of Si-XII generated. This discussion will be continued in section 5.4.1.

The spatial distribution of the plastic deformation adds additional insights into the discussion of the pressure generation mechanisms responsible for plastic deformation. Consistent with investigations in section 4.2, both FM4 and FM5 show signs of plastic deformation below the melt depth and it is restricted to within the surface peaks. Amorphous pockets of material have formed in the core of the surface peak in FM4 and closer to the surface both stacking faults and dislocations were identified (Figure 5.9(d)). Regions of amorphous silicon are also present in the surface peak in FM5 (Figure 5.9(e)), though they are difficult to resolve due to the strain contrast in this region. The amorphous pockets are more visible in the DDF-TEM image of this region (Figure 5.9(f)), which also reveals nanocrystals present predominantly in the amorphous

pockets. Similar to the discussion in section 4.3.2., we cannot confirm the crystal structure of these nanocrystals but their small relative volume and distribution within the a-Si pockets suggest that they are crystalline silicon polymorphs

The TEM image of the 88 shot/area rastered surface (Figure 5.9(c)) shows several valleys that have formed through localized ablation arising from self-focusing effects. These features show no direct relation to the formation of amorphous silicon or any other form of plastic deformation, which supports that ablation does not play a key role in plastic deformation under these conditions. On the other hand, the regions in which pressure-induced amorphous silicon forms is strongly correlated with resolidification on convex portions of the surface. Much of this investigation has focused on the conditions that favor Si-XII formation and the thresholds discussed are specific to Si-XII nucleation, but the spatial distribution of amorphous silicon suggests that resolidification-induced pressures are also responsible for the formation of a-Si pockets.

5.4 Discussion

We began this investigation into pressure-generation mechanisms with the observation that Si-XII nucleation can be quenched in nanoindentation studies by pressure unloading at rates 7 orders of magnitude slower [111] than the pressure unloading rates expected in recoil shock wave or thermoelastic pressure cycles (see Chapter 2). Based on this observation, we hypothesized that resolidification-induced stresses could be responsible for the formation of Si-XII and possibly additional plastic deformation.

We investigated the relationship between irradiation conditions and Si-XII formation in order to (1) confirm the dominant pressure generation mechanisms driving plastic deformation during surface texturing and (2) improve our understanding of the conditions at the surface during fs-laser irradiation. We will begin our discussion by summarizing and expounding upon the Raman and TEM results presented in this chapter, which consistently support the hypothesis that resolidification-induced stresses drive plastic deformation (5.4.1). Next, we use our understanding of the resulting microstructure and the temperature dependence of plastic deformation in silicon to comment on the effects of local heating (5.4.2). Then, several anomalous trends in the Raman data are identified as consequences of low-fluence laser

annealing which occurs during laser rastering (5.4.3). Finally, we discuss the high-fluence threshold for Si-XII formation (5.4.4).

5.4.1 Resolidification-induced stresses and the nucleation of Si-XII

In our investigation into the relationship between pressure-induced phase transformations and irradiation conditions we found that the formation of Si-XII/III is enhanced by the rastering of a Gaussian fs-laser beam across the surface. In order to identify the mechanisms associated with rastering that favor Si-XII/III formation, we explored the fluence dependence using stationary laser spots and found that irradiation with constant fluence produces Si-XII at levels an order of magnitude lower than the levels achieved through laser rastering. The lower-fluence threshold for Si-XII formation was well aligned with the threshold for surface texturing (>1.8 kJ/m^2, 88 pulses), which speaks to the importance of surface texturing for generating resolidification-induced stresses. The amount of Si-XII formed was independent of fluence between 2.0 – 3.2 kJ/m^2, which agrees with the fluence dependence expected for melting occurring concurrently with ablation. Due to the low amounts of Si-XII detected in any stationary spots, we concluded that there must be additional effects at play during laser rastering that favor the formation of crystalline silicon polymorphs.

Next, we investigated the formation of Si-XII/III in a stationary laser spot with varied fluence, beginning at 4 kJ/m^2 and decreasing to 1.6 kJ/m^2 in proportions similar to what was is delivered by laser rastering. We found that a surface textured by high fluence irradiation (4.0 – 2.8 kJ/m^2), when subsequently irradiated with low fluence irradiation (2.4 – 1.6 kJ/m^2) resulted in a 4-fold increase in Si-XII formation over samples irradiated with the same number of pulses at a fixed fluence. This sample also showed signs of Si-III formation, which will be discussed in section 5.4.3. TEM investigations confirmed that the low fluence irradiation increases the thickness of the resolidified layer on the surface (FM4 vs. FM5, Figure 5.9(a,b)). Irradiation with fluences sufficient only to melt the surface can lead to an increasing melt depth with repeated irradiation due to the lower latent heat of melting of amorphous silicon compared to crystalline silicon [132]. Less energy is required to melt a layer of silicon that is already amorphous, and this will result in a slight increase in the amount of material that melts on the surface with repeated irradiation below the ablation threshold. Finally, TEM also revealed that the spatial distribution of amorphous silicon pockets, which are formed by pressure-induced phase

transformations, is closely coupled with resolidification on textured surfaces. The correlation between melting on roughened surfaces and the formation of amorphous silicon suggests that resolidification-driven pressures are responsible not only for Si-XII formation, but for all sub-surface plastic deformation that occurs under these irradiation conditions.

We gained further insights into the role of resolidification-induced pressures by characterizing the residual stresses in Si-XII and in the Si-I substrate after irradiation. The areal raster (Figure 5.3), constant-fluence series of stationary laser-irradiated spots (Figure 5.6) and the fluence modulated series (Figure 5.8) all exhibited a Si-XII mode (350 cm^{-1}) shifted to higher wave numbers, indicating that it is forming under residual compressive stress. In addition, the substrate peak at 520 cm^{-1} is shifted to lower wave numbers, indicating that it is under residual tensile stress. The seemingly conflicting trends in residual stresses, Si-XII existing under compressive stress and the substrate existing under tensile stress, is a consequence of the combination of tensile and compressive stresses that arise through melting and resolidification on such textured surfaces. We can gain insights into the relationship between surface morphology and resolidification-induced stresses by referring to Borowiec et al.'s finite element modeling of residual surface stresses in a 1-D trench due to cooling of a surface layer with a negative thermal expansion coefficient (Figure 2.6) [94]. Note that the negative thermal expansion coefficient is qualitatively accurate for silicon because silicon expands upon solidification. At the bottom of the trench there is a tensile stress and the volume expansion induces compressive stresses on the sides of the trench. This predicted distribution of compressive and tensile stresses, the residual stresses we observe in Si-I and Si-XII, and what we know about the spatial distribution of the pressure induced phase transformations support that resolidification-induced stresses are responsible for the observed plastic deformation. Plastic deformation resulting from compressive stresses (dislocations, a-Si pockets) are present only in the protruding surface peaks, which we would expect to be under compression based on extrapolation of Boroweic's model. The valleys, predicted by Boroweic's model to be under tensile stress, do not show any signs of plastic deformation and are composed entirely of Si-I.

Interestingly, the fs-laser line scan (Fig. 4.3.3) that has a ripple-like surface morphology exhibits a net *compressive* stress in the silicon lattice (positive shift in the Si-I peak) while also exhibiting significant Si-XII formation. Based on this discussion, it is clear that the distribution of sub-surface stresses will strongly depend on surface morphology and thus the ripple structure

would be expected to have a different distribution of stresses within the sample. Moving forward, the rigorous application of finite-element modeling towards understanding the relationship between surface morphology and the stress states in silicon could enable a detailed understanding of stress generation in laser-textured surfaces.

5.4.2 Effects of local heating on plastic deformation mechanisms

The mechanisms of plastic deformation in silicon are temperature sensitive [107] and thus we expect the pressure-induced phase transformations to be strongly influenced by the temperature during pressure cycling. The Si-I→Si-II phase transformation is the preferred mechanism of plastic deformation in silicon at temperatures below 350°C. Above this temperature silicon becomes much softer due to thermally-enhanced dislocation glide and no phase transformations occur. In addition, the nucleation of Si-XII is suppressed at temperatures above ~200°C. Femtosecond laser irradiation has a relatively small thermal footprint compared to longer pulse irradiation, but this does not mean that thermal effects are completely absent. Studies of the heat affected zone (HAZ) in metals have shown that temperature increases of several 100°C can occur over micron length-scales during fs-laser irradiation around the ablation threshold [133].

The temperature dependence of plastic deformation in silicon is clearly illustrated in the surface peak in FM4 (Figure 5.9(d)). The outer ~300 nm contain stacking faults and dislocations, indicating temperatures during pressure loading greater than 350°C. The amorphous pockets of material, indicative of the Si-I→Si-II phase transformation, are present only in the center of the peak. This transition in plastic deformation mechanisms is a direct consequence of the irradiation-induced temperature gradient present during loading. In addition, our investigation into the growth mechanisms of surface peaks in chapter 4 supports that significant temperature increases occur within the surface peaks during irradiation at 4 kJ/m^2 fluence (see Chapter 6).

5.4.3 Low-fluence laser annealing: Si-III formation and surface relaxation

In our investigation into stationary fs-laser irradiation of silicon at constant fluences, no Si-III was detected across the entire fluence range (Figure 5.4(e)). The fluence modulated spots, which received a range of fluences (Figure 5.7(e)), showed detectable levels of Si-III after low fluence irradiation and had a Si-XII/III ratio of 4.5 ± 2.1, higher than what was observed following an areal raster (2.5 ± 0.5) or the line scan (2.2 ± 1.0). Considering the effective

dosages received by the constant fluence spot (Figure 5.4(c)), the FM5 fluence modulated spot (Figure 5.7(c)), the line scan, and the areal raster (Figure 3.2(b)), we can conclude that the formation of Si-III during fs-laser irradiation is favored by very low-fluence irradiation of surfaces in which Si-XII is present. Irradiation at sufficiently low fluences results primarily in annealing, and only very modest temperatures (100-200°C) are necessary to drive the Si-XII→III transition (Figure 4.1) [114]. The higher Si-XII/III ratio in the fluence modulated sample compared to the line scan or areal rastered surface is attributed to the difference in the amount of low fluence irradiation that each sample received. The fluence modulated sample received 12 pulses at 2 kJ/m^2 and 20 pulses at 1.6 kJ/m^2, while an areal raster delivers ~384 pulses between 0.1 - 2kJ/m^2.

Low-fluence annealing also explains the anomalous trends in residual stress when comparing the rastered sample with the fixed- and modulated-fluence investigations. Throughout the stationary-spot investigations the amount of residual strain in both the Si-I and Si-XII peaks was correlated with the formation of Si-XII (Figure 5.6, Figure 5.8). The rastered sample, however, exhibits the most Si-XII of any sample characterized (Figure 5.1(a)) but smaller Si-XII and Si-I peak shifts than the stationary spot samples (Figure 5.8(b)). It seems plausible that the residual stress in both Si-XII and Si-I is relieved with increasing very-low-fluence irradiation. These studies emphasize the subtle but relevant role that the Gaussian tail of the laser beam plays in influencing the resulting microstructure of the surface.

5.4.4 Si-XII suppression at high fluences

The constant-fluence investigation (section 5.3.2) revealed that Si-XII doesn't form after 88 pulses at fluences greater than ~3.2 kJ/m^2. Si-XII formation was suppressed in the center of the 4.0 kJ/m^2 and 3.6 kJ/m^2 laser spots (Figure 5.5), but there were not similar trends in the residual strain of the Si-I lattice (Figure 5.6). There are several possible mechanisms that could explain this: First, the suppression of Si-XII formation could be a result of the temperature dependence of crystalline silicon polymorph nucleation. Si-XII won't form at temperatures above 200 °C, and it is possible that 3.2 kJ/m^2 is the approximate fluence at which the temperature stays sufficiently low to allow for the nucleation of Si-XII. Second, the absence of Si-XII at higher fluences could be due to increasing amounts of ablation affecting the processes at the surface, reducing the extent of resolidification-induced plastic deformation. Third, our

inability to detect Si-XII could be related to the increasing surface roughness. Unless it is a surface-morphology effect, the suppression of Si-XII suggests that the mechanisms of plastic deformation during fs-laser irradiation are affected by increasing fluence. In order to optimize the irradiation conditions for surface texturing it will be necessary to further investigate the mechanisms of plastic deformation as a function of increasing fluence.

5.5 Conclusions

In this chapter we sought to understand the mechanism driving pressure-induced phase transformations in silicon observed during surface texturing with fs-laser irradiation. A systematic investigation into the irradiation conditions that favor the formation of silicon polymorphs using Raman spectroscopy, SEM, and TEM, elucidating the relationships between fs-laser irradiation conditions, surface morphology, and lattice strain, showed that the resolidification of molten silicon on a textured surface plays a central role in driving pressure-induced phase transformations and plastic deformation in general. The spatial distribution of a-Si, dislocations, and stacking faults beneath the melt depth suggests that resolidification-induced pressures are the dominant cause of plastic deformation under these irradiation conditions. In addition, we showed that the rastering of the laser beam has strong effects on the resulting material due to the range and quantity of low-fluence pulses delivered. For example, the low-fluence irradiation in the tail of the Gaussian laser spot drives the Si-XII → Si-III phase transformation and reduces the residual stress present in the substrate. This work represents progress in understanding plastic deformation in silicon during fs-laser irradiation, advancing the development of fs-laser irradiation as a processing technology for both surface texturing and hyperdoping.

Chapter 6 Thin-film Fs-laser Doping pt. 1: Bulk properties, Dopant Distribution & Deactivation

The ultra-fast processes following femtosecond laser irradiation can be used to dope semiconductors to concentrations orders of magnitude beyond their solubility limit. This process, called optical hyperdoping, drastically changes the optical and electronic properties of the material and presents a platform for the synthesis of materials with unique optoelectronic properties. In the past decade of work on fs-laser hyperdoping, a great emphasis has been placed on fs-laser irradiation in the presence of sulfur hexafluoride gas. The resulting sulfur-hyperdoped silicon has many outstanding properties, but the full potential of fs-laser hyperdoping has yet to be explored. In this chapter we investigate the consequences of depositing a thin film of selenium onto the surface followed by fs-laser irradiation in nitrogen. First, structural characterization using SEM and TEM show that the use of a thin-film dopant precursor drastically changes the dopant incorporation process, resulting in polycrystalline, hyperdoped spikes on the surface. The unique dopant distribution and microstructure explains differences in the optical and electronic behavior of the bulk material compared to doping from a gas phase. Next, we take advantage of the strong chemical contrast provided by selenium (compared with sulfur) in silicon and use Z-contrast TEM to study the evolution in selenium distribution with annealing. We observe the nucleation and growth of selenium-rich precipitates and present a kinetic analysis supporting that this process is directly related to optical deactivation during the latter-stages of annealing. Controllable fs-laser doping with a thin film dopant precursor will enable the synthesis of a wide range of new materials; this chapter represents progress towards understanding the fundamental mechanisms behind this process, which will be expanded upon in Chapter 7.

6.1 Introduction

To contextualize and motivate the results presented in this chapter, we begin with an extensive chronological review of the previous work on fs-laser doping of silicon. Femtosecond (fs) laser-doping refers to the use of fs-laser irradiation to drive dopants into a material. Interestingly, the first investigations of fs-laser doping did not begin with doping in mind. In 1998 the Mazur Group at Harvard University published the first report of the fs-laser irradiation of silicon in the presence of sulfur hexafluoride (SF_6) gas [134] and showed that the conical spikes formed in the presence of SF_6 were significantly sharper than those formed during the irradiation of silicon in vacuum, N_2, or He (Figure 6.1).

Soon afterwards, it was reported that fs-laser irradiation of silicon in the presence of SF_6 gas increased the sub-band gap near-infrared absorptance (1.1 – 2.5 μm) from a few percent in unirradiated silicon to roughly 90% [135]. The possible applications of this material in infrared detectors was demonstrated early on, when the surface texturing of an avalanche photodiode in

SF_6 gas resulted in significantly enhanced photocarrier production during excitation with a 1.31 μm illumination, which is below the band gap of silicon [135]. Further investigations revealed that the increase in sub-band gap absorptance was related to the presence of sulfur in the atmosphere (Figure 6.2) and that fs-laser irradiation drove large amounts of impurities from the ambient gas into the textured silicon surface [28, 136].

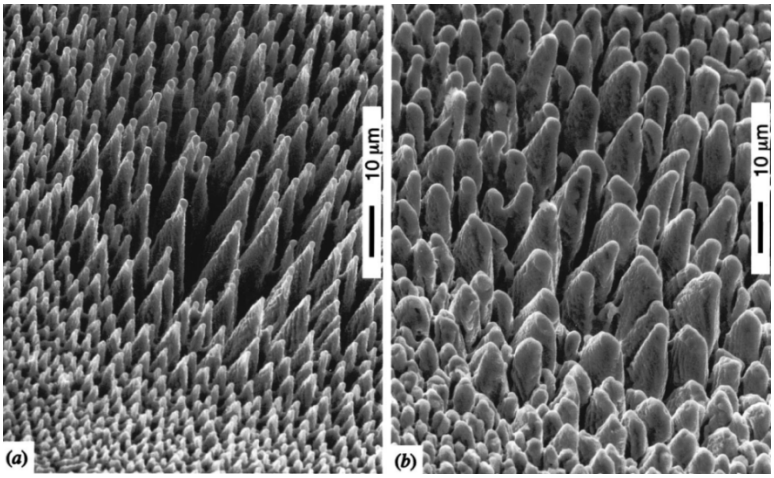

Figure 6.1. Comparison of Si(100) surfaces irradiated with 500 pulses at a peak fluence of 10 kJ/m^2 in the presence of (a) SF_6 and (b) vacuum viewed at an angle of 45° from the surface normal. The laser spot size was 200 μm. Figure from [134].

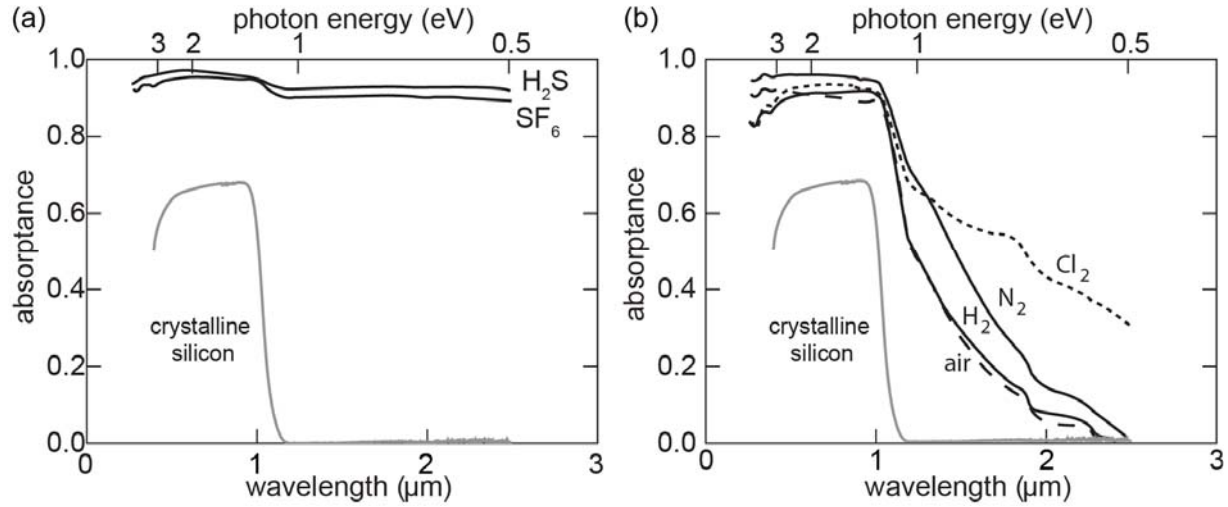

Figure 6.2. (a) Near-unity sub-band gap absorptance exhibited by silicon irradiated in the presence of sulfur containing gases with a fs-laser beam irradiated with a peak fluence of 10 kJ/m^2 and 600 shots/area, compared to unirradiated crystalline silicon. Adapted from [136]. (b) Wavelength dependence of the optical absorptance of silicon irradiated in the presence of non-sulfur-containing gasses, irradiated with a peak fluence of 11 kJ/m^2 with varied translational speeds. Adapted from [28, 50]. Data in both (a) and (b) have been recalibrated by M.-J. Sher to account for errors in originally published data.

Rutherford backscattering spectroscopy (RBS) revealed that silicon textured by fs-laser irradiation in SF_6 forms a layer of silicon on the surface that contains sulfur concentrations on the order of 0.1-1% [29], 3-4 orders of magnitude higher than the chalcogen solubility limit (~10^{16} cm^{-3}) [33-35]. It was discovered through TEM investigations that the ultra-high concentrations of sulfur were present in a nanocrystalline surface layer that was a 100-300 nm thick and composed of grains estimated to be 50 nm or less (Figure 6.3(a)) [29, 137].

Shortly afterwards, femtosecond laser irradiation of silicon in SF_6 was used to produce silicon-based photodiodes with responsivities 2 orders of magnitude higher than commercial silicon photodiodes in the visible and 5 orders of magnitude higher in the infrared (Figure 6.3(b)) [32]. The irradiation of silicon in SF_6, though first reported for its effects on surface texturing, had developed into a viable approach to fabricating silicon-based optoelectronics that operate in the infrared.

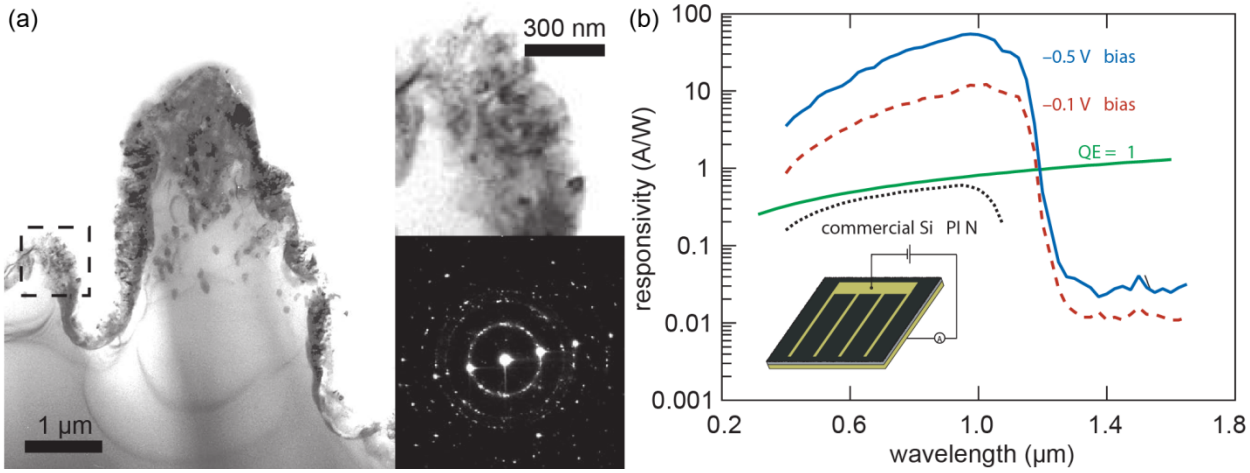

Figure 6.3. (a) Cross-sectional TEM images of a silicon surface irradiated with a peak laser fluence of 8 kJ/m^2, 500 shots/area, in 500 mTorr SF_6. *Upper right:* High-magnification view of the disordered region at the tip of the spike, indicated on main image with dashed square. *Lower right:* Selected area electron diffraction pattern obtained from the disordered region showing polycrystalline nature. Figure adapted from [29]. (b) Responsivity of a photodiode textured with fs-laser irradiation in the presence of SF_6 gas, under various low bias conditions, compared to a commercial silicon p-i-n diode. *Inset:* Device geometry showing both front and back gold electrodes deposited onto irradiated silicon wafer. Figure adapted from [32, 50].

The anomalous sub-band gap absorptance originally reported in silicon hyperdoped using SF_6 gas was shown to occur whenever any of the heavy chalcogens (sulfur, selenium, or tellurium) were present during fs-laser irradiation [12]. Neither selenium nor tellurium are

available as safe gaseous precursors, so in the original report sulfur and selenium were manually dispersed across the surface using toluene, and tellurium with mineral oil, prior to fs-laser irradiation [12]. The surfaces doped using a solid-phase precursor had conical structures on the surface that were roughly twice as large and half as dense as similar structure observed on surfaces irradiated in SF_6 gas (Figure 6.4(a-d)). RBS confirmed that the solid precursor indeed resulted in hyperdoping; RBS estimated that all samples contained hundreds of nanometers of material on the surface containing ~1% chalcogens, similar to what was reported for doping from the gas phase. Sheehy et al. also investigated the thermal stability of the sub-band gap optical absorptance induced by the presence of each chalcogen (S, Se, Te), the results of which are shown in Figure 6.4(e). The heavier the element, the more thermally robust the sub-band gap absorptance was found to be, and this effect was postulated to be due to differences in their respective diffusivities.

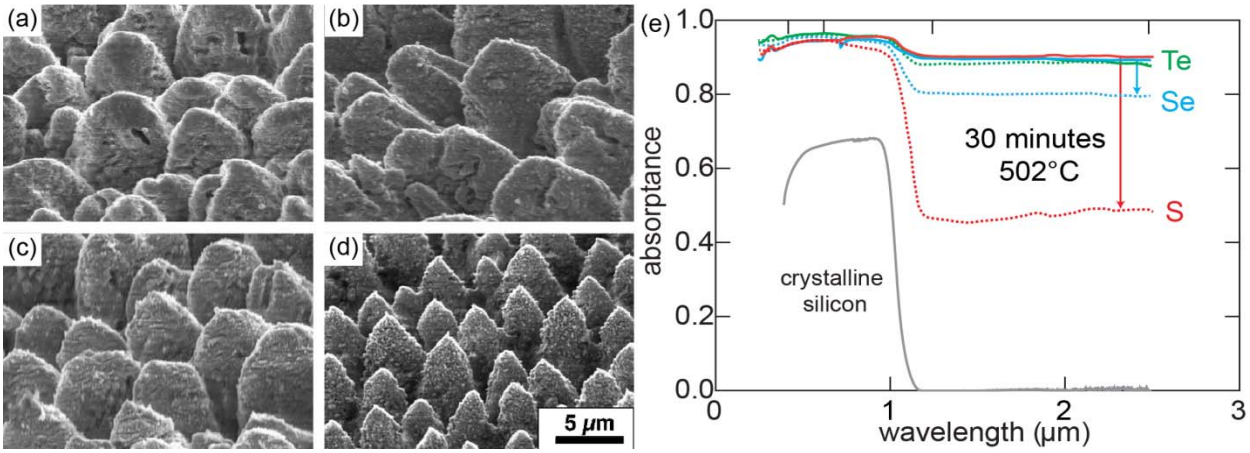

Figure 6.4. Scanning electron microscope images of silicon surfaces irradiated with a rastered beam with a peak fluence of 10 kJ/m^2 such that each point received ~1400 shots/area, using (a) sulfur powder, (b) selenium powder, (c) tellurium powder, (d) sulfur hexafluoride gas as a dopant precursor. In each image the surface is at the 45 angle. Figure from [12]. (d) Absorptance of each of the powder-doped samples imaged in (a-c) before and after a 30 minute anneal at 502°C (775 K). Figure adapted from [12], and absorptance data has been recalibrated by M.-J. Sher to account for errors in originally published data.

Further kinetic investigations by Tull et al. into sub-band gap absorptance supported the idea that the deactivation mechanism is diffusion-limited [122]. In Tull's investigation, 150 nm films of selenium and tellurium were thermally evaporated onto the silicon wafer prior to irradiation and SF_6 gas was used at the sulfur source. Samples were annealed across a range of temperatures (302-702°C, or 575 – 975 K) and times (10 minutes – 24 hours), and the average sub-band gap absorptance (1250 nm to 2500 nm) is shown in Figure 6.5(a). Before moving

forward, there are a couple features that should be noted in the data presented in Figure 6.5(a). First, the absorptance data as plotted has artifacts from the uniform reflector used in the integrated sphere at the time. The reflector has significant spectral features which introduced spurious features and created a general positive slope of the absorptance in the infrared. Second, the absorptance of the selenium-doped samples in Figure 6.5(a,b) do not decay past 0.3. This trend has not been observed in subsequent investigations, and may be a result of contamination during annealing and/or an effect of the non-uniform reflector in the integrating sphere. These artifacts affect the reported data, but do not take away from the powerful insights provided by plotting absorptance versus diffusion length.

For every annealing condition, the diffusion length, l, was estimated based on the relation $l = \sqrt{D \times t}$, where t is the annealing time. The diffusivity, D, was calculated for each temperature using reported values of the diffusion activation energy, E_A, and the pre-exponential D_0 based on the equation:

$$D = D_0 \exp\left(-E_A/_{kT}\right) \tag{6-1}$$

The diffusivity is expected to be concentration dependent and thus largely impacted by the beyond-solubility-limit concentrations of chalcogens, but concentration dependent diffusivities are not readily available for chalcogens in silicon at the concentrations induced through fs-laser hyperdoping. As a best approximation, the reported values for chalcogen diffusivity in silicon at equilibrium concentrations were used and still provided insightful conclusions.

When plotting the data presented in Figure 6.5(a) versus diffusion length, the sub-band gap absorptance in sulfur-, selenium-, and tellurium-hyperdoped silicon collapse onto a single curve (Figure 6.5(b)). This consistent trend across the chalcogens (S, Se, Te) is strong evidence that the deactivation mechanism is diffusion-limited. The authors developed a kinetic model to explain the observed trends based on the assumption that optical deactivation occurs through segregation to grain boundaries, and backed out that the size distribution of grains necessary to explain the observed decay in absorptance with annealing is around 5 nm. Microstructural investigations at the time were limited to sulfur-hyperdoped silicon produced by irradiation in the presence of SF_6 gas, which consisted of 10-50 nm grains in a 300 nm thick polycrystalline layer on the surface (Figure 6.3(a)) [29]. Due to the similarities in deactivation kinetics, the

assumption was made that doping with a thin film produced a similar microstructure and thus the grain boundary segregation model appeared feasible.

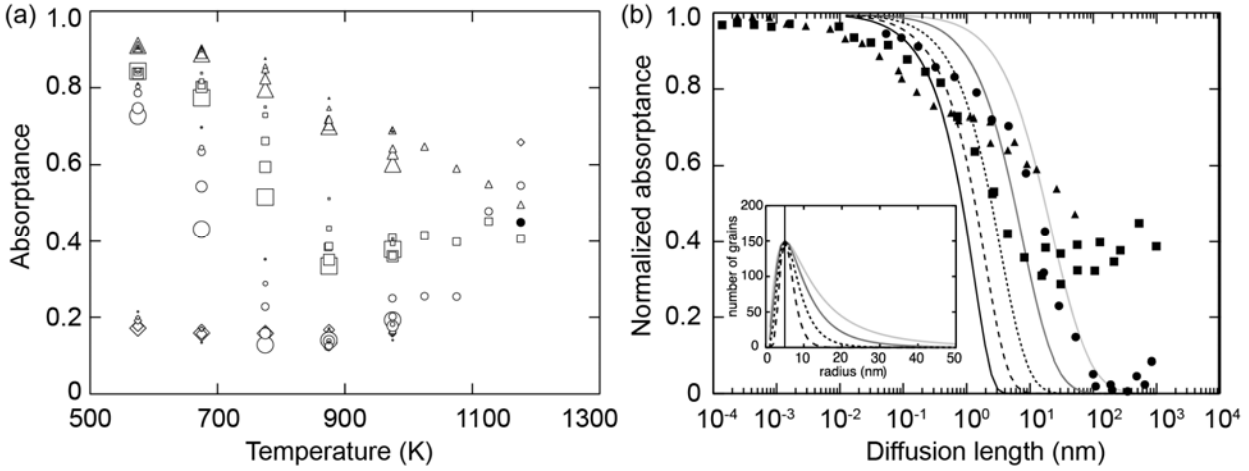

Figure 6.5. Results of kinetic investigation by Tull et al. [122] (a) Average absorptance from 1250 to 2500 nm for sulfur-doped (circles), selenium-doped (squares), tellurium-doped (triangles) silicon and samples irradiated in N_2 (diamonds) after various thermal anneals at T $\leq$702°C. The larger marker indicates the longer anneal (from smallest to largest: 10 min, 30 min, 100 min, 6 h, 24 h). (b) Normalized absorptance spectra for sulfur-doped (circles), selenim-doped (squares) and tellurium doped (triangles) silicon after various thermal anneals versus diffusion length of the respective dopant. The average infrared absorptance from (a) has been re-normalized, so that the maximum is the pre-annealed value and the minimum is the infrared absorptance of the unirradiated silicon wafer. Note also the artifacts in this data discussed on pg. 107.

In order to better understand the distribution of chalcogen impurities in the silicon lattice, extended x-ray absorption fine structure (EXAFS) spectroscopy was used to monitor the evolution of the local chemical state of selenium with annealing [138]. Silicon was hyperdoped with selenium under the exact same conditions as used for studies in this chapter: a 75 nm thin film of selenium was deposited onto silicon prior to fs-laser irradiation at a peak fluence of 4 kJ/m^2 and rastered to deliver 88 s/A. Samples were then subjected to 30 minute anneals at 325°C, 450°C, 575°C, 700°C, 825°C, and 950°C (The not-annealed sample and the samples annealed at 575°C and 950°C are the exact same as structurally investigated in section 6.3). Figure 6.6(a) shows the X-ray absorption spectra for all 7 samples investigated, including a metallic Se film, after normalization and background subtraction. The evolution in the fine structure with annealing reflects changes in the chemical states of the selenium atoms with annealing. Principle component analysis revealed that the evolution in fine structure can be described well (<7% residuals) as arising from only two eigenstates, referred to as A and B and

shown in the inset of Figure 6.6(b). The average IR absorption from 1250 nm to 2500 nm for each anneal shows strong correlation with the fraction of state B (Figure 6.6(b)). It is remarkably insightful that the amount of state A vs. state B, determined by principle component analysis and reflecting the chemical state of selenium in silicon, directly correlates with the optical absorption. These results reveal that the chemical state of selenium is coupled to the sub-band gap absorption, and the identification of only two eigenstates to explain the deactivation suggests that optical deactivation occurs explicitly through selenium redistribution to a single optically-deactivated state (B). The fine structure can also enable the identification of the optically active and optically-deactivated chemical states through theoretical modelling, and this work is currently under way.

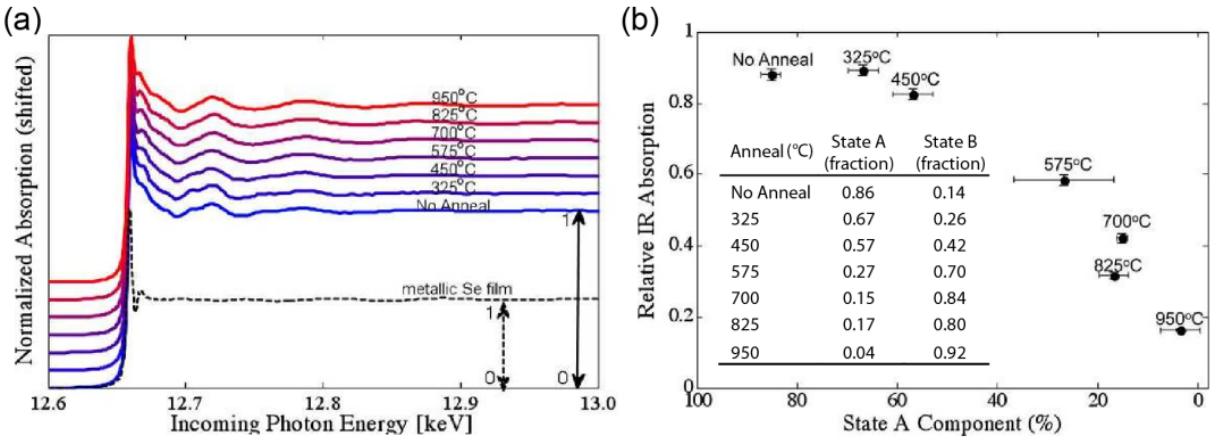

Figure 6.6. (a) Normalized and offset X-ray absorption spectra of highly Se-doped samples annealed at various temperatures. (b) IR absorption versus the component of state A determined by principle component analysis. The inset table gives the fraction of state A and state B after each of the investigated anneals. Figures from [138].

The demonstrated increase in sub-band gap absorptance using a thin-film dopant precursor [12, 122] proved that hyperdoping occurs following fs-laser irradiation of a thin-film on the surface of a silicon wafer. Though it has been proposed that the processes that occur during fs-laser doping from a thin film are comparable to doping from a gas phase, there have been no published reports of devices fabricated using thin-film fs-laser doping and no rigorous investigations into the differences between using a gaseous or thin film dopant precursor during fs-laser hyperdoping. In this chapter, we seek to elucidate the effect of using a thin film dopant precursor on the resulting microstructure and dopant distribution, and use this information to explain differences in the optical and electronic properties of silicon hyperdoped using a thin

film precursor (selenium) and gaseous precursor (SF_6) (Section 6.2). Next, we investigate the optical deactivation of selenium-hyperdoped silicon through in-depth structural characterization, and propose that diffusion-controlled coarsening of selenium-rich precipitates is responsible for optical deactivation in the latter stages of annealing (Section 6.3). In this context, we review previous investigations into the optical deactivation of chalcogens and find good agreement. This work represents progress towards understanding thin-film fs-laser doping for optoelectronic device fabrication, a potentially flexible and unique platform for novel materials synthesis.

6.2 Bulk properties and microstructure

6.2.1 Introduction

A better understanding of thin-film laser doping would expand fs-laser doping as a platform technology for novel materials synthesis. We investigate thin-film fs-laser doping through the optical, electronic, and structural characterization of silicon fs-laser doped using a thin-film dopant precursor and show that the use of a thin film changes the microstructure and dopant distribution, which affects p-n diode behavior and suggests that the surface structuring and dopant incorporation processes are strongly influenced by the phase of the dopant precursor.

6.2.2 Experimental

In order to isolate the role of the dopant precursor, we irradiated silicon under identical conditions and changed only the phase of the dopant precursor. The details of the thin film and gas phase fs-laser doping procedures are described in section 3.1.2. In this investigation, the samples were dipped in 5% HF acid for 30 seconds to remove the native oxide prior to film deposition, and irradiation parameters in this investigation are reported in Table 5.1. The predominant irradiation conditions used in this chapter (peak fluence of 4 kJ/m^2 and 88 shots/area) were selected because they result in significant sub-band gap absorptance when doping from a thin-film dopant precursor. For characterizing the potential p-n diode formation, select samples were annealed at 702°C (975 K) for 30 minutes and aluminum contacts were deposited on the sides using electron beam deposition.

The sample morphology was investigated using a FEI Helios 600 scanning electron microscope (SEM) operated at 5 kV accelerating voltage. Stereoscopic reconstructions of the surface morphology, enabling quantification of the surface roughness and extraction of height

profiles, were created using MeX surface metrology tools and SEM images taken at 0°, -10°, and +10° tilts. Cross-sectional transmission electron microscopy (TEM) samples of the rastered surfaces were prepared using a tripod polisher followed by a brief Ar^+-ion mill at 5 kV. Bright-field (BF) TEM micrographs and selected area diffraction patterns were collected with a JEOL 2011 TEM operated at 200 kV. Dark-field scanning TEM (DF-STEM) and energy dispersive x-ray spectroscopy (EDX) were carried out on a JEOL 2010F TEM operated at 200 kV.

Name	Dopant precursor	Fluence (kJ/m^2)	Shots per area (s/A)	Atmosphere (6.7×10^4 Pa)	Substrate Si(100)
Se:Si-1	Se thin film	4	88	N_2	p-type (1-20 Ω -cm)
SF_6:Si-1	SF_6 gas	8	50	SF_6	
Se:Si-2	Se thin film	4	88	N_2	n-type (3-6 kΩ-cm)
SF_6:Si-2	SF_6 gas			SF_6	
N_2:Si-2	None			N_2	

Table 6.1. Notation and corresponding doping parameters for samples used in section 6.2.

6.2.3 Results and Discussion

Figure 6.7(a) shows the absorptance of the fs-laser doped samples prior to any thermal treatment. Silicon doped with a thin-film precursor (Se:Si-2) has a higher average IR-absorptance (90%) than the sample irradiated under the same conditions but in the presence of SF_6 (SF_6:Si-2). Both samples have significantly greater IR absorptance than silicon irradiated in N_2 without dopant present (N_2:Si-2), which exhibits lower, monotonically decreasing absorptance in this spectral region, likely due to defect states induced by irradiation [122]. To determine the extent to which the optically-active and electrically-active defects are related, we fabricated SF_6-doped (SF_6:Si-1) and Se-doped (Se:Si-1) samples on a p-type substrate with similar optical properties. Se:Si-1 was prepared under identical conditions as Se:Si-2 and the resulting average IR-absorptance are the same (90%), as the type of substrate used does not influence absorptance or the dopant incorporation process. The sulfur-doped sample required a laser fluence of 8 kJ/m^2 and 50 s/A, resulting in an average IR-absorptance of 84%. Interestingly, the Se:Si-1 diode shows rectification but has a higher leakage current and larger forward bias current than the SF_6:Si-1 diode (Figure 6.7(b)).

To better understand the different diode characteristics and laser parameters necessary to achieve high IR-absorptance for gas and thin film precursors, we investigated the morphology,

microstructure, and dopant distribution of each sample using electron microscopy. We studied the effect of the thin film on the surface microstructure by comparing samples irradiated under identical conditions in an N_2 ambient, and with and without a Se thin film (samples Se:Si-2 and N_2:Si-2). We also gain insight into the microstructure and dopant distribution resulting from the thin-film doping process by comparing thin-film doping (Se:Si-2) and gas phase doping (SF_6:Si-1 and SF_6:Si-2) under similar conditions.

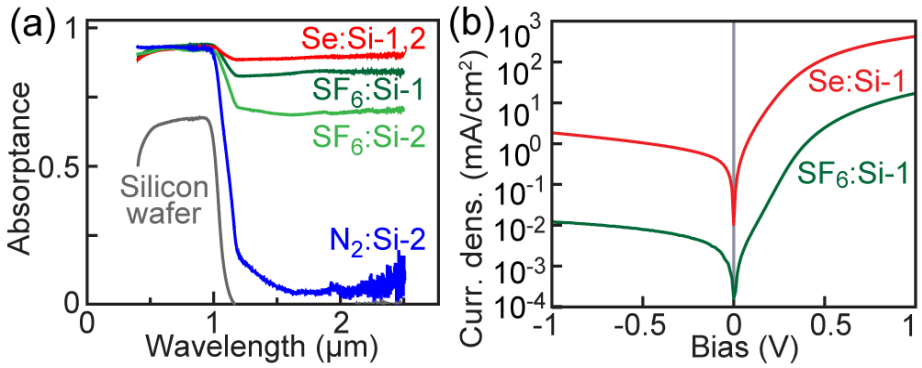

Figure 6.7. (a) Absorptance spectra of all samples studied in section 6.2. (b) Current density vs. bias curves of Se:Si-1 and SF_6:Si-1 at room temperature.

SEM images in Figure 6.8(a-d) show that all of the samples, regardless of the processing conditions, develop micrometer-scale periodic peaks through repeated melting and ablation of Si [79]. The surface morphology, however, is strongly influenced by the dopant precursor phase. The roughness of the surface was quantified by the root-mean-squared (RMS) of the height, calculated from stereoscopically reconstructed models of SEM images taken at 0°, -10°, and +10° tilts (Figure 6.8(e)). The presence of the 75 nm film of Se causes the RMS to increase by over 200%, from 0.96 μm for N_2:Si-2 to 2.36 μm for Se:Si-2, which is more than an order of magnitude larger than the initial Se film thickness, indicated in Figure 6.8(f). From the change in amplitude related to the thin-film dopant precursor, we confirm that the Se thin film significantly influences the morphological modifications of the surface initiated by the laser.

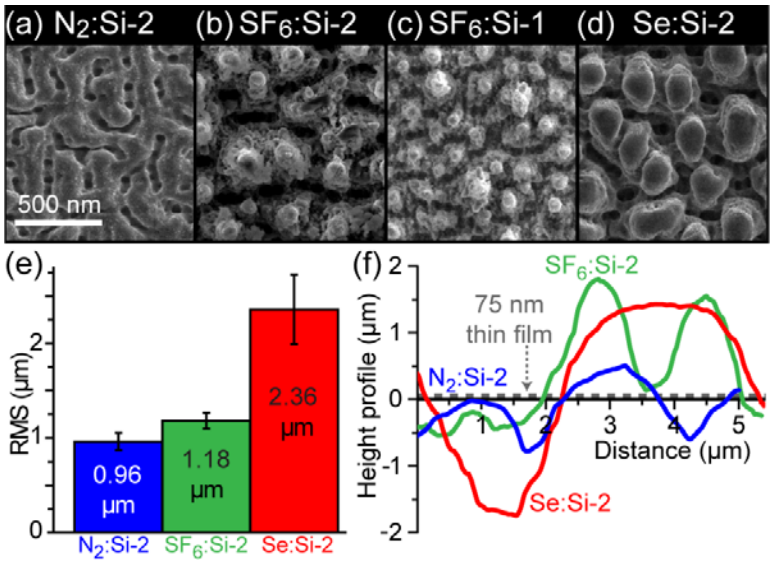

Figure 6.8. (a-d) SEM micrographs showing surface morphology of fs-laser irradiated Si. The laser scan direction and polarization was in the horizontal direction. (e) RMS of the surface height. Error bars reflect standard deviation for five independent measurements. (f) Height profiles of representative surfaces and the relative thickness of the 75 nm Se film (dashed).

The samples' microstructures provide additional insight into the dopant incorporation processes. Figure 6.9 shows BF-TEM images of each sample and corresponding SAD patterns. N_2:Si-2 (Figure 6.9(a)) has a 100 – 300 nm layer of defective material across the surface, and the SAD pattern shows that the surface peaks retain the same crystalline orientation as the substrate, though occasionally a misoriented grain is identified. A sulfur-rich layer forms on the surface in both SF_6:Si samples, as shown in Figure 6.9(b-c), while the peaks retain a single-crystalline, undoped core, consistent with previous findings [29]. The observed contrast within the core of N_2:Si-2 and SF_6:Si peaks are pockets of amorphous silicon which arise due to resolidification-induced pressures (Chapter 4).

The general structure of the control sample (N_2:Si-2) and sulfur-doped samples (SF_6:Si-1,2) is consistent with the current understanding of fs-laser induced surface structuring and dopant incorporation from a gaseous dopant precursor [79, 139]. During fs-laser irradiation above the ablation threshold, a thin layer of material is ablated from the surface and a molten Si layer is left behind. When a gas is present during irradiation, it is atomized by the high intensity of the ultra-short laser pulse and mixes with the molten Si [140], which then resolidifies quickly due to its contact with the cold bulk substrate [51].

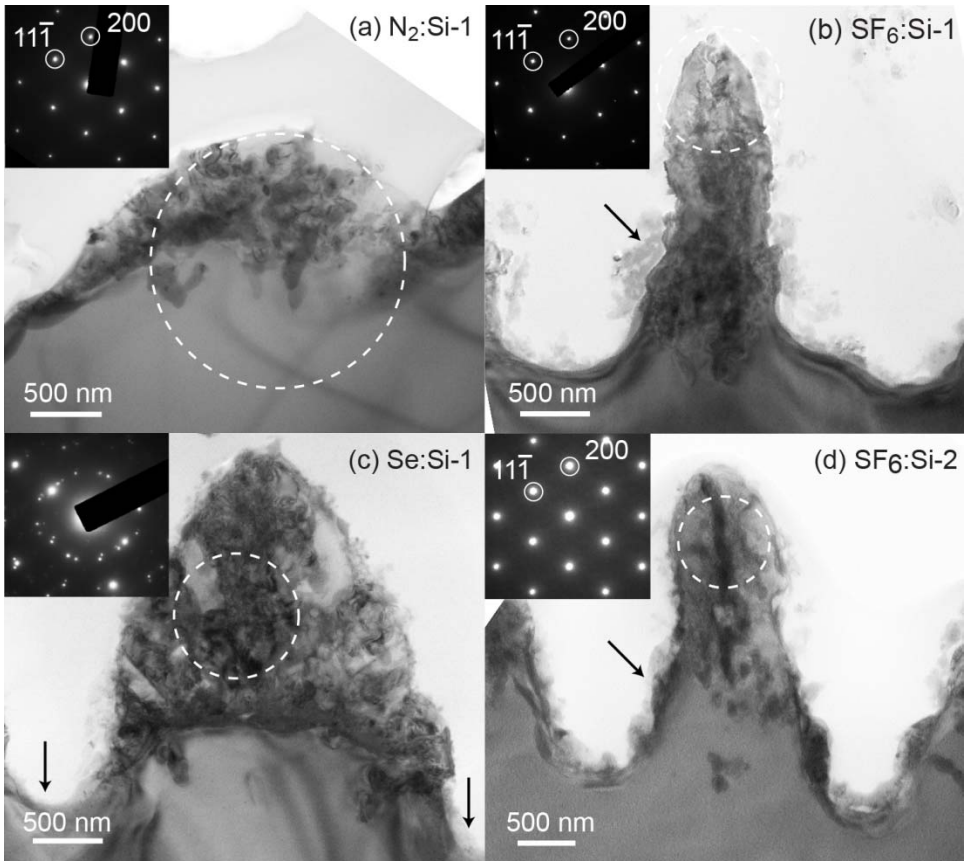

Figure 6.9. Cross-sectional BF-TEM images taken along the Si [011] zone axis with corresponding selected area diffraction patterns (insets). Black arrows indicate selenium-free valleys in (c), and identify the sulfur-rich surface layer in (b,d).

In contrast to silicon irradiated in SF_6 or in N_2 without any dopant present, the sample doped using a thin film (Se:Si-2) exhibits a significantly different dopant distribution and microstructure. As shown in Figure 6.9(c), Se:Si-2 contains micrometer-scale volumes of *polycrystalline* Si within each surface peak, as confirmed by the corresponding SAD patterns. Using DF-STEM and EDX (Figure 6.10), we show that the polycrystalline region is Se-rich. A series of EDX point scans and the corresponding Se-K_α EDX peaks, shown in Figure 6.10(c-d), support that the Se concentration is on the order of $10^{19} – 10^{20}$ cm^{-3} (0.1 – 1%). We note that here EDX can be used only qualitatively, as the measured concentrations are at the lower limit of the EDX chemical resolution. As shown in Figure 6.10(b), an EDX line scan from the Si substrate into the polycrystalline doped region confirms that Se is incorporated throughout the polycrystalline region, and variations in EDX signal intensity suggest that the Se is not homogeneously distributed.

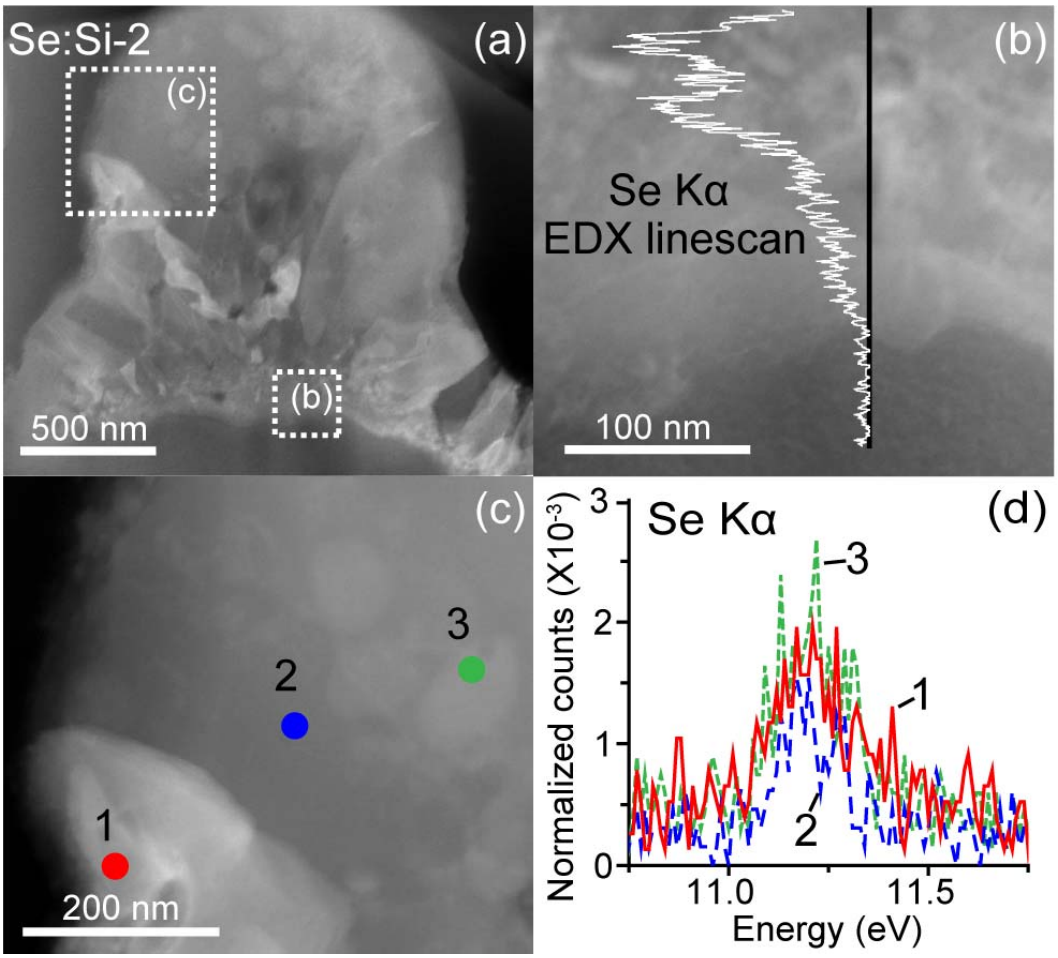

Figure 6.10. (a) DF-STEM image of Se:Si-2, dashed boxes highlight the regions shown in (b) and (c). (b) Selenium EDX line scan across the doped-undoped interface. (c) DF-STEM image showing the location of Se K_α EDX point spectra shown in (d).

The TEM investigations also reveal that the Se-rich Si is not distributed uniformly across the surface, but in discontinuous polycrystalline pockets within the peaks. The lack of dopant in the "valleys" of the Se:Si-2 surface suggests that there is no Se incorporation during later-stage irradiation, as material is ablated away from regions between the peaks (Figure 6.9(d), black arrows). Similar ablation processes occur during irradiation in SF_6, but sulfur is still incorporated due to the continuous presence of a gaseous precursor. We suggest that this discontinuous nature of the Se:Si surface can explain the difference in electrical properties because it creates shunts at the p-n junction, whereas SF_6:Si has a continuous surface layer of doped material. Shunting would explain the increased leakage current observed in the Se:Si-1 p-n junction, and thus this structural difference between the two samples is likely a principal cause of the diode behavior seen in Figure 6.7(b).

The micrometer-scale volumes of Se-doped material generated are an order of magnitude deeper than typical silicon melt depths during fs-laser irradiation. The morphology, microstructure, and dopant distribution in Se:Si-2 cannot be explained by the gas-phase doping model discussed above and together present strong evidence that a thin-film dopant precursor changes dramatically the surface structuring and dopant incorporation processes. The synthesis of a continuous layer of hyper-doped material is necessary for the realization of optoelectronic devices based on these novel materials and will be investigated further in Chapter 7.

6.2.4 Conclusions

The results presented in this section have shown that a thin-film dopant precursor changes both the surface structuring and dopant incorporation processes during fs-laser irradiation compared to a gas precursor. Thin film fs-laser doping generates much larger volumes of doped material than doping from a gas and achieves higher absorptance at lower fluences. The resulting polycrystalline surface and discontinuous dopant distribution, however, affect p-n diode rectification, which is not favorable for device fabrication. Further optimization of fs-laser doping will be addressed in Chapter 6. The differences in microstructure and dopant distribution between fs-laser doping with a thin-film versus gaseous precursor are in contrast to the similarities in optical deactivation described in the introduction, suggesting that the mechanism of optical deactivation may not be strongly related to microstructure. In the next section, we elucidate the dominant optical deactivation mechanisms in selenium-hyperdoped silicon through structural investigations of selenium segregation.

6.3 Optical Deactivation of Selenium Dopant

6.3.1 Introduction

As was discussed in the introduction of this chapter, though the sub-band gap absorptance of chalcogen-hyperdoped silicon has been the subject of extensive investigation, the mechanisms by which the chalcogens become optically deactivated remains an open question. The ability to modify the optical properties with annealing is a useful tool for gaining insights into how ultra-high concentrations of chalcogens enable such a drastic change in the optical properties [12, 122, 138], and is an interesting question in its own right. In addition, silicon hyperdoped with selenium is a well-suited materials system for studying dopant behavior because selenium provides strong chemical contrast due to its higher atomic number. Based on Tull's observation that optical deactivation is diffusion limited, in this section we investigate selenium diffusion with annealing using sophisticated TEM-based structural characterization. Our findings suggest that diffusion-limited precipitation and growth of a selenium-rich phase is the primary mechanism behind the latter stages of selenium deactivation with annealing and this hypothesis is shown to be consistent with previous investigations into the optical deactivation of chalcogens.

6.3.2 Experimental

In this investigation we focus on the structural characterization of silicon hyperdoped with selenium under conditions identical to those reported in the previous section. A 75-nm film of selenium is deposited onto a silicon wafer, followed by fs-laser irradiation at peak fluence of 4 kJ/m^2 and rastered such that 88 shots/area are delivered to any given point. In order to identify the dominant optical deactivation mechanisms, we investigated the evolution of the selenium distribution following annealing for 30 minutes in N_2 at 575°C and 950°C. Trends in the sub-band gap absorptance are monitored by averaging the absorptance from 1250 nm – 2500 nm, identical to the procedure used by Tull et al. in the previous kinetic investigation [122].

Cross-sectional TEM samples were prepared using a tripod polisher and diamond lapping films and initial structural characterization was carried out at Oak Ridge National Labs in collaboration with Dr. Juan Carlos Idrobo. Samples were simultaneously imaged in both BF-STEM and HAADF-STEM in a FEI Titan S 80-300 operated at 300 kV. Further investigations into changes in the selenium distribution with annealing were carried out via electron tomography, performed using HAADF-STEM on a FEI Titan microscope operated at 200kV.

Electron tomography was done at CEA-LETI and performed by Georg Haberfehlner. Cylindrical volumes of material were prepared from the center of the peaks on the surface using a FIB and the tomography series was acquired over a tilt range of -67° to +67° in 1° increments. The images were aligned using a cross-correlation algorithm and three-dimensional reconstruction was carried out using the Simultaneous Iterative Reconstruction Technique.

6.3.3 Results and Discussion.

6.3.3.1 Structural investigations of selenium segregation

The decay in sub-band gap absorptance of selenium-hyperdoped silicon following 30 min anneals at 575°C and 950°C is shown in Figure 6.11(a). For comparison to previous kinetic investigations, the averaged sub-band gap absorptance is normalized with respect to the absorptance prior to annealing, plotted versus diffusion length, and overlaid onto the data collected by Tull et al. in Figure 6.11(b). Values identical to those used by Tull for the activation energy of selenium diffusion (E_A = 2.84 eV) and the pre-exponential (D_o = 2.47 cm^2/s) were used to calculate diffusion length. Though the samples studied in this section were prepared under different irradiation conditions than were used by Tull et al., the decay in absorptance falls onto the same curve when plotted in this manner. This agreement supports that the optical deactivation process is material-dependent and not strongly a function of irradiation conditions.

The Z-contrast image in Figure 6.12(a) provides insights into the selenium distribution in a Se-hyperdoped region without any post-irradiation annealing. The Z-contrast imaging shows that the selenium concentrations are highest at the base of the peak, where the image contrast is diffuse and noticeably inhomogeneous (Figure 6.12(b,d)). The contrast is also inhomogeneous throughout the body of the peak, though this may be exasperated by changes in sample thickness. Close investigation of a grain boundary prior to annealing suggests limited grain boundary segregation (Figure 6.12(c,e)).

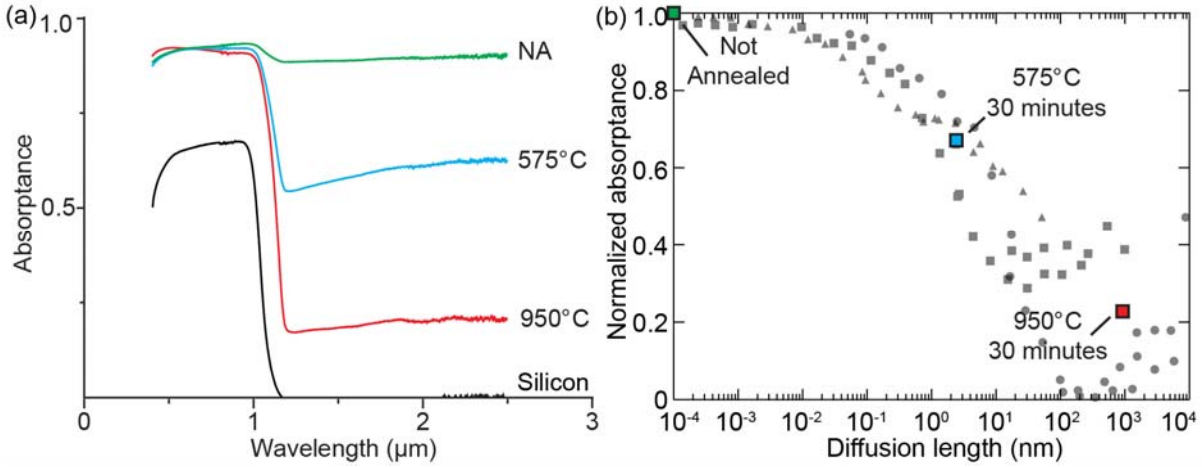

Figure 6.11. (a) Absorptance of Se-hyperdoped silicon without any post-treatment annealing (green), after a 30 min anneal at 575°C (blue) and after a 30 min anneal at 950°C (red), with the absorptance of untreated silicon wafer for reference (black). (b) Normalized and averaged sub-band gap absorptance of samples presented in (a) plotted versus diffusion length, overlaid onto the data collected for sulfur (circle), selenium (square) and tellurium (triangle) hyperdoped silicon in the previous kinetic study of deactivation by Tull et al. [122]. Note that the overlay is only a qualitative comparison due to the artifacts present in Tull's data. The new data does not contain artifacts from imperfect reflection in the integrating sphere and, relatedly, the optical decay doesn't plateau at 0.3.

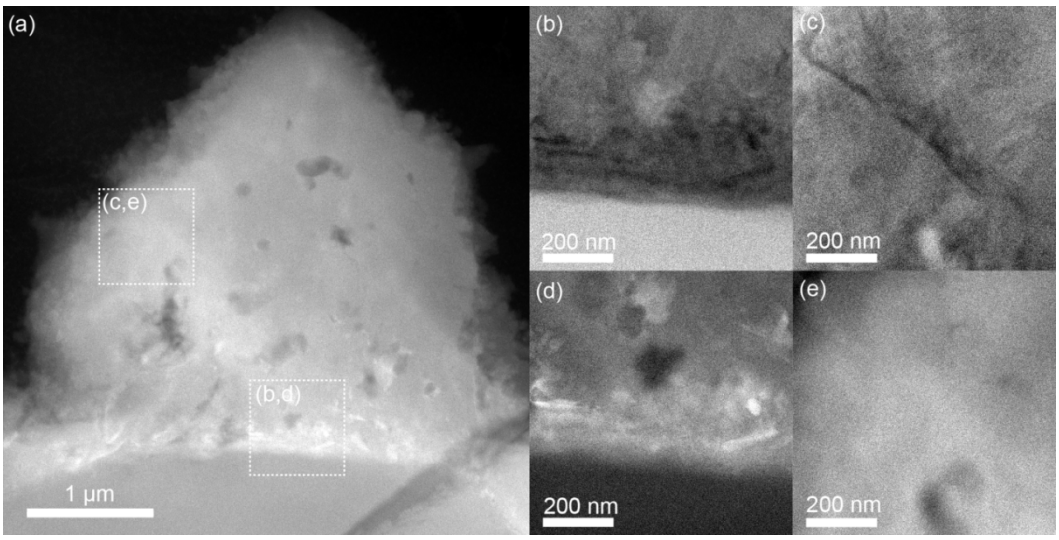

Figure 6.12. (a) Z-contrast image of a peak on the non-annealed surface of selenium-hyperdoped silicon. Brighter contrast within the peak is due to increased concentrations of selenium. (b) Bright-field STEM image of the interface between the polycrystalline hyperdoped region and the undoped silicon substrate, from region indicated in (a). (c) BF-STEM image of a grain boundary within the polycrystalline region. (d) Z-contrast image of the interface in (b), showing diffuse contrast due to increased selenium concentrations, with some segregation already visible. (e) Z-contrast image of the grain boundary in (c), showing no visible signs of segregation. The darks spot visible in the Z-contrast image are voids.

After annealing at 575°C for 30 min the Se-rich regions begin to show signs of segregation (Figure 6.13). It is difficult to quantify the amount of selenium segregation from the Z-contrast image (Figure 6.13(a)) but, looking closely at the interface between the doped and undoped region (Figure 6.13(b)), clear signs of segregation to the edges of the voids and to the nearby grain boundaries can be observed. Annealing at even higher temperatures (950°C for 30 min) produces significant selenium segregation to grain boundaries and the precipitation of selenium-rich material, shown in Figure 6.14(a). At the base of the peak, where there was diffuse contrast before annealing, there is now a high density of selenium-rich precipitates, some of which exhibit faceting (Figure 6.14(b,d)). Z-contrast imaging of a grain boundary, from the region indicated in Figure 6.14(a) shows selenium segregation into a region that is ~3 nm thick (Figure 6.14(c,e)).

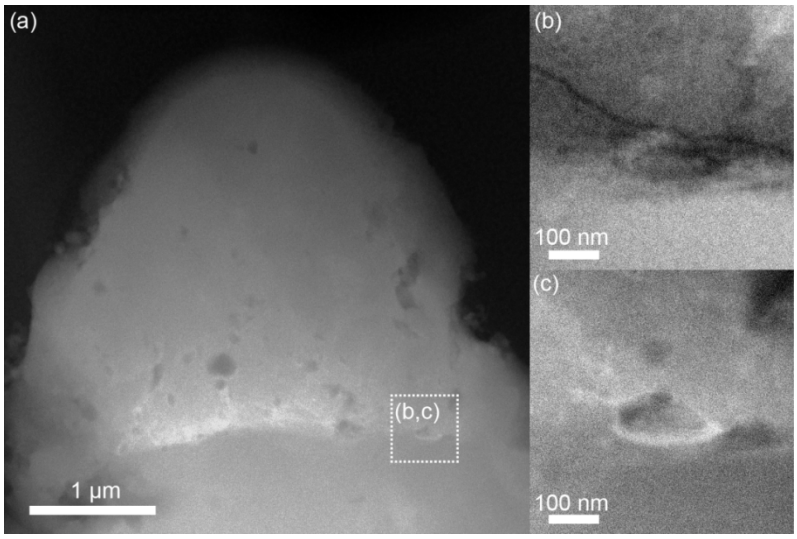

Figure 6.13. (a) Z-contrast image of a peak on the surface of selenium-hyperdoped silicon that was annealed for 30 minutes at 575°C. (b) Bright-field STEM image of the interface between the polycrystalline hyperdoped region from region indicated in (a), showing both a void and a grain boundary. (c) Z-contrast image of the interface in (b), showing evidence of selenium segregation to the boundaries of the void and the grain boundary.

These investigations into the changes in microstructure with annealing support Tull's hypothesis that diffusion-limited segregation is responsible for the optical deactivation with annealing, and highlight the potential significance of nucleation and growth of Se-rich precipitates in the optical deactivation process. The precipitates are concentrated at the base of the peaks, where there was the most selenium present prior to annealing. We next use Z-contrast

electron tomography to study the evolution of the selenium distribution in 3 dimensions to better understand the selenium segregation process and its relation to optical deactivation.

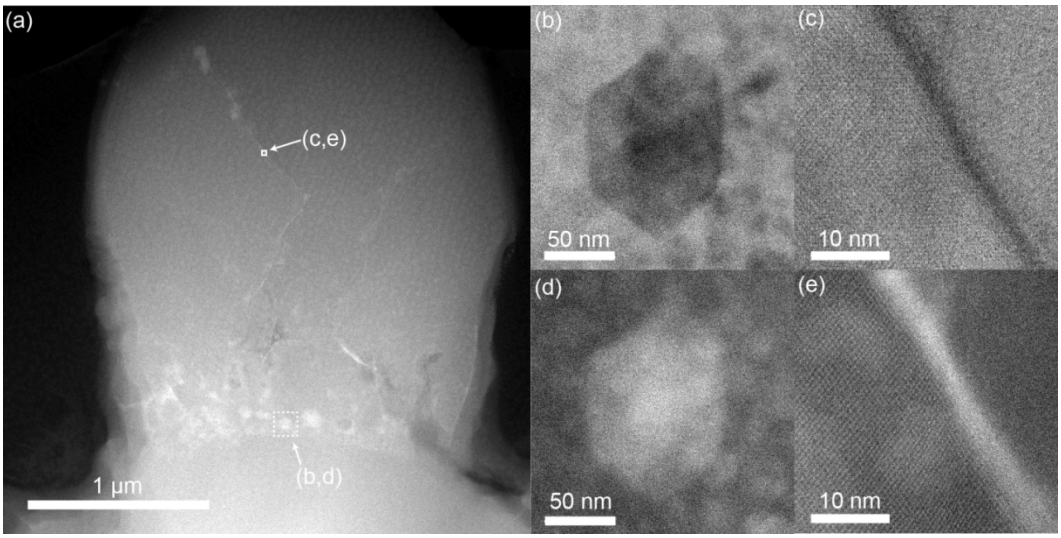

Figure 6.14. (a) Z-contrast image of a peak on the surface of selenium-hyperdoped silicon that was annealed for 30 minutes at 950°C. The base of the peak contains precipitates of selenium-rich material and segregation to grain boundaries in the body of the peak is also visible. (b) Bright-field STEM image of a faceted Se-rich precipitate, from region indicated in (a). (c) BF-STEM image of a grain boundary within the polycrystalline region. Region indicated in (a) is a best estimate of the AOI imaged. (d) Z-contrast image of the precipitate in (b), confirming that it is selenium rich. Lighter contrast visible in (c) and (d) is ion beam damage due to sample preparation. (e) Z-contrast image showing selenium segregation to grain boundary in (c).

Figure 6.15 shows a 3-dimensional reconstruction of the selenium distribution as a function of annealing in a cylindrical volume extracted from the center of surface peaks. The non-annealed sample (Figure 6.15(a)) exhibits diffuse contrast that is the strongest at the bottom, consistent with previous observations that there is more selenium in the bottom of the peaks. Some selenium-rich precipitation is already visible and there is selenium segregation to the grain boundary towards the top of the reconstructed volume. Though this sample has not been annealed, we might expect some amount of segregation due to sample heating during laser irradiation. Comparing the selenium distribution in the non-annealed sample (Figure 6.15(a)), with the selenium distribution after a 30-minute 575°C anneal (Figure 6.15(b)) and 950°C anneal (Figure 6.15(b)) shows clear evidence of the precipitation of a selenium-rich phase and of segregation to grain boundaries.

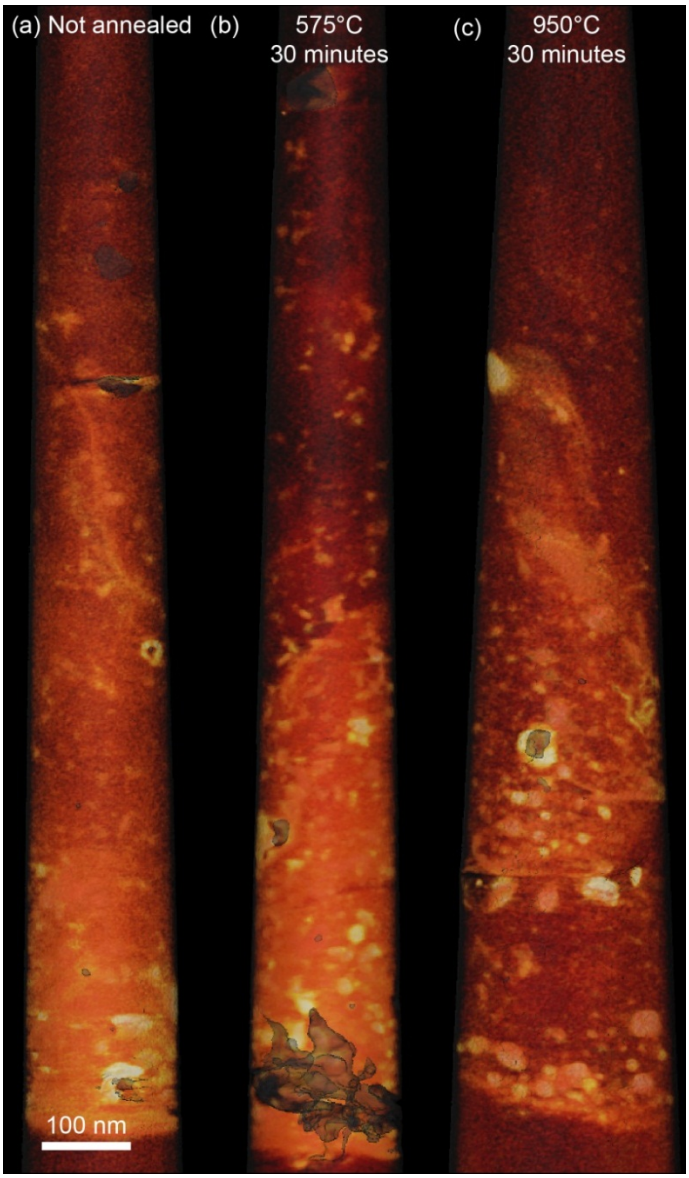

Figure 6.15. HAADF-STEM Tomography reconstruction of selenium-hyperdoped silicon extracted from the center of the polycrystalline peaks, showing selenium distribution (a) before annealing (b) after a 30 minute anneal at 575°C, and (c) after a 30 minute anneal at 950°C.

Structural investigations show that selenium rich precipitates form with annealing, but it cannot be immediately concluded whether this plays an important role in the optical deactivation of selenium in silicon. Segregation of selenium is a viable method of selenium deactivation, but dopants can also be activated or deactivated on the point-defect scale (for example through clustering with vacancies [141], in which case precipitation could be a secondary phenomenon after the deactivation). To determine whether precipitation is a viable mechanism for optical deactivation, we revisit the previous work by Tull [122] and Newman [138] to see if their results

support such a hypothesis in light of our improved understanding of the structural evolution with annealing.

6.3.3.2 Precipitation-driven optical deactivation

In this section we revisit previously published work on the optical deactivation of selenium to test whether the precipitation of a selenium-rich phase, as observed by TEM and electron tomography, is consistent with the kinetics of deactivation [122] and the evolution of the chemical state of selenium monitored using EXAFS [138]. First, we revisit the data presented in Tull et al.'s kinetic study with the hypothesis that deactivation occurs through diffusion-controlled precipitation. We employ the classical theory of particle coarsening from a supersaturated solution, also known at the Liftshitz-Wagner theory, that provides an analytical solution to the kinetics of particle growth and the time dependence of the solute concentration in the matrix [142, 143].

In this analysis we make an assumption that the sub-band gap absorptance is proportional to the degree of chalcogen-supersaturation and compare the rate of optical deactivation with the time dependence of the solute concentration in the matrix based on the Lifshitz-Wagner theory for coarsenening. The asymptotic variation of the solute content in the matrix, c, is predicted to have the following relationship with annealing time, t [143, 144]:

$$c - c_e = \left(\frac{9\gamma^2 c_e^2 V_m}{D(RT)^2}\right)^{1/3} (t)^{-1/3} \qquad (6\text{-}2)$$

Here, c_e is the concentration of the solute in the matrix that is in equilibrium with an infinitely large particle, D is the diffusion coefficient of selenium in silicon, R is the molar gas constant, T the annealing temperature, γ the specific free energy of the precipitate-matrix interface, and V_m is the molar volume of the Se-rich phase. It is important to recognize that the linear relationship between the amount of supersaturation, (c - c_e), and $t^{-1/3}$ applies only to segregation from a supersaturated alloy through coarsening. This is the case only after sufficient precipitate nucleation and growth, and therefore this behavior would only be expected during the latter-most stages of annealing.

The kinetics of segregation predicted by the Lifshitz-Wagner theory are grounded in the Gibbs-Thomson equation, which states that the equilibrium concentration at the particle-matrix interface is a function of precipitate size, and can be expressed for a spherical particle by:

$$C_{eq}(R) = C_{eq}(\infty)\left[1 + \frac{2\gamma V_m}{kTr}\right] \quad (6\text{-}3)$$

Here the symbols have the same meaning as above, r is the particle radius, and k is Boltzmann's constant. The Lifshitz-Wagner theory states that, at a given level of supersaturation, the average particle size will be that whose equilibrium concentration at the surface is equal to the concentration in the matrix. Coarsening results in a gradual increase in the average particle size and this occurs concurrently with a decreasing concentration in the matrix. As such, the predicted linear trend is expected to appear only after an incubation regime allows for sufficient nucleation and growth of new particles.

In order to identify regions of optical deactivation through diffusion-controlled coarsening, we first review the expected trends based on the equations given above. The linear relationship between concentration and $t^{-1/3}$ is predicted only in the regime in which coarsening dominates segregation, and there is a window of time precluding the coarsening regime in which the nucleation of precipitates is the dominant mechanism of segregation. The slope is shallower when nucleation begins and the increasing role of diffusion-controlled coarsening with annealing is reflected in a gradual increase in the magnitude of the slope [144].

Based on the equations presented above, we expect the linear regime to be steeper at lower temperatures due to multiple terms in the denominator of equation 6-2. The diffusivity (D) has an exponential dependence on temperature and it is multiplied by a temperature-squared term in the denominator. Though the equilibrium concentration, c_e, would also increase with temperature, its effects are less pronounced. The equations above show that the y-intercept of the linear regime ($t = \infty$) is the equilibrium concentration of the solute at the annealing temperature. Combining these two expected trends, the decreasing concentration of impurities in the solute should have a steeper slope at lower-temperature anneals and a lower y-intercept than when annealing at higher temperatures. With these trends in mind, we can revisit the data presented by Tull et al. for selenium hyper-doped silicon.

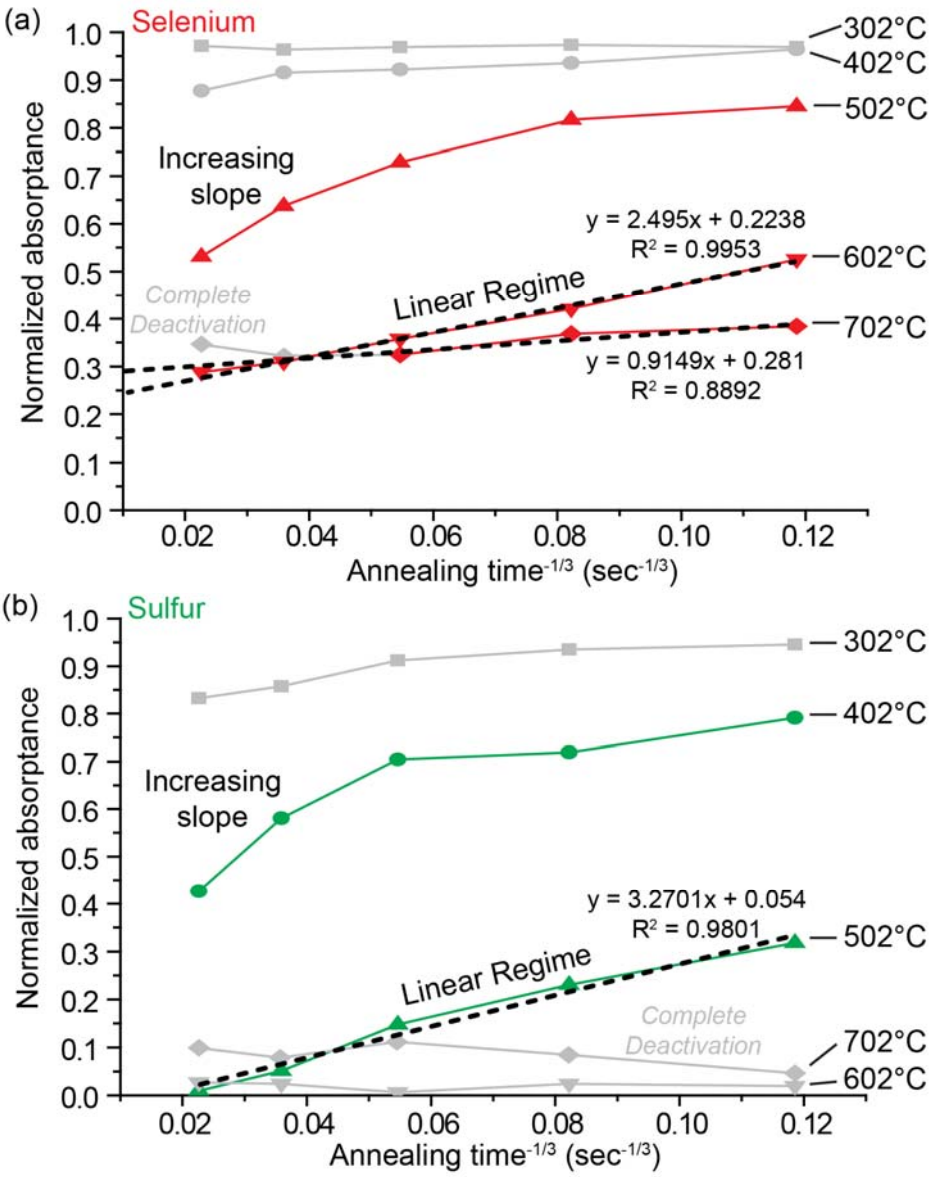

Figure 6.16. The normalized absorptance of (a) selenium- and (b) sulfur-hyperdoped silicon after annealing over a range of temperatures (302°C – 702°C, originally reported as 575 – 975 K) and times (10 m – 24 h) plotted versus $t^{-1/3}$. For clarity, the anneal series relevant to this study of diffusion-controlled coarsening are colored. Linear fits are shown for regions that satisfy the Lifshitz-Wagner theory. The data presented here was collected and published by Tull et al. [122].

Figure 6.16(a) shows the normalized absorptance of selenium hyperdoped silicon plotted versus $t^{-1/3}$. Here, we present the same data that was published by Tull et al. and used to make the initial conclusions about the role of chalcogen diffusion during deactivation (Figure 6.5). Close inspection of Figure 6.16 shows that the criteria discussed above are satisfied in the latter-stages of optical deactivation, though none of the anneal series covered sufficient time span to show the complete transition into coarsening-limited growth (either shorter times at 602°C or longer times

at 502°C could complete a single data set). The 602 °C (875 K) annealing series is linear with respect to $t^{-1/3}$, and this trend continues into the 702°C (975 K) anneal series through the 100 min anneal. A linear fit to the 602°C anneal series and over 10-100 mins at 702°C show all the expected trends mentioned in the previous paragraph: The lower temperature anneal (602°C) has a steeper slope and a lower projected y-intercept. The 6 h and 24 h anneal at 702°C were omitted from the linear fit because the absorptance has leveled off at this point. As discussed previously, the plateau in the selenium absorptance at 0.3 is an artifact. In the context of this study, we treat it to be a constant offset that does not affect the trends in the slope of optical decay. Finally, the 502°C (775 K) anneal series shows an increase in slope as we move towards longer anneals (lower $t^{-1/3}$), and this behavior is indicative of the approaching onset of diffusion-limited coarsening [145].

Our structural investigations using Z-contrast TEM and electron tomography showed significant precipitation after a 30 minute anneal at 575°C, in the same regime that Tull's kinetic investigations begin to exhibit behavior consistent with the Lifshitz-Wagner theory for diffusion-limited coarsening. This analysis therefore supports that precipitation and coarsening could be the dominant mechanism behind optical deactivation during the latter stages of annealing.

In order to test the generality of diffusion-controlled coarsening as the dominant optical deactivation mechanism in chalcogen-doped silicon we conducted a similar analysis on the sulfur data reported by Tull et al. (Figure 6.16(b)). There is a regime of linear absorptance decay in the anneal series at 502°C (R = 0.98) which extends down to zero sub-band gap absorptance. Interestingly, the 402°C anneal series shows the characteristic signs of coarsening-onset, similar to the 502°C anneal series in selenium: the magnitude of the slope is increasing with longer anneals at the temperature that just precludes the regime in which the entire anneal series is linear (502°C for S, 602°C for Se). This suggests that diffusion-controlled coarsening is also an important mechanism in the optical deactivation of sulfur, and possibly hyperdoped chalcogens in general. A more complete annealing study across a broader range of times and temperatures is necessary to confirm these trends, but these investigations are consistent with our hypothesis.

Before moving on, it is important to emphasize that the linear relationship between sub-band gap absorptance and concentration in the solute is a critical assumption underlying this kinetic analysis. This assumption will be true if either (1) the sub-band gap absorptance is truly linearly related with chalcogen concentration or (2) the concentration of the optically active

chalcogen complex is proportional to the concentration in the solute. If the relationship between absorptance and concentration can be quantified, then this type of study could be used to extract the material constants included in equation 6-2, including the true diffusivity of the chalcogens in supersaturated silicon [144].

Next, we revisit the EXAFS investigations (Figure 6.6) of selenium deactivation in the context of our current discussion about diffusion-limited coarsening. The EXAFS investigations into the chemical state of selenium concluded that there is only one optically-deactivated state. The premise that diffusion-controlled coarsening of precipitates is the dominant mechanism of optical deactivation in latter stages of annealing is in agreement with this conclusion, so long as the precipitating phase is the optically-deactivated state. The absorptance vs. $t^{-1/3}$ investigations suggest that diffusion controlled coarsening is the dominant mechanism in selenium-hyperdoped silicon after a 30 min anneal at 602°C, but a 30 min anneal at 502°C is not sufficient to enter this regime. Referring back to EXAFS (table inset in Figure 6.6(b)), there is a jump in the amount of state B in the sample annealed for 30 minutes at 450°C compared to 30 minutes at 575°C. TEM investigations report substantial precipitation after a 30 min anneal at 575°C (Figure 6.15), and this is in the same regime that exhibited coarsening-driven deactivation in the previous kinetic analysis (602°C, 30 minutes). These correlations are far from conclusive, but it is promising that all previous investigations support that precipitation and growth of a selenium-rich phase, as observed by TEM, may be the dominant mechanism for optical deactivation during the latter stages of annealing.

These investigations demonstrated the value of TEM-based investigations into dopant deactivation, so long as the dopant provides sufficient chemical contrast. There are, however, limitations to this approach to studying dopant deactivation. First, the techniques used in this investigation are not capable of detecting clustering or precipitation on length scales below the resolution of electron tomography (nm-scale). The resulting structural insights and kinetic discussion are therefore limited to optical deactivation only in the latter-stages of annealing, when sufficiently large-scale precipitation is relevant. There is substantial optical deactivation at earlier stages of annealing that are likely related to activity on the point-defect scale and which these investigations do not comment on. Second, the small volumes of material probed using atom probe tomography have made it difficult to extract meaningful statistics regarding precipitate size and distribution, which could be used to further elucidate the nucleation, growth,

and coarsening of selenium-rich precipitates. Finally, our TEM-based structural investigations were unable to conclusively identify the structure or the composition of the precipitating phase because the nanoscale precipitates are embedded in a silicon matrix. The equilibrium Se-Si phase diagram[146] shows that the only stable compound at moderate temperatures (<900°C) is $SiSe_2$, but precipitation can also produce metastable phases [147]. Work is underway to identify the chemical state of the optically activated and deactivated states identified by EXAFS, which will be a valuable complement to the structural investigations presented in this chapter.

6.3.4 Conclusions

In this section we used TEM-based investigations into the evolution of microstructure with annealing to gain insights into the dominant mechanism of optical deactivation in selenium-hyperdoped silicon. Plan-view TEM investigations showed selenium segregation to grain boundaries, precipitates, and the internal surfaces of voids with annealing. Tomographic reconstructions of the selenium distribution with annealing showed clearly the precipitation of selenium-rich particles. The role of selenium precipitation in the optical deactivation of hyperdoped silicon was tested by revisiting the investigations of Tull et al. into the kinetics of optical deactivation, whose work originally showed that optical deactivation was diffusion-limited. By assuming that the sub-band gap absorptance is proportional to the amount of supersaturation in the hyperdoped silicon, the rate of optical deactivation with annealing time showed good agreement with the Lifshitz-Wagner theory for diffusion-controlled coarsening in a supersaturated system. EXAFS investigations into the chemical state of selenium with annealing show that there is a single optically deactivated state (i.e. the precipitated Se-rich phase) which becomes drastically more prevalent after a 30 min anneal at 575°C (the temperature range in which kinetic studies suggest diffusion-limited coarsening, and at which we observe precipitation in TEM). The data presented in this analysis consistently supports that diffusion-limited coarsening is the principle mechanism responsible for optical deactivation during later-stage annealing. Additional investigations into the deactivation kinetics and their correlation with microstructure will allow a more precise identification of the regime in which diffusion-controlled precipitation is the dominant deactivation mechanism.

6.4 Conclusions

This chapter set out to understand the consequences of using a thin-film dopant precursor during the fs-laser doping of silicon. Previous investigations had shown that the deposition of a chalcogen thin film prior to irradiation results in broad sub-band gap absorptance [12, 122], but little was understood about the effect of using a thin film on the doping process. In section 6.2 we undertook a systematic investigation into the effect that the phase of the dopant precursor has on resulting absorptance, p-n diode rectification, surface morphology, microstructure and dopant distribution. The presence of a selenium thin film results in large peaks with a polycrystalline, selenium-rich core, and no significant selenium hyperdoping in the valleys between the peaks. This is in contrast to the microstructure of surfaces irradiated in the presence of sulfur hexafluoride, which is composed of a single crystalline core and a continuous sulfur-rich surface layer. The unique microstructure of the thin-film doped silicon is likely the cause of the poor rectification observed in p-n diodes.

In section 6.3 we used Z-contrast imaging to investigate optical deactivation with annealing, taking advantage of the strong chemical contrast provided by selenium in silicon. Plan-view TEM of samples annealed for 30 minutes at 575°C and 950°C shows evidence of grain boundary segregation, segregation to the edges of voids, and the formation of selenium-rich precipitates. Tomographic reconstructions were carried out to better understand the selenium distribution and showed substantial precipitation at the base of the peak after a 30-minute anneal at 575°C. In order to clarify the role that selenium segregation and, specifically, precipitation plays in the optical deactivation process we compared the kinetics of optical deactivation, published by Tull et al., with the expected kinetics due to diffusion-controlled coarsening. In the latter stages of optical deactivation the Tull data shows good agreement with the Lifshitz-Wagner theory for diffusion-controlled coarsening, suggesting that segregation through coarsening is the dominant deactivation mechanism in this annealing regime. EXAFS investigations studying the chemical state of selenium with annealing concluded the existence of a single “optically deactivated” state which, in the context of this study, could be attributed to the formation of selenium-rich precipitates. A kinetic study of optical deactivation over a broader range of annealing times and temperatures, and with complementary structural characterization, will provide a more detailed understanding of the role of precipitation with respect to optical deactivation.

This chapter focused on understanding selenium-doped silicon fabricated under irradiation conditions chosen to maximize sub-band gap absorptance. Our structural investigations, however, showed that dopant incorporation is inhomogenous and discontinuous and that this is likely the cause for the poor rectification observed in diodes made using a thin-film dopant precursor. The application of thin-film fs-laser hyperdoping in optoelectronic devices requires a more continuous and homogeneous dopant distribution. In the next chapter we investigate the dopant incorporation and surface texturing mechanisms responsible for the observed microstructure and use this understanding to improve the dopant distribution across the surface.

Chapter 7 Thin-film Fs-laser Hyperdoping pt. 2: Dopant incorporation mechanisms

The purpose of this investigation is to understand the dopant incorporation process during thin-film fs-laser doping and demonstrate the ability to control it through optimization of the fs-laser irradiation conditions. This chapter begins by motivating the development of thin-film fs-laser doping with a review of the variety of pulsed laser doping processes developed over the past 4 decades. We use SEM, TEM, and profilometry to understand the dopant incorporation and surface texturing mechanisms that lead to the unique microstructure and dopant distribution reported in Chapter 6. We show that the crystallization of hyperdoped silicon occurs only within features protruding from the surface, likely due to the combined effects of the surface morphology on the effective fluence and heat dissipation. The polycrystalline hyperdoped "bumps" grow into large polycrystalline peaks through the crystallization of amorphous silicon at the surface with continued pulsed laser irradiation. With this understanding of the interdependence of crystallization and surface texturing during thin-film fs-laser doping, which is not conducive to device fabrication, we investigate the effect of changing the fluence and pulse number on the resulting surface morphology and microstructure. A low-fluence regime is identified in which a thin layer of selenium remains on the surface during early stages of irradiation and evolves into a continuous surface layer of hyperdoped material in parallel with the formation of laser-induced periodic surface structures. This investigation demonstrates the ability to tune the dopant distribution through a thorough understanding of the relationship between irradiation conditions, dopant distribution, and microstructure. Such systematic investigations into the doping process are necessary for the development of fs-laser irradiation as a flexible platform for synthesizing materials with unique optoelectronic properties.

7.1 Introduction

Investigations in the previous chapter found that the use of a thin-film precursor is drastically different and more complicated than fs-laser doping from a gaseous precursor. The effectively infinite dopant source present in the ambient atmosphere during doping from SF_6 gas enables the formation of a continuous hyperdoped surface layer in parallel with surface texturing. Fs-laser doping from a thin film, however, produces hyperdoped material isolated to the bodies of the polycrystalline peaks and this affects the resulting device performance. Fs-laser doping with a thin film precursor could enable synthesis of a wide range of novel materials, but realizing this potential requires understanding and optimizing the dopant incorporation and surface structuring processes.

Before beginning this exploration of thin film fs-laser doping as a platform for novel materials synthesis, it is necessary to contextualize our research in the larger field of pulsed-laser doping. Pulsed-laser doping has long been considered an attractive route to fabricating n-type emitters in silicon-based photovoltaics due to the ability to implant dopants in high

concentrations, very shallow profiles, and a minimal thermal footprint on the rest of the device [148]. Pulsed lasers in the nanosecond regime and shorter deposit energy at rates that exceed the rate of thermal energy dissipation within the material [45]. This energy accumulation in the absorbing region can heat the material above the melting temperature, resulting in a thin molten layer on the surface typically 50-500 nm thick [54, 149, 150]. Impurity diffusivity in molten silicon is on the order of 10^{-4} cm^2/sec [151], allowing for facile dopant incorporation or redistribution within the molten layer during the brief duration of the melt. The thermal gradient between the molten surface layer and the near-room-temperature substrate results in large heat fluxes away from the molten layer and rapid resolidification. The resolidification front moves through the molten layer at speeds exceeding 10 m/s [82, 152], which is too fast for thermodynamic equilibrium to be reached at the liquid-solid interface [152]. Through a process called solute trapping, impurities in the melt are trapped into the resolidified silicon at concentrations beyond their equilibrium solubility limit [152-154]. The resolidification velocity, which is a result of the thermal gradient present at the solid-liquid interface, will strongly influence the resulting impurity concentration [152], whether the impurities remain in a solid solution or cause cellular breakdown [103], and whether the silicon solidifies as a single crystal in epitaxy with the substrate, forms a polycrystalline layer, or is quenched as an amorphous solid [66].

Pulsed laser melting of silicon was an active area of research in the 1970s and1980s, but this extensive body of this work was carried out using pulsed lasers in the nanosecond regime [155-158]. The absorption process during nanosecond laser irradiation is linear and all resulting processes are thermal in nature, resulting in longer melt durations and deeper melt depths compared fs-laser irradiation, which is complicated by nonlinear absorption and non-thermal energy dissipation (Chapter 2). Central to the controllable synthesis of hyperdoped materials using nanosecond laser irradiation was the development of predictive models that allowed for control of the melt depth, resolidification velocities, and resulting solidification processes through tuning the irradiation conditions [149, 158].

A number of different techniques for impurity introduction have been successfully coupled with nanosecond pulsed laser melting. Ion implantation followed by pulsed laser melting is an attractive method because it allows for careful control of the impurity concentration, which is central to predicting the resolidification dynamics and resulting

microstructure. This approach has been recently used to synthesize single-crystalline silicon supersaturated with chalcogens, which shows a metastable broad-band increase in sub-band gap absorption similar to silicon fs-laser doped with chalcogens (Figure 7.1) [11, 158, 159].

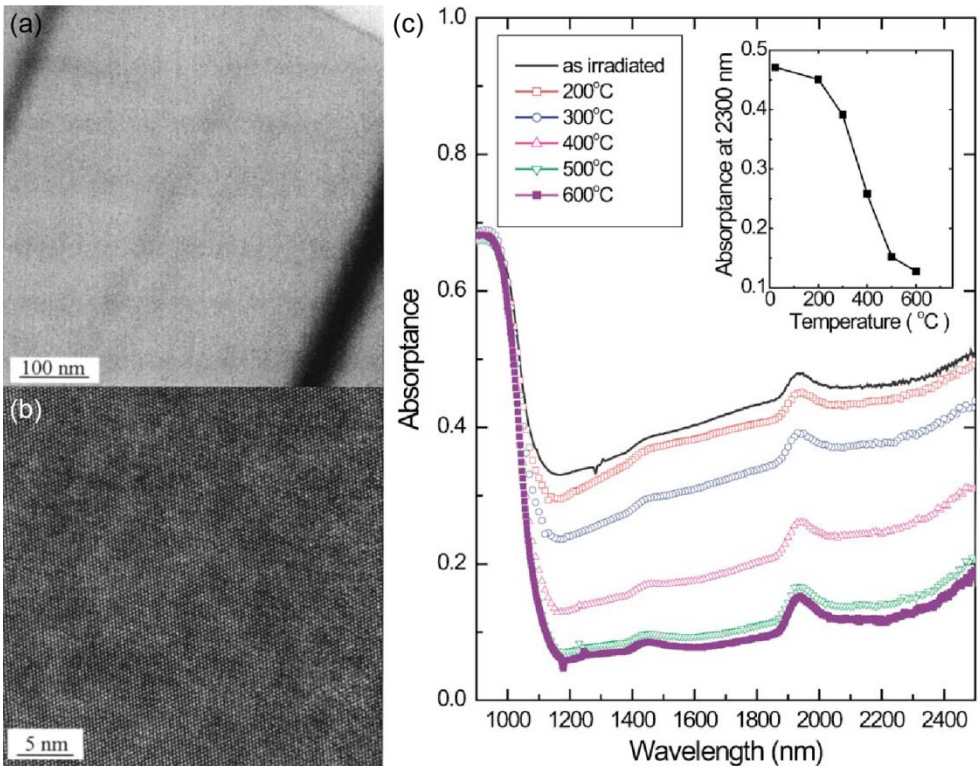

Figure 7.1. (a) Cross-sectional TEM of a n-Si(111) wafer ion implanted with sulfur to a dose of 1×10^{16} ions/cm^2 and irradiated with a single 18 kJ/m^2 fluence laser pulse from an $XeCl^+$ excimer laser pulse ($\lambda = 308$ nm, $\tau_p = 50$ ns). (b) Lattice resolved TEM image of the same sample showing crystallinity. Figure from [159]. (c) Sub-band gap absorptance spectra of sulfur-hyperdoped Si(111) prepared the same way but with a peak fluence of 14 kJ/m^2. Annealing data is for sequential 30 minute anneals at each temperature, conducted on the same sample. Figure from [11].

The deposition of a thin film of material onto the surface is an elegant and low cost approach to introducing dopants during pulsed laser melting [155, 160]. Interestingly, some of the earliest reports of laser doping were done using a "painted-on" thin film following by laser irradiation [161]. During pulsed laser irradiation of the thin film on the surface, the precursor layer evaporates and produces a dense vapor phase with a high concentration of dopant atoms at the interface to the molten silicon. These atoms in the vaporized precursor diffuse through the vapor/liquid interface into the liquid silicon. A portion of the unincorporated but evaporated precursor layer recondenses on the wafer surface and can serve as a dopant source for subsequent laser pulses [148]. Silicon hyperdoped with selenium has been synthesized by depositing a thin

layer of selenium onto the surface prior to nanosecond-duration irradiation [160]. It was shown that a sufficiently thin layer (<5 nm) was necessary to prevent cellular breakdown. The resulting material was single crystalline and exhibited broad sub-band gap absorptance comparable to what was achieved using ion implantation.

Nanosecond laser irradiation in the presence of a gaseous precursor, better known as Gas Immersion Laser Doping (GILD), is a well-established approach to optical hyperdoping. Dopant incorporation can occur either by photolysis or pyrolysis, depending on the transparency of the ambient gas to the incident laser light. If the gas molecules absorb the wavelength of the laser light, then molecules are photodissociated at the surface (photolysis) and dissociated dopant atoms diffuse into the molten surface layer. This is the case for many common dopant precursors, such as AsH_3, BCl_3, B_2H_6, PCl_3, and PH_3 under UV irradiation [162]. If the gas does not absorb the incident laser light then the gas molecules can still be thermally dissociated at the molten silicon-gas interface; such is the case for BF_3 during ArF-laser irradiation [162]. In a hybrid of gas and solid phase doping, it has also been demonstrated that doping can be accomplished through the deposition of an adlayer on the surface by flooding the chamber with a gas and then evacuating the chamber prior to irradiation [156]. The adlayer serves as a finite source of dopants, enabling the formation of flat doping profiles over multiple laser pulses. Adlayer laser doping requires strong adsorption of the parent molecule to the substrate and has been demonstrated with BCl_3, B_2H_6, BF_3, and PCl_3 [156].

In the context of the aforementioned development of optical hyperdoping using ns-laser pulses, several unique aspects of optical hyperdoping with fs-laser irradiation warrant a thorough investigation of this technique as a platform for novel materials synthesis. Femtosecond laser irradiation creates a unique environment arising from energy deposition at the surface that occurs on a time scale 5 orders of magnitude faster than experienced during nanosecond laser irradiation. The ultra-high irradiance can produce electric fields in the absorbing material that are orders of magnitude greater than the binding fields of an electron to an atom in the solid. In addition, the high energy density of the fs-laser pulse and the shallow absorption depths arising from nonlinear absorption can result in surface temperatures on the order of $10^4 – 10^5$ K [51], on timescales such that the surface retains the density of the solid. These extreme conditions at the surface are sufficient to drive the material into highly non-equilibrium states and can result in the synthesis of new materials upon energy dissipation. Silicon hyperdoped with chalcogens using

ion implantation followed by nanosecond pulsed laser melting exhibits sub-band gap absorption similar to silicon hyperdoped with fs-laser irradiation (Figure 7.1) [11, 163], but optoelectronic devices fabricated using fs-laser hyperdoping exhibit a photoresponse at longer wavelengths into the infrared than those fabricated via ns-laser techniques [30, 32]. We also expect that differences in the nature of resolidification, a consequence of the irradiation conditions, will influence the incorporation of the impurities within the lattice and the resulting bulk properties [160]. Finally, the reduction in photon penetration depth arising from nonlinear absorption can enable the processing of thinner layers on the surface [64].

Coupled with the exciting potential of optical hyperdoping using fs-laser irradiation is a unique set of challenges associated with its development. The non-equilibrium conditions described above, arising from non-linear energy absorption, results in more complex heat-flow dynamics following laser irradiation [10, 79]. The lack of a predictive model for fs-laser hyperdoping, as was developed for ns-laser hyperdoping in the 1980s [158], presents a major challenge in using this technique to design new materials [104]. Compared to ns-laser doping, the synthesis of materials using fs-laser doping is still relatively undeveloped; this work presents progress in understanding the interplay between irradiation conditions, laser-material interactions, and relevant doping mechanisms in fs-laser hyperdoping with a thin film dopant precursor.

In the previous chapter we reported that fs-laser doping over many laser pulses above the ablation threshold resulted in a dopant distribution and microstructure that can not be explained by the accepted models for dopant incorporation from a gaseous dopant precursor. In this chapter we explain how dopant incorporation and surface texturing occurs when using a thin-film dopant precursor and demonstrate the ability to influence thin film incorporation mechanisms by varying laser pulse number and laser fluence.

7.2 Effect of thin film on surface texturing and dopant incorporation

7.2.1 Introduction

The previous chapter showed that the thin film dopant precursor affects the surface structuring and dopant incorporation mechanisms. The successful synthesis of hyperdoped materials using fs-laser doping from a thin film dopant precursor therefore requires an in-depth understanding of surface structuring and dopant incorporation processes, which will enable more rational control of the resulting microstructure and dopant distribution. The first step towards enabling rational control over the doping process is to understand the mechanisms behind the formation of the large polycrystalline peaks identified in section 6.2. In this section, we seek to understand the surface structuring and dopant incorporation processes by investigating the evolution of the surface with an increasing number of laser shots. This systematic investigation reveals that the surface texturing process is directly coupled to the localized crystallization of selenium-rich amorphous material on the surface, and this understanding enables more informed identification of optimal irradiation conditions for thin-film laser doping (section 7.3).

7.2.2 Experimental

Samples were irradiated under conditions similar to those presented in section 7.2.2. To improve our understanding of the effect of laser irradiation conditions on the resulting microstructure, stationary spots were used rather than rastered surfaces. A Ti:sapphire laser (λ = 800 nm, τ = 80 fs, f = 100 Hz) was used to irradiate silicon under 500 Torr N_2 with 1, 2, 5, 10, 15, 20, 30, 50, and 100 stationary pulses, each with a peak fluence of 4 kJ/m^2. Characterization of the surface morphology was done with a Zeiss Field Ultra55 Field Emission Scanning Electron Microscope (FESEM), operating at 5 kV, with the InLens detector. TEM samples were prepared from specific regions within each stationary laser pulse using the lift-out method on a FEI Helios 600 dual-beam FIB. BF-TEM, DF-STEM, and EDX were carried out on a JEOL 2010F TEM operated at 200 kV.

To understand the evolution of the surface morphology, profilometry was performed on each of the 9 stationary laser spots using a Veeco Dektak 6M Profilometer. The profilometry line scans were performed across the entire laser-irradiated spot, such that height changes in the center of the laser spot could be quantified with respect to the initial plane of the unirradiated silicon wafer. The width of the profilometer tip (5 μm) prevents detecting the valleys between

the peaks, but allows for extraction of the average peak height (Figure 7.2(a)). To obtain the height of the spikes at the center of the laser spot, we average the height measurement across the center 30 μm of the laser modified spot (Figure 7.2(b)).

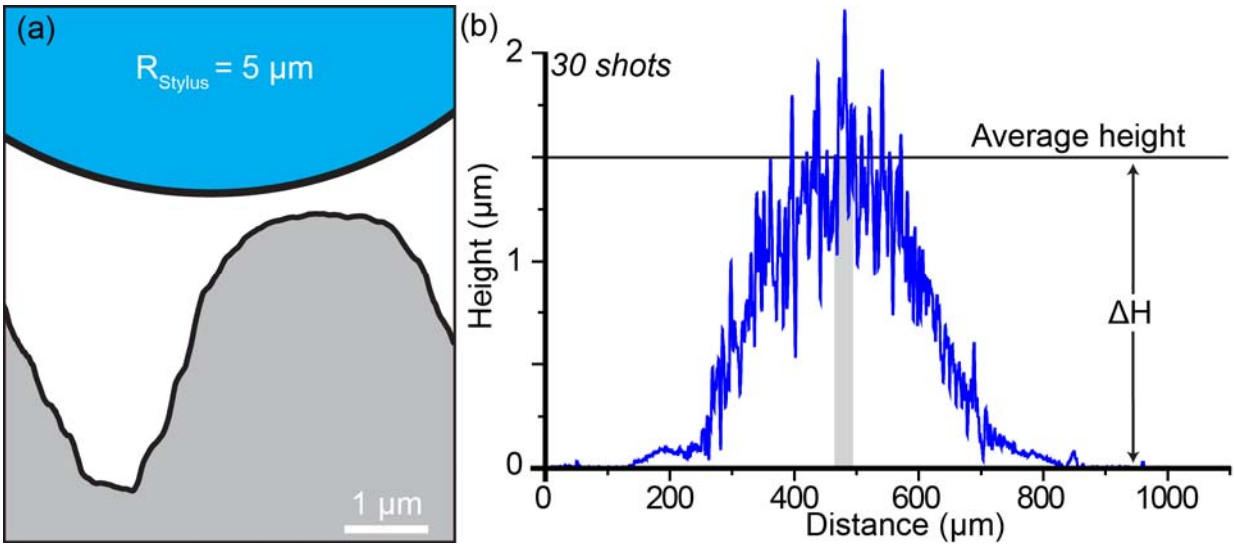

Figure 7.2. (a) Schematic showing relative size of laser-structured surface and profilometer stylus with 5 μm radius of curvature. (b) Example profilometry line scan across a stationary laser spot irradiated with 30 pulses. The average height in the center 30 μm (shaded) is measured with respect to the height of the unirradiated silicon wafer and used to quantify trends in the height of the surface (ΔH) with shot number.

7.2.3 Results and Discussion

7.2.3.1 Surface morphology

SEM images of the center of the laser-irradiated spot document the evolution of surface morphology with increasing laser irradiation, shown in Figure 7.3(a). In the initial pulses (1-2), the continuity of the selenium thin film is disrupted, likely through a combination of evaporation and coalescence. With continued irradiation (2-5 pulses) the silicon surface roughens via melting and resolidification at the surface. Finally, by 10 pulses peaks form from the roughened surface, and continue to grow in size with increasing irradiation (20-100 pulses).

Whether peaks grow through material addition to the peaks or by material removal from between the peaks depends on the irradiation conditions (see section 2.2.2). Profilometry across the laser spots (Figure 7.3(b)) show that there is upward growth at a rate of 75 nm/pulse between 5-30 laser pulses; this finding is in contrast to what is understood about fs-laser doping with SF_6,

in which peak growth is predominantly driven by material removal [79]. From 30-100 pulses, the absolute peak height begins to decrease with increasing laser irradiation at an average rate of 4 nm/pulse. The peak amplitude of the surface structure continues to grow, as seen in SEM micrographs (Figure 7.3(a)) indicating a transition into peak growth through material ablation.

In the following sections, we will address the dopant incorporation process and the role of the thin film dopant precursor on surface structuring in each of the stages discussed above: thin film removal and coalescence (1-2 pulses), surface roughing (5 pulses), peak formation and growth (10-20 pulses), and ablation-driven peak growth (30-100 pulses).

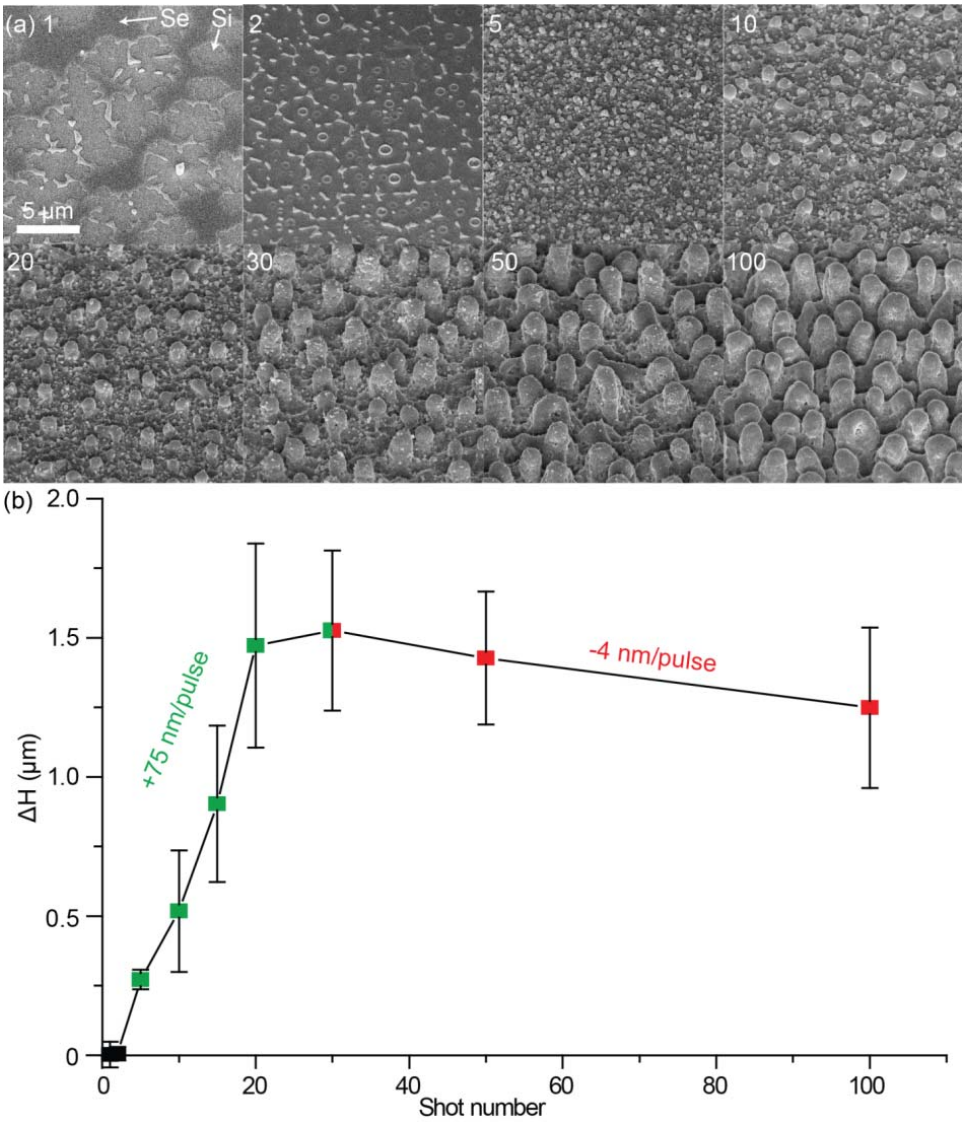

Figure 7.3. (a) SEM images of the evolving surface morphology taken at a 45° angle. The numbers in the upper left indicate the number of stationary laser shots. (b) Average height of the features with respect to the native silicon substrate (ΔH), measured using a profilometer line scan across the entire laser spot.

7.2.3.2 Thin Film Removal and Coalescence (1-2 pulses)

It is important to understand the dopant incorporation during the initial laser pulses, as this will influence the processes that occur during all subsequent irradiation. SEM images (Figure 7.3(a)) show that a single laser pulse at 4 kJ/m^2 results in the removal of much of the film and does not produce noticeable surface roughness. A second laser pulse removes more of the selenium thin film and craters are visible in the silicon wafer, suggesting silicon melting and localized ablation. In order to understand the extent to which the silicon is hyperdoped following a single pulse, we investigate the microstructure of the resulting samples using TEM (Figure 7.4). After a single laser pulse at 4 kJ/m^2 the native oxide layer (3 nm) stays intact. Beneath the SiO_2 layer there is 10 nm of amorphous silicon, resulting from the melting and ultra-fast resolidification of silicon. The melting temperature of the native oxide (1713°C) is higher than the silicon substrate (1410°C) and thus the oxide remains on the surface during the melting process, preventing selenium incorporation. A 1 nm layer of increased contrast on the surface appears to be selenium, though the layer is too thin to conclusively resolve by EDX. Dewetting of the film resulted in a selenium droplet that is ~100 nm high, slightly thicker than the original thin film (~75 nm) (Figure 7.4(a)).

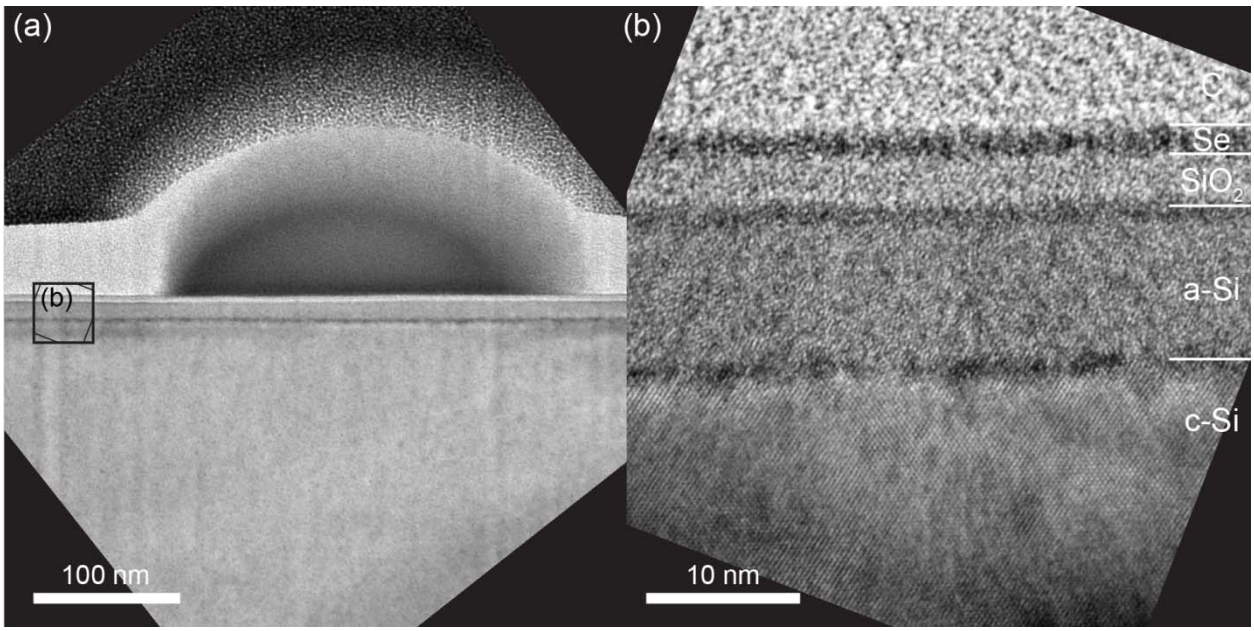

Figure 7.4. (a) Bright-field TEM image of silicon surface after a single laser pulse, including a selenium droplet on the surface. (b) High-magnification TEM of the modified silicon surface, from the region indicated in (a).

Though fs-laser irradiation of selenium has not been rigorously investigated, we can contextualize the behavior of the selenium thin film by considering the difference in material properties between selenium, silicon and silicon dioxide. Selenium melts at a much lower temperature (217°C) than silicon (1410°C) or silicon dioxide (1713°C), which implies that the melting and ablation thresholds during fs-laser irradiation will also be much lower, as confirmed by these investigations. In addition to the ablation of selenium from the surface, the evaporation temperature of selenium is only 685°C and thus evaporation will also contribute to selenium removal following initial fs-laser irradiation.

7.2.3.3 Surface roughening (5 pulses)

With additional irradiation, there is considerable modification to the silicon surface, as shown in the SEM in Figure 7.3(a). TEM investigations into the microstructure of the surface after 5 shots reveal both amorphous and crystalline features contributing to the surface roughness (Figure 7.5). A 40-50 nm layer of amorphous silicon covers the entire surface and there are also larger mounds (200-400 nm) of amorphous silicon, which likely form through the coalescence of molten silicon. EDX of the amorphous silicon shows that there is 1-2% selenium and 1-2% oxygen in the amorphous silicon, suggesting that both selenium and oxygen mix with molten silicon before resolidification. The amount of selenium remaining on the surface is significantly less than originally deposited, as might be expected based on our understanding of selenium ablation/evaporation during the first several laser pulses (the 30 nm film of ~1% selenium we observe is ~0.4% of the originally deposited 75 nm pure Se). The levels of oxygen detected are likely introduced by the native silicon oxide observed in the previous section. It should be noted that selenium could not be detected in the crystalline-silicon substrate at levels above the resolution limit of EDX (>0.1%), suggesting that there was no melting and resolidification beyond the amorphous surface layer. In addition, there are no grain boundaries or dislocations in the substrate, which would also indicate melting and crystalline resolidification.

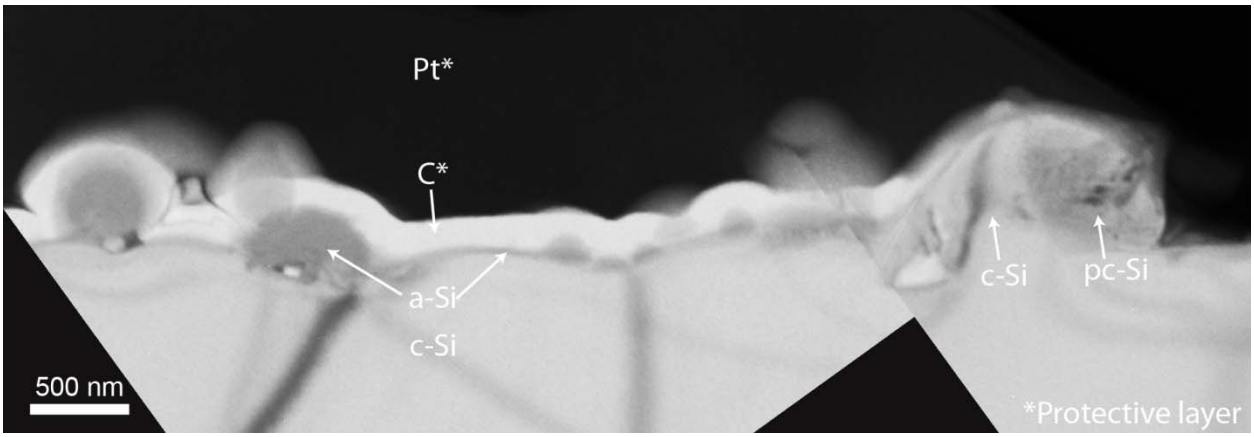

Figure 7.5. BF-TEM micrograph of the roughened surface following 5 fs-laser pulses at 4 kJ/m^2. Platinum (Pt*) and carbon (C*) layers were deposited during FIB sample preparation.

We also observe in the TEM micrographs the formation of polycrystalline mounds, visible in Figure 7.5 and presented with quantified selenium concentration in Figure 7.6. These formations are 200-300 nm high, on the order of the height increase detected using profilometry (272 ± 38 nm). EDX shows that the recrystallized regions are hyperdoped and contain 1-2% selenium. Selenium is also incorporated into the single-crystalline region of the mounds, indicating that in some regions there was melting following by epitaxial recrystallization.

We can gain insights into the processes driving recrystallization by looking at the grain structure in the polycrystalline regions. In Figure 7.6(a) it can be seen that the grain size within the polycrystalline region increases from the interface with the crystalline substrate toward the surface. Such microstructure is indicative of explosive recrystallization [157]. Explosive recrystallization occurs following the melting of amorphous silicon, because the melting point of amorphous silicon is 300-450°C lower than crystalline silicon and the latent heat of melting amorphous silicon is 20% lower than crystalline silicon [132]. Therefore a highly undercooled liquid forms when the laser energy is sufficient to heat the amorphous silicon above its melting temperature. If kinetically allowed, small grains (<10 nm) form in the liquid and the grain size increases as the crystallization front sweeps to the surface. It has also been reported that explosive recrystallization can occur in parallel with random nucleation and growth, producing equiaxed nanoscale grains [157], which appears to have occurred on the left portion of the mound in Figure 7.6(b).

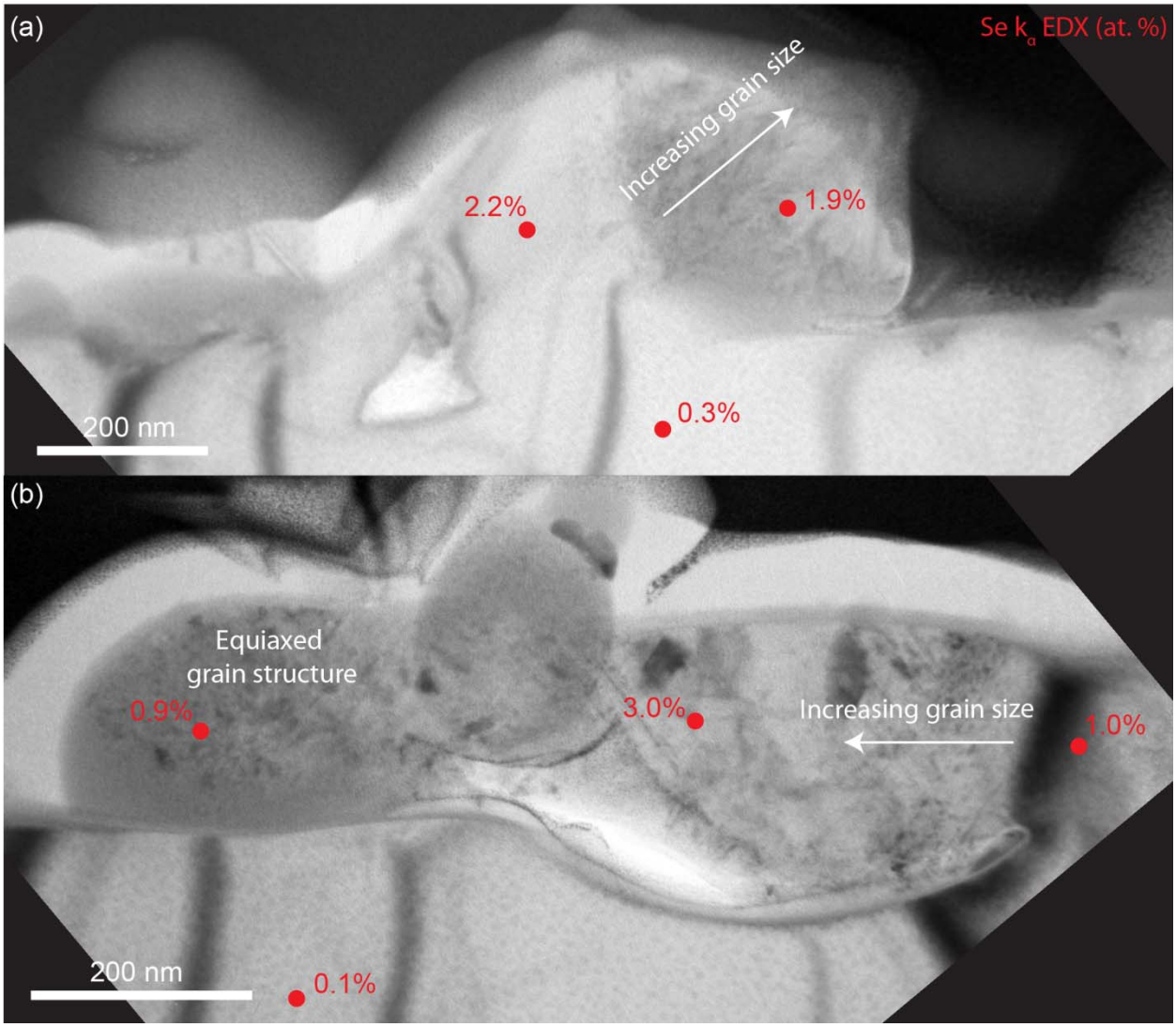

Figure 7.6. BF-TEM images of representative crystallized regions following 5 laser pulses at 4 kJ/m^2. The selenium composition (at. %) was determined using EDX (red spots).

Femtosecond laser irradiation produces steeper temperature gradients than nanosecond laser irradiation and often results in resolidification velocities that exceed the threshold for the crystallization of silicon (15 m/s) [66]. Silicon has been reported to recrystallize on planar surfaces following fs-laser irradiation at sufficiently high fluences (5.8 kJ/m^2 single shot threshold), because the excess energy from the laser heats the silicon substrate and reduces the thermal gradient at the surface [59]. We are irradiating silicon at fluences just around the ablation threshold (3-4 kJ/m^2), however, and observe fs-laser induced recrystallization only in regions protruding from the surface (Figure 7.5). In order to understand the effect of surface morphology

on crystallization, it is important to consider its influence on both the local fluence deposition and on subsequent heat dissipation.

In these investigations the surface is irradiated with fs-laser irradiation normal to the surface of the silicon wafer with a fluence of 4 kJ/m^2. Surfaces that are not normal to the direction of irradiation receive a lower effective fluence due to the increasing surface area. The local effective fluence in a region that is at the angle θ° from the surface normal scales with cos(θ), approaching 0 kJ/m^2 as θ approaches 90°. As such, surfaces on a protruding feature receive a range of fluences lower than the peak fluence achieved at normal incidence. The physical response of the material is strongly dependent on incident fluence: at θ = 40° the fluence is reduced to 3 kJ/m^2, roughly the single shot ablation threshold, and at θ = 60° fluence is reduced to below the single shot melting threshold (~2 kJ/m^2). In the lowest fluence range, there is no melting and the sample is heated via carrier relaxation. From this simple model, it is clear that the overall ablation of protruding material can be reduced and lower-fluence reactions may be favored despite the normal fluence being above the ablation threshold. Note that these laser modification thresholds are also a function of pulse number (see section 2.2.1) and that we have ignored contributions from reflection off adjacent roughened surfaces. Reflection from adjacent peaks becomes particularly relevant in the discussion of ablation-driven peak growth (section 7.2.3.5).

The previous fundamental work done on heat dissipation has been on planar surfaces in which the bulk silicon substrate acts as an infinite heat sink for the energy deposited on the surface [158]. The situation is subtly different, however, within a surface protrusion. The core of the peak is not necessarily an *infinite* heat sink for the surrounding surfaces and, following this, the thermal gradients experienced by molten silicon protruding from the surface will be less extreme than what is experienced in a film on a planar surface. Supporting the relationship between morphology and crystallization, Boroweicz et al. investigated the microstructure of a silicon surface following a single laser pulse and observed crystallization only in the protruding ring around the laser spot [94].

Though selenium is present only in small concentrations, its presence will influence the surface texturing process through both thermodynamic and kinetic effects. With respect to thermodynamics, the presence of impurities in silicon will affect the melting temperature. The selenium-silicon phase diagram is shown in Figure 7.7 and can be used to estimate the extent to

which mixing silicon and selenium will decrease the melting temperature of the selenium-silicon alloy. The presence of 1% selenium decreases the melting temperature of silicon by several degrees, though extremely high concentrations of selenium (>50%) could drastically reduce the melting temperature of silicon. The decrease in melting temperature resulting from the presence of selenium would slightly increase both the melt depth and the melt duration during fs-laser irradiation [164], enhancing the roughening on the surface.

The presence of selenium and oxygen will also influence the kinetics of recrystallization. The presence of 1% oxygen in amorphous silicon, which we observe in the amorphous silicon layer, increases the nucleation rate by a factor of 10 [127]. Group III and group V impurities, however, decrease the rate of nucleation when present at atomic concentrations of 0.1-1% [127]. Much less is understood about the effect of the chalcogens (group VI) on crystallization, but we expect chalcogen concentrations around ~1% (combined with oxygen concentrations around 1%) will significantly affect the crystallization kinetics.

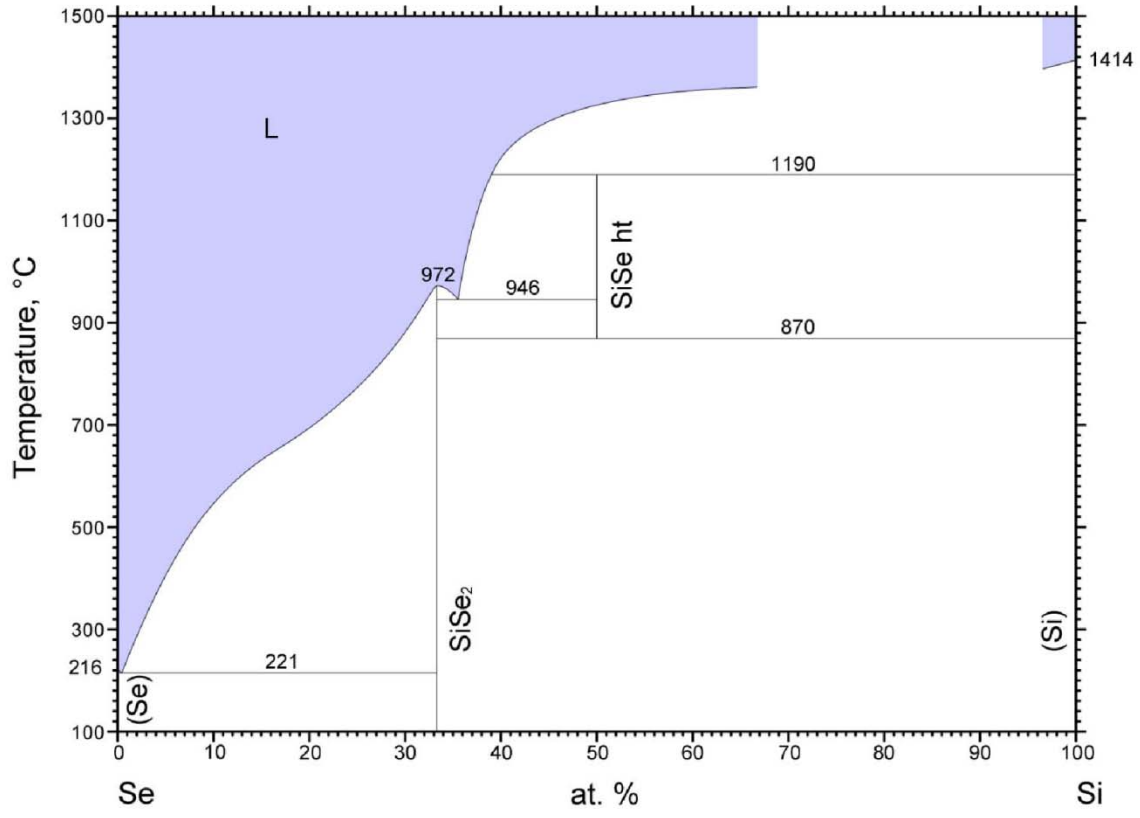

Figure 7.7. Binary phase diagram of selenium-silicon [146].

In this section it was reported that after 5 laser pulses at 4 kJ/m^2 the crystallization of selenium-hyperdoped silicon occurs only in features protruding from the surface. Based on the above discussion, it is clear that the crystallization of hyperdoped material is a result of the complex relationship between surface morphology, laser-material interactions, heat dissipation, and the thermodynamic and kinetic effects of the thin film. A quantitative theoretical assessment of the relationship between surface morphology and crystallization would provide a valuable framework for further understanding morphology-driven crystallization.

7.2.3.4 Peak Formation and Growth (10-30 pulses)

Profilometry (Figure 7.3(b)) showed that between 5 and 30 pulses the peak height is growing at approximately 75 nm per pulse. After 10 pulses the surface peaks have grown visibly above the surrounding roughened surface (Figure 7.3(a)), reaching 517 ± 218 nm above the native silicon surface, and the peaks grow to an average height of 1472 ± 367 nm over the 10 subsequent laser pulses. TEM micrographs of the surfaces (Figure 7.8) show that the growing peaks are polycrystalline and that the surrounding surface is covered in an amorphous layer, consistent with the previous observations that the surface morphology is related to the crystallization process (section 7.2.3.3). Interestingly, the selenium concentration is highest (1-2%) at the base of the peaks (Figure 7.8(a,c)).

In the previous section we discussed the formation of crystalline protrusions by identifying a grain structure representative of explosive crystallization. Similarly, we can gain insight into the growth of peaks with continued irradiation by understanding the grain structure and impurity distribution. Both the 10 shot and 20 shot peaks exhibit larger grains towards the center and top of the peaks, with ~100 nm columnar grains at the bottom edges of the peaks where the pc-Si and a-Si meet. For clarity, a schematic of a peak after 20 pulses is shown in Figure 7.9. The columnar grain structure at the base of the peaks is characteristic of solid phase epitaxy [127], a solid-phase transition of amorphous silicon into crystalline silicon. Voids, which are often observed in the body of the polycrystalline peaks, seem to arise through inhomogeneous crystallization and growth at the amorphous/crystalline interface, as depicted clearly at the base of the left 20 shot peak in Figure 7.9.

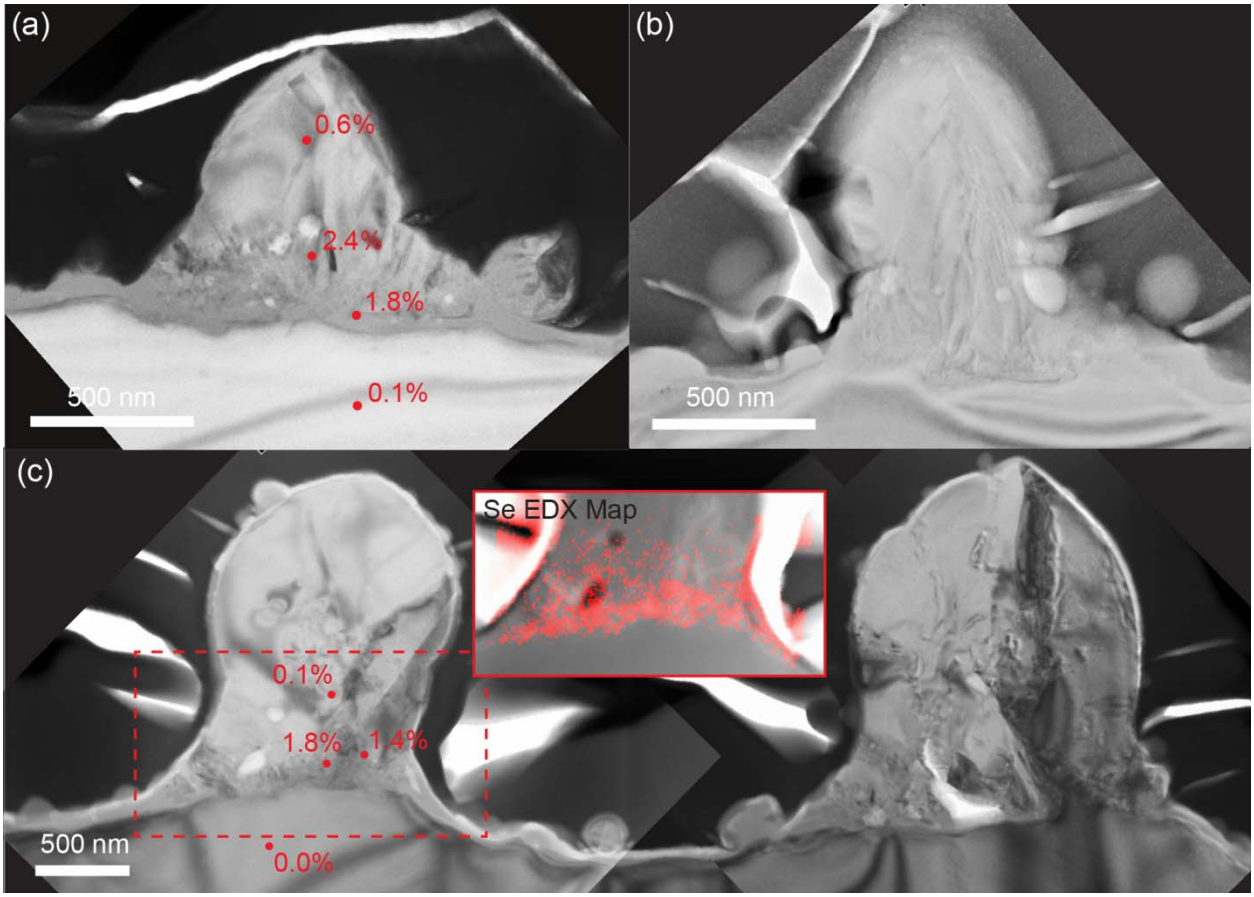

Figure 7.8. BF-TEM images of polycrystalline peaks on the surface 10 pulses (a,b) and 20 pulses (c) at 4 kJ/m^2. EDX point scans in (a) and (c) show the selenium composition in different regions of the surface. Inset in (c) is an EDX map of the selenium signal at the base of the peak (red dashed box).

Consistent with the observed grain structure, the temperatures required to drive solid-phase crystallization of a-Si are within the temperature range that we expect to be achieved beneath the surface during fs-laser irradiation. Solid phase epitaxy can be induced by heating of amorphous silicon to temperatures as low as 500°C [127], whereas crystallization mechanisms that involve melting of amorphous silicon (random nucleation and growth, explosive crystallization, etc.) require temperatures greater than 1200°C. Fs-laser irradiation of a silicon thin film at 9 kJ/m^2 was shown to achieve temperatures over 500°C at distances 3 μm away from the laser spot; therefore seems feasible that temperatures ~500°C will be reached in some regions beneath the surface [165].

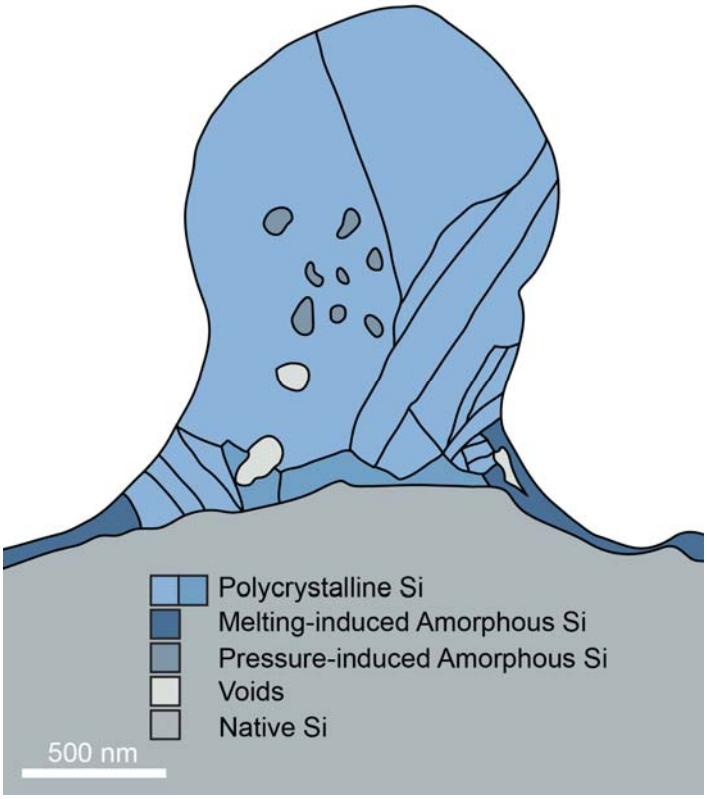

Figure 7.9. Schematic of the microstructure of the 20-shot peak shown in Fig. 6.7(c). The columnar grain structure at the base of the peaks is indicative of solid phase epitaxy. The darker blue color for polycrystalline silicon indicates regions in which there was too much contrast to easily resolve the grain structure. The formation of pressure-induced amorphous silicon is discussed in Chapters 4 and 5.

As was discussed for liquid-phase crystallization in the previous section, selenium and oxygen impurities in the amorphous silicon will influence the kinetics of solid phase epitaxy. Non-doping impurities such as oxygen, nitrogen, and carbon significantly reduce the solid phase epitaxy rate [127]. Concentrations of electrically active group III and V dopants up to 1% can increase the rate of solid phase epitaxy by an order of magnitude [127]. The effect of selenium, a group VI dopant, might be expected to increase the kinetics similar to the group V dopants, but as selenium is an unorthodox dopant for silicon, this effect has not been investigated.

The increasing grain size in the center of the peaks suggests that coarsening occurs within the crystalline region during continued fs-laser irradiation. In the 20 shot sample, the majority of the peak is composed of only 2 grains despite the population of smaller grains at the base (Figure 7.9). In studies of silicon crystal growth with annealing, substantial grain growth occurs at temperatures around 800-900°C [166]. Though fs-laser irradiation is known for its minimal

thermal imprint, investigations into the heat affected zone following fs-laser irradiation have shown that it can drive grain growth in metals microns away from the laser-irradiated region [133, 165, 167]. The observed crystallization and evolution of the silicon microstructure suggests that temperatures from 500-1000°C can be achieved within the peak during fs-laser irradiation.

The concentrations of selenium are highest towards the bottom of the peak, as shown by EDX in Figure 7.8, indicating that substantial dopant segregation occurs during crystallization and coarsening. It should be noted that solid phase epitaxy does not preclude hyperdoping; it is well understood that impurities at concentrations well in excess of solid solubility limits can be incorporated into the crystalline phase during solid phase epitaxy, despite the lack of an intermediate liquid phase [127].

Investigations into the microstructure and dopant distribution have shown that the formation of selenium-hyperdoped crystalline silicon is coupled with protruding surface features from the earliest stages of laser irradiation, resulting in the discontinuous dopant distribution initially reported in section 6.2. The large size of the surface peaks that form during thin-film fs-laser irradiation arises through a unique regime of crystallization-driven peak growth.

7.2.3.5 Ablation driven growth (30-100 pulses)

With continued irradiation (30-100 pulses) the surface peaks continue to grow in amplitude (Figure 7.3(a)) while the absolute peak height begins to gradually decrease (Figure 7.3(b)). This is evidence that peak "growth" is now occurring predominantly through material removal. This process is well understood and is the dominant form of surface structuring during fs-laser doping from SF_6 gas [79]: laser light is preferentially reflected into the valleys between the peaks, creating localized regions of increased fluence and heightened rates of material ablation. The focusing effect increases as the peaks grow larger, increasing the rate of material removal from between the peaks and the overall peak amplitude.

Investigations into the microstructure support this transition into ablation driven growth (Figure 7.10). The valleys between the peaks are significantly recessed from the polycrystalline-crystalline interface. The microstructure reveals that the crystallization of amorphous silicon continues at the base of the peaks (Figure 7.10, white circles); regions of columnar grains extend laterally and partially into the valleys. Though upwards growth of the peaks has ceased, it appears to be a consequence of the removal of crystalline silicon between the peaks allowing

lateral solid-phase epitaxy. The layer of amorphous silicon in the valleys between the peaks varies in thickness from 25-150 nm due to the local increase in fluence.

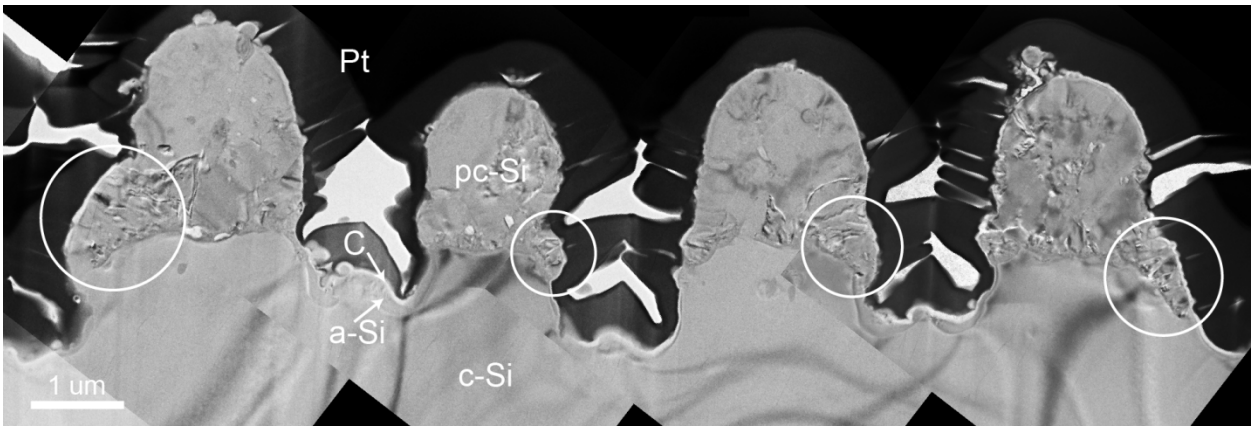

Figure 7.10. BF-TEM of the surface structure following 50 pulses at a fluence of 4 kJ/m^2. White circles highlight the columnar grain structure that is evidence of continued crystallization-driven growth during fs-laser irradiation.

7.2.4 Conclusions

In this study, we set out to understand the formation of the large, hyperdoped, polycrystalline surface peaks reported in section 6.2. By investigating the evolution of the surface with an increasing number of laser pulses, we identified the dominant mechanisms behind dopant incorporation and surface structuring during each stage of laser irradiation. During the first laser pulse much of the selenium thin film is evaporated/ablated and the presence of the native oxide layer prevents dopant incorporation from the thin film. With continued irradiation (5 pulses) the surface roughens and is covered predominantly in a selenium and oxygen-rich amorphous silicon layer. Explosive recrystallization occurs only within protruding bumps on the surface, indicating that the relationship between crystallization and surface morphology begins very early in the irradiation process. The reduced effective fluence and delayed heat dissipation within surface protrusions are identified as potential factors enabling recrystallization only within protruding surfaces. Rapid peak growth is shown to be driven by the solid-phase crystallization of amorphous silicon with continued irradiation. Grain coarsening is observed within the peak, suggesting that the core of the peaks are reaching temperatures 500-1000°C following fs-laser irradiation. As the peaks grow by crystallization, the self-focusing effect also increases, eventually resulting in substantial material removal from between the peaks.

Investigations into the microstructure reveal that the crystallization of amorphous silicon continues at the base of the peaks, suggesting that the material removal allows for lateral crystallization and thus the crystallization of amorphous silicon ceases to drive the peak height upwards. Most importantly, this investigation revealed that during irradiation under these conditions there is a strong relationship between surface morphology and crystallization from the earliest stages of irradiation. Investigating the peak formation process elucidates the significant role that the evolving surface morphology has on laser-material interactions and the resulting formation of crystalline hyperdoped material. With this understanding of the dopant incorporation and recrystallization-driven surface structuring processes during thin-film fs-laser doping, in the next section we aim to identify irradiation conditions that are more favorable the uniform synthesis of hyperdoped silicon.

7.3 Optimizing parameter space for thin-film laser doping

7.3.1 Introduction

Investigations into peak formation and growth during selenium thin-film fs-laser doping have shown that the dopant incorporation, surface structuring, and crystallization of hyperdoped material are closely related during irradiation with 4 kJ/m^2 fluence. In this section, we investigate the surface structuring and dopant incorporation as a function of laser fluence with the ultimate goal of identifying irradiation conditions conducive to the synthesis of a continuous, crystalline hyperdoped surface layer.

7.3.2 Experimental

We use the same stationary-shot laser spots described in section 6.2.2, and access a range of fluences by characterizing regions away from the center of the spot irradiated with a Gaussian laser beam. The laser beam profile was determined using a CCD camera and has a full-width half-max of 343 μm in the direction of beam polarization and 436 μm in the direction perpendicular to it. Through measuring the distance from the center of each point, we can determine the effective fluence at that point and understand the effect of fluence on the surface morphology and dopant incorporation. TEM samples were prepared from specific regions within each stationary laser pulse using the lift-out method on a FEI Helios 600 dual-beam FIB. BF-TEM, DF-STEM, and EDX were carried out on a JEOL 2010F TEM operated at 200 kV.

7.3.3 Results and Discussion

7.3.3.1 Surface morphology

Figure 7.11 shows SEM images of the surface morphology across a range of shot numbers and fluences. The stages of surface structuring and dopant incorporation identified in section 7.2 (thin film removal, surface roughening, peak formation and growth) occur down to fluences of roughly 2 kJ/m^2. Because peak formation during thin-film fs-laser doping is driven by melting and recrystallization, it is interesting that peak growth requires fluences roughly above the single-shot melting threshold of silicon (2 kJ/m^2).

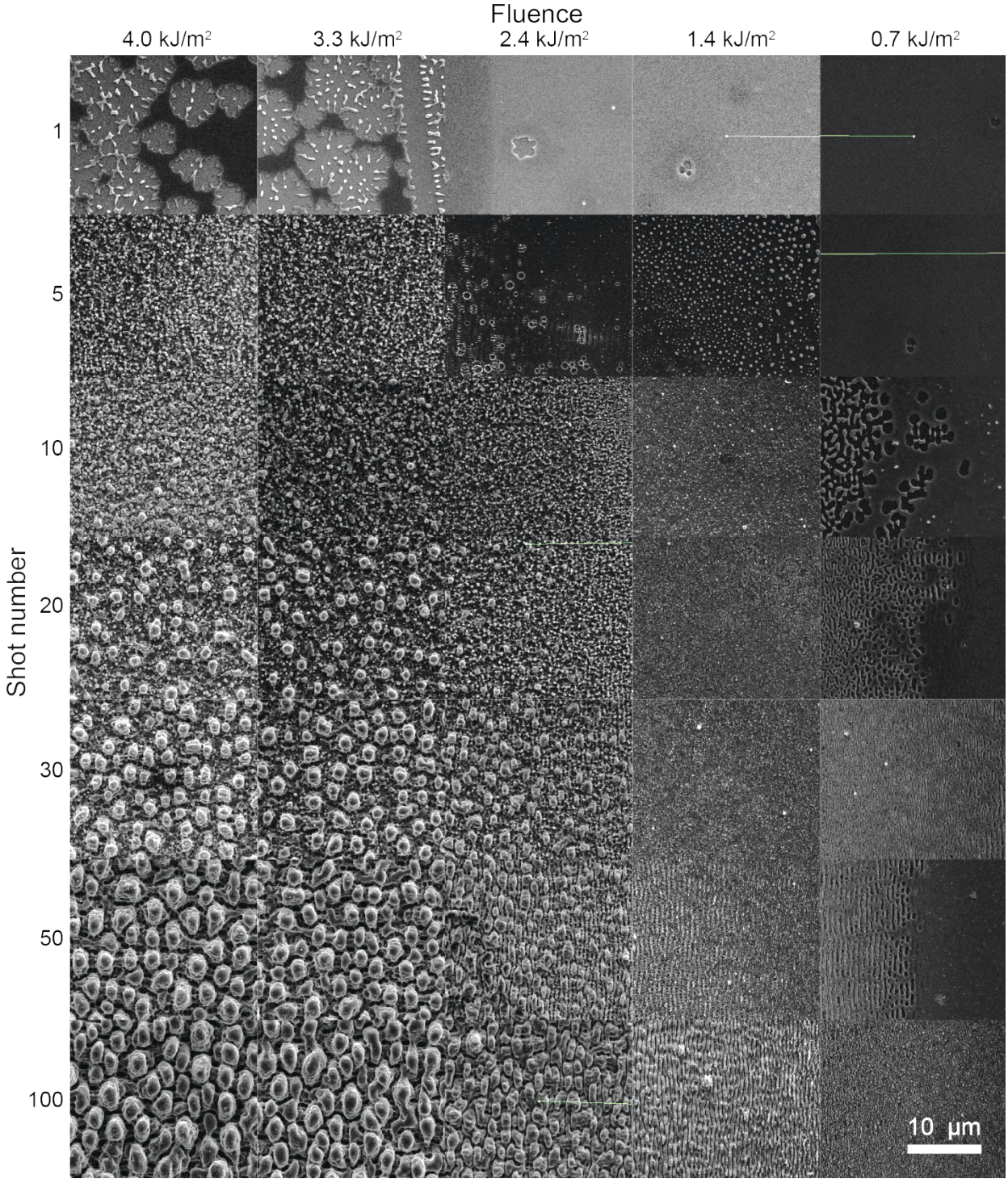

Figure 7.11. SEM images of the evolving surface morphology as a function of fs-laser pulse number (1-100) and laser fluence (0.7 – 4 kJ/m^2).

At lower fluences (<2 kJ/m^2) the peak formation does not occur and instead ripples form after many laser pulses. These ripples, known as laser-induced periodic surface structures (LIPSS), are perpendicular to the polarization of the electric field and have a periodicity of around 500-600 nm, slightly less than the wavelength of the laser (see section 2.2.2). Such *low-frequency LIPSS* [83] arise through a well-known mechanism of scattering/diffraction and subsequent local-field enhancement via interference at the surface [168, 169]. Though there is a rich history of studying the formation of these surface structures on a variety of materials, dopant incorporation from a thin film during LIPSS formation has not been previously investigated and may offer a route to achieving a more continue dopant distribution. In order to understand the thin-film dopant incorporation process at fluences below the single-shot melting threshold of silicon, we investigate the microstructure and dopant distribution following low-fluence irradiation (~1.2-1.6 kJ/m^2).

7.3.3.2 Surface structure after 10 laser pulses

A low magnification SEM image of the fs-laser spot after 10 shots is shown in Fig. Figure 7.12(a) and the low-fluence region being investigated is highlighted in Figure 7.12(b). This region was selected because it corresponds to the fluence range in which LIPSS will eventually form with increasing irradiation. As indicated in Figure 7.12(b), the region characterized is estimated to span from 1.27 – 1.68 kJ/m^2, though uncertainty in both the fluence and the beam profile limits the resolution with which we can discuss the fluence that each region received. For the sake of discussion we will still refer to values out to 0.01 kJ/m^2 resolution, but acknowledge that these are best treated as relative estimates.

Figure 7.12(c) shows the microstructure of the surface after irradiation with 10 pulses of 1.66 kJ/m^2 fluence, and most of the selenium thin film has been removed. There is an amorphous layer ~10 nm thick across the surface. Quantifying EDX in this region is difficult because the length scale of the features being probed is less than the spatial resolution of EDX. Nevertheless, EDX signal shows that the surface layer is predominantly silicon but also contains selenium and oxygen. Quantification suggests selenium concentrations similar to what was observed in the amorphous surface layer after 5 pulses at 4 kJ/m^2 (Figure 7.5).

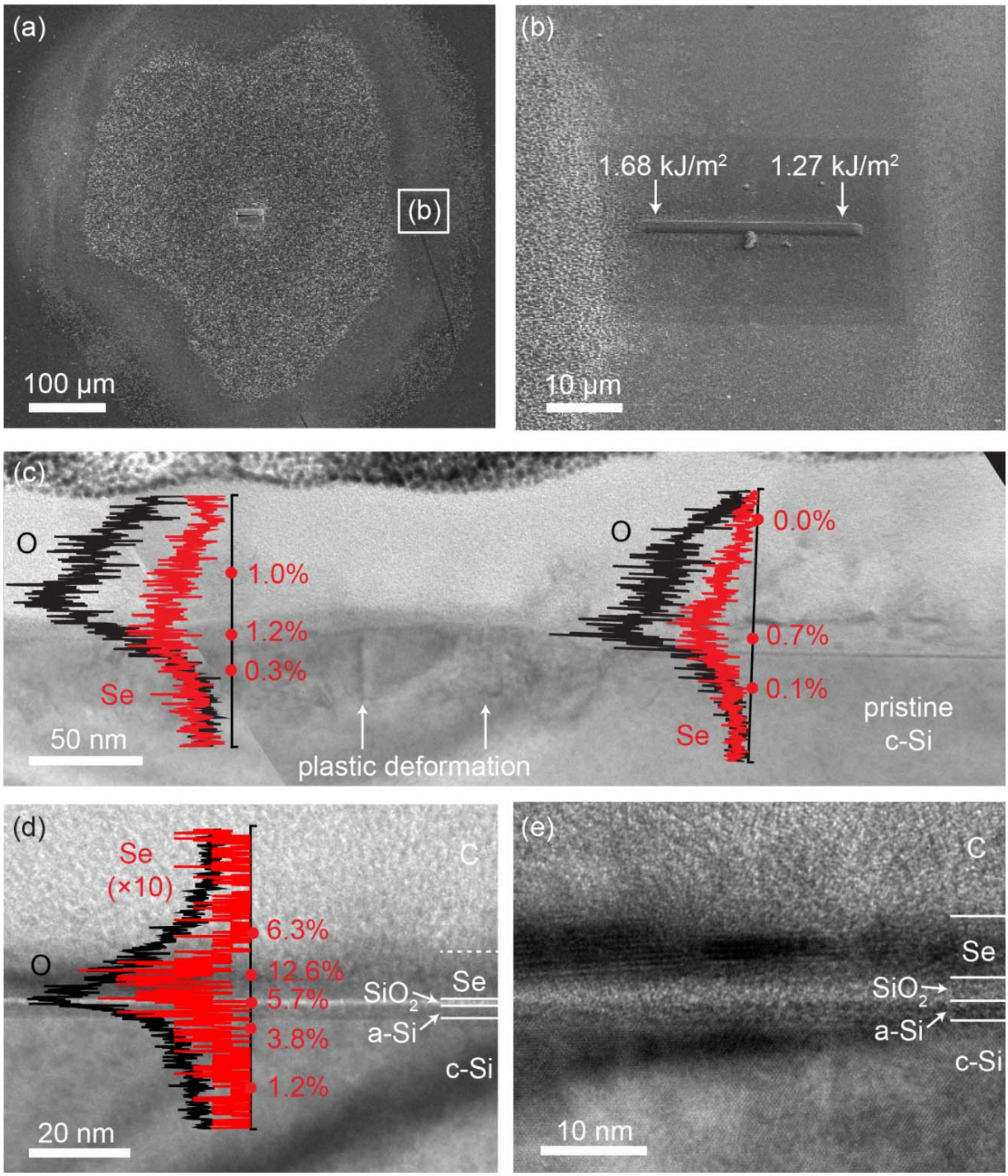

Figure 7.12. (a) SEM image of laser spot after 10 pulses at a peak fluence of 4 kJ/m^2. The white box indicates the low-fluence region investigated, shown in (b). (c) Cross-sectional BF-TEM image of a region irradiated with ~1.66 kJ/m^2 fluence. EDX line scans show oxygen and selenium distribution, and point scans quantify the amount of selenium present. (d) BF-TEM image of a region irradiated with ~1.27 kJ/m^2 fluence with EDX line scans and point scans quantifying the amount of selenium present. (e) High-magnification image of the region presented in (d).

Beneath the amorphous surface layer there are regions of pristine silicon (Figure 7.12(c), right) and areas with defects associated with plastic deformation (Figure 7.12(c), left). We were unable to detect selenium in the silicon wafer in either region within the chemical limit of EDX (~0.1 at. %). The complete removal of the selenium film after 10 pulses at 1.66 kJ/m^2 suggests that continued pulsed-laser irradiation at this fluence will not lead to the successful hyperdoping of silicon, though lower fluences could favor incorporation of selenium film rather than removal.

Figure 7.12(d-e) shows cross-sectional BF-TEM of the surface after irradiation with 10 fs-laser pulses in the low-fluence regime (1.27 kJ/m^2) and selenium film roughly 10 nm thick remains on the surface. Though EDX quantification suggests that the thin film is only ~12% (Figure 7.12(d)), the relatively low amount of selenium in the quantification is likely a consequence of the surrounding material and the limited spatial resolution of EDX. Similar to what was observed after a single laser pulse at 4 kJ/m^2 (Figure 7.4), there is a 1-2 nm thick layer of SiO_2 beneath the selenium film. There appears to be 2-3 nm layer of amorphous silicon beneath the native oxide layer Figure 7.12(e), much shallower than the 10 nm of amorphous silicon observed after 1 laser pulse at 4 kJ/m^2. The presence of the SiO_2 layer suggests that no selenium has been incorporated into the silicon after 10 pulses at 1.27 kJ/m^2. The presence of selenium at the surface, however, means the possibility of selenium hyperdoping may be possible with continued irradiation.

7.3.3.3 100 shots

Irradiation at low fluences (1.27 – 1.66 kJ/m^2) did not lead to significant hyperdoping after 10 pulses, but ~10 nm of selenium film was still present on the surface at fluences around 1.3-1.4 kJ/m^2 (Figure 7.12). It is in this same fluence range that we observe LIPSS formation with continued irradiation. To investigate dopant incorporation during LIPSS formation, a TEM sample was prepared from the outer rim of the 100 pulse laser spot, as shown in Figure 7.13. This sample covers fluences from approximately1.21 kJ/m^2 to 1.45 kJ/m^2.

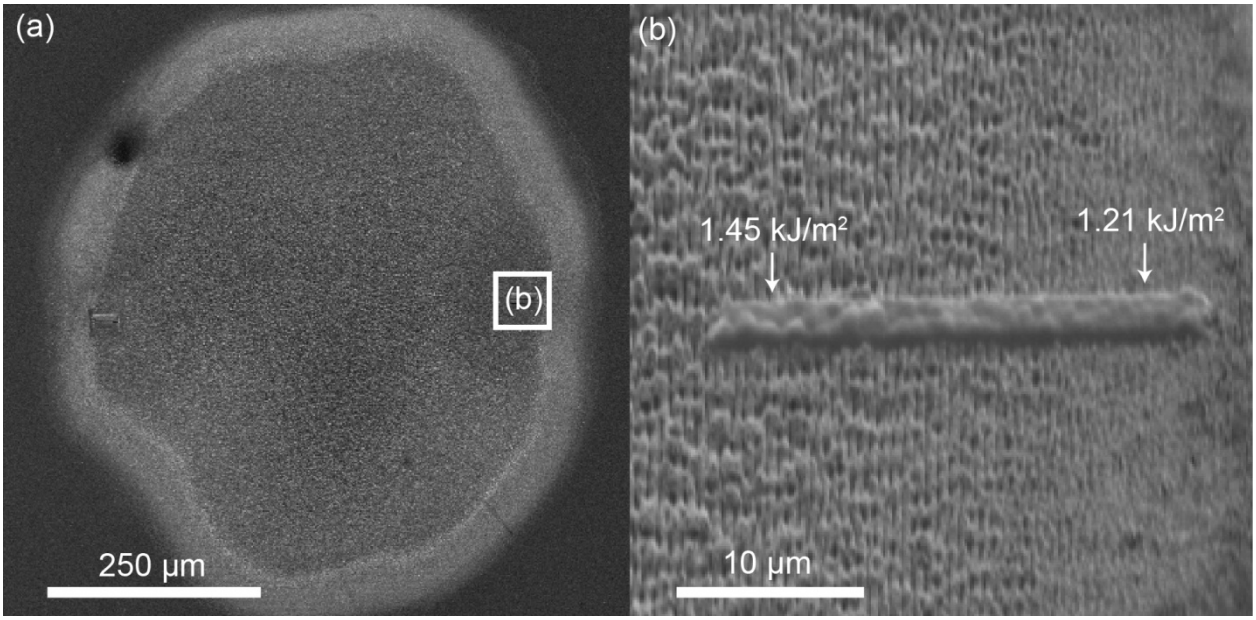

Figure 7.13. (a) SEM image of laser spot after 100 pulses at a peak fluence of 4 kJ/m^2. The low-fluence region investigated is shown in (b).

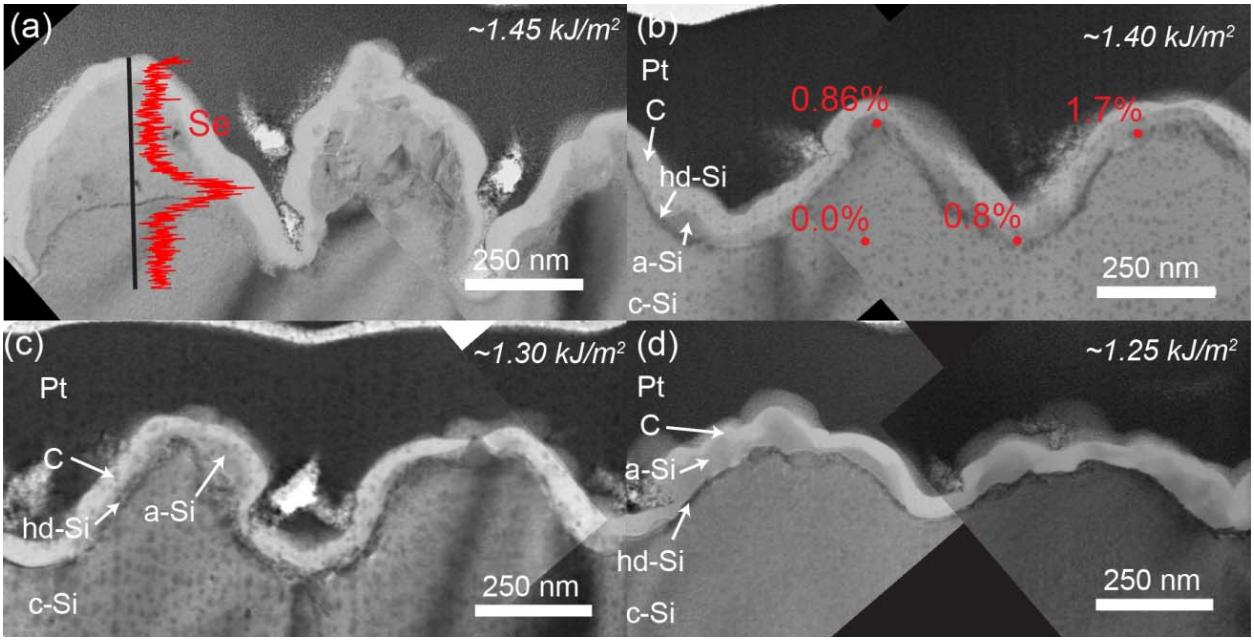

Figure 7.14. (a) Cross-sectional BF-TEM of surface irradiated with 100 pulses at a fluence of roughly 1.45 kJ/m^2 reveals polycrystalline spikes. EDX line scan shows selenium is concentrated at the base of the spike. (b) BF-TEM image of surface irradiated with 100 pulses at 1.4 kJ/m^2 shows LIPPS have a continuous crystalline surface layer with a discontinuous distribution of a-Si on the surface. EDX point scans indicate selenium composition in surface layer of around 1%. For clarity, the crystalline substrate (c-Si), hyperdoped silicon (hd-Si), amorphous silicon (a-Si), and protective coatings (C, Pt) are indicated. Similar features are visible after irradiation at 1.30 kJ/m^2 (c) and 1.25 kJ/m^2 (d).

Figure 7.14(a) shows the microstructure of the LIPSS that form after irradiation with 100 pulses at ~1.45 kJ/m^2. The microstructure in this regime has similar characteristics to the micron-scale peaks observed after irradiation at higher fluences. The ripples have a polycrystalline core with valleys that extend below the polycrystalline region. EDX shows a similar dopant distribution as well, with selenium predominantly present at the base of the polycrystalline regions.

Moving to lower fluences ($\leq$1.4 kJ/m^2) the microstructure changes and polycrystalline peaks are no longer present within the LIPSS, as shown in Figure 7.14(b-d). In this regime, we observe a continuous hyperdoped layer across the surface of the ripples, as confirmed by EDX (Figure 7.14(b)). This surface layer has oxygen concentrations that are comparable to what is resolved in the single-crystalline substrate, indicating that there is no significant oxygen incorporation. High-resolution imaging of the surface was used to confirm that the surface layer is crystalline (not shown), and there is a discontinuous layer of a-Si on the surface. Monitoring the thickness of the crystalline layer across the 1.4 – 1.25 kJ/m^2 range reveals that the average thickness of the hyperdoped layer increases with increasing fluence (Figure 7.15) from 11.2 ± 3.6 nm at 1.25 kJ/m^2 to 24.8 ± 12.3 nm at 1.40 kJ/m^2. Based on this trend, it appears that there is an optimal fluence for thin-film hyperdoping that maximizes the thickness of the surface layer while avoiding the formation of polycrystalline peaks.

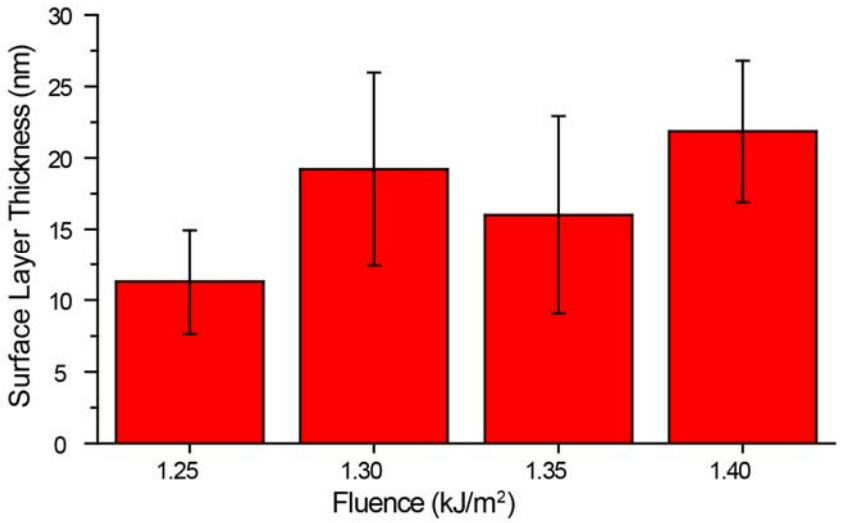

Figure 7.15. Thickness of the hyperdoped surface layer plotted as a function of fluence show slight trend of increasing surface layer thickness with increasing fluence. The thickness measurements were made across the entire 100-pulse TEM sample (Figure 7.14) and then binned into 4 groups.

In order to elucidate the dopant incorporation mechanisms between 10 and 100 shots and at fluences between 1.25 and 1.4 kJ/m^2, it is helpful to review what is understood about fs-laser irradiation of silicon in this low-fluence regime. The single shot melting threshold of silicon irradiated under these conditions (λ = 800 nm, τ = 100 fs) has been experimentally observed to be around 1.5 – 2 kJ/m^2 [47]. Melting during fs-laser irradiation, however, can occur through both thermal and non-thermal pathways and each has different thresholds. Non-thermal melting occurs when a large number (>10%) of the valence electrons are excited, resulting in a disordering of the lattice. This process is unique to fs- laser irradiation and occurs over 100's of femtoseconds [45, 49], whereas thermal melting takes tens of picoseconds to develop [49] and also occurs during slower (nanosecond-picosecond) pulsed laser irradiation. During fs-laser irradiation both non-thermal and thermal processes contribute to the melting process, but it is generally observed that the non-thermal melting threshold is ~1.5 times the fluence required for thermal melting [54].

The formation of selenium-hyperdoped silicon after 100 laser pulses necessitates sufficient melting at the surface to allow for the mixing of selenium with molten silicon. Laser irradiation at 1.25 – 1.4 kJ/m^2 is lower than the commonly-reported single-shot melting threshold for silicon (1.5 – 2 kJ/m^2), but it is empirically understood that laser modification thresholds decrease with increasing pulse number (section 2.2.1) [58]. For silicon, the modification thresholds follow the relationship:

$$\emptyset_{mod}(N) = \emptyset_{mod}(1) \times N^{\xi-1}$$

Here N is the number of laser pulses, and ξ is a material-dependent coefficient reported to be around 0.7 [80] to 0.84 [58] for silicon. If we take the single-shot thermal melting threshold of silicon to be 2 kJ/m^2, then the non-thermal melting threshold is around 3 kJ/m^2 and these values will decrease to <1 kJ/m^2 and <1.5 kJ/m^2, respectively, after 100 laser pulses. In agreement with these estimations, Izawa et al. reported non-thermal melting in silicon after 100 pulses (λ = 800 nm, τ = 100) at 1.5 kJ/m^2, and thermal melting after 100 pulses at 1.0 kJ/m^2 [170]. TEM investigations in the same study showed that non-thermal melting at 1.5 kJ/m^2 produced 30-40 nm of amorphous silicon on the surface, whereas thermal melting conditions at 1.0 kJ/m^2 resulting in a melt depth of 13 nm and was followed by regrowth of crystalline silicon.

Between 1.25-1.4 kJ/m^2 we observe a regrown layer of crystalline silicon that is 10-20 nm thick and hyperdoped with selenium. Comparing our results with those of Izawa et al., there

is strong evidence that the hyperdoped surface layer forms through thermal melting and recrystallization, which dominates only at sufficiently low fluences. Irradiation at higher fluences results in large volumes of amorphous silicon [104, 170], which we have observed leads to surface roughening and morphology-driven crystallization during thin-film femtosecond laser doping.

7.3.4 Conclusions

With the understanding that peak formation during thin-film fs-laser doping is coupled with local crystallization of dopant-rich amorphous material on the surface, we investigated dopant incorporation at fluences below which peak formation occurs (1.2-1.6 kJ/m^2). Irradiation with 10 pulses is insufficient to drive selenium incorporation in this fluence range, but after 100 pulses we observe selenium incorporation occurring in parallel with the formation of LIPSS. A 10-20 nm thick hyperdoped surface layer forms at fluences less than ~1.4 kJ/m^2. The fluence range over which this process occurs, the depth of dopant incorporation, and the epitaxial recrystallization support that hyperdoping is occurring through thermal melting. In addition to producing a continuous hyperdoped surface layer, irradiation under these conditions results in a flatter surface that is more conducive to conventional device processing.

7.4 Summary and Conclusions

In summary, by systematically investigating the relationship between irradiation conditions, surface morphology, dopant distribution, and microstructure, we have elucidated the fundamental mechanisms driving dopant incorporation during femtosecond laser doping from a selenium thin film.

Following the first laser pulse at 4 kJ/m^2, much of the selenium thin film is ablated/evaporated before any dopant incorporation occurs. This behavior is related to the different laser-modification thresholds of selenium, silicon, and the native silicon oxide, and presents a major challenge for using fs-laser irradiation to drive dopant incorporation from a thin film with drastically different material properties. With additional irradiation the surface roughens through to the formation and coalescence of amorphous silicon that contains ~1-2% of both oxygen and selenium. The crystallization of hyperdoped silicon occurs only in features protruding sufficiently from the surface, and we discussed the role that surface morphology has

in creating favorable conditions for the localized crystallization of hyperdoped silicon. TEM investigations into the microstructure show that the peaks grow through the incorporation and crystallization of amorphous silicon at the base of the peaks, likely through solid phase epitaxy. The crystallization of amorphous silicon continues with increasing laser irradiation, though material ablation drives the increase in peak amplitude during latter stages of irradiation. This mechanism of crystallization-driven peak growth at the surface explains both the increased size of the peaks on the surface as well as their polycrystalline structure. It also makes clear the point that, under these irradiation conditions, the crystallization of selenium-hyperdoped silicon is closely tied to the formation of spikes on the surface.

In order to synthesize a continuous layer of crystalline hyper-doped silicon using a selenium thin film dopant precursor, it was therefore necessary to explore the crystallization and dopant incorporation processes under different irradiation conditions. It was shown that peak formation is suppressed at sufficiently low fluences, instead forming LIPSS on the surface. After 10 laser pulses with fluences around 1.2-1.4 kJ/m^2 there is still a 10 nm selenium thin film on the surface, though it is still separated from the silicon substrate by the native silicon oxide layer. After 100 laser pulses in this fluence regime LIPSS form, with a 10-20 nm thick layer of crystalline, hyperdoped silicon on the surface. Irradiation in this lower fluence regime enables the formation of a hyperdoped surface layer because it does not ablate the selenium dopant precursor during early stage irradiation and, based on the resulting microstructure, favors thermal melting and recrystallization. The 10-20 nm thick hyperdoped layer is much thinner than what is achieved by gas phase doping under conventional irradiation conditions, but we anticipate the thickness can be increased through further refinement of the laser irradiation conditions.

This investigation exposes critical differences in the mechanisms behind doping from a selenium thin film and doping from a sulfur gaseous precursor, which have strong consequences on the irradiation conditions necessary to fabricate a continuous layer of hyperdoped material. Irradiation of silicon with many laser pulses at 4 kJ/m^2 creates micron-scale peaks on the surface during both the gas-phase and thin-film fs-laser doping. Peak formation during gas-phase fs-laser doping occurs through the removal of material from between the peaks due to self-focusing effects increasing the rate of material ablation from the regions between the peaks. When using a thin-film precursor, however, there exists a unique regime between 5-30 laser pulses during which the peaks grow rapidly upwards from the surface through the incorporation of amorphous

silicon at the base of the peaks. During gas-phase doping, increasing the fluence increases the thickness of the resulting hyperdoped surface layer [29], and thus irradiation above the ablation threshold is traditionally used to drive sufficient dopant incorporation. A gaseous dopant precursor acts as an effectively infinite source of dopants regardless of the irradiation conditions. In contrast, we have shown that high fluences ablate/evaporate the selenium thin film before substantial dopant incorporation can take place and proceeds to drive localized crystallization of hyperdoped material only within protruding surface features. Moving to fluences low enough to prevent complete ablation/evaporation (<1.4 kJ/m^2) of the selenium thin film enables uniform dopant incorporation through thermal melting and recrystallization. Irradiation at lower fluences results in less surface texturing, which is more conducive to incorporation into planar devices.

This progress in developing thin-film femtosecond laser doping as a platform for novel materials synthesis points to several outstanding questions for future investigation. First, we found that the differences in melting/ablation/evaporation thresholds between the selenium thin film and silicon substrate play an important role in the fs-laser doping process. It would be interesting to understand how the use of a more robust thin-film dopant precursor influences the dopant incorporation process. Second, we have fabricated of a selenium hyperdoped film that is only 10 – 20 nm thick. It will be important to establish how the thickness of the hyperdoped layer can be increased through further optimization of the irradiation conditions. Finally, hyperdoping across large length scales and characterization of the resulting bulk properties will require adapting the conclusions of this work to hyperdoping with a rastered laser beam.

Chapter 8 Conclusions

8.1 Summary of the thesis

This thesis investigated fs-laser irradiation as a platform for tailoring the optoelectronic properties of silicon through surface texturing and optical hyperdoping. In the first half of this thesis we investigated the extent of pressure-induced plastic deformation during the fs-laser irradiation of silicon and identified resolidification-induced stresses as a dominant source of pressure generation during surface texturing, with or without dopants present. The latter half of the thesis focused on the use of thin-film fs-laser doping as a platform for synthesizing hyperdoped silicon with improved absorption in the visible and infrared. Through understanding the thin-film dopant incorporation mechanisms we identified promising areas of parameter space for synthesizing device-compatible surface layers of hyperdoped silicon.

The incorporation of fs-laser irradiation into optoelectronic device fabrication necessitates a complete understanding of the mechanisms responsible for laser-induced damage. Our investigation into pressure-induced plastic deformation during fs-laser irradiation began in Chapter 4 with an investigation into the relationship between hyperdoping and pressure-induced phase transformations. It was found that pressure-induced phase transformations in silicon are relatively insensitive to the doping process but closely coupled with surface texturing. TEM investigations found that silicon polymorphs form due to pressure cycling in the core of the micron-scale spikes, far beneath the laser melt depth. The relative volumes of a-Si, Si-XII and Si-III that form are small and Si-XII is preferred over Si-III, all of which can be explained by the fast pressure cycles generated during fs-laser irradiation. Finally, by coupling Raman investigations with absorptance measurements and annealing trials, we show that the silicon polymorphs can be removed by annealing for 30 minutes at 700°C, similar to what is used in device processing. Questions remain, however, about the extent of plastic deformation that remains after annealing.

Chapter 4 showed a strong correlation between surface morphology and pressure-induced phase transformations, which raises questions about the mechanisms underlying the relationship between plastic deformation and surface texturing. The formation of Si-XII and Si-III can be easily suppressed in nanoindentation studies by pressure unloading on the scale of microseconds, indicating that the pressure-generation mechanism has a pressure decay time that is at least ten orders of magnitude longer than the duration of the laser pulse. Through a systematic

investigation into the relationship between laser irradiation conditions, surface texturing, silicon polymorph formation, and microstructure, Chapter 5 showed that resolidification-induced stresses are responsible for driving plastic deformation. This conclusion was supported by Raman investigations showing the dependence of silicon polymorph formation on irradiation conditions (laser fluence and fluence modulation), the residual strain in the silicon lattice, and TEM investigations confirming the amount of resolidification on the surface and the spatial distribution of amorphous silicon within the textured surface.

In the investigation into pressure-generation mechanisms, we also identified side-effects of laser rastering that are relevant to both surface texturing and hyperdoping. The rastering of a pulsed laser beam with a Gaussian profile delivers a wide range of fluences to each point on the surface, and the low-fluence irradiation has non-negligible consequences on the resulting material. The fluence modulation that occurs with rastering generates high concentrations of crystalline silicon polymorphs compared to irradiation with a stationary laser spot and, relatedly, increases the cumulative melt depth at the surface. The sub-surface annealing that occurs during low-fluence irradiation both drives the Si-XII → Si-III transformation and relaxes some of the residual stress in the material generated by resolidification of the molten surface layer.

Chapter 6 presented the first structural characterization of silicon fs-laser doped using a thin-film dopant precursor. The development of thin-film fs-laser irradiation for optical hyperdoping requires a thorough understanding of the dopant incorporation mechanisms, and little was understood about the effect of the phase of the dopant precursor on the doping process. We showed that thin film fs-laser doping generates much larger volumes of doped material than doping from a gas, and achieves higher absorptance at lower fluences. The resulting polycrystalline surface and discontinuous dopant distribution, however, affect p-n diode rectification and is not favorable for device fabrication. Structural investigations into the dopant distribution showed that the selenium is concentrated at the base of the surface peak and forms selenium-rich precipitates in this region with annealing. With this insight into the behavior of selenium dopants during moderate-to-high temperature anneals (575 - 900°C), we revisited previous investigations into the optical deactivation of selenium and found that they are consistent with a model for optical deactivation by diffusion-limited coarsening during the latter stages of absorptance decay. Though additional investigations are necessary to conclusively

demonstrate this, it appears likely that segregation plays a key role in the optical deactivation of selenium in silicon.

The application of thin-film fs-laser hyperdoping in optoelectronic devices requires a more continuous and homogeneous dopant distribution than what was studied in Chapter 6. The objective of Chapter 7 was to understand how dopant incorporation and surface structuring occurs when using a thin film dopant precursor, and to apply this knowledge to improving the overall dopant distribution. We showed that the crystallization of hyperdoped material on the surface is closely coupled with the evolution of surface roughness, likely as a result of the relationship between surface morphology, laser-material interactions, and the subsequent heat dissipation. Explosive recrystallization leads to polycrystalline protrusions on the surface, which grow into large polycrystalline peaks with continued irradiation. Investigations into microstructure and dopant distribution suggest that peak growth upwards is driven by the crystallization of material at the base of the peaks.

With this understanding of the relationship between surface texturing and localized crystallization, we investigated the dopant distribution at the surface following fs-laser irradiation under conditions that do not significantly texture the surface. Irradiation with many pulses (100) at sufficiently low fluences ($\leq$1.4 kJ/m^2) results in a 10-20 nm thick hyperdoped surface layer. Comparing the microstructure under these laser irradiation conditions with those of published pump-probe investigations suggest that hyperdoping occurs under these conditions through thermal melting. This investigation into the effect of the thin film exposed critical differences in the thin-film doping mechanisms. The unique dopant incorporation mechanisms have a strong consequence on the irradiation conditions necessary to fabricate a continuous layer of hyperdoped material, but our investigations suggest it is possible with optimal selection of irradiation conditions.

Investigations in this thesis have elucidated multiple fundamental mechanisms that are critical to the application of fs-laser irradiation to silicon-based photovoltaics. These studies illustrate how systematic investigations into the relationship between irradiation conditions, the microstructure and dopant distribution, and the resulting bulk properties are an effective and necessary approach to developing fs-laser irradiation as a platform for surface texturing and optical hyperdoping.

8.2 Suggested future work

8.2.1 Pulsed-laser surface texturing and laser-induced damage

Our investigations into pressure-induced phase transformations during fs-laser irradiation revealed that pulsed-laser irradiation of silicon is a unique system due to the temperature dependence of the plastic deformation mechanisms in silicon, and there are many open questions to be addressed. For example, this thesis focused primarily on the formation of silicon polymorphs, but we reported in section 5.3.2 that there is an upper limit on fluences that will generate Si-XII (over 88 pulses). This suggests that the plastic deformation mechanisms in silicon are dependent on fluence, though the effect of surface morphology on the resulting Raman spectra could also influence the observed trend. Based on this understanding, it will be valuable to investigate further the relationship between irradiation conditions, the resulting temperature, and plastic deformation. In addition to laser fluence, additional laser irradiation parameters that could have an effect on temperature at the surface include: pulsed laser frequency, temperature of the substrate, and pressure of the surrounding environment (ambient, vacuum, ultra-high vacuum). Once a complete understanding of the fluence dependence is developed, it will be possible to minimize plastic deformation by optimizing the beam profile and rastering speeds.

These investigations brought to light the role of resolidification-induced stresses on plastic deformation in silicon. Moving forward, it may be possible to reduce plastic deformation during surface texturing by mitigating resolidification induced stresses. For example, heating the sample during irradiation could slightly slow resolidification at the surface, resulting in less frustration and possibly reducing the magnitude of the resulting pressures. This might, however, be offset by the reduced hardness of silicon at elevated temperatures. Variation in the pulse duration should also be investigated as a route to reducing resolidification-induced stresses. It has been shown that fs-laser irradiation can result in drastically different stress distributions than ns-laser irradiation, even when used to create surface structures of similar geometry [94]. Finally, removing silicon polymorphs and healing plastic deformation in silicon with post-treatment annealing presents a straightforward route to reducing laser-induced damage. A better understanding of the microstructure as related to annealing conditions could motivate the introduction of an additional annealing step in the solar cell fabrication process, after surface texturing but before formation of the emitter.

The results of this thesis, which were based on investigations into the structure-property-processing relationships behind fs-laser irradiation of silicon, also suggest potential areas for complementary theoretical work. First, we observed that resolidification-induced stresses are strongly a function of surface morphology and this thesis drew on the previous work of Boroweic in order to interpret our findings (Figure 2.6). A more refined understanding of how surface morphology influences the distribution of residual stresses in silicon could inform optimal design of surface textures for minimized plastic deformation. A second area for complementary theoretical work is understanding the evolution in temperature beneath the surface and its relationship to surface morphology. Theoretical work on fs-laser irradiation often focuses on the melting/ablation processes occurring in a very shallow surface layer, and discussions about temperature evolution focus on temperature above or around the melting temperature [171-173]. Our investigations have shown that it would be valuable to study temperature evolution as related to surface texturing and at temperature ranges below the melting threshold of silicon (1414°C). Plastic deformation mechanisms are strongly affected by temperatures in the range of 200 – 500°C, and the thin-film investigations demonstrated that crystallization and coarsening can occur in the bulk of the peaks, which require only temperatures between 500°C - 1000°C.

8.2.2 Thin-film fs-laser doping

The understanding of thin-film fs-laser doping developed in this thesis addressed fundamental open questions about the use of a thin-film dopant precursor, and naturally raises another round of important questions surrounding the development of thin-film fs-laser doping as a platform for materials synthesis. Chapter 7 concluded by demonstrating the synthesis of a continuous layer of hyperdoped material on the surface, but there are still open questions about the realization of a large hyperdoped area suitable for device incorporation. The proof-of-concept hyperdoped layer synthesized in this thesis is only 10-20 nm thick, which is an order of magnitude thinner than what can be synthesized using gas-phase doping. It may be possible to increase the thickness of the doped layer by continuing to optimize the irradiation conditions, for example by moving to higher pulse numbers and lower fluences. Relatedly, the investigations in Chapter 7 were conducted on stationary laser spots, and in order to prepare large areas our findings in this thesis need to be adapted to laser-rastering. This conversion may assist in the

generation of thicker hyperdoped layers; we observed a much thicker resolidified layer in the rastered surface (Figure 7.14(c)) due to the large amount of low fluence irradiation produced by rastering the laser beam across the surface. For similar reasons, Shieh et al. observed improved recrystallization of an a-Si layer when the laser beam was rastered across the surface [174]. Shieh also heated the substrate to 400°C during irradiation, and a similar approach could aid in increasing the thickness of the laser-doped layers.

Beyond laser irradiation conditions, these investigations revealed that the properties of the thin film compared with the substrate will drastically influence the laser doping process. We found that the differences in melting/ablation/evaporation thresholds between the selenium thin film and silicon substrate required irradiation at very low fluences to avoid extensive removal of the thin film prior to dopant incorporation. This thesis demonstrated the drastic impact that using a thin-film precursor has on the dopant distribution and microstructure that form during fs-laser doping process, but there is still a wide range of parameter space for which the processing-structure relationship has not been elucidated. An attractive alternative to exploring all of processing parameter space experimentally would be to develop a theoretical framework that enables more rational material design. Such a framework is currently under development for gas-phase doping [104], and these investigations will aid the development of a framework for thin-film doping in the future.

Bibliography

[1] K. Emsley, *Nature's building blocks: An A-Z guide to the elements*. Oxford, U.K.: Oxford University Press, 2001.

[2] D. M. Powell*, et al.*, "Crystalline silicon photovoltaics: a cost analysis framework for determining technology pathways to reach baseload electricity costs," *Energy & Environmental Science,* vol. 5, pp. 5874-5883, 2012.

[3] S. Wilkinson, *Solar Industry,* vol. 4, 2011.

[4] R. Hull, *Properties of Crystalline Silicon*, 1 ed. London, UK: INSPEC, 1999.

[5] B. R. Tull, "Femtosecond Laser Ablation of Silicon: Nanoparticles, Doping and Photovoltaics," Doctor of Philosophy, School of Engineering and Applied Sciences, Harvard University, Cambridge, MA, 2007.

[6] K. R. Catchpole and A. Polman, "Plasmonic solar cells," *Opt. Express,* vol. 16, pp. 21793-21800, 2008.

[7] A. Bosio*, et al.*, "The second-generation of CdTe and CuInGaSe2 thin film PV modules," *Crystal Research and Technology,* vol. 46, pp. 857-864, 2011.

[8] M. A. Green and M. Keevers, "Optical properties of intrinsic silicon at 300 K," *Progress in Photovoltaics,* vol. 3, pp. 189-192, 1995.

[9] "ASTM Standard G173 - 03: Tables for Reference Solar Spectral Irradiances," ed. West Conshohocken, PA: ASTM International, 2008.

[10] M.-J. Sher*, et al.*, "Pulsed-laser hyperdoping and surface texturing for photovoltaics," *MRS Bulletin,* vol. 36, pp. 439-445, 2011.

[11] T. G. Kim, Jeffrey M. Warrender, and Michael J. Aziz, "Strong sub-band-gap infrared absorption in silicon supersaturated with sulfur," *Applied Physics Letters,* vol. 88, p. 3, 2006.

[12] M. A. Sheehy*, et al.*, "Chalcogen doping of silicon via intense femtosecond-laser irradiation," *Mat. Sci. Eng: B,* vol. 137, pp. 289-294, 2007.

[13] M. A. Green, "Lambertian light trapping in textured solar cells and light-emitting diodes: analytical solutions," *Progress in Photovoltaics: Research and Applications,* vol. 10, pp. 235-241, 2002.

[14] S. E. Han and G. Chen, "Toward the Lambertian Limit of Light Trapping in Thin Nanostructured Silicon Solar Cells," *Nano Letters,* vol. 10, pp. 4692-4696, 2010/11/10 2010.

[15] B. K. Nayak*, et al.*, "Efficient light trapping in silicon solar cells by ultrafast-laser-induced self-assembled micro/nano structures," *Progress in Photovoltaics: Research and Applications,* vol. 19, pp. 631-639, 2011.

[16] Y. Inomata*, et al.*, "Surface texturing of large area multicrystalline silicon solar cells using reactive ion etching method," *Solar Energy Materials and Solar Cells,* vol. 48, pp. 237-242, 1997.

[17] C. Zechner*, et al.*, "Systematic study towards high efficiency multicrystalline silicon solar cells with mechanical surface texturization," in *Photovoltaic Specialists Conference, 1997., Conference Record of the Twenty-Sixth IEEE*, 1997, pp. 243-246.

[18] H. M. Branz*, et al.*, "Nanostructured black silicon and the optical reflectance of graded-density surfaces," *Applied Physics Letters,* vol. 94, p. 231121, 2009.

[19] K. Nishioka*, et al.*, "Formation of antireflection nanostructure for silicon solar cells using catalysis of single nano-sized silver particle," *Applied Surface Science,* vol. 255, pp. 9504-9507, 2009.

[20] U. Gangopadhyay*, et al.*, "Comparative study of different approaches of multicrystalline silicon texturing for solar cell fabrication," *Solar Energy Materials and Solar Cells,* vol. 91, pp. 285-289, 2007.

[21] Y. Nishimoto and K. Namba, "Investigation of texturization for crystalline silicon solar cells with sodium carbonate solutions," *Solar Energy Materials and Solar Cells,* vol. 61, pp. 393-402, 2000.

[22] E. Vazsonyi, *et al.*, "Improved anisotropic etching process for industrial texturing of silicon solar cells," *Solar Energy Materials and Solar Cells,* vol. 57, pp. 179-188, 1999.
[23] R. Younkin, "Surface studies and microstructure fabrication using femtosecond laser pulses," Doctor of Philosophy, Division of Engineering and Applied Sciences, Harvard University, Cambridge, MA, 2001.
[24] R. Torres, *et al.*, "Femtosecond laser texturization for improvement of photovoltaic cells: black silicon," *J. Optoelectron. Adv. Mater.,* vol. 12, pp. 621-625, 2010.
[25] C. Vineis, *et al.*, "Ultrafast Laser Texturing for Enhanced Solar Cell Performance and Lower Cost - White Paper," in *http://sionyx.com/pdf/solarcellperformancewhitepaper.pdf*, ed: SiOnyx.
[26] L. A. Dobrzański, *et al.*, "Laser surface treatment of multicrystalline silicon for enhancing optical properties," *Journal of Materials Processing Technology,* vol. 201, pp. 291-296, 2008.
[27] M. Abbott and J. Cotter, "Optical and electrical properties of laser texturing for high-efficiency solar cells," *Progress in Photovoltaics: Research and Applications,* vol. 14, pp. 225-235, 2006.
[28] R. Younkin, *et al.*, "Infrared absorption by conical silicon microstructures made in a variety of background gases using femtosecond-laser pulses," *Journal of Applied Physics,* vol. 93, pp. 2626-2629, 2003.
[29] C. H. Crouch, *et al.*, "Infrared absorption by sulfur-doped silicon formed by femtosecond laser irradiation," *Applied Physics A: Materials Science & Processing,* vol. 79, pp. 1635-1641, 2004.
[30] A. J. Said, *et al.*, "Extended infrared photoresponse and gain in chalcogen-supersaturated silicon photodiodes," *Appl. Phys. Lett.,* vol. 99, pp. 073503/1-073503/3, 2011.
[31] E. Ertekin, *et al.*, "Insulator-to-Metal Transition in Selenium-Hyperdoped Silicon: Observation and Origin," *Physical Review Letters,* vol. 108, p. 026401, 2012.
[32] J. E. Carey, *et al.*, "Visible and near-infrared responsivity of femtosecond-laser microstructured silicon photodiodes," *Opt. Lett.,* vol. 30, pp. 1773-1775, 2005.
[33] R. O. Carlson, *et al.*, "Sulfur in silicon," *Journal of Physics and Chemistry of Solids,* vol. 8, pp. 81-83, 1959.
[34] E. Janzen, *et al.*, "Diffusion of tellurium dopant in silicon," *Journal of Applied Physics,* vol. 53, pp. 7367-7371, 1982.
[35] H. R. Vydyanath, *et al.*, "Defect pairing diffusion, and solubility studies in selenium-doped silicon," *Journal of Applied Physics,* vol. 49, pp. 5928-5937, 1978.
[36] A. Luque and A. Martí, "Increasing the Efficiency of Ideal Solar Cells by Photon Induced Transitions at Intermediate Levels," *Physical Review Letters,* vol. 78, p. 5014, 1997.
[37] W. Shockley and H. J. Queisser, "Detailed Balance Limit of Efficiency of p-n Junction Solar Cells," *Journal of Applied Physics,* vol. 32, pp. 510-519, 1961.
[38] N. F. Mott, "Metal-Insulator Transition," *Reviews of Modern Physics,* vol. 40, pp. 677-683, 1968.
[39] W. Walukiewicz, *et al.*, "Interaction of Localized Electronic States with the Conduction Band: Band Anticrossing in II-VI Semiconductor Ternaries," *Physical Review Letters,* vol. 85, p. 1552, 2000.
[40] K. M. Yu, *et al.*, "Diluted II-VI Oxide Semiconductors with Multiple Band Gaps," *Physical Review Letters,* vol. 91, p. 246403, 2003.
[41] N. López, *et al.*, "Engineering the Electronic Band Structure for Multiband Solar Cells," *Physical Review Letters,* vol. 106, p. 028701, 2011.
[42] A. Martí, *et al.*, "Production of Photocurrent due to Intermediate-to-Conduction-Band Transitions: A Demonstration of a Key Operating Principle of the Intermediate-Band Solar Cell," *Physical Review Letters,* vol. 97, p. 247701, 2006.
[43] W. Wang, *et al.*, "Intermediate-band photovoltaic solar cell based on ZnTe:O," *Applied Physics Letters,* vol. 95, pp. 011103-3, 2009.
[44] E. Antolin, *et al.*, "Lifetime recovery in ultrahighly titanium-doped silicon for the implementation of an intermediate band material," *Applied Physics Letters,* vol. 94, pp. 042115/1-042115/3, 2009.
[45] S. K. Sundaram and E. Mazur, "Inducing and probing non-thermal transitions in semiconductors using femtosecond laser pulses," *Nat Mater,* vol. 1, pp. 217-224, 2002.

[46] Y. Izawa, *et al.*, "Ablation and amorphization of crystalline Si by femtosecond and picosecond laser irradiation," *Japanese Journal of Applied Physics Part 1-Regular Papers Brief Communications & Review Papers,* vol. 45, pp. 5791-5794, Jul 2006.
[47] D. P. Korfiatis, *et al.*, "Conditions for femtosecond laser melting of silicon," *J. Phys. D: Appl. Phys.,* vol. 40, pp. 6803-6808, 2007.
[48] A. Rousse, *et al.*, "Non-thermal melting in semiconductors measured at femtosecond resolution," *Nature,* vol. 410, pp. 65-68, 2001.
[49] K. Sokolowski-Tinten, *et al.*, "Ultrafast laser-induced order-disorder transitions in semiconductors," *Physical Review B,* vol. 51, pp. 14186-14198, 1995.
[50] M. T. Winkler, "Non-Equilbrium Chalcogen Concentrations in Silicon: Physical Structure, Electronic Transport, and Photovoltaic Potential," Doctor of Philosophy, Physics, Harvard University, Cambridge, MA, 2009.
[51] T. E. Glover, "Hydrodynamics of particle formation following femtosecond laser ablation," *J. Opt. Soc. Am. B,* vol. 20, pp. 125-131, 2003.
[52] D. Perez and L. J. Lewis, "Molecular-dynamics study of ablation of solids under femtosecond laser pulses," *Physical Review B,* vol. 67, p. 184102, 2003.
[53] K. Sokolowski-Tinten and D. von der Linde, "Generation of dense electron-hole plasmas in silicon," *Physical Review B,* vol. 61, pp. 2643-2650, 2000.
[54] A. Cavalleri, *et al.*, "Femtosecond melting and ablation of semiconductors studied with time of flight mass spectroscopy," *Journal of Applied Physics,* vol. 85, pp. 3301-3309, 1999.
[55] D. von der Linde, *et al.*, "Laser–solid interaction in the femtosecond time regime," *Applied Surface Science,* vol. 109–110, pp. 1-10, 1997.
[56] D. H. Reitze, *et al.*, "Two-photon spectroscopy of silicon using femtosecond pulses at above-gap frequencies," *J. Opt. Soc. Am. B,* vol. 7, pp. 84-89, 1990.
[57] A. Borowiec, *et al.*, "Transmission and scanning electron microscopy studies of single femtosecond- laser-pulse ablation of silicon," *Appl. Phys. A: Mater. Sci. Process.,* vol. 76, pp. 201-207, 2003.
[58] J. Bonse, *et al.*, "Femtosecond laser ablation of silicon–modification thresholds and morphology," *Applied Physics A: Materials Science & Processing,* vol. 74, pp. 19-25, 2002.
[59] J. Bonse, *et al.*, "Modifying single-crystalline silicon by femtosecond laser pulses: an analysis by micro Raman spectroscopy, scanning laser microscopy and atomic force microscopy," *Applied Surface Science,* vol. 221, pp. 215-230, 2004.
[60] S. I. Kudryashov and V. I. Emel'yanov, "Structural Transitions in Silicon Induced by a Femtosecond Laser Pulse: The Role of an Electron-Hole Plasma and Phonon-Phonon Anharmonicity," *J. Exp. Theor. Phys.,* vol. 94, pp. 94-107, 2002.
[61] T. Y. Choi and C. P. Grigoropoulos, "Observation of Femtosecond Laser-Induced Ablation in Crystalline Silicon," *Journal of Heat Transfer,* vol. 126, pp. 723-726, 2004.
[62] K. Sokolowski-Tinten and D. von der Linde, "Ultrafast phase transitions and lattice dynamics probed using laser-produced x-ray pulses," *Journal of Physics: Condensed Matter,* vol. 16, p. R1517, 2004.
[63] M. C. Downer and C. V. Shank, "Ultrafast heating of silicon on sapphire by femtosecond optical pulses," *Physical Review Letters,* vol. 56, pp. 761-764, 1986.
[64] R. R. Gattass and E. Mazur, "Femtosecond laser micromachining in transparent materials," *Nat Photon,* vol. 2, pp. 219-225, 2008.
[65] J. M. Liu, *et al.*, "Phase transformation on and charged particle emission from a silicon crystal surface, induced by picosecond laser pulses," *Applied Physics Letters,* vol. 39, pp. 755-757, 1981.
[66] M. O. Thompson, *et al.*, "Silicon Melt, Regrowth, and Amorphization Velocities During Pulsed Laser Irradiation," *Physical Review Letters,* vol. 50, pp. 896-899, 1983.
[67] K. Sokolowski-Tinten, *et al.*, "Transient States of Matter during Short Pulse Laser Ablation," *Physical Review Letters,* vol. 81, pp. 224-227, 1998.

[68] G. Paltauf and H. Schmidt-Kloiber, "Microcavity dynamics during laser-induced spallation of liquids and gels," *Applied Physics A: Materials Science & Processing,* vol. 62, pp. 303-311, 1996.
[69] R. Evans*, et al.*, "Time- and Space-Resolved Optical Probing of Femtosecond-Laser-Driven Shock Waves in Aluminum," *Physical Review Letters,* vol. 77, p. 3359, 1996.
[70] A. Borowiec*, et al.*, "Sub-surface damage in indium phosphide caused by micromachining of grooves with femtosecond and nanosecond laser pulses," *Appl. Phys. A: Mater. Sci. Process.,* vol. 79, pp. 1887-1890, 2004.
[71] A. Luft*, et al.*, "A study of thermal and mechanical effects on materials induced by pulsed laser drilling," *Applied Physics A: Materials Science & Processing,* vol. 63, pp. 93-101, 1996.
[72] S. Liu*, et al.*, "Laser induced plasma in the formation of surface-microstructured silicon," *Mater. Lett.,* vol. 62, pp. 3881-3883, 2008.
[73] T. Sano*, et al.*, "Femtosecond laser synthesis of polymorphic diamond from highly oriented pyrolytic graphite," in *Pricm 6: Sixth Pacific Rim International Conference on Advanced Materials and Processing, Pts 1-3*. vol. 561-565, Y. W. Chang*, et al.*, Eds., ed Stafa-Zurich: Trans Tech Publications Ltd, 2007, pp. 2349-2352.
[74] A. Ng*, et al.*, "Heat front propagation in femtosecond-laser-heated solids," *Physical Review E,* vol. 51, pp. R5208-R5211, 1995.
[75] M. Tsujino, "Quenching of High-Pressure Phases of Silicon Using Femtosecond Laser-driven Shock Wave," *The Review of Laser Engineering,* vol. 36, pp. 1218-1221, 2008.
[76] T. Sano*, et al.*, "Femtosecond laser quenching of the epsilon phase of iron," *Applied Physics Letters,* vol. 83, pp. 3498-3500, 2003.
[77] J. P. Cuq-Lelandais*, et al.*, "Spallation generated by femtosecond laser driven shocks in thin metallic targets," *Journal of Physics D: Applied Physics,* vol. 42, p. 065402, 2009.
[78] D. J. Funk*, et al.*, "Ultrafast measurement of the optical properties of aluminum during shock-wave breakout," *Physical Review B,* vol. 64, p. 115114, 2001.
[79] B. R. Tull*, et al.*, " Surface morphologies of silicon surfaces after femtosecond laser irradiation," *Mat. Res. Soc. Bull.,* vol. 31, p. 7, 2006.
[80] E. Coyne*, et al.*, "Characterization of laser ablation of silicon using a Gaussian wavefront and computer generated wavefront reconstruction," *Appl. Surf. Sci.,* vol. 229, pp. 148-160, 2004.
[81] Y. Jee*, et al.*, "Laser-induced damage on single-crystal metal surfaces," *J. Opt. Soc. Am. B,* vol. 5, pp. 648-659, 1988.
[82] P. L. Liu*, et al.*, "Picosecond laser-induced melting and resolidification morphology on Si," *Applied Physics Letters,* vol. 34, pp. 864-866, 1979.
[83] J. Bonse*, et al.*, "Structure formation on the surface of indium phosphide irradiated by femtosecond laser pulses," *Journal of Applied Physics,* vol. 97, pp. 013538-9, 2005.
[84] H. M. van Driel*, et al.*, "Laser-induced coherent modulation of solid and liquid surfaces," *Journal of Luminescence,* vol. 30, pp. 446-471, 1985.
[85] U. Chakravarty*, et al.*, "Nano-ripple formation on different band-gap semiconductor surfaces using femtosecond pulses," *Journal of Applied Physics,* vol. 109, pp. 084347-8, 2011.
[86] E. M. Hsu*, et al.*, "Cross-sectional study of periodic surface structures on gallium phosphide induced by ultrashort laser pulse irradiation," *Applied Physics Letters,* vol. 92, pp. 221112-3, 2008.
[87] R. Le Harzic*, et al.*, "Generation of high spatial frequency ripples on silicon under ultrashort laser pulses irradiation," *Applied Physics Letters,* vol. 98, pp. 211905-3, 2011.
[88] D. H. Lowndes*, et al.*, "Early stages of pulsed-laser growth of silicon microcolumns and microcones in air and SF6," *Applied Surface Science,* vol. 154-155, pp. 647-658, 2000.
[89] C. H. Crouch, J.E. Carey, J. M. Warrender, M. J. Aziz, E. Mazur, F.Y. Genin, "Comparison of structure and properties of femtosecond and nanosecond laser-structured silicon," *Applied Physics Letters,* vol. 84, p. 3, 2004.

[90] V. Zorba*, et al.*, "Laser microstructuring of Si surfaces for low-threshold field-electron emission," *Thin Solid Films,* vol. 453–454, pp. 492-495, 2004.
[91] S. Schoenfelder*, et al.*, "Strength Characterization of Laser Diced Silicon for Application in Solar Industry," in *European Photovoltaic Solar Energy Conference*, 2006.
[92] A. Hedler*, et al.*, "Amorphous silicon exhibits a glass transition," *Nat Mater,* vol. 3, pp. 804-809, 2004.
[93] M. S. Amer*, et al.*, "Induced stresses and structural changes in silicon wafers as a result of laser micro-machining," *Applied Surface Science,* vol. 187, pp. 291-296, 2002.
[94] A. Borowiec*, et al.*, "Imaging the strain fields resulting from laser micromachining of semiconductors," *Applied Physics Letters,* vol. 83, pp. 225-227, 2003.
[95] V. Domnich and Y. G. Gogotsi, "Phase Transformations in Silicon under Contact Loading," *Rev. Adv. Mater. Sci. ,* vol. 3, p. 36, 2002.
[96] A. Kailer*, et al.*, "Phase transformations of silicon caused by contact loading," *Journal of Applied Physics,* vol. 81, pp. 3057-3063, 1997.
[97] H. Olijnyk and A. P. Jephcoat, "Effect of Pressure on Raman Spectra of Metastable Phases of Si and Ge," *Phys. Status Solidi B,* vol. 211, pp. 413-420, 1999.
[98] M. Born and E. Wolf, *Principles of Optics*. Cambridge: Cambridge University Press, 1999.
[99] D. B. Williams and C. B. Carter, *Transmission Electron Microscopy*, 8th ed.: Springer Science, 2009.
[100] L. Reimer, *Scanning Electron Microscopy*, 2nd ed. vol. 45. Berlin Heidelberg New York: Springer, 1998.
[101] K. Hayakawa*, et al.*, "Experimental and full multiple scattering approaches to energy-loss near-edge structures (ELNES) for c-Si, a-Si and a-Si:H," *Chemical Physics Letters,* vol. 371, pp. 498-503, 2003.
[102] R. F. Egerton, "Electron energy-loss spectroscopy in the TEM," *Reports on Progress in Physics,* vol. 72, p. 016502, 2009.
[103] D. E. Hoglund*, et al.*, "Experimental test of morphological stability theory for a planar interface during rapid solidification," *Physical Review B,* vol. 58, pp. 189-199, 1998.
[104] M. T. Winkler*, et al.*, "Model Systems for Studying Femtosecond-laser Hyperdoping," *Journal of Applied Physics,* vol. 111, p. 093511, 2012.
[105] M. Schade*, et al.*, "High-resolution investigations of ripple structures formed by femtosecond laser irradiation of silicon," *Analytical and Bioanalytical Chemistry,* vol. 396, 2010.
[106] F. Costache*, et al.*, "Sub–damage–threshold femtosecond laser ablation from crystalline Si: surface nanostructures and phase transformation," *Applied Physics A: Materials Science & Processing,* vol. 79, pp. 1429-1432, 2004.
[107] V. Domnich*, et al.*, "Temperature Dependence of Silicon Hardness: Experimental Evidence of Phase Transformations," *Rev. Adv. Mater. Sci.,* vol. 17, pp. 33-41, 2008.
[108] A. Jayaraman, "Diamond anvil cell and high-pressure physical investigations," *Reviews of Modern Physics,* vol. 55, p. 65, 1983.
[109] S. R. Jian*, et al.*, "Nanoindentation-induced phase transformation in (110)-oriented Si single-crystals," *Current Opinion in Solid State and Materials Science,* vol. 14, pp. 69-74, 2010.
[110] A. George, "High pressure phases of c-Si," in *Properties of Crystalline Silicon*, R. Hull, Ed., ed London, United Kingdom: INSPEC, 1999.
[111] S. Ruffell*, et al.*, "High pressure crystalline phase formation during nanoindentation: Amorphous versus crystalline silicon," *Applied Physics Letters,* vol. 89, 2006.
[112] J. Crain*, et al.*, "Reversible pressure-induced structural transitions between metastable phases of silicon," *Physical Review B,* vol. 50, p. 13043, 1994.
[113] J.-i. Jang*, et al.*, "Indentation-induced phase transformations in silicon: influences of load, rate and indenter angle on the transformation behavior," *Acta Materialia,* vol. 53, pp. 1759-1770, 2005.

[114] S. Ruffell, *et al.*, "Annealing of nanoindentation-induced high pressure crystalline phases created in crystalline and amorphous silicon," *Journal of Applied Physics,* vol. 105, p. 8, May 2009.
[115] S. Ruffell, *et al.*, "Annealing kinetics of nanoindentation-induced polycrystalline high pressure phases in crystalline silicon," *Applied Physics Letters,* vol. 90, p. 3, Mar 2007.
[116] S. Ruffell and et al., "Nanoindentation-induced phase transformations in silicon at elevated temperatures," *Nanotechnology,* vol. 20, p. 135603, 2009.
[117] B. D. Malone, *et al.*, "Ab initio study of the optical properties of Si-XII," *Physical Review B,* vol. 78, p. 161202, 2008.
[118] G. Weill and et al., "Characterisation of Si III and Si IV, metastable forms of silicon at ambient pressure," *Semiconductor Science and Technology,* vol. 4, p. 280, 1989.
[119] Y. Yan, *et al.*, "Atomic structure and electronic properties of c-Si/a-Si:H heterointerfaces," *Applied Physics Letters,* vol. 88, p. 121925, 2006.
[120] Y. Izawa, *et al.*, "Ultrathin amorphous Si layer formation by femtosecond laser pulse irradiation," *Applied Physics Letters,* vol. 90, pp. 044107-2, 2007.
[121] D. Ge, *et al.*, "Thermal stability of metastable silicon phases produced by nanoindentation," *Journal of Applied Physics,* vol. 95, p. 2725, 2004.
[122] B. R. Tull, *et al.*, "The role of diffusion in broadband infrared absorption in chalcogen-doped silicon," *Appl. Phys. A: Mater. Sci. Process.,* vol. 96, pp. 327-334, 2009.
[123] B. R. Tull, *et al.*, "The role of diffusion in broadband infrared absorption in chalcogen-doped silicon," *Appl. Phys. A,* vol. 96, pp. 327-334, 2009.
[124] S. Ruffell, *et al.*, "Formation and growth of nanoindentation-induced high pressure phases in crystalline and amorphous silicon," *Journal of Applied Physics,* vol. 102, pp. 063521-8, 2007.
[125] J. I. Jang, *et al.*, "Indentation-induced phase transformations in silicon: influences of load, rate and indenter angle on the transformation behavior," *Acta Materialia,* vol. 53, pp. 1759-1770, 2005.
[126] T. H. R. Crawford, *et al.*, "Crystalline orientation effects on conical structure formation in femtosecond laser irradiation of silicon and germanium," *Applied Surface Science,* vol. 256, pp. 1749-1755, 2010.
[127] G. L. Olson and J. A. Roth, "Kinetics of solid phase crystallization in amorphous silicon," *Materials Science Reports,* vol. 3, pp. 1-77, 1988.
[128] Q. Feng, *et al.*, "Femtosecond laser micromachining of a single-crystal superalloy," *Scripta Materialia,* vol. 53, pp. 511-516, 2005.
[129] R. O. Piltz, *et al.*, "Structure and properties of silicon XII: A complex tetrahedrally bonded phase," *Physical Review B,* vol. 52, p. 4072, 1995.
[130] T. Q. Jia, *et al.*, "Microscopic mechanisms of ablation and micromachining of dielectrics by using femtosecond lasers," *Applied Physics Letters,* vol. 82, pp. 4382-4384, 2003.
[131] M. S. Amer, *et al.*, "Femtosecond versus nanosecond laser machining: comparison of induced stresses and structural changes in silicon wafers," *Applied Surface Science,* vol. 242, pp. 162-167, 2005.
[132] F. Falk and G. Andrä, "Laser crystallization — a way to produce crystalline silicon films on glass or on polymer substrates," *Journal of Crystal Growth,* vol. 287, pp. 397-401, 2006.
[133] Y. Li, *et al.*, "Numerical Simulation and Analysis on 3D Temperature Field of the Metal Ablated with Femtosecond Pulse Laser," *Journal of Physics: Conference Series,* vol. 276, p. 012032, 2011.
[134] T.-H. Her, *et al.*, "Microstructuring of silicon with femtosecond laser pulses," *Applied Physics Letters,* vol. 73, pp. 1673-1675, 1998.
[135] C. Wu, *et al.*, "Near-unity below-band-gap absorption by microstructured silicon," *Appl. Phys. Lett. ,* vol. 78, pp. 1850-1852, 2001.
[136] M. A. Sheehy, *et al.*, "Role of the Background Gas in the Morphology and Optical Properties of Laser-Microstructured Silicon," *Chem. Mat. ,* vol. 17, pp. 3582-3586, 2005.

[137] C. H. Crouch*, et al.*, "Comparison of structure and properties of femtosecond and nanosecond laser-structured silicon," *Appl. Phys. Lett.,* vol. 84, pp. 1850-1852, 2004.
[138] J. T. S. B.K. Newman, M.T. Winkler, M.J. Sher, M.A. Marcus, M.J. Smith, S. Gradecak, E. Mazur, T. Buonassisi, "Illuminating The mechanism for Sub-bandgap absorption in chalcogen doped silicon materials for PV applications," in *25th European Photovoltaic Solar Energy Conference Proceedings*, Feria Valencia, Spain, 2009.
[139] V. Zorba*, et al.*, "Ultraviolet femtosecond, picosecond and nanosecond laser microstructuring of silicon: structural and optical properties," *Appl. Opt.,* vol. 47, pp. 1846-1850, 2008.
[140] A. J. Pedraza*, et al.*, "Silicon microcolumn arrays grown by nanosecond pulsed-excimer laser irradiation," *Applied Physics Letters,* vol. 74, pp. 2322-2324, 1999.
[141] Y. Takamura*, et al.*, "Thermal stability of dopants in laser annealed silicon," *Journal of Applied Physics,* vol. 92, pp. 230-234, 2002.
[142] I. M. Lifshitz and V. V. Slyozov, "The kinetics of precipitation from supersaturated solid solutions," *Journal of Physics and Chemistry of Solids,* vol. 19, pp. 35-50, 1961.
143] C. Wagner, "Theorieder Al Terung Von Niederschlagen Durch Umlosen (Ostwald-Reifung)," *Zeitschrift Fur Elektrochemie,* vol. 65, pp. 581-591, 1961.
[144] A. J. Ardell, "Further applications of the theory of particle coarsening," *Acta Metallurgica,* vol. 15, pp. 1772-1775, 1967.
[145] A. Ardell, "The growth of gamma prime precipitates in aged Ni−Ti alloys," *Metallurgical and Materials Transactions B,* vol. 1, pp. 525-534, 1970.
[146] H. Okamoto, "Se-Si (Selenium-Silicon)," *J. Phase Equilib.,* vol. 21, 2000.
[147] A. J. Ardell and R. B. Nicholson, "The coarsening of γ' in Ni-Al alloys," *Journal of Physics and Chemistry of Solids,* vol. 27, pp. 1793-1794, 1966.
[148] J. R. Köhler and S. Eisele, "Influence of precursor layer ablation on laser doping of silicon," *Progress in Photovoltaics: Research and Applications,* vol. 18, pp. 334-339, 2010.
[149] J. A. Kittl*, et al.*, "Complete experimental test of kinetic models for rapid alloy solidification," *Acta Materialia,* vol. 48, pp. 4797-4811, 2000.
[150] L. A. Lompre*, et al.*, "Time-resolved temperature measurement of picosecond laser irradiated silicon," *Applied Physics Letters,* vol. 43, pp. 168-170, 1983.
[151] E. Landi*, et al.*, "Numerical simulation of the gas immersion laser doping (GILD) process in silicon," *Computer-Aided Design of Integrated Circuits and Systems, IEEE Transactions on,* vol. 7, pp. 205-214, 1988.
[152] C. W. White*, et al.*, "Supersaturated substitutional alloys formed by ion implantation and pulsed laser annealing of group-III and group-V dopants in silicon," *Journal of Applied Physics,* vol. 51, pp. 738-749, 1980.
[153] R. Reitano*, et al.*, "Solute trapping of group III, IV, and V elements in silicon by an aperiodic stepwise growth mechanism," *Journal of Applied Physics,* vol. 76, pp. 1518-1529, 1994.
[154] V. I. Emel'yanov and D. V. Babak, "Defect capture under rapid solidification of the melt induced by the action of femtosecond laser pulses and formation of periodic surface structures on a semiconductor surface," *Applied Physics A: Materials Science & Processing,* vol. 74, pp. 797-805, 2002.
[155] K. Affolter*, et al.*, "Properties of laser-assisted doping in silicon," *Applied Physics Letters,* vol. 33, pp. 185-187, 1978.
[156] D. Bäuerle, Ed., *Laser Processing and Diagnostics* (Springer Series in Chemical Physics. Berlin Heidelberg New York Tokyo: Springer-Verlag, 1984, p.^pp. Pages.
[157] J. Narayan*, et al.*, "Explosive recrystallization during pulsed laser irradiation," *J. Vac. Sci. Technol., A,* vol. 2, pp. 1495-7, 1984.
[158] M. J. Aziz and T. Kaplan, "Continuous growth model for interface motion during alloy solidification," *Acta Metallurgica,* vol. 36, pp. 2335-2347, 1988.

[159] M. Tabbal*, et al.*, "Excimer laser processing of novel materials for optoelectronic and spintronic applications," *Photon Processing in Microelectronics and Photonics VI,* vol. Proc. SPIE 6458, 2007.
[160] M. Tabbal*, et al.*, "Fabrication and sub-band-gap absorption of single-crystal Si supersaturated with Se by pulsed laser mixing," *Appl. Phys. A: Mater. Sci. Process.,* vol. 98, pp. 589-594, 2010.
[161] J. M. Fairfield and G. H. Schwuttke, "Silicon diodes made by laser irradiation," *Solid-State Electronics,* vol. 11, pp. 1175-IN6, 1968.
[162] D. Bäuerle, *Laser Processing and Chemistry*, 3rd ed. Berlin Heidelberg New York: Springer-Verlag, 2000.
[163] B. P. Bob*, et al.*, "Fabrication and subband gap optical properties of silicon supersaturated with chalcogens by ion implantation and pulsed laser melting," *Journal of Applied Physics,* vol. 107, pp. 123506-5, 2010.
[164] E. P. Fogarassy*, et al.*, "UV laser incorporation of dopants into silicon: Comparison of two processes," *Journal of Applied Physics,* vol. 58, pp. 2167-2173, 1985.
[165] Y. N. Picard and S. M. Yalisove, "Femtosecond laser heat affected zones profiled in Co/Si multilayer thin films," *Appl. Phys. Lett.,* vol. 92, pp. 014102/1-014102/3, 2008.
[166] S. Roorda*, et al.*, "Solid Phase Epitaxial Regrowth of Microcrystalline Si Films on a (100) Si Substrate," *MRS Online Proceedings Library,* vol. 100, pp. null-null, 1988.
[167] S. Valette*, et al.*, "Heat affected zone in aluminum single crystals submitted to femtosecond laser irradiations," *Applied Surface Science,* vol. 239, pp. 381-386, 2005.
[168] Z. Guosheng*, et al.*, "Growth of spontaneous periodic surface structures on solids during laser illumination," *Physical Review B,* vol. 26, pp. 5366-5381, 1982.
[169] J. E. Sipe*, et al.*, "Laser-induced periodic surface structure. I. Theory," *Physical Review B,* vol. 27, pp. 1141-1154, 1983.
[170] Y. Izawa*, et al.*, "Ultra fast melting process in femtosecond laser crystallization of thin a-Si layer," *Appl. Surf. Sci.,* vol. 255, pp. 9764-9769, 2009.
[171] C. Cheng and X. Xu, "Molecular dynamic study of volumetric phase change induced by a femtosecond laser pulse," *Applied Physics A: Materials Science & Processing,* vol. 79, pp. 761-765, 2004.
[172] P. Lorazo*, et al.*, "Thermodynamic pathways to melting, ablation, and solidification in absorbing solids under pulsed laser irradiation," *Physical Review B,* vol. 73, p. 134108, 2006.
[173] X. Qi and C. S. Suh, "Generalized thermo-elastodynamics for semiconductor material subject to ultrafast laser heating. Part I: Model description and validation," *International Journal of Heat and Mass Transfer,* vol. 53, pp. 41-47, 2010.
[174] J.-M. Shieh*, et al.*, "Near-infrared femtosecond laser-induced crystallization of amorphous silicon," *Appl. Phys. Lett.,* vol. 85, pp. 1232-1234, 2004.